THE UNIVERSITY *of* EDINBURGH

Probing Dark Energy and Modified Gravity with Galaxy Clustering and Weak Lensing

Maria Tsedrik

Supervised by Alkistis Pourtsidou

Doctor of Philosophy
The University of Edinburgh
October 2024

Lay Summary

For decades cosmologists have been searching for a simple and elegant model that describes our Universe, its components and laws. Right now, the standard cosmological model, fully described by six parameters, is the gold standard of the field. It tells us that all matter in the Universe interacts according to the laws of General Relativity and that the majority of this matter is invisible dark matter. Another dominating component of the model with a mysterious origin is called dark energy. It causes the accelerated expansion of the Universe. Despite the lack of clear understanding about the nature of dark matter and dark energy, their existence within the standard cosmological model is required to explain numerous observations. One of these observations is the relic light, called Cosmic Microwave Background, which was emitted just 370 thousand years after the hot Big Bang. Small temperature fluctuations in the relic light correspond to small matter fluctuations that eventually grow due to gravitational interactions into all of the structures we observe around us today: from stars to galaxies and galaxy clusters.

In this thesis, we discuss two ways of looking at galaxies in the late-time Universe, 5-14 billion years after the Big Bang: spectroscopic galaxy clustering and weak gravitational lensing. In the first approach, we treat galaxies as points and analyse their distributions across the sky and along time. In the second approach, we treat distant galaxies as ellipses and analyse how their observed shapes are weakly distorted, or sheared. The distortion is caused by the bending of their light on its way to us by gravitationally intervening massive structures. Interestingly, galaxy clustering and weak lensing measurements both consistently result in a lower amount of matter clustering than the one expected from the Cosmic Microwave Background measurement. This disagreement between the observations implies that in the standard cosmological model it is impossible to bridge the amplitude of matter fluctuations measured at late times with the one measured at early times.

As a potential solution for this intriguing conundrum we propose the so-called extended cosmologies. Such cosmological models extend the standard parameter space of six cosmological parameters by introducing several additional parameters. The additional parameters correspond to modifications of gravity or dark energy. These modifications impact structure formation on all scales. In particular, we are interested in the alternations of structure growth on smaller scales as they correspond to the regime of complex nonlinear physics. The older the Universe becomes, the more nonlinear structures evolve. Despite its complexity there is a great amount of cosmological information in this regime, especially helpful to distinguish between various non-standard cosmologies. Hence, we must develop and test robust modelling tools for extended cosmologies down to smaller scales.

Here, we address this challenge in the light of the newest generation of cosmological surveys. Dark Energy Spectroscopic Instrument (DESI), Euclid, Vera Rubin Observatory (VRO/LSST) – these powerful surveys have started (DESI, Euclid) or will soon start (VRO/LSST) observing millions of galaxies, their positions and shapes. Their

excellent measurements will unambiguously weaken or strengthen the tension between the clustering amplitudes. The only restriction of our knowledge of the Universe will be the efficiency of our methods and accuracy of our models.

In this thesis, we apply advanced theoretical models and state-of-the-art numerical methods to study the interplay between numerous different parameters. For instance, these parameters aim to capture the complexity of nonlinear structure formation, or the connection between visible and non-visible matter. Extended cosmologies introduce an additional degree of complexity that we investigate with simulated and real data. The methods and techniques developed and tested in this thesis are timely given the beginning of the precision cosmology era with the new generation of surveys. Most of the codes used in our projects are (or soon will be) publicly available. They will facilitate efficient and accurate probing of the Large Scale Structure, and help us to determine the correct model describing our Universe.

Abstract and Outline

The new generation of cosmological surveys, called Stage-IV surveys, provides measurements of unprecedented volume and quality. This, in turn, leads to increased statistical precision. Now our knowledge of the Universe is restricted by the efficiency of our methods and accuracy of our models, rather than by our measurements (assuming that observational systematics are fully understood). Therefore, our goal is to develop and test methods and models for analysing the data in order to reliably extract as much information as possible. We do so by extending standard modelling techniques into the nonlinear regime. We apply the nonlinear techniques to non-standard cosmological models, such as evolving and interacting dark energy models, modified gravity theories, and massive neutrinos. These alternative models attempt to resolve tensions between the cosmological parameters extracted from the early-time (high-redshift) and late-time (low-redshift) Universe, which arise in the paradigm of the standard cosmology, ΛCDM.

We refer to the measurements with which we study the laws and constituents of our Universe as cosmological probes. In this thesis we work with two cosmological probes of the late-time Universe: galaxy clustering and weak lensing. The redshifts of galaxies can be precisely measured with spectroscopic instruments. From the distribution of galaxies in redshift space we can build and then model summary statistics. Here we focus on the power spectrum and bispectrum multipoles as our main galaxy clustering observables. Regarding weak gravitational lensing, this phenomenon corresponds to the coherent distortion in the observed shapes of distant galaxies due to the bending of light by the Large Scale Structure. The degree of distortion, or shear, depends on the amount and concentration of matter along the propagation of light. Based on the measured galaxy shape distribution from photometric images, we again can build various statistics. In this thesis we focus on the cosmic shear power spectrum as our main weak lensing observable.

The goal of Chapter 1 and Chapter 2 is to provide the background information required to grasp the findings of the latter chapters. Chapter 1 familiarises the reader with the main cosmological and theoretical concepts that are necessary to understand the modelling of our main observables. We motivate our interest in the extensions of the standard cosmological model, as well as demonstrate explicitly what changes they introduce at the level of the observables. Chapter 2 establishes the notion of probability in two frameworks, Bayesian and Frequentist, that allows us to assess the accuracy of a model given the data. In the same chapter we also describe the mechanisms of the probability distribution sampling, i.e., the mechanisms of geometrically exploring the regions of the model's parameter space that describe the data best.

In Chapter 3, we analyse the redshift space power spectrum and bispectrum multipoles of dark matter halos from a large set of simulations. Interacting dark energy, in particular the "Dark Scattering" model in which dark energy and dark matter are coupled by pure momentum exchange, is the main focus of this chapter. We find a substantial improvement of constraints on the dark energy parameters when the bispectrum multipoles are

combined with the power spectrum multipoles. In Chapter 4, using the same perturbative framework, we analyse the power spectrum multipoles from a Stage-III spectroscopic survey, BOSS DR12. Now we focus on constraining a generalised parameterisation of modified gravity via the growth index and massive neutrinos. Albeit without a crucial statistical significance, we find values of the growth index which deviate from its ΛCDM limit and lead to the suppression of structure growth at late-times. Such behaviour might resolve the so-called S_8 tension. In a nutshell, this cosmological tension corresponds to the contradiction between the high- and low-redshift measurements of the matter fluctuation amplitude in the standard cosmological model. Additionally, in both chapters we observe strong projection effects in the parameter space, which are pedagogically introduced in Chapter 2. We explore the projection effects in the context of spectroscopic surveys and propose possible solutions.

In Chapter 5, we develop a model-independent approach with a generalised screening function to model the nonlinear matter power spectrum for many dark energy and modified gravity models. Screening is a mechanism that allows for a theory to recover the classical gravitational interactions at small scales and in dense regions, such as our Solar System. This time we work in the halo-based reaction framework. Then, in Chapter 6, we apply this approach in the modelling of the cosmic shear power spectra. When tested on mock Stage-IV cosmic shear data, we discover promising hints of detecting the screening transition. We also explore a strong degeneracy between baryonic physics and the screening transition, as well as the impact of massive neutrinos.

In the final chapter, Chapter 7, we summarise the studies presented in this thesis and list our next steps in probing and constraining extended cosmologies with galaxy clustering and weak lensing.

Declaration

I declare that this thesis was composed by myself, that the work contained herein is my own except where explicitly stated otherwise in the text, and that this work has not been submitted for any other degree or professional qualification except as specified.

Details of collaboration and publications:

- **M. Tsedrik**, B. Bose, P. Carrilho, A. Pourtsidou, S. Pamuk, S. Casas, J. Lesgourgues, 2024, *Stage-IV cosmic shear with modified gravity and model-independent screening*. Published in JCAP: doi:10.1088/1475-7516/2024/10/099.
- C. Moretti, **M. Tsedrik**, P. Carrilho, A. Pourtsidou, 2023, *Modified gravity and massive neutrinos: constraints from the full shape analysis of BOSS galaxies and forecasts for Stage-IV surveys*. Published in JCAP: doi:10.1088/1475-7516/2023/12/025.
- B. Bose, **M. Tsedrik**, J.Kennedy, L. Lombriser, A. Pourtsidou, A. Taylor, 2023, *Fast and accurate predictions of the nonlinear matter power spectrum for general models of Dark Energy and Modified Gravity*. Published in MNRAS: doi:10.1093/mnras/stac3783.
- **M. Tsedrik**, C. Moretti, P. Carrilho, F. Rizzo, A. Pourtsidou, 2023, *Interacting dark energy from the joint analysis of the power spectrum and bispectrum multipoles with the EFTofLSS*. Published in MNRAS: doi:10.1093/mnras/stad260.

Not discussed in this thesis:

- Y. Mellier et al, 2024, *Euclid. I. Overview of the Euclid mission*. Paper submitted as part of the A&A special issue "Euclid on Sky". arXiv:2405.13491.
- V. Mainieri et al, 2024, *The Wide-field Spectroscopic Telescope (WST) Science White Paper*. arXiv:2403.05398.
- P. Carrilho, C. Moretti, **M. Tsedrik**, 2023 *Probing solutions to the S_8 tension with galaxy clustering*. Contribution to the 34th Rencontres de Blois on Particle Physics and Cosmology (Blois 2023). arXiv:2310.07344.
- Contribution to the Euclid collaboration: major contribution to the official modelling code PBJ, forecasting the joint power spectrum and bispectrum galaxy clustering analysis for the key paper by C. Moretti et al, producing HMcode2020-emulator for use in Euclid's nonlinear weak lensing pipeline.

.

(*Maria Tsedrik, October 2024*)

Acknowledgements

First and foremost, I would like to thank my supervisor, Alkistis Pourtsidou. I really believe it is impossible to fully capture my admiration and gratitude for her as a professional and a human-being. Here I just shortly list some things I am forever grateful to Alkistis: her undoubtful support, the informal catch-ups and tolerating my oversharing, her empathy and knowing when to push and when to let go, the patience by correcting my typical Russian lack of *the*'s and *a*'s in our papers, brilliant art-exhibition/book/film recommendations, cat-sitting Cheesy despite his sporadic misbehaving, the boat tour and liters of raki in Chania, advises on finding the balance between a healthy enthusiasm about your work and your own sanity, connecting me with amazing cosmologists, showing the best pubs of Edinburgh, and lighting any room she enters with laughter and joy.

Then I must thank Chiara, Pedro, and Ben who made this PhD journey so enjoyable and productive. I want to thank them for always finding time to answer my questions, to share their expertise of cosmology and life, to boost my confidence and speed up our progress. Without their feedback, advises and motivation this thesis would not exist. I always learned so much in our interactions and felt so inspired afterwards, thank you for this intellectual fuel. Also thank you for never making me feel stupid, for protecting me from the telecons, for treating me as a colleague from the very beginning and for cultivating our safe space. Working with you was truly magical.

I would like to thank Alessandra and Guada for fantastic months in Leiden. This research visit was very fulfilling and scientifically fruitful, it was also very dear to my heart for various personal reasons. Thank you for bringing more interest to the theoretical aspects of this thesis, for sparking new ideas, for getting me into ESA and Zumba classes. For the unforgettable research visit at JPL, I would like to thank Dida, Sujeong and Eric. Thank you for showing me the starriest Californian night sky, infecting me with your limitless curiosity, giving master-classes on public speaking and cultivating an addiction to the maple syrup cookies.

Additionally, I would like to thank all the people who make the Institute for Astronomy and the Royal Observatory such a special place. Especially, I would like to thank Philip, Ken, Trent, John, Florian, Andy, Alex, Sam, Marcos, and Joe.

Finally, I want to thank my closest friends and family for reminding me about the wonderful world without posterior distributions. Thank you, Yuliya, Zlata and Anike, for sweating out our anxieties on the dance floor, for flying over to the moldy grey island to explore the Highlands together, for being so compassionate and understanding, and for crawling through the trenches of adulthood with me. Thanks to mom, dad, and Rina for sending their love and warmth over kilometers that separate us. I dream of the times when we can celebrate all our wins and losses with each other at the same table. Your support means everything to me. And lastly, Marvin, thank you too (without the *too*).

Contents

List of Figures

List of Tables

Chapter 1

Cosmology with Galaxy Clustering and Weak Lensing

According to the standard cosmological model, today our Universe features $\sim 5\%$ of baryonic matter, $\sim 25\%$ of cold dark matter (CDM), negligible contribution from radiation and $\sim 70\%$ of dark energy. The simplest model of the latter is the cosmological constant (Λ), whose energy density is constant in time and space everywhere in the Universe. It exerts negative pressure causing the accelerated expansion. The standard concordance model, ΛCDM, shows excellent agreement with various observations, ranging from Solar System tests to the detection of gravitational waves. However, the nature of both dark components, matter and energy, of ΛCDM is unknown. Moreover, in recent years tensions related to the determination of the expansion rate and matter clustering amplitude between the early-time and late-time Universe have emerged. The search for alternatives to ΛCDM that could also explain the apparent tensions has led to a plethora of exotic dark energy, dark matter, and modified gravity theories. In this chapter we will introduce a set of dark energy models, modifications of General Relativity (GR) on large cosmological scales, and massive neutrinos – three extensions of the standard cosmological model, which we also call beyond-ΛCDM and extended cosmologies. We will discuss the corresponding effects these extensions have on cosmological probes – spectroscopic Galaxy Clustering (GC) and Weak gravitational Lensing (WL). We will also layout the foundation of the GC and WL formalism. Lastly, we will describe the cosmological probes crucial for understanding of our results, as well as the Stage-IV cosmological experiments that will provide us with their powerful measurements. When not explicitly cited, the introductory background is based on Refs. [12, 13].

1.1 Correlation Functions and Expansions

Prior to introducing the background on cosmology, we lay out the mathematics behind the correlation functions of random fields. Practically, a random field is a continuous and infinite collection of random variables in space and time. In cosmology we refer to the notion of random fields when dealing with fluctuations in density or temperature, for example, with respect to a smooth background. The observed galaxies trace these density fluctuations in the underlying Large Scale Structure (LSS) that is not randomly distributed and exhibits interesting correlations.

Correlation Functions

The two-point correlation function of random fields A and B in three-dimensional real space, $\boldsymbol{x}$, is given by:

$$\xi(|\boldsymbol{x}-\boldsymbol{x}'|) \equiv \langle A(\boldsymbol{x})B^*(\boldsymbol{x}')\rangle \tag{1.1}$$

with brackets $\langle ...\rangle$ denoting an ensemble average over many realisations of the fields, and * denoting the complex conjugate operation. Realistically, we have only one observable Universe, hence, only one realisation of a random field. The assumption of ergodicity helps to relate our theory and observations. Ergodicity states that for infinitely large volumes, ensemble averages become equal to spatial averages. Again, in reality, we do not observe an infinite volume. The finite volume of a survey or simulation introduces statistical fluctuations, called sample variance. If the finite volume is the size of the observable Universe itself, then the corresponding sample variance is called cosmic variance.

With the Fourier transforms of the fields

$$\hat{A}(\boldsymbol{k}) = \int \mathrm{d}\boldsymbol{x} A(\boldsymbol{x})\mathrm{e}^{-\mathrm{i}\boldsymbol{k}\cdot\boldsymbol{x}},\ \ \hat{B}(\boldsymbol{k}') = \int \mathrm{d}\boldsymbol{x}' B(\boldsymbol{x}')\mathrm{e}^{-\mathrm{i}\boldsymbol{k}'\cdot\boldsymbol{x}'}, \tag{1.2}$$

we can relate the cross-correlation power spectrum $P_{AB}(k)$ in Fourier space to the two-point correlation function as

$$\langle \hat{A}(\boldsymbol{k})\hat{B}^*(\boldsymbol{k}')\rangle \equiv (2\pi)^3\delta_{\mathrm{D}}(\boldsymbol{k}-\boldsymbol{k}')P_{AB}(k) \tag{1.3}$$

with a Dirac delta function δ_{D}. Here, we assume that the fields are statistically homogeneous (ξ is invariant under translation) and isotropic (ξ is invariant under rotation). Therefore, the power spectrum only depends on the norm of the vector $\boldsymbol{k}$ and not on its direction.

Analogously, we can define a bispectrum of three random fields:

$$\langle \hat{A}(\boldsymbol{k})\hat{B}^*(\boldsymbol{k}')\hat{C}(\boldsymbol{k}'')\rangle \equiv (2\pi)^6\delta_{\mathrm{D}}(\boldsymbol{k}-\boldsymbol{k}'+\boldsymbol{k}'')B_{ABC}(k,k',k'')\,, \tag{1.4}$$

which vanishes for perfectly Gaussian fields. For a Gaussian random field the probability of realising some field configuration is a Gaussian functional. In other words, the density-values at different spatial locations are drawn from a Gaussian (also called normal) distribution. It also means that all joint probability distributions of the density at different points in space can be expressed as multivariate normal distributions. The initial conditions of the Universe are well described by a random Gaussian field according to inflation predictions (more on that in Subsection 1.2.2). Mathematically it means that we can completely specify the initial density field via the initial (linear) power spectrum, which prescribes the fluctuation amplitude as a function of scale. While the amplitude for each scale (or mode) is specified by the power spectrum, the corresponding phase is uniformly random. Later the density fluctuations evolve in time, their gravitational evolution induces non-Gaussianity: modes begin to couple and phases become non-random. However, in the linear regime on large scales, where the Fourier modes evolve independently, the statistics remains Gaussian.

In numerical simulations, the initial density field is often specified on a grid and follows the main principle described above. Namely, the distribution of a finite number of dark matter point particles is fully described by random phases and a linear power spectrum rescaled to the initial redshift of the simulation. Once these linear density fluctuations are specified, the equal-mass particles are displaced from a uniform grid with positions and velocities assigned via Zel'dovich approximation or a perturbative approach.

Legendre Expansion

In redshift space we cannot assume isotropy anymore (more on this in Section 1.4) and the power spectrum now depends not only on the norm of the vector $\boldsymbol{k}$ but also on its position with respect to the line-of-sight $\mu = \hat{\boldsymbol{k}} \cdot \hat{\boldsymbol{n}}$[1]. These anisotropies are apparent due to the additional contribution in observed redshifts from peculiar velocities of the observed objects. Another source of anisotropies is a potential discrepancy between the fiducial cosmology, assumed to measure distances, and the true cosmology. The redshift space anisotropies are symmetric around the line-of-sight and follow a reflectional symmetry along the same axis in the distant-observer limit. Thus these field anisotropies can be written as a function of μ^2. Because of the symmetries, we can expand the power spectrum in a subset of the spherical harmonics that is invariant under the rotation about the line-of-sight axis – Legendre polynomials:

$$P_{AB}(k, \mu) = \sum_{\ell=0}^{\infty} P_\ell(k) \mathcal{P}_\ell(\mu) \tag{1.5}$$

[1]Hatted vector properties denote unit vectors, while hatted scalars denote functions in Fourier space.

with the power spectrum multipoles

$$P_\ell(k) = \frac{2\ell+1}{2}\int_{-1}^{+1} \mathrm{d}\mu P_{AB}(k,\mu)\mathcal{P}_\ell(\mu)\,. \tag{1.6}$$

The first Legendre polynomials with even ℓ-values are given by

$$\mathcal{P}_0(\mu) = 1\,,\;\; \mathcal{P}_2(\mu) = \frac{3\mu^2-1}{2}\,,\;\; \mathcal{P}_4(\mu) = \frac{35\mu^4-30\mu^2+3}{8}\,, \tag{1.7}$$

while the odd powers of μ are integrated to zero.

Expansion in Spherical Harmonics

Angular correlation functions are widely used in cosmology. For example, Cosmic Microwave Background anisotropy or cosmic shear maps can be represented as a spherical surface with fluctuations filtered by a smoothing kernel. We denote the angular two-point correlation function for fields A and B with points on the spherical surface $\hat{\boldsymbol{n}}$ and $\hat{\boldsymbol{m}}$, correspondingly, as $w_{AB}(\hat{\boldsymbol{n}}\cdot\hat{\boldsymbol{m}})$. It is connected to the spherical harmonic transform, $C_{AB}(\ell)$, also known as the angular power spectrum, as:

$$w_{AB}(\tilde{\mu}) = \sum_{\ell=0}^{\infty}\frac{2\ell+1}{4\pi}C_{AB}(\ell)\mathcal{P}_\ell(\tilde{\mu})\,, \tag{1.8}$$

where $\tilde{\mu} = \hat{\boldsymbol{n}}\cdot\hat{\boldsymbol{m}}$ corresponds to the cosine of the separation angle between points on the sphere. We can project the fields into the sphere using some kernels $F_{A,B}(r)$ which control the sensitivity of our observation in the radial direction, r:

$$\tilde{A}(\hat{\boldsymbol{n}}) = \int \mathrm{d}r F_A(r)A(r\hat{\boldsymbol{n}})\,,\;\; \tilde{B}(\hat{\boldsymbol{m}}) = \int \mathrm{d}r F_B(r)B(r\hat{\boldsymbol{m}})\,. \tag{1.9}$$

On a sphere we can express unit vectors, $\hat{\boldsymbol{n}}$ and $\hat{\boldsymbol{m}}$, in spherical coordinates $\Omega = (\theta,\phi)$. We can also expand the projected field in spherical harmonics $Y_{\ell m}$ with the corresponding harmonic coefficients:

$$\tilde{A}(\hat{\boldsymbol{n}}) = \sum_{\ell=0}^{\infty}\sum_{m=-\ell}^{\ell} A_{\ell m}Y_{\ell m}(\hat{\boldsymbol{n}})\,,\;\; A_{\ell m} = \int \mathrm{d}\Omega \tilde{A}(\hat{\boldsymbol{n}})Y^*_{\ell m}(\hat{\boldsymbol{n}}) \tag{1.10}$$

with similar expressions for the field B. In the Fourier transformation (Eq. 1.2) we have a "plane wave"-like term that we can express as a linear combination of spherical waves with the spherical Bessel function, j_ℓ:

$$\mathrm{e}^{\mathrm{i}\boldsymbol{k}\cdot\boldsymbol{x}} = 4\pi\sum_{\ell=0}^{\infty}\sum_{m=-\ell}^{\ell}\mathrm{i}^\ell j_\ell(kr)Y^*_{\ell m}(\hat{\boldsymbol{k}})Y_{\ell m}(\hat{\boldsymbol{n}})\,. \tag{1.11}$$

With the plane-wave expansion and the normalisation $\int \mathrm{d}\hat{\boldsymbol{n}} Y^*_{\ell m}(\hat{\boldsymbol{n}}) Y_{\ell' m'}(\hat{\boldsymbol{n}}) = \delta_{\ell\ell'}\delta_{mm'}$ we derive

$$A_{\ell m} = \frac{\mathrm{i}^\ell}{2\pi^2} \int \mathrm{d}^3\boldsymbol{k} \hat{A}(\boldsymbol{k}) Y^*_{\ell m}(\hat{\boldsymbol{k}}) \int \mathrm{d}r F_A(r) j_\ell(kr)\,. \tag{1.12}$$

Note that $\mathrm{d}^3\boldsymbol{k} = k^2 \sin\theta \mathrm{d}\theta \mathrm{d}\phi \mathrm{d}k\hat{\boldsymbol{k}}$. Overall the angular power spectrum is given by

$$C_{AB}(\ell) = \langle A_{\ell m} B^*_{\ell m} \rangle = \int \mathrm{d}k \frac{2k^2 P_{AB}(k)}{\pi} \mathcal{F}^A_\ell(k) \mathcal{F}^B_\ell(k) \tag{1.13}$$

with the Bessel function kernels $X = A, B$

$$\mathcal{F}^X_\ell = \int F_X(r) j_\ell(kr) \mathrm{d}r\,. \tag{1.14}$$

For numerical methods to evaluate this projection integral see Refs. [14–18]. The projection integral in k is well-behaved since the power spectrum P_{AB} generally decays for small and large wave-numbers. It is the kernel integral, $\mathcal{F}_\ell$, that is hard to evaluate, especially for large values of multipole moment ℓ, as the Bessel functions grow monotonically from zero to $kr = \ell + 1/2$ and start to oscillate rapidly afterwards. The Limber approximation [19] approximates the peak of the spherical Bessel function by a Dirac delta function:

$$j_\ell(kr) \to \sqrt{\frac{\pi}{2\ell+1}} \delta_\mathrm{D}(\ell + 1/2 - kr) \tag{1.15}$$

This approximation is widely used in the context of WL that we discuss in detail in Section 1.5.

1.2 Standard Cosmology

Throughout this work the speed of light is set to $c = 1$.

1.2.1 Background Evolution

On large scales (greater than 100 Mpc) the Universe looks isotropic (the same in all directions) and homogeneous (the same at every point in space). Isotropy and homogeneity introduce symmetries which significantly restrict the metric choice of the corresponding spacetime. Requiring further that the fundamental observer's proper time be equal to the coordinate time, we obtain a simple description of the spacetime geometry via the Friedmann-Lemaître-Robertson-Walker (FLRW) metric:

$$\mathrm{d}s^2 = \mathrm{d}t^2 - a^2(t) \left[\mathrm{d}x^2 + f_k^2(x)(\mathrm{d}\theta^2 + \sin^2\theta \mathrm{d}\varphi^2)\right]\,, \tag{1.16}$$

with x denoting comoving radial coordinate, θ and ϕ are spherical spatial coordinates, and $a(t)$ is the (dimensionless) scale factor, which describes the expansion of a homogeneous, isotropic universe. The scale factor can be set to unity at the current time. The function $f_k(x)$ depends on the curvature parameter, k, as

$$f_k(x) = \begin{cases} \sinh x & k = -1 \quad \text{hyperbolic space,} \\ x & k = 0 \quad \text{flat space,} \\ \sin x & k = 1 \quad \text{spherical space}\,. \end{cases} \tag{1.17}$$

In our works we always assume spatial flatness, i.e., $k = 0$, as supported by observations [20–22].

The dynamics of the FLRW metric reduce to the dynamics of the scale factor. They are governed by the so-called Friedmann equations:

$$H^2 \equiv \left(\frac{\dot{a}}{a}\right)^2 = \frac{8\pi G}{3}\rho + \frac{\Lambda}{3}\,, \tag{1.18}$$

$$\frac{\ddot{a}}{a} = -\frac{4\pi G}{3}\left(\rho + 3p\right) + \frac{\Lambda}{3}\,, \tag{1.19}$$

where H is the Hubble parameter, $\rho = \rho(t)$ is the matter energy density of a (homogeneous) perfect fluid and $p = p(t)$ is the corresponding pressure. Thus, in order to specify the dynamics of the scale factor, the prescription for the scaling behaviour of the density $\rho(t)$ is required. This is defined by the equation of state of the density components, expressed as the ratio of pressure and density:

$$w \equiv \frac{p}{\rho}\,. \tag{1.20}$$

Pressureless cold dark matter is characterised by $w = 0$, relativistic matter by $w = 1/3$ and the value $w = -1$ corresponds to the cosmological constant Λ. We can define the critical density in a flat universe as $\rho_{\rm crit}(a) = 3H^2(a)/(8\pi G)$ and express the dimensionless density parameters as

$$\Omega_i(a) \equiv \frac{\rho_i(a)}{\rho_{\rm crit}(a)}\,. \tag{1.21}$$

For the density parameters at $a = 1$ we omit the brackets with the scale factor dependency. This allows us to bring the first Friedmann equation (Eq. 1.18) into the familiar and widely used form:

$$H^2(a) = H_0^2\left(\frac{\Omega_{\rm m}}{a^3} + \frac{\Omega_{\rm r}}{a^4} + \Omega_\Lambda\right) = H_0 E(a)\,. \tag{1.22}$$

The subscripts "m" and "r" denote the matter and radiation energy densities respectively, and the present value of the Hubble parameter is given by $H(a = 1) = H_0 = 100\,h$

km s^{-1} Mpc^{-1}. Since the radiation density component at the redshifts of our interest is very low we will omit its contribution in this work. However, it should not be ignored in the early-time Universe at redshifts $z \geq 3400$, i.e., before the matter-radiation equality. The redshift and scale factor are related via $a = 1/(1 + z)$.

1.2.2 Structure Formation

Isotropy and homogeneity on large scales are the foundation of the cosmological principle. One of the main evidences of the cosmological principle's validity is the Cosmic Microwave Background (CMB), which corresponds to the relic electromagnetic radiation from the epoch of recombination. These relic photons decoupled from matter after the early Universe was cool enough for protons and electrons to form neutral hydrogen. After this epoch of recombination, the photons could travel uninhibited trough the Universe, without being constantly absorbed or scattered by charged particles in the baryonic plasma as before. The CMB radiation we observe is highly isotropic but not perfectly isotropic: the observed temperature, and hence, the matter density fluctuations indicate an anisotropy of order 10^{-5}. Thus, the inhomogeneities on small scales already existed in the very early Universe, reflecting the initial state of the gravitationally evolved highly inhomogenous cosmic structures we see today. Currently, the widest accepted mechanism for the generation of these primordial fluctuations is inflation: the fluctuations are seeded by quantum fluctuations of the inflaton field, which drives an era of rapid accelerated expansion in the early Universe.

Another observed feature that propagates from the epoch of recombination is called Baryonic Acoustic Oscillations (BAO). Before decoupling, the "gravity versus radiation pressure" interaction in the photo-baryon plasma caused acoustic waves in the matter content of the early Universe. After decoupling, these oscillations are frozen. We can see them in the CMB angular power spectrum in the form of acoustic peaks, but also in the distribution of galaxies in the late Universe. As galaxies are forming from the concentrations of mass, there is an excess of galaxies at the separation length corresponding to the first acoustic peak, or the distance travelled by a sound wave between the Big Bang and the recombination epoch. This imprint looks like a "bump" in the two-point correlation function of galaxies at $\sim$110 Mpc h^{-1}, which in Fourier space corresponds to the oscillations in the galaxy power spectrum.

Linear Growth

To map small inhomegenities observed in the CMB to today's LSS, we first introduce linear perturbation theory. We can apply the linearised perturbative approach to describe the evolution of inhomogeneities, as long as they remain small. Here, we outline the formalism in Newtonian gravity, but the same can be done in full GR. The Newtonian

framework is a good approximation when all velocities are slower than the speed of light and spacetime curvature is not important (i.e., on scales smaller than the Hubble radius, $1/H$). As the matter budget of the Universe is dominated by cold dark matter, the focus is on a collisionless, self-gravitating medium in a homogeneous and isotropic background expanding at the Hubble rate. Its density is decomposed into a homogeneous time-dependent background part, $\bar{\rho}$, and its small perturbation, $\delta\bar{\rho}(\boldsymbol{x}, t)$, which includes the density contrast, $\delta(\boldsymbol{x}, t)$, defined as

$$\delta(\boldsymbol{x}, t) = \frac{\rho(\boldsymbol{x}, t) - \bar{\rho}(t)}{\bar{\rho}(t)} \,. \tag{1.23}$$

Under the assumption that cold dark matter behaves like a collisionless fluid on large scales and $\delta \ll 1$, its dynamics are described by the following set of fluid equations, namely, the continuity equation, the linearised Euler equation and the Poisson equation:

$$\frac{\partial \delta}{\partial \eta} + \nabla \cdot \boldsymbol{v} = 0 \,, \tag{1.24}$$

$$\frac{\partial \boldsymbol{v}}{\partial \eta} + \mathcal{H}\boldsymbol{v} = -\nabla\Phi \,, \tag{1.25}$$

$$\nabla^2\Phi = 4\pi G\delta\bar{\rho}a^2 = \frac{3}{2}\Omega_{\mathrm{m}}(a)\mathcal{H}^2\delta \,. \tag{1.26}$$

The conformal time, η, is related to the time coordinate by $\mathrm{d}\eta = \mathrm{d}t/a$, $\mathcal{H} = aH$ is the conformal Hubble factor, $\Omega_{\mathrm{m}}(a) = 8\pi G\bar{\rho}(a)/(3H^2(a))$, ∇ is the spatial derivative with respect to the comoving distance $\boldsymbol{x}$, $\boldsymbol{v} = \mathrm{d}\boldsymbol{x}/\mathrm{d}\eta$ is the velocity field of the cosmic fluid and Φ the gravitational potential. The comoving coordinate is connected to the proper distance or the position vector in spherical physical coordinates as $\boldsymbol{x} = \boldsymbol{r}/a$.

We obtain the evolution of the density contrast by combining the linearised fluid equations in comoving coordinates:

$$\frac{\mathrm{d}^2\delta}{\mathrm{d}a^2} + \frac{1}{a}\left(3 + \frac{\mathrm{d}\ln H}{\mathrm{d}\ln a}\right)\frac{\mathrm{d}\delta}{\mathrm{d}a} = \frac{3\Omega_{\mathrm{m}}(a)}{2a^2}\delta \,. \tag{1.27}$$

The second term, proportional to $\mathrm{d}\delta/\mathrm{d}a$, acts as a friction term and is sometimes called the Hubble drag, since it reflects the Hubble expansion counteracting the attraction due to gravity. Although the density contrast depends on the comoving space coordinates as well as on time, Eq. 1.27 does not contain derivatives with respect to position, nor does $\boldsymbol{x}$ appear explicitly in the coefficients. Therefore, the solution of this equation can be decomposed into separated time- and space-dependent components as

$$\delta(\boldsymbol{x}, a) = D_+(a)\delta_+(\boldsymbol{x}) + D_-(a)\delta_-(\boldsymbol{x}) \,, \tag{1.28}$$

in which $D_\pm(a)$ are the linear growth factors of the growing $(+)$ and decaying $(-)$ modes.

During the matter-dominated era the density contrast grows proportionally to $D_+(a)$ and is responsible for structure growth on large scales. The second solution decays with time and consequently cannot describe the amplification of density perturbations. Another quantity for description of structure growth is called the growth rate, $f(a)$, and is expressed as a derivative of the linear growth factor with respect to the logarithm of the scale factor $f = \mathrm{d}\ln D/\mathrm{d}\ln a$.

Linear Structure Formation

The density fluctuations, $\delta(\boldsymbol{x}, t)$, are considered to be Gaussian random variables with $\langle\delta(\boldsymbol{x})\rangle = 0$ at a fixed time. By calculating the variance of the density contrast in Fourier space we define the matter fluctuation power spectrum, $P_{\delta\delta}(k)$, with independent modes as (see Section 1.1)

$$\langle\hat{\delta}(\boldsymbol{k})\hat{\delta}^*(\boldsymbol{k}')\rangle = (2\pi)^3\delta_{\mathrm{D}}(\boldsymbol{k}-\boldsymbol{k}')P_{\delta\delta}(k)\,. \tag{1.29}$$

The shape of the primordial spectrum is determined by the mechanism of inflation. Most models predict a power law [23]:

$$P_{\delta\delta,\mathrm{ini}}(k) \propto k^{n_s}\,, \tag{1.30}$$

where n_s is known as the spectral index. Then there are two effects that should be considered: linear growth of the density perturbations in time and different growth of super- and sub-horizon perturbations. The first effect is established by the growth factor, $D_+ = D$, from the previous subsection. The second effect is accounted for by the transfer function, $T(k)$. The main idea behind the transfer function is based on the fact that before the equality epoch, i.e., before the transition from the radiation domination to matter domination, matter perturbations grow differently. The ones that are larger than the horizon size grow $\propto a^2$, while the growth of perturbations within the horizon is suppressed to be logarithmic in the scale-factor. After the equality epoch, both types of perturbations begin to grow at the same rate $\propto a$. Combining the described effects we arrive at the following expression for the linear power spectrum of density fluctuations:

$$P_{\mathrm{L}}(k,a) \propto D^2(a)T_k^2(k)P_{\delta\delta,\mathrm{ini}}(k)\,. \tag{1.31}$$

The linear clustering and evolution of the total matter density, as well as other components of the Universe, can be computed numerically by Boltzmann solvers, such as `CAMB` [24] and `CLASS` [25]. Statistical homogeneity is preserved in the linear power spectrum: the redshift evolution only changes the amplitude of the spectrum, not its shape. However, as we will see in the next section, the redshift dependence for nonlinear wave-numbers with $k > 0.1\ h\ \mathrm{Mpc}^{-1}$ is less trivial due to the mode-coupling. To fully describe the linear

power spectrum, in addition to the spectral index and the transfer function, the matter fluctuation amplitude must be provided. At early times, the amplitude is described by the primordial amplitude A_s, while at later times the normalisation is often characterised by the σ_8 parameter. The latter corresponds to the variance of the density field smoothed within a radius $R = 8$ Mpc h^{-1}:

$$\sigma_R^2(a) = \frac{1}{2\pi^2} \int \mathrm{d}k k^2 P_{\mathrm{L}}(k, a) W^2(kR)\,, \tag{1.32}$$

where $W(kR)$ denotes a top-hat filter function.

Nonlinear Structure Formation

The linear theory is a valid approach on scales bellow 0.1 h Mpc^{-1} in Fourier space or above 100 Mpc h^{-1} in configuration space. At smaller length scales the collisionless fluid approximation breaks, wave-number modes couple, and the density contrast becomes $\delta \gg 1$. There are roughly three options[2] to include nonlinear scales:

1. Numerically: N-body and hydrodynamical simulations, allow us to trace the structure formation evolution in a controlled way. For hydrodynamical simulations the sizes of the simulation boxes are small in comparison to CDM only simulations, which does not allow to easily bridge a vast range of large scales. Additionally, hydrodynamical simulations demonstrate a strong dependence on the sub-grid physics (any unresolved physical processes on small scales, e.g., black hole accretion), and are hard to calibrate with real observations. However, the summary statistics from N-body and hydro-simulations are the gold standard for stress-testing the validity of our analytical models. In Chapter 3, we work with measurements from the Minerva simulations [30]. Recently, several emulators trained with neural networks on large sets of simulations, such as `bacco` [31] and `EuclidEmulator2` [32], were offered as a fast and reliable modelling option for the matter power spectrum. However, such emulators are restricted by the parameter range and gravity laws of the corresponding simulations. Additionally, the validity of the nonlinear power spectrum breaks at scales dictated by the resolution of a simulation. For instance, the largest wave-number for the nonlinear `bacco` emulator is 5 h Mpc^{-1}.

2. Analytically: one expands the density contrast and velocity around their linear solution in a perturbative way, so that the higher-order corrections become progressively smaller, thus the theory is convergent. Various perturbation theories have been developed [33, 34]. In this thesis, we use the Effective Field Theory

[2] We do not explicitly mention semi-analytical methods, e.g., PATCHY [26], Pinocchio [27], or hybrid methods [28, 29]. The former is, however, a practical tool for covariance matrix production, while the latter allows to include scales beyond the standard perturbative regime. In Chapter 3 and Chapter 4, we use covariance matrices computed from mock catalogs created by the semi-analytical methods.

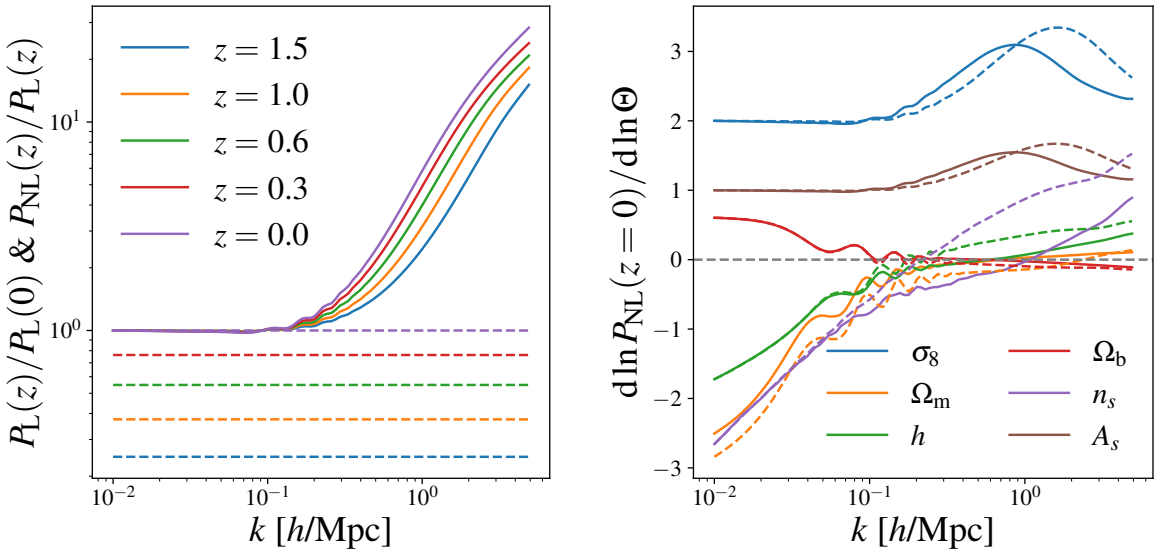

Figure 1.1 *Matter power spectrum with the* `bacco` *emulator. Left panel: ratios between linear power spectra at various redshifts specified in the legend with respect to the linear power spectrum at redshift $z = 0$ (dashed lines); ratios between the nonlinear and linear power spectra for each redshift (solid lines). Right panel: sensitivity of the nonlinear matter power spectrum to cosmological parameters in ΛCDM cosmology at two redshifts $z = 0$ (solid lines) and $z = 1$ (dashed lines). The units of the power spectra are* $[\mathrm{Mpc}^3/h^3]$.

of Large Scale Structure (EFTofLSS), which takes into account the large scale effects of poorly understood small-scale physics (more on this in Section 1.4). The perturbative approach breaks at wave-numbers above $k = 0.3 - 0.4\ h\ \mathrm{Mpc}^{-1}$.

3. Phenomenologically: the halo-model approach [35] is a phenomenological approach where the nonlinear power spectrum is a sum of two terms – the one-halo and two-halo contributions. The two-halo term, corresponds to the clustering of individual halos on large and quasi-linear scales, whereas the one-halo term corresponds to the clustering of dark matter particles within the same halo on small scales. Separate components of the recipe for the halo-model can be fitted and calibrated on simulations. Still this approach is less accurate than simulations and less theoretically motivated than the perturbative approaches. The halo-model allows to include nonlinear scales up to $\sim 5\ h\ \mathrm{Mpc}^{-1}$.

Above we have introduced the key 6 parameters of the standard cosmological model, ΛCDM: $\Theta = \{\Omega_{\rm m}, \Omega_{\rm b}, \Lambda, h, n_s, A_s(\text{or } \sigma_8)\}$. These parameters describe the time evolution of the components, the expansion history, the geometry and the formation of structures in the Universe. Taking the total matter power spectrum as our structure formation summary statistics, in Fig. 1.1 we show how structures evolve with redshift in the left panel. On linear scales the growth is scale-independent (dashed lines), while on nonlinear scales structure growth is a scale-dependent and nonlinear function of redshift (solid lines).

In the right panel of the same figure, we demonstrate the sensitivity of the nonlinear power spectrum at two redshifts $z = 0$ (solid lines) and $z = 1$ (dashed lines) in the ΛCDM scenario to the cosmological parameters on different scales using the state-of-the-art `bacco` emulator. In the following we briefly discuss the dependencies of the matter power spectrum on Θ, and, hence, the origin of constraints on these parameters. The amplitude parameters, A_s and σ_8, show a similar trend in their impact on the power spectrum at different scales. Their lines (blue and brown) would overlap for variations in σ_8 and $\sqrt{A_s}$, because $P_\mathrm{L} \propto A_s$ and $P_\mathrm{L} \propto \sigma_8^2$ by definition. From Eq. 1.26 we see that $P_{\delta\delta} \propto k^4(\Omega_\mathrm{m}h^2)^{-2}P_{\Phi\Phi}$. Combining it with Eq. 1.31 we get $P_\mathrm{L} \propto D^2(z)A_s k^{n_s}\Omega_\mathrm{m}^{-2}h^{-4}T_k^2$. In the linear regime, the transfer function can be approximated as

$$T_k(k) \approx \begin{cases} 1 & k \ll k_\mathrm{eq}\,, \\ \left(\frac{k_\mathrm{eq}}{k}\right)^2 \ln\left(\frac{k}{k_\mathrm{eq}}\right)\alpha_\Gamma(\omega_\mathrm{m},\omega_\mathrm{b}) & k \gg k_\mathrm{eq} \end{cases} \tag{1.33}$$

with $\omega_i = \Omega_i h^2$, and the matter-radiation equality scale $k_\mathrm{eq} = a_\mathrm{eq}H(a_\mathrm{eq}) \propto \Omega_\mathrm{m}h^2 = \omega_\mathrm{m}$ for fixed ω_r. We can integrate the transfer function squared to assess the amplitude of the power spectrum, this leads to $\sigma_8^2 \propto D^2(z)A_s\Omega_\mathrm{m}^{1.05}h^{3.5}$ for $n_s \approx 1$ and fixed baryonic density [36]. For fixed σ_8 this explains the behaviour of the orange and green lines that correspond to Ω_m and h, respectively (note that we use units with h for the wave-numbers and the power spectrum, that absorbs some contribution of h). At large scales we notice a change in dependence on Ω_m with redshift, this is due to the dependence of $D(z)$ on Ω_m: at redshift $z = 0$ this can be estimated as $D \propto \Omega_\mathrm{m}^{0.23}$, while at $z = 1$ we find a weaker dependence $D \propto \Omega_\mathrm{m}^{0.06}$. We find these relations by solving the growth equation from Eq. 1.27. In the nonlinear regime the sensitivity to h grows slightly with redshift, while the Ω_m sensitivity remains weak. Both trends can be interpreted in the halo-model framework via the 1-halo term contribution (for more details see Ref. [11]). The behaviour of the 1-halo term also explains the "bump" around $k \sim 1\ h\ \mathrm{Mpc}^{-1}$ in the σ_8 and A_s dependencies. The dependence on the spectral index (purple line) is straightforward to read out from $P_\mathrm{L} \propto k^{n_s}T_k^2$. Finally, the variation in the baryon density is mostly contributing to the slope of the linear power spectrum at very large scales. The main effect of the baryons in the transfer function, beyond the introduction of oscillations, is the suppression of power below the sound horizon in the $1/k^2$ tail, i.e., the suppression in growth rates between the equality and the drag epochs. Bellow the sound horizon the photon-baryon plasma is pressure supported, this prohibits baryons from clustering at smaller scales. As already discussed above, in the radiation-dominated epoch the growth of density perturbations outside the horizon is $\propto a^2$ or $\propto k^2$, while inside the horizon the growth is logarithmic. From Eq. 31 in Ref. [37] we can approximate the function $\alpha_\Gamma \propto \omega_\mathrm{m}^{0.36}\omega_\mathrm{b}^{-0.2}$, leading to an additional contribution of $\omega_\mathrm{b}^{-0.4}$ to σ_8^2. This explains the red curve for fixed σ_8.

1.3 Extended Cosmologies

In the standard cosmological model, the laws of gravity are fully described by Einstein's theory of GR. GR is indeed in remarkable agreement with a plethora of observations from the Solar System: such as the anomalous perihelion of Mercury, the Shapiro time–delay measured by the Cassini spacecraft and Lunar laser ranging experiments. GR works not only in our neighbourhood, the tests in the so-called strong gravity regime around black holes (e.g., the imaging of the black hole in M87 [38]) and pulsars [39] align perfectly with Einstein's theory. Another test of GR that it passed with flying colours was the detection of gravitational waves emitted by merging black holes [40] and neutron stars, simultaneously with the detection of their electromagnetic counterpart [41].

The standard cosmological model requires an additional dark energy component to explain the observed accelerated expansion of the Universe via Supernovae type 1a (SNIa) [42], as well as CMB and BAO observations (see *The road to dark energy* in Ref. [43]). In the standard model the Cosmological Constant (CC), Λ, is responsible for the accelerated expansion. However, the introduction of the cosmological constant poses certain theoretical problems (below we repeat our arguments from Ref. [44]).

Testing GR and various dark energy scenarios at a sub-percent level on cosmological scales is a primary motivation behind both current and upcoming surveys. Uncovering the physical mechanism responsible for the accelerated expansion remains one of the most significant unresolved issues in modern physics. In addition to that, recent LSS observations (e.g., [45–47]) point towards discrepancies between the cosmological parameters derived from the early-time and late-time cosmological probes. These so-called tensions, which we discuss in this section, provide further motivation to test alternatives for the standard cosmological model.

Tensions

The first tension we consider is the Hubble tension. The inferred value of the expansion rate from the CMB is equal to $H_0 \sim 67$ km s^{-1} Mpc^{-1}[22]. In contrast, direct measurements of the Hubble constant from low redshift data via the standard distance ladder yield $H_0 \sim$ 71-73 km s^{-1} Mpc^{-1}. The higher value of H_0 corresponds to SNIa distance measurements calibrated on cepheids [48]. The lower value corresponds to calibrations on the Tip of Red Giant Branch (TRGB) [49]. Both analyses were done with the Hubble Space Telescope (HST) data and performed by the "Supernovae and H_0 for the Equation of State of DE" (SH0ES) collaboration. This disagreement between Planck and the local distance ladder is quantified by a 4-5σ tension. As one of the attempts to resolve the Hubble tension was a class of early dark energy models proposed [50] (which alone will always fall short to fully resolve the tension according to Ref. [51]).

However, recently new results with the James Webb Space Telescope (JWST) were

obtained by the Chicago-Carnegie Hubble Program (CCHP) [52]: while the values of H_0 via cepheids and TRGB distance calibrations are slightly lower but still in agreement with SH0ES, a new distance indicator – Carbon-rich J-region Asymptotic Giant Branch (JAGB) stars [53] – leads to $H_0 \sim 68$ km s^{-1} Mpc^{-1}reconciling with the CMB value of the expansion rate. Immediate response from the SH0ES collaboration explained CCHP's findings by the sub-sample bias and various decisions made in their analysis [47]. Based on their previous studies (e.g., Ref. [54]) SH0ES argued for the synergy between HST and JWST. In addition, they found an excellent agreement between the combined 3 distance indicators with JWST and SNIa-Cepheid measurement with HST for the same (larger than CCHP's one) sample of SNIa, recovering the tension with Planck and $H_0 \sim 73$ km s^{-1} Mpc^{-1}. Nevertheless, there is an additional disagreement between SH0ES' findings for SNIa calibrated via the direct distance ladder at redshifts $z < 0.01$ and the Dark Energy Survey's (DES) Year 5 findings from SNIa calibrated on BAOs via the inverse distance ladder at redshifts $z > 0.1$ [55]. The latter is in excellent agreement with the CMB value of H_0, while also keeping the window of possibility open for non-standard cosmologies [56]. The dispute continues with local measurements of the Coma Cluster at $z \approx 0.023$ with DESI via the fundamental plane (FP) relation arguing for even larger $H_0 \sim 76$ km s^{-1} Mpc^{-1}[57, 58]. The latest findings of the strong lensing community in Ref. [59], also seem to imply larger value of the expansion rate than the one from the previous studies of TDCOSMO+SLACS [60], and closer to the one from H0LiCOW [61]. For more examples of H_0 probes see the Review [1]. Clearly, the Hubble tension is a topic of high interest and active discourse in the age of precision cosmology.

The second tension we consider is called the S_8 or σ_8 tension, and corresponds to certain inconsistencies in the strength of matter clustering, i.e., the amplitude of density fluctuations. The parameter S_8 is directly measured with WL and is closely related to $f\sigma_8$ measured by GC. While having a smaller significance than the Hubble tension, i.e., only $\sim 2\sigma$, the matter clustering tension is consistently found in GC and WL probes. These probes measure $S_8 \sim 0.75$ [62], which is in disagreement with the CMB prediction under the assumption of the standard cosmology, $S_8 \sim 0.83$ [22]. Currently, there are two possible explanations for the fact that the clustering amplitude at lower redshifts is smaller than the one extrapolated from the high redshift measurements: a) unaccounted systematic effects, such as uncertainties in either observational systematics or inaccurate modelling of the nonlinear scales (e.g., for WL probes this might contaminate the angular spectra at all multipoles [63, 64]); b) new physics (beyond-ΛCDM cosmologies) [65–67]. Regarding the latter, any modification of structure growth, which leads to a growth rate at late times weaker than in ΛCDM, would qualify for a potential solution of the S_8-tension, as long as it does not significantly change other physical effects like galaxy formation or CMB.

In Fig. 1.2 we demonstrate the Hubble and clustering tensions from different probes

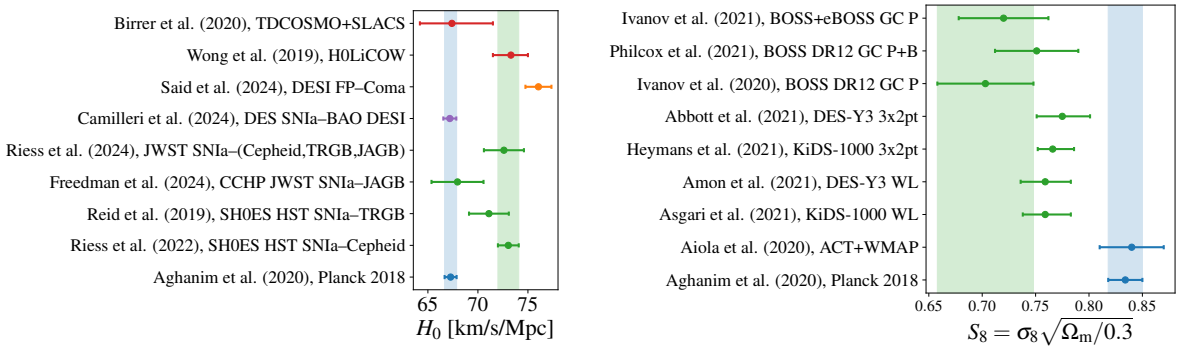

Figure 1.2 *Tensions from various probes in the flat ΛCDM framework. Left panel: H_0 constraints with CMB (blue), direct measurements of the expansion rate with the Hubble diagram via the local distance ladder (green), via the inverse distance ladder (purple), via FP distances with the Coma cluster (orange), strong lensing constraints (red). Right panel: $S_8 = \sigma_8\sqrt{\Omega_m/0.3}$ constraints in the early-time probes (blue) and late-time probes (green). Values with corresponding 68% errors are taken from Ref. [1] and other references in the main text.*

discussed above. Can we solve both tensions simultaneously, if we believe that both of them have a physical nature? One can find various attempts in the literature (e.g., Ref. [68]), but we are yet to find a single alternative cosmological model that would be in agreement with both cosmological and astrophysical observations.

Cosmological Constant Problem(s)

The cosmological constant is measured to be non-zero by a suite of cosmological probes such as the CMB [22], SNIa [42, 69], and optical galaxy surveys (see, for example, Ref. [70]). Consistently, we would expect a non-zero cosmological constant from quantum field theory (QFT) predictions, as all vacuum states of standard model particle fields will contribute an energy density, $\rho_{\rm vac}$, to the Universe that appears as a constant in the model's action. Unfortunately, this results in one of the biggest problems in physics (see Ref. [71] for a review). The first aspect of the problem is that our naive QFT predictions for the energy density of Λ is at least 60 orders of magnitude larger than the cosmological measured value[3]. We can still make a fine-tuning of the "bare" constant, $\Lambda_{\rm bare}$, in the potentials of these fields to cancel the other vacuum energy contributions to yield the observed value for Λ.

One might be fine with this, after all QFTs are used to removing divergences through renormalisation techniques. The real problem is that we need to repeatedly fine-tune every time a new energy scale or particle field is considered which changes $\rho_{\rm vac}$ (this can also happen through phase transitions, see Ref. [72] for an overview). In other words, the cosmological value of Λ, which is a low energy physics parameter, is incredibly sensitive

[3]This depends on the energy scales we are considering in the QFT calculation.

to the high energy physics, which is not technically natural and in apparent opposition to our wide spread employment of effective field theories. These two aspects of the problem are often referred to collectively as the "cosmological constant problem". We refer the interested reader to the seminal paper – Ref. [73] – for a review and the famous no-go theorem which implicitly delineates possible solutions to the problem.

Prospective solutions to these problems include gravitationally screening the vacuum energy from our observations by using a scalar field [74–77] or using extra spacetime dimensions [78]. These solutions would of course also need to produce a small residual energy that can be used to explain our cosmological measurements, in particular those associated with an accelerated spatial expansion. This distinct issue can be called the "dark energy problem", which may be explained through a variation in the fundamental constants of nature such as Newton's gravitational constant, or having the acceleration driven by a scalar field.

Another perplexing feature of the measured value of the cosmological constant is that we appear to be living at a very special moment of the history of the Universe. Namely, because of $\Omega_\Lambda \sim \Omega_\mathrm{m}$, the dark energy domination started fairly recently. This appears to be further fine-tuning of the model's parameters, and is known as the coincidence problem or "new cosmological constant problem" [79]. The coincidence problem was historically one of the motivations for the class of interacting dark-energy models, a promising subclass of which we study in Chapter 3.

1.3.1 Dark Energy and Modified Gravity

In order to resolve the apparent tensions and CC problems various alternative models have been suggested. We start their introduction from Einstein's field equations:

$$G_{\mu\nu} + \Lambda g_{\mu\nu} = 8\pi G T_{\mu\nu} \,. \tag{1.34}$$

Here, Λ is the cosmological constant, and $G_{\mu\nu}$ is the Einstein field tensor that can be directly computed from the first and second derivatives of the metric tensor as $G_{\mu\nu} = R_{\mu\nu} - g_{\mu\nu}R/2$ with the Ricci scalar R, the Ricci tensor $R_{\mu\nu}$, and the energy-momentum tensor $T_{\mu\nu}$ of the cosmic fluid. On the one hand, we can modify its left-hand-side, for example, by modifying the Einstein–Hilbert action. On the other hand, we can modify the right-hand-side with the stress-energy tensor. The first type of modification can be understood as changing the gravitational sector and, hence, is called Modified Gravity (MG). The second type of modification is an alteration of the content of the Universe by adding a new component, hence, it is called Dark Energy (DE). Interacting Dark Energy (IDE) further includes a non-gravitational coupling between dark energy and dark matter. Although there are models which unambiguously belong to one category or the other, for various models a strict division into these two categories is to some extent cumbersome.

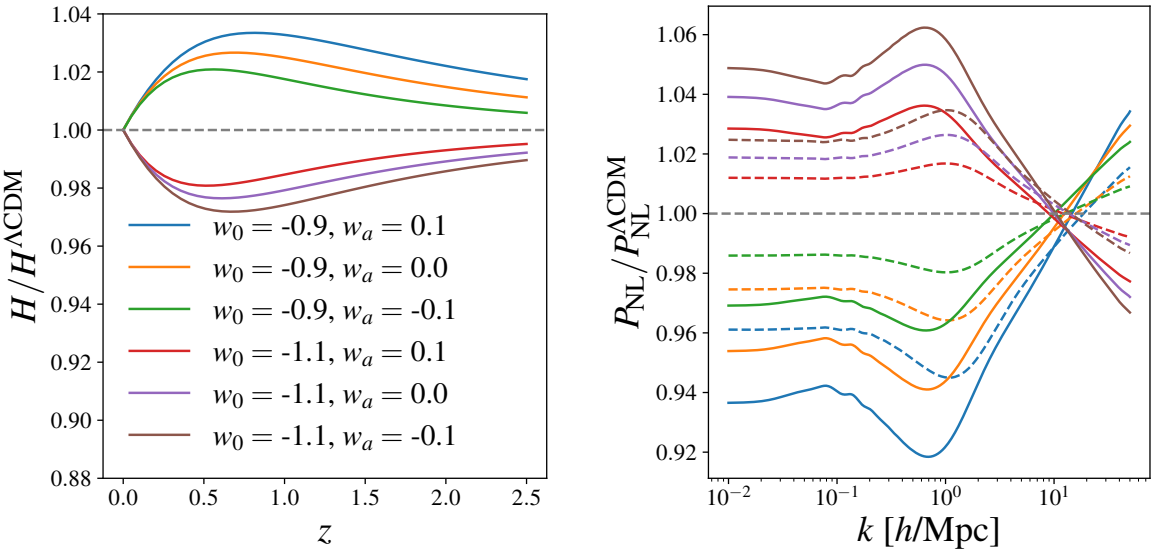

Figure 1.3 *Time evolving dark energy: the expansion history ratio to the reference ΛCDM model (left panel) and the nonlinear matter power spectrum ratio at two different redshifts $z = 0$ (solid lines), $z = 1$ (dashed lines) computed with an* `HMcode` *emulator for model parameters specified in the legend. The emulator was produce for our work in Ref. [2].*

For alternative classifications, we refer the reader to Ref. [80] or Ref. [81].

Dark Energy

In general, DE models are distinguished from a cosmological constant in that they are dynamical, meaning that the equation-of-state parameters from Eq. 1.20 is not fixed at $w = -1$ at all times. One can either assume some functional form of the time-dependence $w(z)$, or be agnostic about it and reconstruct it from data by either applying a Principle Component Approach (PCA) [82] or a direct binning-scheme [83, 84]. In our works we assume the following time-evolution: in the wCDM model $w(a) = w_0 = \text{const}$, while in the w_0w_aCDM model $w(a) = w_0 + w_a(1 - a)$. We forecast the corresponding constraints in Chapter 3 in a Stage-IV setup. The time-dependent model is sometimes called the Chevallier-Polarski-Linder (CPL) parameterisation [85–87]. It has been studied extensively in the literature [88, 89] and we discuss it in Chapter 5 as part of our "minimal parameterisation". Especially, the latest DESI Year 1 BAO results [90, 91], seem to prefer CPL over the standard cosmology. It can fit many scalar field theories[4] and some MG expansion histories [94, 95]. However, can we say something about the microphysics of DE, i.e., about the fundamental mechanism at play which is driving the accelerated expansion,

[4]Here, by "scalar field theories" that can be described by the CPL parameterisation, we mean a subset of Horndeski theories, where an additional scalar field ϕ appears in the action $S = \int \mathrm{d}^4x\sqrt{-g}[\omega(\phi)R - K(X,\phi)]/(2\kappa^2)$ with $\kappa^2 = 8\pi G$ and $X = -\nabla^\nu\nabla_\nu\phi/2$ being the canonical kinetic term of the scalar field. For GR $\omega = 1, K = \Lambda$, while for quintessence [92] $\omega = 1, K = X - V$ with V being a scalar field's potential. This potential can be mapped to the CPL parameterisation [93].

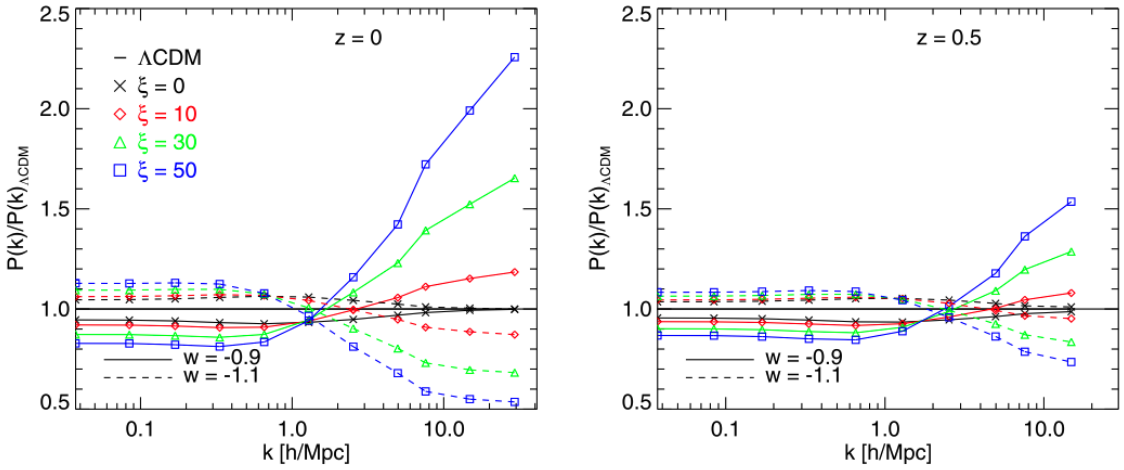

Figure 1.4 *Interacting dark energy: the nonlinear matter power spectrum ratio measured from simulations to the reference ΛCDM model (i.e., $\xi = 0$, $w = -1$) at two different redshifts $z = 0$ (left panel), $z = 0.5$ (right panel) for model parameters specified in the legend. Image credit: Ref. [3].*

if we find precise values of w_0 and w_a far away from their ΛCDM values? Ref. [96] argues that the CPL parameterisation is too ambiguous to reconstruct the corresponding potential $V(\phi)$. Instead they suggest a parameterisation in terms of (V_0, V'') [97, 98]. In any case, both parameterisations, $w = \text{const}$ and $w(a)$, affect the background evolution, i.e., they modify Friedmann equations, but not the form of the Euler or Poisson equations. Changing the amount of DE in the Universe with respect to the standard cosmology impacts the structure formation as well. In Fig. 1.3 we show the effects on the expansion history (left panel) and power spectrum (right panel) in these scenarios.

In Chapter 3, we work with a sub-class of DE models that are interacting with dark matter. It is a rich class of models that assume energy and/or momentum exchange between the two components of the dark sector: dark energy and dark matter. More information about the model we specifically consider is provided in the corresponding Chapter 3. The model has been tested with the Kilo-Degree Survey (KiDS-1000) cosmic shear data [67] and the Baryon Oscillation Spectroscopic Survey (BOSS DR12) data using a full-shape analysis [99], providing a potential solution for the S_8 tension in both cases. In Fig. 1.4 we demonstrate the impact on the power spectrum of the two model parameters, w and ξ, as measured from N-body simulations [3]. The parameter w is the constant DE equation-of-state we have already defined, while the parameter ξ characterises the rate of interaction between CDM and DE.

In Chapter 5, we introduce the Effective Field Theory of Dark Energy (EFTofDE). Despite having DE in the title, this framework incorporates MG as well. This framework reformulates in the unitary gauge the full covariant approach of adding a scalar field into the action. In Chapter 5, we discuss different EFTofDE parameterisations, the most

popular in the literature being the α-parameterisation. These 4 functions of time describe the evolution of linear cosmological perturbations in Horndeski theories and have the following physical meaning [100]:

- $\underline{\alpha_K}$: the kineticity term corresponds to the kinetic energy of the scalar field. Large values of α_K correspond to the suppression of the sound speed of scalar perturbations. However, α_K does not enter the equations of motion in the quasi-static approximation, and, hence, is unconstrained by the current WL and GC data.

- $\underline{\alpha_B}$: the braiding term corresponds to the mixing of the scalar field with the metric kinetic term. This can be interpreted as a fifth force (see *Modified Gravity* next).

- $\underline{\alpha_M}$: the Planck-mass running corresponds to the time-evolution of the effective gravitational coupling.

- $\underline{\alpha_T}$: the tensor speed excess corresponds to the deviations of the propagation speed of gravitational waves from the speed of light.

The EFTofDE framework describes linear perturbations, although there have been attempts to include higher-order corrections [101, 102]. Whereas, the fully nonlinear EFTofDE modelling requires a different, non-perturbative approach (see Chapter 5).

Modified Gravity

Starting from the action, a coupling of a scalar field with the Ricci scalar or energy components in the Universe (one is equivalent to another by going from the Jordan to the Einstein frames [103]) introduces an additional fifth force in the equations of motion. The fifth force typically leads to stronger gravitational interactions than in GR. However, as listed above, GR satisfies various small scale experiments, typically within our Solar System [104]. In order to comply with these small-scale constraints, any viable MG theory should be able to suppress the fifth force on these scales. The mechanism of restoring the gravitational interaction to that of GR on small scales is called screening and is discussed in Chapter 5 and Chapter 6. Comprehensive reviews on screening mechanisms can be found in Refs. [81, 105, 106]. Screening mechanisms are activated in regions where either the gravitational potential or its derivatives become large, which leads to the following classification:

- $\underline{\text{Large } \Phi}$: the coupling of the scalar field with matter weakens, or the mass of the scalar field increases, or the self-coupling to the field becomes large. An example of such screening is the Chameleon mechanism. Chameleon screening occurs in theories where the scalar field takes a background value $\bar{\phi}$ determined by the background density or curvature. The potential introduces a mass term for the scalar field perturbation $m(\phi)$ which depends on the background field. The scalar

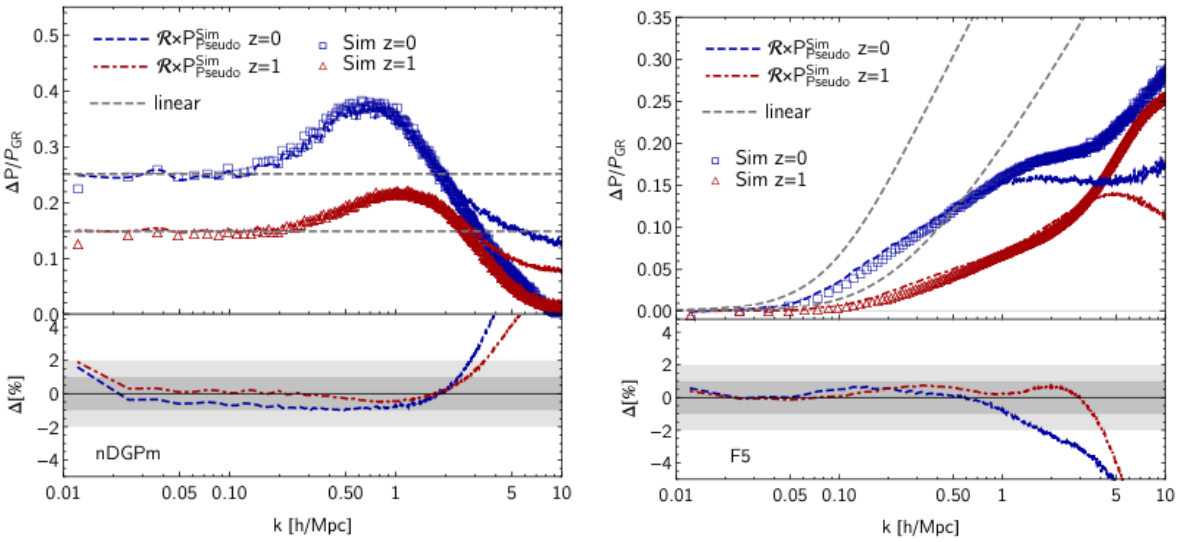

Figure 1.5 *Modified gravity: matter power spectrum fractional enhancements relative to GR for nDGP with $r_cH_0 = 0.5$ or $\Omega_{rc} = 1$ (left panel) and for $f(R)$ gravity with $|f_{R0}| = 10^{-5}$ (right panel). The data points correspond to the results from simulations at $z = 0$ (blue squares) and $z = 1$ (red triangles). Coloured lines denote predictions based on the halo-model reactions at $z = 0$ (dashed blue) and $z = 1$ (dot-dashed red). The linear theory predictions are denoted as dashed grey lines. Image credit: Ref. [4].*

field perturbations do not propagate beyond the Compton wavelength m^{-1}. Dense regions on small scales lead to a large $m(\phi)$ and hence to the screening activation. On the other hand, on large scales the density is low, allowing for a large Compton wavelength and, hence, deviations from GR.

- Large $\nabla\Phi$: an example is given by the k-mouflage type screening. In dense environments of mass M, the screening scale – the scale below which GR is recovered – goes as $M^{1/2}$. Note that it is not capable of screening large cosmological structures effectively.

- Large $\nabla^2\Phi$: the case for models where nonlinearities of the second derivative of the scalar field are present in the equation of motion. An example is Vainshtein screening that introduces a clear screening scale within which GR is recovered. This screening scale is at smaller scales than in k-mouflage, with a dependence on the environmental mass being $M^{1/3}$.

Note that for MG models, screening is not a phenomenological "fudge" factor imposed artificially to reconcile them with the Solar System observations. In contrast, it is a natural part of a model, arising through the choice of the interaction potential.

In our studies we focus mainly on two models, nDGP and $f(R)$. Both models should be treated as representative models for the class of MG theories with scale-independent linear growth with Vainshtein screening and scale-dependent linear growth with Chameleon

screening, respectively. In Fig. 1.5, we show the nonlinear power spectra for these models as measured from numerical simulations and the semi-analytic halo-reaction approach predictions (see Section 5.2 and Subsection 6.1.1).

- The DGP model, proposed by Dvali, Gabadadze and Porrati in Ref. [107], belongs to the group of higher dimensional modifications. Its main principle is based on the assumption that in the corresponding Universe matter lives on a four-dimensional brane which is embedded in a five-dimensional Minkowski spacetime. In this way, gravity operates in five dimensions on large scales which gets reduced to four dimensions on small scales, where the model mimics an effective scalar-tensor theory with a massless scalar degree of freedom. This degree of freedom, also known as the brane-bending mode, shows a strong self-coupling in high-density regions, which leads to restoring GR through the Vainshtein mechanism. In our work we focus on the normal branch of this model, nDGP. The other branch is called the self-accelerating branch (sDGP). sDGP leads to the self-acceleration of the Universe at late times without any cosmological constant needed. However, it suffers from a ghost instability [108] (a ghost is a mode with a negative kinetic energy). The normal branch is indeed free from ghost instabilities, but requires an additional dark-energy contribution on the brane in order to reproduce the observed expansion history (see Section D.4). The strength of deviation from GR is characterised either by $H_0 r_c$ or by $\Omega_{rc} \equiv 1/(4H_0^2 r_c^2)$ with the GR limits being $H_0 r_c \to \infty$ or $\Omega_{rc} = 0$, where r_c is defined as a ratio between gravitational coupling constants in 5 and 4 dimensions. The screening mechanism for nDGP is Vainshtein screening. The fifth force in this scenario for two test particles separated by r has the following form $\propto r^{-2}(r/r_\mathrm{V})^3[\sqrt{1+(r_\mathrm{V}/r)^3}-1]$, which recovers Newtonian gravity with $\propto r^{-2}$ deep within the Vainshtein radius, i.e., for $r \ll r_\mathrm{V}$. The Vainshtein radius depends on the strength of modification, redshift and mass of the screening object.

- $f(R)$ models introduce field equations that are higher order in the Ricci scalar R. This is done by the addition of a nonlinear function of the Ricci scalar to the Einstein-Hilbert action. This additional function introduces a light scalar degree of freedom, which leads to a long-range fifth force, hence a dissociation of the space-time curvature with the matter density. An accelerated expansion of the Universe in $f(R)$ theory is produced in a natural fashion by generating an effective cosmological constant instead of introducing it explicitly. The functional form of $f(R)$ should satisfy two basic requirements: stability and agreement with cosmological and Solar System tests. The model by Wayne Hu and Ignacy Sawicki [109] does indeed satisfy the requirements. In the Hu-Sawicki model of $f(R)$ gravity the function of the Ricci scalar is given by

$$f(R) = -m^2 \frac{c_1 (R/m^2)^n}{c_2 (R/m^2)^n + 1}\,, \tag{1.35}$$

with free dimensionless parameters n (typically 1), c_1 and c_2, and the mass scale $m^2 \equiv H_0^2 \Omega_\mathrm{m}$. These specific models mimic the background expansion of the ΛCDM model if we fix

$$\frac{c_1}{c_2} = 6\frac{\Omega_\Lambda}{\Omega_\mathrm{m}}\,, \quad \frac{c_1}{c_2^2} = -\frac{1}{n}\left[3\left(1+4\frac{\Omega_\Lambda}{\Omega_\mathrm{m}}\right)\right]^{n+1} f_{R0}\,, \tag{1.36}$$

in which the parameter f_{R0} is the value of $f_R = \mathrm{d}f(R)/\mathrm{d}R$ today, whose absolute value is much smaller than one. The screening mechanism for $f(R)$ is the Chameleon mechanism and the corresponding mass of the scalar field is given by $m(\phi) = m_{f_R} = (3f_{RR})^{-1/2} \propto \rho_\mathrm{m}^{3/2}$, where f_{RR} is the second derivative of $f(R)$ with respect to R. The fifth force in this scenario has a Yukawa-type potential and for two test particles separated by r decays exponentially as $\propto r^{-2}\exp\left(-m_{f_R} r\right)$, which recovers Newtonian gravity for high density regions.

Models like DGP and $f(R)$ models are fairly well studied, they are equipped with linear and nonlinear prescriptions, CDM simulations and observational (astrophysical and cosmological) constraints. However, there is still a large amount of other theories without a comparable degree of development. Instead of studying each MG model on a case by case basis, we can develop a generalised approach, i.e., a parameterisation, which, when constrained, could narrow down the class of realistic models. Analogously to the CPL parameterisation (see *Dark Energy* above) of $w(a)$ for various DE quintessence models, we can assume a parameterisation of the linear growth as a function of time. One example is the α-parameterisation from EFTofDE mentioned above (see Subsection 5.4.4). Another example is the growth index γ-parameterisation discussed in Chapter 4 and Chapter 6. Both of these approaches can be extended to incorporate a scale-dependence in the linear growth. In principle, they can also be mapped to specific MG models.

μ-Σ Parameterisation

Another commonly used approach for MG parameterisation involves a direct modification of the Poisson equations. Considering linear scalar perturbations on a FLRW metric, one can write the spatially flat line element in the conformal Newtonian gauge as

$$\mathrm{d}s^2 = -(1+2\Phi)\mathrm{d}t^2 + a^2(1-2\Psi)\mathrm{d}\boldsymbol{x}^2\,, \tag{1.37}$$

with Φ being the Newtonian potential and the intrinsic spatial curvature potential being Ψ. We can then modify the linear Poisson equations in Fourier space neglecting the

anisotropic shear as

$$-\left(\frac{k}{aH(a)}\right)^2 \hat{\Phi}(\boldsymbol{k},a) = \frac{3\Omega_{\rm m}(a)}{2}\mu(k,a)\,\hat{\delta}(\boldsymbol{k},a)\,, \tag{1.38}$$

$$\hat{\Psi} = \eta(k,a)\hat{\Phi}\,, \tag{1.39}$$

where η is the slip parameter, and which simplifies to the standard GR case for $\mu = \eta = 1$. We now obtain a Poisson equation for the Weyl potential, $\Psi_{\rm W} = (\Phi + \Psi)/2$, as

$$-\left(\frac{k}{aH(a)}\right)^2 \hat{\Psi}_{\rm W}(\boldsymbol{k},a) = \frac{3\Omega_{\rm m}(a)}{2}\Sigma(k,a)\,\hat{\delta}(\boldsymbol{k},a)\,, \tag{1.40}$$

with $\Sigma(k,a) \equiv \mu(1+\eta)/2$, which equals unity in the GR case. The functions μ and Σ are often referred to as $G_{\rm matter}$ and $G_{\rm light}$: the gradient of Φ determines the force felt by non-relativistic particles, while the gradient of $\Psi_{\rm W}$ determines the geodesics of massless particles. Generally, most viable MG theories exhibit a strong preference to a no-slip condition so that $\Phi \approx \Psi$ (see Fig. 2-4 in Ref. [110]), hence, $\Sigma \approx \mu$.

The main advantage of this parametric approach is that it is model-agnostic and allows us to test gravity with few assumptions, e.g., assumptions about the time-dependence of growth. The scale-dependence in μ and Σ can be expressed via a ratio of quadratic polynomials in k [111]. Additionally, it is worth noting that an established mapping to the general properties of Horndeski theories is feasible in this approach [112]. The main disadvantage, however, is a great degree of freedom: a discretisation or binning of μ and Σ introduces $2 \times N_k \times N_z$ free parameters. Attempts to explore this approach without scale-dependency and with additional constraints from theoretically motivated priors can be found in Refs. [98, 113]. While Refs. [89, 114, 115] show constraints under some assumptions on the functional form for the time-dependent $\mu(z)$ and $\Sigma(z)$.

1.3.2 Massive Neutrinos

Finally, we discuss the least speculative extension of the standard cosmological model: massive neutrinos. Neutrinos are neutral leptonic particles produced by weak force interactions. They come in three flavours associated with the corresponding charged leptons: electron, muon and tau neutrinos. Neutrinos oscillate between these three flavours as has been demonstrated by solar and atmospheric neutrino experiments [116, 117], which implies that they have finite mass eigenstates. The current best fits to the particle physics oscillation experiments measure two square mass splittings between neutrino flavours $\Delta m^2_{21} \approx 7.4 \times 10^{-5}$ eV^2 (from solar neutrinos) and $|\Delta m^2_{31}| \approx 2.5 \times 10^{-3}$ eV^2 (from atmospheric neutrinos) [118, 119]. These experiments also imply that at least two of the neutrino types have a non-vanishing mass. The sign of Δm_{31} is unknown, which suggests two possible mass hierarchies: normal with $m_1 < m_2 < m_3$ (2 light

neutrinos and 1 heavy one) and, hence, the lower bound $\sum m_\nu \geq 0.06$ eV; or inverted with $m_3 < m_1 < m_2$ (2 heavy neutrinos and 1 light one) and the lower bound $\sum m_\nu \geq 0.1$ eV. While particle physics can put constraints on the mass splittings and the upper bound from the beta decay of tritium [120, 121], cosmology can constrain the total mass of neutrinos through their indirect effects on CMB and LSS (see Ref. [122] for a review). The current typical constraints are around $\sum m_\nu \leq 0.1 - 0.2$ eV [123]. Therefore, in the following arguments we will always assume that the mass of neutrinos is in this range.

We will now provide a brief summary of the role of neutrinos in the thermal history of the Universe. In the beginning neutrinos are coupled to the thermal plasma in the hot bath of elementary particles. However, they soon decouple when the expansion rate becomes comparable with the rate of the weak interactions, and the latter become less frequent. After decoupling neutrinos are still relativistic and they propagate freely, following the Fermi-Dirac distribution. With the further expansion, neutrinos follow the same temperature as the plasma.

The next event in the thermal history is the electron-positron annihilation, after which the photon plasma gets reheated. After this, the photon temperature is higher than the temperature of the earlier decoupled neutrinos. By comoving entropy conservation, we can relate these temperatures as $T_\nu = (4/11)^{1/3} T_\gamma$. This relation holds until today, allowing us to find the neutrino background temperature from the CMB temperature $T_{\gamma,0} \approx 2.73$ K, giving $T_{\nu,0} \approx 1.95$ K. Of course, in reality the processes of annihilation and neutrino decoupling do not happen instantaneously. Neutrinos in the high-energy tail of their distribution that are still not decoupled from the plasma will feel the reheating effect too. This leads to a higher neutrino temperature than the one we get from the simplification above. This can be taken into account by introducing the effective number of relativistic degrees of freedom, $N_{\rm eff}$, so that the total energy density of radiation in the early Universe is given by

$$\rho_{\rm r} = \rho_\gamma \left(\frac{T_\gamma}{T_\gamma}\right)^4 + \frac{7}{8} \sum \rho_\nu \left(\frac{T_\nu}{T_\gamma}\right)^4 = \left[1 + \frac{7}{8}\left(\frac{4}{11}\right)^{4/3} N_{\rm eff}\right] \rho_\gamma \,. \tag{1.41}$$

The factor (7/8) comes from the integration of the Fermi-Dirac distribution. The energy densities of neutrinos and photons, ρ_γ and ρ_ν, include the same statistical weights $g = 2$ (due to 2 polarisation/helicity options). $N_{\rm eff} = 3.044$ is computed within the standard model of particle physics when neutrino oscillations and quantum electrodynamical effects are taken into account [124]. This value is in agreement with the findings from CMB experiments [89].

Massive neutrinos start behaving non-relativistically when the Universe cools down to a temperature of the same magnitude as the mass of neutrinos. With the temperature scaling linearly with redshift $T_\nu(z) = T_{\nu,0}(1+z)$, the average energy density of neutrinos

(analogous to other fermions) is $\langle E \rangle \approx 3.15 T_\nu$. For each neutrino species with mass m_ν, the non-relativistic transition happens at redshift

$$1 + z_{\rm nr} \approx \frac{m_\nu}{3.15\ T_{\nu,0}} \approx 189 \frac{m_\nu}{0.1\ \text{eV}}\,. \tag{1.42}$$

From this we see that different neutrino species become non-relativistic at slightly different times. We also see from Eq. 1.42 that neutrinos of $\mathcal{O}(0.1)$ eV mass and smaller become non-relativistic during the matter domination era.

In the non-relativistic limit, the neutrino energy density is a function of mass: $\rho_\nu = n_\nu \sum m_\nu$ with the number density per flavour, n_ν, being determined by integrating the Fermi-Dirac distribution function. We can now express the present day energy density of massive neutrinos as

$$\Omega_\nu = \frac{n_\nu \sum m_\nu}{\rho_{\rm crit}} \approx \frac{\sum m_\nu}{93.14\ h^2\ \text{eV}}\,. \tag{1.43}$$

From this, we can see that neutrinos of $\mathcal{O}(0.1)$ eV mass today contribute to less than 1% of the present-day total energy budget.

Neutrinos' large momentum prevents them from clustering on scales smaller than they can move in a Hubble time. In other words, neutrinos cannot remain confined inside potential wells with wavelength smaller than the horizon. We can define the free-streaming scale as

$$k_{\rm FS} = \sqrt{\frac{3}{2}} \frac{\mathcal{H}}{c_{\rm s}} \propto \frac{H(z) m_\nu}{(1+z)^2 T_{\gamma,0}}\,, \tag{1.44}$$

where we approximate the neutrino sound velocity, $c_{\rm s}$, by the neutrino velocity dispersion after they become non-relativistic following Ref. [125]. The free-streaming scale is close to the horizon size with $c_{\rm s} \to 1$ and $k_{\rm FS} \propto (1+z)^{1/2}$ until the non-relativistic transition. Afterwards, the free-streaming wave-number increases as $k_{\rm FS} \propto (1+z)^{-1/2}$ with decreasing redshift. The minimum of the free-streaming scale is at the moment neutrinos become non-relativistic, which can be approximated by

$$k_{\rm nr} = k_{\rm FS}(z_{\rm nr}) \approx 0.0057\ \Omega_{\rm m}^{1/2} \left(\frac{m_\nu}{0.1\ \text{eV}}\right)^{1/2} h\ \text{Mpc}^{-1}\,. \tag{1.45}$$

From this we see that neutrinos of $\mathcal{O}(0.1)$ eV mass start to suppress growth already in the linear regime with $k_{\rm nr} \sim \mathcal{O}(0.001)\ h\ \text{Mpc}^{-1}$. Neutrino perturbations are completely erased at length scales much smaller than the free-streaming scale which leads to the suppression of the matter power spectrum, i.e., damping of structure growth on small scales. On scales larger than the free-streaming scale neutrino perturbations act like CDM perturbations. For more details see the review in Ref. [126].

The main feature of massive neutrinos becomes measurable at late times after the non-relativistic transition. With late-time probes, GC and WL, we can constrain $N_{\rm eff}$ and $\sum m_\nu$ by their impact on structure formation. Both parameters have similar effects

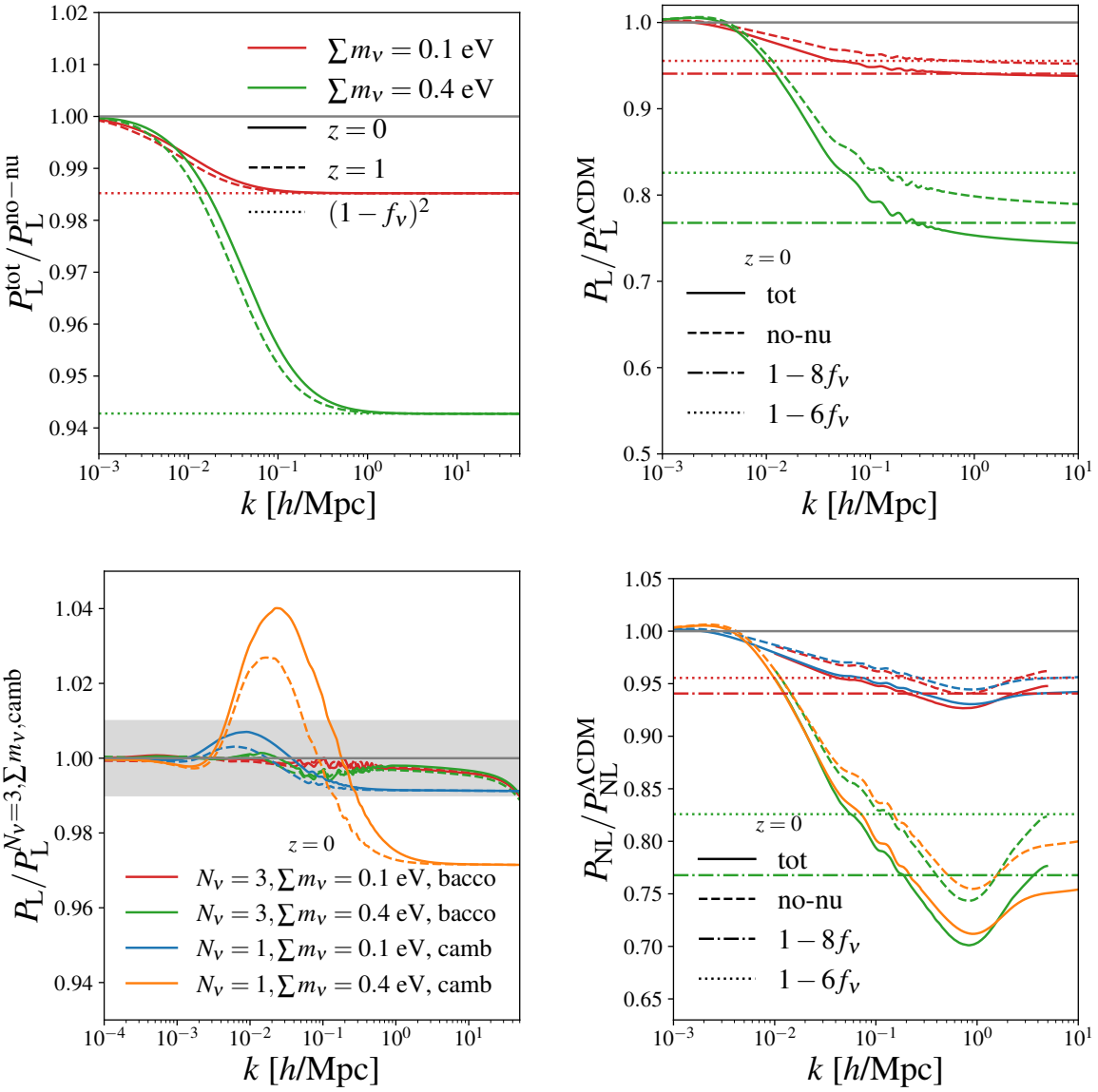

Figure 1.6 *Upper left panel: ratios of the total linear matter power spectrum to the linear power spectrum without the massive neutrino contribution at redshifts $z = 0$ (solid lines) and $z = 1$ (dashed lines) for two different values of the sum of neutrino masses specified in the legend with $N_\nu = 3$ and computed with* `CAMB`*. Dotted lines denote the asymptotic limit. Upper right panel: ratios at $z = 0$ of the total linear matter power spectrum (solid lines) and no-neutrino linear power spectrum (dashed lines) to the ΛCDM prediction. Dash-dotted and dotted lines denote the asymptotic limits. Lower left panel: ratios at $z = 0$ of the total (solid lines) and no-neutrino linear power spectra (dashed lines) with respect to the linear* `CAMB` *prediction for 3 massive neutrinos species given different codes, number and total mass of neutrinos specified in the legend. Lower right panel: the same colour-coding as on the lower left panel but for nonlinear power spectrum ratios with respect to the ΛCDM expectations computed with the* `bacco` *emulator (red and green) and with the* `HMcode` *emulator (blue and orange).*

on the level of the two-point statistics. In our work we focus only on constraining the total mass of neutrinos. At later times massive neutrinos contribute to the background expansion but cluster only on length scales larger than the free-streaming scale. This way of clustering clearly introduces a scale-dependent linear growth that we showcase in the top right panel of Fig. 1.6.

In our work we use two different approaches for massive neutrino contributions to the linear and nonlinear clustering of matter:

- In Chapter 4 we use the linear `bacco` emulator. The simulations on which the nonlinear power spectrum emulator is trained are initialised with the `CLASS` linear power spectra prediction, computed for 3 massive neutrinos of the same mass, i.e., $N_\nu = 3$. Linear power spectra for the linear emulator are computed with the same settings and the same Boltzmann solver. This approach is widely used in the literature, for example, in Refs. [84, 89, 127].

- In Chapter 6 we compute transfer functions with `CAMB` for 2 massless/relativistic neutrinos and one massive neutrino that is equal to the total mass $\sum m_\nu$ with $N_\nu = 1$ and the number of relativistic species today $N_\mathrm{r} = 2.046$. In other words, the two lower mass neutrino species are set to zero in the normal hierarchy. This approach is also common in the literature, for example, in Refs. [21, 128, 129]. The nonlinear structure growth is then modelled with the reaction function in the halo-model framework following Ref. [130].

In the top left panel panel of Fig. 1.6 we show the ratio of the total matter, $P_\mathrm{L}^\mathrm{tot}$, and no-neutrino, $P_\mathrm{L}^\mathrm{no-nu} = P_\mathrm{L}^\mathrm{CDM+b}$ [5], linear power spectra for 3 massive neutrino species and different total mass choices with redshifts specified in the legend. In the top right panel of the same figure we show the ratio of the linear power spectra for 3 massive neutrinos with the respect to the case without massive neutrinos, $P_\mathrm{L}^\Lambda\mathrm{CDM}$, and different mass choices with the same colour-coding and at redshift $z = 0$. As quantified in Ref. [131], the suppression is proportional to the neutrino mass fraction, $f_\nu \equiv \Omega_\nu/\Omega_\mathrm{m}$, as

$$\frac{P_\mathrm{L}^\mathrm{tot}(f_\nu, \Omega_\mathrm{m})}{P_\mathrm{L}^\Lambda\mathrm{CDM}(f_\nu = 0, \Omega_\mathrm{m})} \approx 1 - 8f_\nu, \qquad \frac{P_\mathrm{L}^\mathrm{no-nu}(f_\nu, \Omega_\mathrm{m})}{P_\mathrm{L}^\Lambda\mathrm{CDM}(f_\nu = 0, \Omega_\mathrm{m})} \approx 1 - 6f_\nu. \tag{1.46}$$

In the bottom left panel panel of Fig. 1.6 we demonstrate the linear growth for 1 and 3 massive neutrinos for different mass choices specified in the legend and redshift $z = 0$. Even for extreme cases of very massive neutrinos we are always bellow 4% deviation. The observed difference between 1 and 3 neutrino species of the same total mass is explained by the difference in the free-streaming scale (see Eq. 1.45): while the total matter density is the same, k_nr is $\sqrt{3}$ times smaller for 3 neutrinos case since the individual masses are

[5] This means a power spectrum of CDM and baryonic matter in a cosmology with massive neutrinos.

smaller. For one massive neutrino of the same total mass, the free-streaming length scale is smaller ($k_{\rm nr}$ is larger), hence there is more clustering on the large scales which is what we observe in the "bump" in blue and orange curves. The top panel plots in the one massive neutrino species scenario look similar but the non-relativistic transition happens earlier at larger $k_{\rm nr}$, hence the analogous curves are shifted towards higher wave-numbers. Both configurations are unique: matching $k_{\rm nr}$ between 1 and 3 neutrino species would imply changes in the CDM and baryonic density component, i.e., in $\Omega_{\rm m} - \Omega_\nu$. In the same figure we note the slight difference between `CAMB` and `bacco` (`CLASS`) for the same setup of neutrinos, i.e., same number of species, same total mass. This leads to a 1% deviation at high k-values, which is a known difference between the two Boltzmann solvers for the massive neutrino case [132, 133].

In the bottom right panel of the same figure we show the nonlinear power spectrum from simulations emulated with `bacco` and from the halo-model with `HMcode` for 3 massive neutrinos species of the same mass. In the nonlinear regime we observe a well-known spoon-like shape [134, 135], characterised by a dip around $k \sim 1\ h\ {\rm Mpc}^{-1}$. This form can be explained by the combination of the matter clustering suppression induced by neutrinos' free streaming, combined with a rise at smaller scales occurring due to insensitivity of the most massive halos to neutrinos. Despite observing a significant difference between no massive neutrinos and $N_\nu > 0$, the difference between 1 and 3 massive species is such that the data considered in Chapter 4 and Chapter 6 is not capable to distinguish between these scenarios. However, the combined measurements of Stage-IV WL, GC and CMB experiments might be sensitive to it. For a comparison of different models for massive neutrinos see, for example, Ref. [136]. For a comparison of different nonlinear models and codes for massive neutrinos see Ref. [137], for a fully relativistic simulation see Ref. [138]. Finally we note that the no-nu matter power spectrum is more useful for the various GC and halo statistics (e.g., Refs. [131, 139]), but the total matter power spectrum is practical for WL analyses.

1.4 Galaxy Clustering

Formalism

In Subsection 1.2.2 we discussed the formation of structures, linear and nonlinear, in three spatial dimensions. When observing galaxies, their positions are informed with redshifts that can be measured either with spectroscopic methods, or via photometric methods (derived from broad-band colours with larger uncertainties). In this thesis, we work only with spectroscopic GC, and, hence, will focus on it here. The measured redshift, $z_{\rm obs}$, captures velocities due to the expansion of the Universe, z, as well as due to the peculiar motion of the objects, $\boldsymbol{v} = \boldsymbol{v}_\parallel + \boldsymbol{v}_\perp$. Therefore, instead of working with three-dimensional

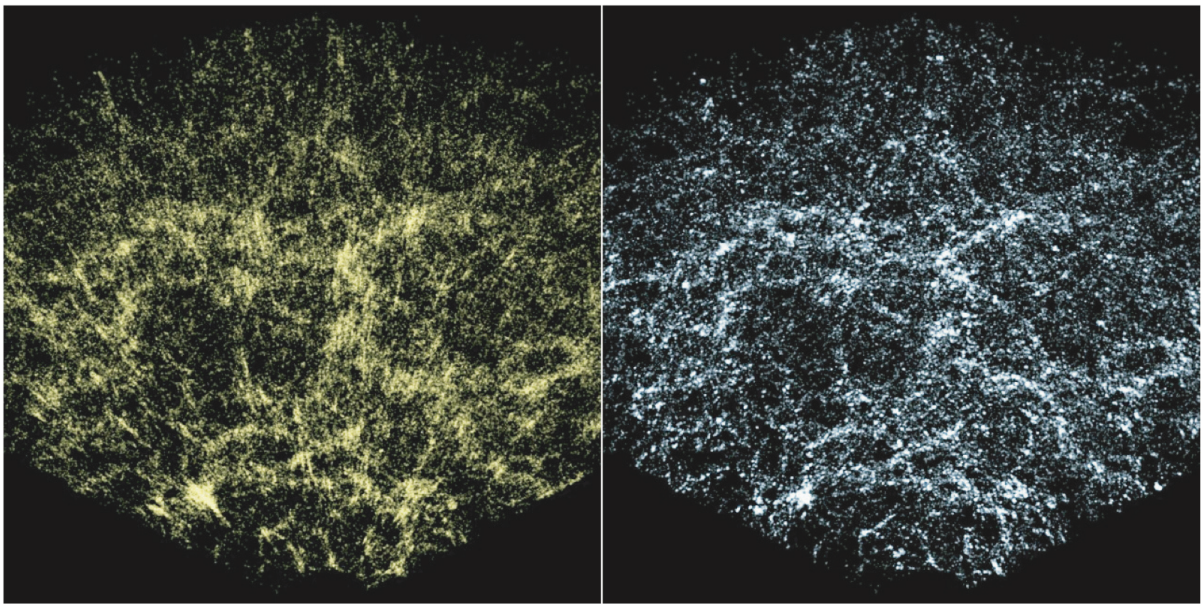

Figure 1.7 *Effect of the RSDs in the Sloan Digital Sky Survey (SDSS) galaxy distribution: before (left panel) and after (right panel) FoG compression. Image credit: Ref. [5].*

space coordinates $\boldsymbol{x} = (x_1, x_2, x_3)$, we observe the position of an object in redshift-space $\boldsymbol{s} = (x_1, x_2, z_{\rm obs})$. Both can be mapped to each other as

$$\boldsymbol{s} = \boldsymbol{x} + \frac{(1+z)v_{\parallel}(\boldsymbol{x})}{H(z)}\hat{\boldsymbol{x}} \tag{1.47}$$

with the contribution due to the peculiar motion in the radial, line-of-sight direction, $v_{\parallel}$. This peculiar velocity introduces Redshift Space Distortions (RSDs) that lead to anisotropies in correlation functions. At large scales, objects tend to move coherently towards high-density regions, causing the density field in redshift space to become "squashed" and the clustering amplitude to increase along the line-of-sight, a phenomenon known as the Kaiser effect [140]. Conversely, at small scales, objects are virialised and moving randomly, leading to a stretched density field in redshift space and a reduced clustering amplitude in the radial direction, referred to as the Finger-of-God (FoG) effect. In Fig. 1.7 the SDSS galaxy distributions with (left panel) and without (right panel) the FoG effect are demonstrated.

Galaxies, quasars and other light emitting sources are biased tracers of the underlying CDM distribution. Note that CDM halos from numerical simulations are also biased tracers of the CDM distribution. On large scales we can assume a linear bias, i.e., direct proportionality between observed objects and underlying invisible matter: $\delta_{\rm g} = b_1\delta_{\rm m}$. When including nonlinear scales, the bias can either be treated perturbatively or derived from simulations. In simulations, halos are populated with galaxies following an analytical Halo Occupation Distribution (HOD) [141] prescription calibrated on observations or

subhalo abundance matching methods (SHAM) [142]. In Chapter 3 and Chapter 4 (with CDM halos and galaxies as tracers, respectively) we apply the perturbative approach [33] and expand the bias up to the corresponding order. In broad strokes, the matter-to-tracer correspondence depends on (for more details see Subsection 3.2.1)

- Local effects: $b_1, b_2, ...$ bias-parameters correspond to the expansion in a power series in δ, are also called local-in-matter-density bias, they emphasise collapsed regions.
- Environmental effects: tidal or shear fields, formation history of halos and galaxies – effects that enhance the sheet-like and filament-like structure of the cosmic web.
- Higher-derivatives: they correspond to the Laplacian of δ, physically they capture the smoothing effects of collapsed regions and also take into account non-gravitational physics that impacts the galaxy formation process.
- Properties of the observed objects, such as the mass and luminosity; e.g., red galaxies are more clustered than blue galaxies of the same mass.

In general, there are two ways of looking at the CDM fluid: Eulerian and Lagrangian approaches. Standard Perturbation Theory (SPT) uses the Eulerian ansatz, where the evolution of the CDM fluid is considered at specific locations in space, where we can study its density and velocity fields. Lagrangian approach suggests to track the trajectories of CDM particles: we start with some initial distribution of comoving particles that are then mapped into their final position by means of a displacement field [143]. Lagrangian bias is more physically motivated, however it can be mapped into the Eulerian bias approach [144, 145].

In the linear regime, after applying the conservation of matter density field in both coordinates, $\rho^s_{\rm m}(\boldsymbol{s})\mathrm{d}\boldsymbol{s} = \rho_{\rm m}(\boldsymbol{x})\mathrm{d}\boldsymbol{x}$, and the linearised continuity equation (see Eq. 1.24) $\delta_{\rm L} = \theta_{\rm L}$ with $\theta = -\nabla v/(a\ H(a)\ f)$, we can connect the observed density perturbation in galaxies with the underlying CDM distribution in Fourier space as

$$\begin{aligned}\hat{\delta}^{s,\rm L}_{\rm m}(\boldsymbol{k}) &= (1 + f\mu^2)\hat{\delta}^{\rm L}_{\rm m}(\boldsymbol{k})\,,\\ \hat{\delta}^{s,\rm L}_{\rm g}(\boldsymbol{k}) &= (b_1 + f\mu^2)\hat{\delta}^{\rm L}_{\rm m}(\boldsymbol{k})\,.\end{aligned} \tag{1.48}$$

This is the famous Kaiser formula [140]. It is based on the following assumptions: distant observer and plain-parallel approximation (the wide angle effects [146] are ignored), and no velocity bias. From the Kaiser formula, we can find an expression for the linear power power spectrum of the observed tracers and expand it in Legendre polynomials (as

explained in Section 1.1) with $\beta = f/b_1$:

$$P^{\rm L}_{{\rm g},\ell=0}(k) = \left(1 + \frac{2\beta}{3} + \frac{\beta^2}{5}\right) b_1^2 P^{\rm L}_{\rm m}(k)\,,$$
$$P^{\rm L}_{{\rm g},\ell=2} = \left(\frac{4\beta}{3} + \frac{4\beta^2}{7}\right) b_1^2 P^{\rm L}_{\rm m}(k)\,,$$
$$P^{\rm L}_{{\rm g},\ell=4} = \frac{8\beta^2}{35} b_1^2 P^{\rm L}_{\rm m}(k)\,. \tag{1.49}$$

We can see that in the linear regime the ratio between the monopole and quadrupole is constant. RSDs give rise to a measurable quadrupole and hexadecapole, and enhance the isotropic part, the monopole, by $2\beta/3 + \beta^2/5$. While the monopole provides good constraints on $(b_1\sigma_8)$, $(f\sigma_8)$ is best measured by the anisotropic power spectrum. Here, σ_8 is the redshift zero value of the matter density fluctuation variance from Eq. 1.32 within $R = 8$ Mpc h^{-1}.

In the nonlinear regime, in order to include smaller scales we expand the density and velocity fields (Eulerian PT) or the displacement field (Lagrangian PT) perturbatively [33]. However, any PT suffers from divergencies when integrating the PT-kernels up to $k \to \infty$. To avoid the divergencies, we can introduce a cut-off scale following an Effective Field Theory (EFT) philosophy. The EFTofLSS framework [147–149] also treats the CDM fluid as a non-ideal fluid and includes marginalised contribution from astrophysical scales. Currently, the EFTofLSS is established in the field as an accurate and well-tested modelling tool for a full-shape analysis [150, 151]. There are several codes and approaches for the power spectrum and bispectrum modelling with the EFTofLSS that slightly vary in their parameterisation of nuisance parameters and Infrared-Resummation (IR) implementations: `pyBIRD` [152], `CLASS-PT` [150], `PBJ` [153] – Eulerian PT (for a comparison between the so-called East and West Coast codes see Ref. [154], for mapping between parameters see Ref. [155]), and `Velocileptors` [156, 157] – Lagrangian PT. We work with `PBJ`, the model is similar to the one in `CLASS-PT`, but the calculations are faster due to the usage of the `FAST-PT` algorithm [158, 159] and the `bacco` emulator for the linear power spectrum. In general, any PT in redshift space starts to deviate from the exact solution at larger scales than in real space, because the redshift-space mapping is only treated approximately.

Infrared-resummation schemes are important for the EFTofLSS. A straightforward implementation of the SPT fails around the BAO scale because the wiggly part of the power spectrum gets a large contribution from the infrared or long-wavelength scales in the loop integral[6]. We demonstrate it here via several approximations. The 1-loop integral

[6]In perturbative theories correlation functions in the density contrast are convolutions of the initial density fields, they can be expressed as momentum integrals over a corresponding number of initial linear power spectra. We call these integrals loop integrals (see, e.g., Ref. [160]).

has the following form:

$$P_{1-\mathrm{loop}}(k) \propto \int \mathrm{d}^3q \frac{(\boldsymbol{q}\cdot\boldsymbol{k})^2}{q^4}[P_L(|\boldsymbol{k}-\boldsymbol{q}|)+P_L(|\boldsymbol{k}+\boldsymbol{q}|)-2P_L(|\boldsymbol{k}|)]P_L(q)\,. \tag{1.50}$$

On very large scales, in the linear regime we can approximate the linear power spectrum as a non-wiggly power law $P_L^{\mathrm{nw}} \propto k^n$ (with $n = n_s \approx 1$ before the turn-around peak, i.e., equality scale, and $n = n_s - 4 \approx -3$ afterwards) and we find that the square brackets can be Taylor expanded to $P_L^{\mathrm{nw}}(k)q^2/k^2$. Hence, the loop correction to the smooth non-wiggly power spectrum from large scales is negligible with

$$P^{\mathrm{nw}}_{1-\mathrm{loop}}(k) \propto P_L^{\mathrm{nw}}(k)\int_0^{p\ll k}\mathrm{d}^3qP_L^{\mathrm{nw}}(q) \ll 1\,. \tag{1.51}$$

However, when we apply the same logic to a wiggly part of the matter power spectrum around the BAO scale, ℓ_{osc}, by approximating $P_L^{\mathrm{w}} \propto \sin(k\ell_{\mathrm{osc}})$, the square brackets in the integrand yield $P_L^{\mathrm{w}}(k)\left[\cos(q\ell_{\mathrm{osc}})-1\right]$. Therefore, the contribution to the wiggly component is not negligible anymore with

$$P^{\mathrm{w}}_{1-\mathrm{loop}}(k) \propto k^2P_L^{\mathrm{w}}(k)\int_{\ell_{\mathrm{osc}}^{-1}}^{k}\mathrm{d}^3q\frac{P_L^{\mathrm{w}}(q)}{q^2} \approx P_L^{\mathrm{w}}(k). \tag{1.52}$$

This leads to percent-level oscillatory inaccuracies. In order to avoid insufficient damping of the baryon acoustic oscillations, we apply the wiggle-no-wiggle decomposition. We discuss the details of the IR implementation in our analyses in Subsection 3.2.2 and Subsection 4.1.3 (for massive neutrinos).

Lastly, in Chapter 3, we also work with the leading-order contribution from the bispectrum in redshift space. Analogously to the power spectrum, the information on RSDs is contained in the quadrupole and hexadecapole of the bispectrum. However, the isotropic part, i.e., the bispectrum monopole, allows to break the $(b_1\sigma_8)$ degeneracy present in the power spectrum monopole. To demonstrate this, similar to the power spectrum case in Eq. 1.49, we can write the leading contribution of the bispectrum monopole (or "linear squashing" in Ref. [161]) as:

$$B_{\mathrm{g},\ell=0}(k_1,k_2,k_3) = \left(1+\frac{2\beta}{3}+\frac{\beta^2}{9}\right)b_1^3P_{\mathrm{m}}^{\mathrm{L}}(k_1)P_{\mathrm{m}}^{\mathrm{L}}(k_2)\left[F_2(\boldsymbol{k}_1,\boldsymbol{k}_2)+\frac{b_2}{b_1}\right]+\mathrm{cycl.} \tag{1.53}$$

with a quadratic SPT kernel

$$F_2(\boldsymbol{k}_1,\boldsymbol{k}_2) = \frac{5}{7}+\frac{\hat{\boldsymbol{k}}_1\cdot\hat{\boldsymbol{k}}_2}{2}\left(\frac{k_1}{k_2}+\frac{k_2}{k_1}\right)+\frac{2}{7}\left[S(\boldsymbol{k}_1,\boldsymbol{k}_2)+1\right] \tag{1.54}$$

and

$$S(\boldsymbol{k}_1,\boldsymbol{k}_2) = (\hat{\boldsymbol{k}}_1\cdot\hat{\boldsymbol{k}}_2)^2-1 = \frac{(\boldsymbol{k}_1\cdot\boldsymbol{k}_2)^2}{k_1^2k_2^2}-1\,. \tag{1.55}$$

The different behaviour of the first (function of the triangular configuration) and second terms (an additive constant) in the squared brackets in Eq. 1.53 allows for constraining the linear and quadratic bias simultaneously. This is why bispectrum greatly improves constraints of the galaxy bias parameters.

Observations

A spectroscopic survey provides a catalog with millions of galaxies where each single galaxy is recorded with its position (ra, dec, z). The observed power spectrum and bispectrum multipoles are constructed from catalogues with corresponding estimators [162–164]. Of course, no survey is ideal and various systematics should be taken into account. This is done via assigning weights to the galaxies to correct for redshift failures, fiber collisions, and seeing conditions. Additionally, all measured multipoles are averaged within their k-bins (see a discussion on binning in Subsection 3.3.4).

With the power spectrum and bispectrum multipoles we are working with observables in Fourier space, while the observations are done in the real (configuration) space. The transformation involves a Fourier integral over the infinite space, while in reality we observe only a finite volume of the survey. The measured field statistics are always convolved with the surveys window function that takes into account the geometry of the survey. As a consequence, in the analysis the model must be convolved with the window function as well. The window function convolution is a standard procedure for the power spectrum [165, 166], but is much less trivial for the bispectrum [167]. Alternatively, the multipoles can be computed from a catalogue with the so-called Windowless Estimator [168–170]. This is the approach we use in Chapter 4.

Another observational effect that one must take into account at the level of modelling is the assumption of the fiducial cosmology when redshift is converted to radial comoving distances. This effect is called Alcock-Paczynski (AP) effect [171]. Suppose we have assumed a wrong fiducial cosmology and we measure a distance to the galaxy to be $\boldsymbol{r}^{\rm fid} = \boldsymbol{r}^{\rm fid}_{\parallel} + \boldsymbol{r}^{\rm fid}_{\perp}$, while the true comoving distance is $\boldsymbol{r}^{\rm true}$. The component parallel to the line-of-sight is $r_{\parallel} = r\mu = cz/H(z)$ (first-order approximation), while the component perpendicular to the line-of-sight and separated from it by an angle $\Delta\theta$ equals $r_{\perp} = r\sqrt{1-\mu^2} = (1+z)D_{\rm A}(z)\Delta\theta$ with the angular distance

$$D_{\rm A}(z) = \frac{1}{(1+z)H_0}\int_0^z \frac{dz'}{E(z')} \tag{1.56}$$

and $\mu = \cos\Delta\theta$. We can assume that, if geometries of space and time in both cosmologies do not differ significantly, then the true and assumed parallel and perpendicular

components are proportional to each other by a constant:

$$q_\parallel = \frac{r_\parallel^{\rm true}}{r_\parallel^{\rm fid}} = \frac{H^{\rm fid}(z)}{H^{\rm true}(z)}, \quad q_\perp = \frac{r_\perp^{\rm true}}{r_\perp^{\rm fid}} = \frac{D_{\rm A}^{\rm true}(z)}{D_{\rm A}^{\rm fid}(z)}. \tag{1.57}$$

Then we can construct a map between the true and assumed space coordinates $\boldsymbol{r}^{\rm fid} = \boldsymbol{S}\boldsymbol{r}^{\rm true}$ with the diagonal matrix

$$\boldsymbol{S} = \begin{pmatrix} q_\perp^{-1} & 0 & 0 \\ 0 & q_\perp^{-1} & 0 \\ 0 & 0 & q_\parallel^{-1} \end{pmatrix}. \tag{1.58}$$

Clearly, the Fourier transform coordinates are related via $\boldsymbol{k}^{\rm fid} = \boldsymbol{S}^{-1}\boldsymbol{k}^{\rm true}$. Hence, the observed power spectrum is related to the true power spectrum by

$$P^{\rm fid}(k^{\rm fid}) = \int {\rm d}^3 r^{\rm fid} \xi^{\rm fid}(r^{\rm fid}) {\rm e}^{{\rm i}\boldsymbol{k}^{\rm fid}\cdot\boldsymbol{r}^{\rm fid}} = A^{\rm AP} P^{\rm true}(\boldsymbol{S}\boldsymbol{k}^{\rm fid}), \tag{1.59}$$

with the matrix determinant $A^{\rm AP} = |\boldsymbol{S}| = (q_\perp^2 q_\parallel)^{-1}$, $\boldsymbol{k}^{\rm true} = \boldsymbol{S}\boldsymbol{k}^{\rm fid}$, and where we use the fact that the measured density correlations are equal in both geometries $\xi^{\rm fid}(r^{\rm fid}) = \xi^{\rm true}(r^{\rm true})$. Finally, from

$$q_\parallel = \frac{k_\parallel^{\rm fid}}{k_\parallel^{\rm true}} = \frac{k^{\rm fid}\mu^{\rm fid}}{k^{\rm true}\mu^{\rm true}}, \quad q_\perp = \frac{k_\perp^{\rm fid}}{k_\perp^{\rm true}} = \frac{k^{\rm fid}\sqrt{1-(\mu^{\rm fid})^2}}{k^{\rm true}\sqrt{1-(\mu^{\rm true})^2}} \tag{1.60}$$

we can express the corrected coordinates as

$$\bar{k}^2 = k^2 \left(\frac{1-\mu^2}{q_\perp^2} + \frac{\mu^2}{{q_\parallel}^2} \right), \tag{1.61}$$

$$\bar{\mu}^2 = \frac{\mu^2}{{q_\parallel}^2} \left(\frac{1-\mu^2}{q_\perp^2} + \frac{\mu^2}{{q_\parallel}^2} \right)^{-1}, \tag{1.62}$$

where barred variables are computed in the true cosmology, while un-barred variable are calculated in the assumed fiducial cosmology. The same transformation is applicable for the bispectrum too. Note that in our code we use comoving units $h/{\rm Mpc}$ and ${\rm Mpc}^3/h^3$, which implies

$$q_\parallel \to \frac{E^{\rm fid}(z)}{E^{\rm true}(z)}, \quad q_\perp \to \frac{h^{\rm true} D_{\rm A}^{\rm true}(z)}{h^{\rm fid} D_{\rm A}^{\rm fid}(z)}. \tag{1.63}$$

This also means that there is no direct dependence on h in the AP-effect for comoving coordinates, for a flat cosmology it only depends on h indirectly via the expansion function $E(\omega_c/h^2, \omega_b/h^2, \Omega_\Lambda(w))$. These parameters should not be confused with the dilation scale

factors

$$\alpha_{\parallel} = \frac{H^{\rm fid}(z) r_d^{\rm fid}}{H(z) r_d} = \frac{h^{\rm fid} E^{\rm fid}(z) r_d^{\rm fid}}{h E(z) r_d}\,, \tag{1.64}$$

$$\alpha_{\perp} = \frac{D_{\rm A}(z) r_d^{\rm fid}}{D_{\rm A}^{\rm fid}(z) r_d}\,, \tag{1.65}$$

where the sound horizon at the drag epoch is computed with the following approximation [172]:

$$r_d = \frac{55.154 \exp\left[-72.3(\omega_\nu + 0.0006)^2\right]}{\omega_b^{0.12807}(\omega_c + \omega_b)^{0.25351}}\,{\rm Mpc}\,. \tag{1.66}$$

These dilation scale factors are what we call BAO-measurements in Chapter 4. Alternatively, the sound horizon at the drag epoch can be computed via a Boltzmann solver, which is a slower but more accurate computation than the approximation above.

Beyond-ΛCDM Effects

RSDs are sensitive to any modification of the gravitational potential, μ from Eq. 1.38, and any extended cosmology that changes structure growth can be tested with RSDs. Any extended parameters impacting the overall amplitude of the clustering introduce degeneracies with the linear bias, b_1, and clustering amplitudes, A_s and σ_8. This can be improved by better constraints on the bias parameters with higher-order statistics (see Chapter 3) or by measurements from various redshift bins combined (see Chapter 4). In general, higher-order statistics, such as the bispectrum, can improve constraints on the parameters that control the clustering amplitude (not only due to better constraining the bias parameters, but also by breaking degeneracies and adding more data points). At the same time, higher-order statistics also probe non-Gaussianity in the LSS. Hence, any extended cosmology that changes the growth parameters (e.g., MG) and/or adds non-Gaussianity (e.g., massive neutrinos) would benefit from the inclusion of higher-order statistics into the analysis. The drawback, however, is that the main advantages from including the bispectrum are first noticeable either from considering the anisotropic bispectrum multipoles or from inclusion of the semi-nonlinear scales, i.e., after the inclusion of a very large number of triangular configurations. We discuss this in Chapter 3.

1.5 Weak Lensing

Formalism

One of the main GR predictions is that gravity causes light to be distorted and bent in ways different from the predictions of Newtonian gravity. This was confirmed by Sir

Figure 1.8 *Illustration of the weak gravitational lensing effects. Image credit: Agency of the Ruhr-Bochum University, April 2020.*

Arthur Eddington during the solar eclipse in 1919. Later experimental confirmations, such as the Twin Quasars, the first observations of Einstein Rings, were followed by manifestation of gravitational lensing in various cosmological surveys: e.g., weak and cluster lensing with HST [173], or CMB lensing with Planck [174].

Gravity of massive objects bends the light of distant sources like in a presence of an optical lens – hence, the name of the phenomenon. Unlike strong gravitational lensing, which creates visible distortions, like arcs, and multiple images, WL results in subtle, small distortions that can only be detected statistically by analysing the shapes of many background galaxies (see Fig. 1.8). The light is bent not only by visible objects, such as massive galaxy clusters, but also by the CDM distribution, which does not emit light and is otherwise invisible. Therefore, WL is an excellent method to map CDM distributions in an unbiased way. In other words, it allows us to map CDM distributions directly, without assuming any galaxy-CDM connection. Overall, the integrated distortion of galaxy images by the LSS is called cosmic shear.

To first order, distortions of galaxy images due to the lensing effects can be characterised by two properties: convergence κ – an isotropic dilation, and shear γ – an anisotropic distortion. To understand these WL components, we start from the lensing equation (for comprehensive reviews, see Refs. [175–177]). The lensing equation maps the observed angle between an observer and object's image, θ, to the true angle between an observer and an object, β:

$$\boldsymbol{\beta} = \boldsymbol{\theta} - \boldsymbol{\alpha}\,, \tag{1.67}$$

where α is a reduced deflection angle, related by Fermat's principle to the deflection potential, ϕ, as $\boldsymbol{\alpha} = \nabla_\theta \phi$. The Jacobian matrix of this map is given by

$$A = \frac{\partial \beta_i}{\partial \theta^j} = \begin{pmatrix} 1-\kappa & 0 \\ 0 & 1-\kappa \end{pmatrix} - \begin{pmatrix} \gamma_1 & \gamma_2 \\ \gamma_2 & -\gamma_1 \end{pmatrix} , \tag{1.68}$$

which allows us to express convergence and shear as

$$\kappa = \frac{1}{2}\left(\frac{\partial^2 \phi}{\partial(\theta^1)^2} + \frac{\partial^2 \phi}{\partial(\theta^2)^2}\right) = \frac{\nabla_\theta^2 \phi}{2} , \tag{1.69}$$

$$\gamma_1 = \frac{1}{2}\left(\frac{\partial^2 \phi}{\partial(\theta^1)^2} - \frac{\partial^2 \phi}{\partial(\theta^2)^2}\right) , \tag{1.70}$$

$$\gamma_2 = \frac{\partial^2 \phi}{\partial \theta^1 \partial \theta^2} . \tag{1.71}$$

From this form of the Jacobian we can easily interpret the geometrical impact of convergence – isotropic stretching of the image, and shear – elongation of the image. Its determinant characterises the magnification due to lensing. Note that the coordinates θ_i are Cartesian coordinates in the plane perpendicular to the line-of-sight. We can express shear as a complex property with $\gamma = \gamma_1 + \mathrm{i}\gamma_2 = |\gamma| \exp(2\mathrm{i}\varphi)$, with the polar angle φ. Shear transforms as an ellipse, i.e., as a spin-2 quantity.

In the space-time defined by Eq. 1.37, the deflection potential at the position $\boldsymbol{x} = (\chi\boldsymbol{\theta}, \chi)$ with χ corresponds to the radial separation in the line-of-sight direction is defined by the Weyl potential as

$$\phi(\boldsymbol{\theta}, \chi) = 2\int_0^\chi \mathrm{d}\chi' \; \Psi_\mathrm{W}(\chi'\boldsymbol{\theta}, \chi') \; \frac{(\chi - \chi')}{\chi\chi'} , \tag{1.72}$$

under the assumption of spatial flatness, and integration in Born's approximation, i.e., along the unperturbed light path. With Eq. 1.69 we can now express the convergence as

$$\kappa(\boldsymbol{\theta}, \chi) = \int_0^\chi \mathrm{d}\chi' \; \nabla^2 \Psi_\mathrm{W}(\chi'\boldsymbol{\theta}, \chi') \; \frac{(\chi - \chi')\chi'}{\chi} , \tag{1.73}$$

keeping in mind the connection between derivatives $\nabla_\perp = \chi'^{-1}\nabla_\theta$. This allows us to connect the averaged convergence to the matter distribution via the Poisson equation in Eq. 1.40:

$$\kappa(\boldsymbol{\theta}) = \frac{3\Omega_\mathrm{m} H_0^2}{2} \int_0^{\chi_\mathrm{max}} \mathrm{d}\chi \left(\int_\chi^{\chi_\mathrm{max}} \mathrm{d}\chi' p(\chi') \; \frac{(\chi' - \chi)}{\chi'}\right) (1+z)\chi\Sigma(\chi\boldsymbol{\theta}, \chi)\delta(\chi\boldsymbol{\theta}, \chi) \tag{1.74}$$

where the weight function $p(\chi)$ describes how the sources are distributed along the line-of-sight and $\Sigma(\chi\boldsymbol{\theta}, \chi)$ corresponds to the modification of the Weyl potential in real space. We

can now write the convergence as a compact expression $\kappa(\boldsymbol{\theta}) = \int \mathrm{d}\chi q(\chi)\delta(\chi\boldsymbol{\theta}, \chi)$. Hence, under the assumption that only modes perpendicular to the line-of-sight contribute, the two-point correlation function equals to

$$\xi^{\kappa\kappa}(\Delta\boldsymbol{\theta}) = \langle\kappa(\boldsymbol{\theta})\kappa^*(\boldsymbol{\theta}')\rangle = \int \mathrm{d}\chi q^2(\chi) \int \frac{\mathrm{d}^2k}{(2\pi)^2} P_{\delta\delta}(k)\mathrm{e}^{-\mathrm{i}\chi\Delta\boldsymbol{\theta}\boldsymbol{k}}\,, \tag{1.75}$$

with $\boldsymbol{\theta}' = \boldsymbol{\theta} + \Delta\boldsymbol{\theta}$, so that the angular power spectrum of the convergence can be expressed as

$$C^{\kappa\kappa}(\ell) = \frac{\langle\hat{\kappa}(\boldsymbol{\ell})\hat{\kappa}^*(\boldsymbol{\ell}')\rangle}{(2\pi)^2\delta_{\mathrm{D}}(\boldsymbol{\ell} - \boldsymbol{\ell}')} = \int \mathrm{d}\Delta\theta\xi^{\kappa\kappa}(\Delta\boldsymbol{\theta})\mathrm{e}^{\mathrm{i}\boldsymbol{\ell}\Delta\boldsymbol{\theta}} = \int \mathrm{d}\chi \frac{q^2(\chi)}{\chi^2} P_{\delta\delta}(\ell/\chi)\,. \tag{1.76}$$

Using the definitions from Equations 1.69-1.71, we find that in Fourier space κ and γ are connected as

$$\hat{\gamma}(\boldsymbol{l}) = \frac{(l_1 + \mathrm{i}l_2)^2}{l^2}\hat{\kappa} = \mathrm{e}^{2\mathrm{i}\varphi_l}\hat{\kappa}(\boldsymbol{l})\,, \tag{1.77}$$

with the wave-vector $\boldsymbol{l} = (l_1, l_2)$ being the Fourier space coordinate for $\boldsymbol{\theta}$ in real space and φ_l being the polar angle of the complex wave-vector. From this we can see that the power spectra of shear and of convergence are equal $C^{\kappa\kappa}(\ell) = C^{\gamma\gamma}(\ell)$.

In observations, we assign galaxies to different bins according to their redshifts, z_i and z_j. The slices of galaxy populations in each z-bin, $n_i(z)$, are related to the distribution along the line-of-sight via $n_i(z)\mathrm{d}z = p_i(\chi)\mathrm{d}\chi$ (see the left panel of Fig. 1.9 for Euclid-like $n_i(z)$). Now, the intra- and inter-bin correlations of the cosmic shear field can be computed as

$$C^{\kappa\kappa}_{ij}(\ell) = C^{\gamma\gamma}_{ij}(\ell) = \int \frac{\mathrm{d}\chi}{\chi^2} q_i(\chi)q_j(\chi)P_{\delta\delta}(\ell/\chi)\,, \tag{1.78}$$

with the lensing kernels (see the right panel of Fig. 1.9)

$$q_i(\chi) = \frac{3\Omega_{\mathrm{m}}H_0^2}{2}\chi(1 + z(\chi))\Sigma(\ell/\chi, z(\chi)) \int_{\chi}^{\chi_{\mathrm{max}}} \mathrm{d}\chi' p_i(\chi') \frac{(\chi' - \chi)}{\chi'}\,. \tag{1.79}$$

From this we see that the angular power spectra are sensitive to the matter distribution via the matter power spectrum, $P_{\delta\delta}(\ell/\chi)$. In the left panel of Fig. 1.10, we show the correspondence between wave-numbers (for which we have developed an intuition in the previous sections) and angular scales within a fiducial cosmology. At the same time, in Eq. 1.79 the geometrical factor $(\chi - \chi')/\chi'$ implies sensitivity of the angular power spectra to the distance-redshift relation and, hence, the geometry of a cosmological model. Unfortunately, due to the 2-dimensional projection, i.e., the integration along the line-of-sight, the redshift-evolution information gets erased. Separating galaxies into redshift bins reduces the range of the projection to the width of the bins and allows for substantial gain of information through their cross-correlations. Still, in the projection, different spatial scales are mixed, which leads to the loss of sensitivity to parameters that impact nonlinear

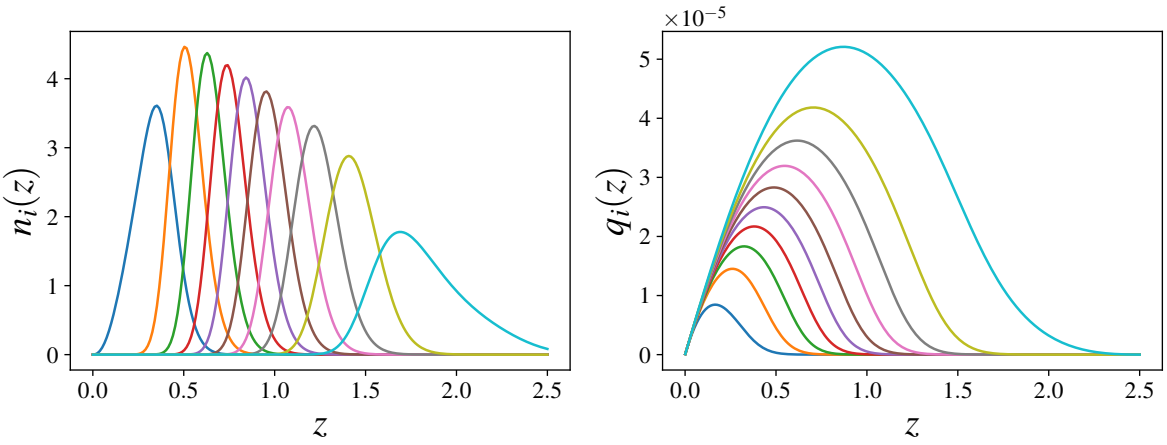

Figure 1.9 *Euclid-like photo-z binning. Left panel: number density distribution of galaxies in 10 redshift bins. Right panel: lensing kernels of the same binned galaxies. Lensing kernels peak around half way between the observer ($z = 0$) and the source galaxies.*

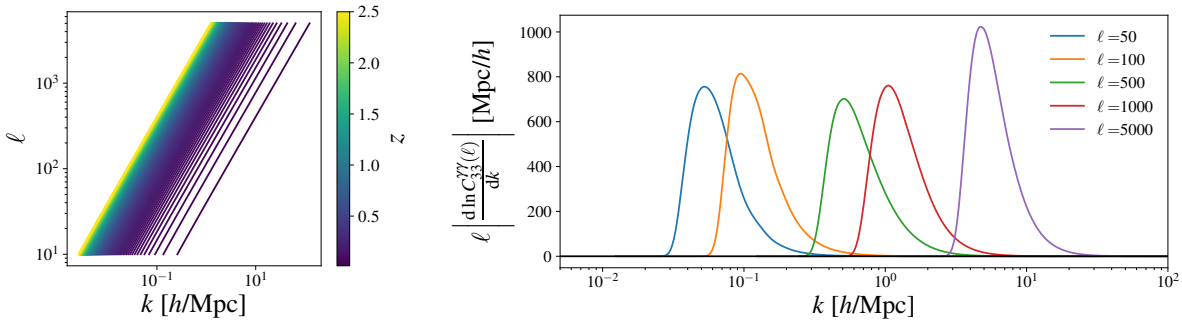

Figure 1.10 *Euclid-like photo-z binning with fiducial standard cosmology. Left panel: angular scales ℓ as a function of wave-numbers k for different redshifts z. Right panel: the response function from Eq. 1.80 for the auto-correlation in the 3-3 redshift bin, this showcases that a single angular scale ℓ contains projected information from various k-scales.*

scales. We illustrate this mixing in Fig. 1.10, where we plot the response of the angular shear power spectrum from Eq. 1.78 to the wave-number $k = \ell/\chi$:

$$\left|\frac{\mathrm{d}\ln C_{ij}^{\gamma\gamma}(\ell)}{\mathrm{d}k}\right| = \frac{q_i(\ell/k)q_j(\ell/k)P_{\delta\delta}(k)}{C_{ij}^{\gamma\gamma}(\ell)\ell}\,. \tag{1.80}$$

We see that for the shear angular power spectrum due to the width of the lensing kernel a broad range of the wave-number contribute to a single ℓ-value. This makes it hard to separate the scales in our analysis where we believe our model is insufficiently accurate.

The derivation above is done under the flat-sky approximation, we use it in Chapter 6. However, on large scales where the curvature of the space becomes important, derivatives must be expressed in terms of the $\eth$ operator and its complex conjugate, and the shear, convergence and lensing potential should be expanded in spherical coordinates. When properly derived on a sphere, the shear angular power spectra is given by [178]

$$\begin{aligned} C_{ij}^{\gamma\gamma} &= \frac{1}{4}\frac{(\ell+2)!}{(\ell-2)!}C_{ij}^{\phi\phi}(\ell) \\ &= \frac{2}{\pi}\frac{(\ell+2)!}{(\ell-2)!}\int \mathrm{d}\chi q_i(\chi)\int \mathrm{d}\chi' q_j(\chi')\int \mathrm{d}k\; k^2 P_{\delta\delta}(k,\chi,\chi')\frac{j_\ell(k\chi)}{(k\chi)^2}\frac{j_\ell(k\chi')}{(k\chi')^2}\,, \end{aligned} \tag{1.81}$$

where j_ℓ are spherical Bessel functions. Analogously, we can derive the angular power spectrum for convergence [179]:

$$C_{ij}^{\kappa\kappa} = \frac{\ell^2(\ell+1)^2}{4}C_{ij}^{\phi\phi}(\ell) = \frac{\ell(\ell+1)}{(\ell-1)(\ell+2)}C_{ij}^{\gamma\gamma}(\ell)\,. \tag{1.82}$$

From this we can conclude that the convergence power spectrum is larger than the shear power spectrum: by 7% for $\ell = 5$, by 1.85% for $\ell = 10$, by 0.5% for $\ell = 20$, and by less than 0.1% for $\ell \geq 45$.

In our projects, we apply the Limber approximation, i.e., $k = (\ell + 1/2)/\chi$ and the Bessel functions are approximated by a Dirac delta function (see Section 1.1). According to Ref. [180], this decreases the error in the first order Limber approximation in comparison to $k = \ell/\chi$. In the same work, the authors derive a second-order correction to the Limber approximation, which works well for large multipoles and slowly varying kernels, and performs better than the standard approach for more widely separated redshift bins. Note that for Stage-IV surveys with their huge survey volume, the Limber approximation is not sufficient at all, when large angular separations $\ell < 100$ are considered. For $\ell > 100$ due to the high resolution of Stage-IV surveys, the first order Limber approximation is again insufficiently accurate, while the second-order approximation might suffice (see, e.g., Refs. [179, 181]).

Beyond-ΛCDM Effects

WL is sensitive to the lensing mass proportional to the Weyl potential. This implies that WL is a probe sensitive to extended cosmologies via two channels: changes in structure growth in $\mu = G_{\rm matter}$ and modifications in the propagation of light in $\Sigma = G_{\rm light}$ (see Eq. 1.40). Cosmic shear essentially measures the late-universe amplitude and probes the redshift-regime most impacted by the extended cosmologies we consider. On top of the clustering amplitude, DE models also affect the comoving distances and expansion function, introducing additional sensitivity to the DE parameters in the shear angular power spectrum. Therefore, the ultimate advantage of WL in probing extended cosmologies is the coverage of a broad redshift range. Additionally, WL's high sensitivity to nonlinear scales in the new generation of surveys allows us to explore scenarios with non-standard nonlinear dynamics (e.g., screening mechanisms). This blessing is simultaneously a curse, since the nonlinear scales are extremely hard to model accurately (see Chapter 6). Finally, similar to the GC discussion, inclusion of the bispectrum in weak gravitational lensing breaks degeneracies in amplitude-controlling parameters and helps constraining massive neutrinos [182].

1.6 Cosmological Surveys

In the following chapters we will refer to various cosmological surveys – either to extract cosmological information from, or to put extra constraining power, or to forecast Stage-IV cosmological constraints. Here, we list brief descriptions of the cosmological surveys and probes necessary for understanding of our results.

- The Planck Satellite: the CMB telescope conducted observations from 2009 to 2013, it was launched by the European Space Agency and positioned at the L2 Lagrangian point of the Earth-Sun system. The Planck Satellite was equipped with highly sensitive detectors capable of measuring the polarisation of CMB photons with exceptional accuracy and the temperature spectrum with remarkable resolution. Collecting data across nine different frequencies, the Planck Collaboration has released three sets of cosmological parameter estimates: Planck 2013 [20] with data from the first 15.5 months of the operation, Planck 2015 [21] and 2018 [22] – both using data from the full mission. The main observables used in the cosmological inference included temperature and polarisation auto- and cross-power spectra, and CMB lensing. The most recent findings [22], represent some of the most precise and reliable cosmological measurements to date, providing percent-level constraints on early Universe parameters such as the primordial power spectrum amplitude, A_s; the scalar spectral index, n_s; and the optical depth of reionisation, τ. We use these constraints as priors on the primordial parameters in Chapter 3, Chapter 4 and

Chapter 6.

- Big Bang Nucleosynthesis (BBN): observations of helium, deuterium and hydrogen emission lines from metal-poor extragalactic regions allow us to compute abundances of the "light elements" – first nuclei formed at the early stages of the Universe (see Ref. [183] for a review). The fractions of deuterium and helium with respect to hydrogen are sensitive to the baryonic content of the Universe. After formation of the neutral hydrogen and decoupling of photons, the equilibrium between neutrons and protons is broken. First, deuterium is formed from a proton and a neutron via strong-force interactions. Although some newly formed deuterium nuclei get destroyed by the abundant photons, the Universe continues to expand and cool. Then the density of the deuterium becomes sufficient to build a helium nucleus from two deuterium nuclei. From this it follows that for larger baryon-to-photon ratio less deuterium would be destroyed by photons and more helium would be formed. It also means that deuterium would be converted into helium more efficiently leading to smaller residual deuterium abundance. We use our knowledge of the baryonic fraction from BBN calculations based on deuterium and helium abundances [184, 185] as prior on $\omega_{\rm b} = \Omega_{\rm b}h^2$ in our analyses (Chapter 4 and Chapter 6). Finally, neutrinos, fully relativistic at the time of BBN, impact the resulting helium abundance too: larger N_ν or smaller density of electron neutrinos would imply a decay of fewer neutrons, which results in more helium cores formed.

- Baryon Oscillation Spectroscopic Survey (BOSS): the largest Stage-III galaxy survey, part of the Sloan Digital Sky Survey (SDSS) Phase-III, ran from 2008 to 2014 and used a multiple-object spectrograph located in New Mexico. The last BOSS data release, DR12, is the main dataset used in Chapter 4. Together with the main objectives of the survey, such as measuring BAOs in the distribution of galaxies and quasars, BOSS data allowed for exploration of various cosmological topics of interest listed in Fig. 1.11. For example, the Collaboration obtained angular diameter distance and expansion rate measurements with approximately 2% precision for intermediate redshifts using Luminous Red Galaxies (LRGs), with a similar precision attained using Ly-α quasars at higher redshifts [186].

- Dark Energy Spectroscopic Instrument (DESI): a spectroscopic instrument [187] located at the Kitt Peak National Observatory in Arizona, USA. It was designed to capture precise positions of millions of galaxies and quasars using a robotic fiber-optic system. The main mission operation started in 2021 and is planned to run for five years. The main scientific objective (see also Fig. 1.11) is to investigate the effects and properties of dark energy. The first year data release already shows hints of evolving dark energy, as reported in Ref. [90]. DESI covers a broad range of redshifts and all samples can be separated into the following groups: low redshift

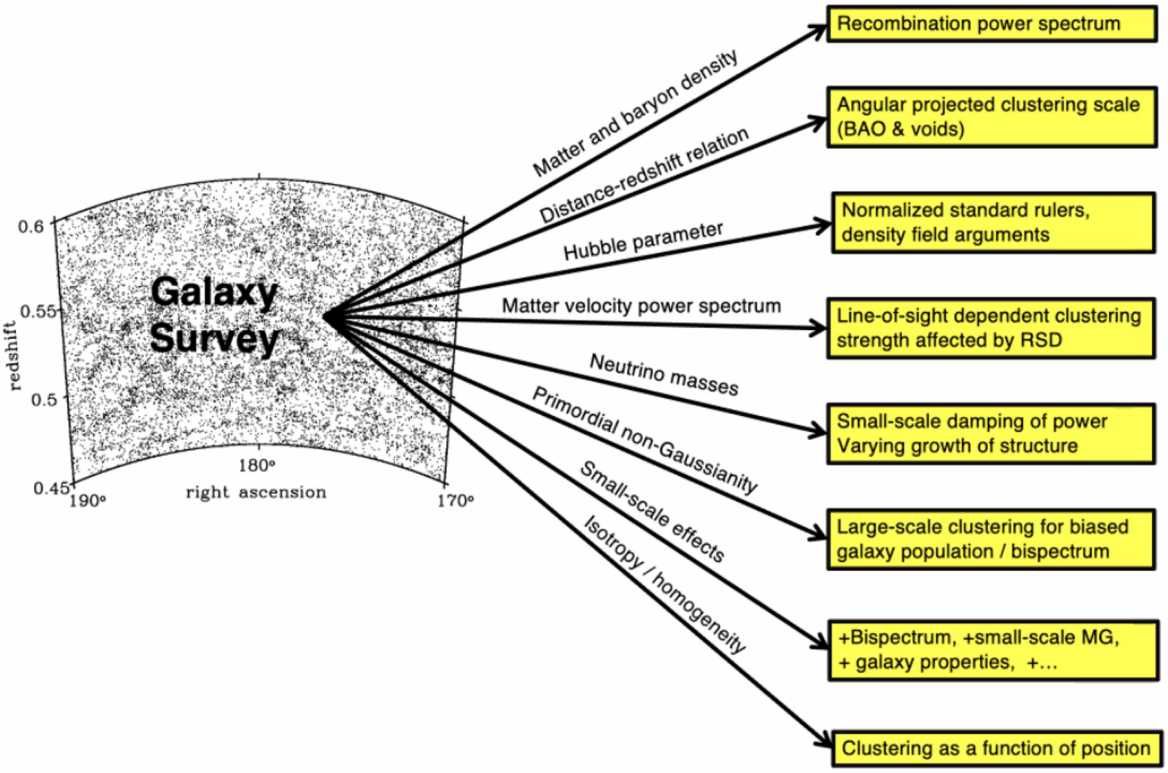

Figure 1.11 *Cosmology from galaxy redshift surveys. Image credit: W. Percival's talk "Measuring H_0 and dark energy with DESI" at the Royal Observatory Edinburgh, April 2024.*

Bright Galaxy Sample (BGS), LRGs, Emission Line Galaxies (ELGs), and quasars. We use DESI galaxy samples in our forecasts in Chapter 4.

- Euclid Satellite: a European Space Agency mission launched in July 2023. The mission will perform 6-10 years long near-infrared and optical observations of nearly one third of the whole sky. The telescope is equipped with two instruments:
  - Visible Imaging Channel (VIS) for high-resolution photometric imaging in the visible spectrum;
  - Near-Infrared Spectrometer and Photometer (NISP) for photometry and slitless spectroscopy in the near-infrared range, essential for measuring redshifts and galaxy shapes.

  This means that Euclid is simultaneously a spectroscopic galaxy and weak lensing survey, making it ideal for cross-correlations and combined probes analyses. Combining these probes is key to achieve Euclid's main science goals [188], namely measuring and constraining the following parameters: the evolution of the dark energy equation-of-state, $w(z)$; the growth index as a probe of modified gravity, γ; the sum of neutrino masses, $\sum m_\nu$; and the non-Gaussianity parameter, $f_{\rm NL}$, connected to inflationary models. A Euclid-like setup is our primary forecasting

setup for GC probes in Chapter 3 and WL probes in Chapter 6. Together with DESI, they are part of the ground-breaking Stage-IV era of precision cosmology.

Chapter 2

Cosmological Inference

In this thesis, we refer to cosmological inference as the likelihood analysis of the surveys or simulation data that aims to provide information about the cosmological parameters. Essentially, we want to answer what are the values and probabilities of the parameters, cosmological and nuisance, that optimally describe some given data, $\boldsymbol{d}$, within a model, M. To quantify the uncertainty of these parameter values one can either perform a Bayesian analysis to find credible intervals, or perform a Frequentist analysis to define confidence regions. In this chapter we review both approaches, in Section 2.1 and Section 2.2, as well as the corresponding prior-volume or projection effects in Section 2.3. Finally, we describe the sampling tools used in our works in Section 2.4. When not explicitly cited, the inference background is based on Refs. [189, 190].

2.1 Bayesian Inference

The Bayesian approach relies on Bayes' theorem [191] that states that the probability of obtaining parameters $\boldsymbol{\theta}$ given data $\boldsymbol{d}$, model assumptions M and prior beliefs about these parameters $\Pi(\boldsymbol{\theta})$ is expressed by

$$\mathcal{P}(\boldsymbol{\theta}|\boldsymbol{d}, M) = \frac{\mathcal{L}(\boldsymbol{d}|\boldsymbol{\theta}, M)\Pi(\boldsymbol{\theta})}{\mathcal{Z}(\boldsymbol{d}|M)} \,. \tag{2.1}$$

Here, $\mathcal{L}(\boldsymbol{d}|\boldsymbol{\theta}, M)$ is the likelihood function that represents the distribution of the data given the model and the parameters. In the denominator we have a normalising factor $\mathcal{Z}(\boldsymbol{d}|M)$ called evidence that has no dependence on the model parameters. Evidence can be used for model comparison and convergence tests.

The probability from Eq. 2.1 is called the posterior distribution. It is sampled in the full parameter space, which typically has a large number of dimensions. We usually (e.g.,

Fig. 2.1) plot posterior distributions as 2- and 1-dimensional marginalised distributions:

$$\mathcal{P}_{\rm m}(\theta_1,\theta_2|\boldsymbol{d},M)=\int {\rm d}\theta_3...{\rm d}\theta_n\mathcal{P}(\boldsymbol{\theta}|\boldsymbol{d},M),\ \mathcal{P}_{\rm m}(\theta_1|\boldsymbol{d},M)=\int {\rm d}\theta_2...{\rm d}\theta_n\mathcal{P}(\boldsymbol{\theta}|\boldsymbol{d},M)\,. \quad (2.2)$$

From these marginalised posteriors we can summarise the results of our analysis in the form of point estimates with their corresponding errors: e.g., the maximum a posteriori probability (MAP) estimator, or the 1D marginalized mean. Ideally, these marginalised posteriors provide an unbiased estimation. An estimation is unbiased if the expectation value, i.e., the value of the parameter weighted by the posterior function, is the true value of the parameter θ_0. In reality, when data is not a noiseless synthetic data-vector, this is rarely the case and we always expect statistical fluctuations. For instance, in Chapter 3 and Chapter 6 we run "precision versus accuracy" tests by assessing our analytical models against simulations or against other models. There we aim for the point estimates of each cosmological parameter to have a bias, with respect to the fiducial parameters within the 2σ credible interval. The Bayesian credible interval corresponds to a region of the parameter space that contains $X\%$ of the posterior distribution. It is a common practice to refer to $68.3\%,\ 95.5\%,\ 99.7\%$ credible intervals as $1\sigma,\ 2\sigma,\ 3\sigma$ credible regions.[1]

From the fact that the true parameter values correspond to the maximum likelihood, we can expand the log-likelihood around them and obtain

$$\mathcal{L}(\boldsymbol{d}|\boldsymbol{\theta},M)=\mathcal{L}(\boldsymbol{d}|\boldsymbol{\theta}_0)\exp\left[-\frac{1}{2}(\boldsymbol{\theta}_i-\boldsymbol{\theta}_{0i})H_{ij}(\boldsymbol{\theta}_j-\boldsymbol{\theta}_{0j})\right], \quad (2.3)$$

with the Hessian matrix $H_{ij}=-\frac{\partial^2\ln\mathcal{L}}{\partial\theta_i\partial\theta_j}$. This matrix also represents the level of correlation between the parameter estimates θ_i and θ_j. The expectation value of the Hessian, is called the Fisher matrix [192, 193] and is often used for future experimental design under the Gaussian likelihood assumption: $F_{ij}=\langle H_{ij}\rangle$. The minimum standard deviation of the parameter follows from the Cramer-Rao inequality [194] for an unbiased estimator:

$$\sigma_{\theta_i}\geq\sqrt{F_{ii}^{-1}}\,. \quad (2.4)$$

This is also called the marginal error. However, in the presence of data, the posterior is probed via sampling techniques (see Section 2.4), and marginalisation is performed numerically.

[1] For instance, 68.3% of the values lie within one standard deviation, i.e., 1σ, from a mean under the assumption of a normal distribution.

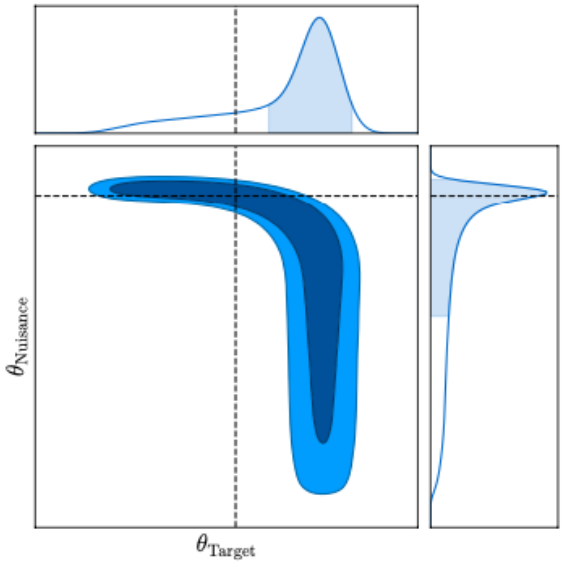

Figure 2.1 *Prior-volume or projection effect: 2-dimensional example with 2- and 1-dimensional marginalised posterior distributions within* 1σ *(dark blue) and* 2σ *(blue) confidence region. Image credit: Ref. [6].*

2.2 Frequentist Approach

Instead of applying the Bayesian approach and quoting credible intervals, one can compute confidence regions in the Frequentist approach. The confidence region corresponds to a subset of the parameter space, which contains the true parameters in repeated trials. It represents a probability distribution in the dimension of all possible observations for each specific parameter value. However, it does not represent a probability distribution in the parameter dimension. Since it is not a probability density, in the Frequentist approach, the best estimator of the parameter is the value that maximizes the likelihood function. There are various codes that perform this computation: e.g., minuit [195], Procolli [196], PROSPECT [197], CONNECT [198].

A 68% confidence interval means that there is a 68% probability that the true value of a parameter will be inside that interval when the measurement is repeated. A 68% credible interval means that there is a 68% "degree of belief" that the true value of a parameter will be inside that interval. In cosmology the inferred errors are sometimes interpreted in a Frequentist way: 1σ discrepancies are considered normal as they have a 31.7% probability of occurring, while a 3σ difference between two measurements is interpreted as a real discrepancy because there is only a 0.3% probability for this to happen.

2.3 Projection Effects

The Bayesian approach relies on the prior information on the parameters we aim to estimate. The contribution of the prior-volume can bias the MAP with respect to its true value when the non-Gaussian posterior is marginalised over multi-dimensional parameter space. As shown in Fig. 2.1 for a case of a non-Gaussian 2-dimensional posterior, while the posterior maximum in the full parameter space is centered around the true values, after the marginalisation of the nuisance parameter, $\theta_{\rm Nuisance}$, the peak of the probability distribution (i.e., the marginalised MAP) for the target parameter, $\theta_{\rm Target}$, is shifted from its true value. We first use a toy model to explain the nature of such projection effects, then we continue with examples from cosmological analyses, and finally we discuss different techniques to minimise the projections. We emphasise that the prior-volume or projection effects are a natural part of the Bayesian analysis and a consequence of our complex modelling for cosmological and systematical parameters.

2.3.1 Toy Model

Before moving to complex models with high-dimensional parameter spaces, we construct a toy model to illustrate the main concepts of the projection or prior-volume effects. Consider a simple model:

$$M(\Omega, n) = nk^{\Omega} \ , \tag{2.5}$$

where Ω contains cosmological information that we want to constrain, n is a nuisance parameter controlling the amplitude, k is some variable in the range of $k \in [1, 10]$ binned into $N_{\rm bin} = 32$ log-bins. We pick a toy model of this form, because, for instance, in the EFTofLSS model of the power spectrum we have nuisance parameters that appear linearly in the model as factors in front of nonlinear functions that depend on cosmological parameters (for example, the counterterms in Eq. 3.16). For the Bayesian analysis we compute a noiseless mock data vector, $\boldsymbol{d}$, with the same model and true values $n_{\rm fid} = 4$, $\Omega_{\rm fid} = 1.5$; we assume the covariance to be a diagonal matrix ${\rm Cov}_{kk'} = \sigma^2 \mathbb{1}_{N_{\rm bin}\times N_{\rm bin}}$; we also assume a Gaussian likelihood, Gaussian priors $n \in \mathcal{N}(n_{\rm fid}, \sigma_n)$, and no prior on Ω.

Our goal is to find the posterior distribution marginalised over the nuisance parameter, n. First, we compute the marginalised posterior function, $\mathcal{P}_{\rm m} = \mathcal{P}(\Omega|\boldsymbol{d})$, explicitly:

$$\begin{aligned}\mathcal{P}_{\rm m} &= \int {\rm d}n \ \mathcal{P}(\Omega, n|\boldsymbol{d}) = \exp\left[-\frac{F_0}{2}\right] \int {\rm d}n \exp\left[-\frac{n^2 F_2 - 2nF_1}{2}\right] \\ &= \sqrt{\frac{2\pi}{F_2}} \exp\left[-\frac{F_0}{2} + \frac{F_1^2}{2F_2}\right], \end{aligned} \tag{2.6}$$

where

$$\mathcal{P}(\Omega, n|\boldsymbol{d}) = \exp\left[-\frac{(\boldsymbol{d} - n\boldsymbol{k}^{\Omega})^T \cdot (\boldsymbol{d} - n\boldsymbol{k}^{\Omega})}{2\sigma^2}\right]\Pi(n)\,, \tag{2.7}$$

$$\Pi(n) = \exp\left[-\frac{(n - n_{\rm fid})^2}{2\sigma_n^2}\right], \tag{2.8}$$

$$F_0 = \sum_{j=1}^{N_{\rm bin}} \frac{d_{k_j}^2}{\sigma^2} + \frac{n_{\rm fid}^2}{\sigma_n^2}\,, \tag{2.9}$$

$$F_1 = \sum_{j=1}^{N_{\rm bin}} \frac{k_j^{\Omega} d_{k_j}}{\sigma^2} + \frac{n_{\rm fid}}{\sigma_n^2}\,, \tag{2.10}$$

$$F_2 = \sum_{j=1}^{N_{\rm bin}} \frac{(k_j^{\Omega})^2}{\sigma^2} + \frac{1}{\sigma_n^2}\,. \tag{2.11}$$

In terms of the marginalised goodness-of-fit or "chi–squared" we define:

$$\chi^2_{\rm m}(\Omega) = F_0 - \frac{F_1^2}{F_2} + \ln F_2 + \text{const}\,, \tag{2.12}$$

where $\chi^2_{\rm m} = -2\ln\mathcal{P}_{\rm m}$. We then repeat the computation using the approach from Ref. [199], where we approximate the marginal distribution using a second-order Taylor expansion around the best-fit value of the nuisance parameter. The best-fit value of the nuisance parameter maximises the posterior and is defined for a fixed Ω-value as:

$$n_*(\Omega) = \arg\,\max_n \mathcal{P}(\Omega, n|\boldsymbol{d})\ , \tag{2.13}$$

where, by construction in our example, $n_*(\Omega_{\rm fid}) = n_{\rm fid}$. It also follows that the first derivative of $\chi^2 = -2\ln\mathcal{P}$ with respect to n evaluated at n_* equals zero. From this condition we find for our example from Eq. 2.7:

$$\left.\frac{{\rm d}\chi^2}{{\rm d}n}\right|_{n_*} = 0 \Rightarrow n_*(\Omega) = \frac{F_1}{F_2}\,. \tag{2.14}$$

We expand χ^2 with $\chi^2_*(\Omega) = \chi^2(\Omega, n_*)$ and $\Delta n = n - n_*$ up to the second order as

$$\chi^2(\Omega, n) \approx \chi^2_* + \mathcal{F}_*\Delta n^2\ , \tag{2.15}$$

where

$$\mathcal{F}_* = \left.\frac{1}{2}\frac{\partial^2\chi^2}{\partial n^2}\right|_{n_*}\,. \tag{2.16}$$

For our case we find

$$\chi^2_* = F_0 - \frac{F_1^2}{F_2}, \quad \mathcal{F}_* = F_2\,. \tag{2.17}$$

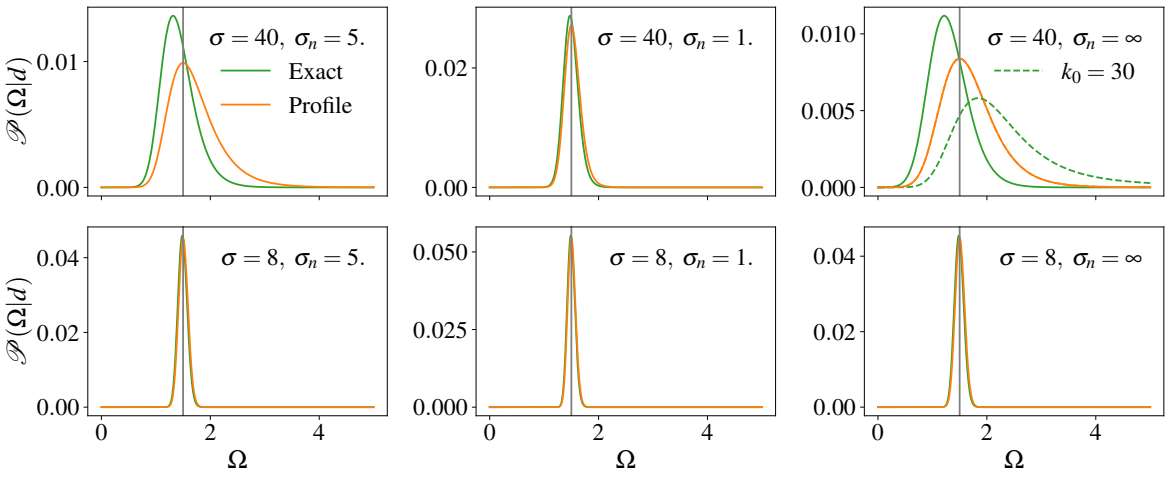

Figure 2.2 *Toy model: (normalised) marginalised posterior distributions. See a detailed description in the text.*

Marginalising the posterior over n with $\mathcal{P} = \exp\left[-\chi^2/2\right]$ and χ^2 from Eq. 2.15 results in the marginalised chi-squared given by

$$\chi^2_{\rm m}(\Omega) \approx \chi^2_*(\Omega) + \ln \mathcal{F}_*(\Omega) + \text{const}\,. \tag{2.18}$$

Both approaches, Taylor expansion and direct analytical marginalisation, result in the same marginalised distribution in Eq. 2.18 and Eq. 2.12, because a) n appears linearly in the model and, hence, quadratically in the likelihood; b) the covariance is parameter-independent, and c) the likelihood is Gaussian. These factors make the Laplace approximation exact [200]. The first term in Eq. 2.18 is what we call the "profile likelihood", while the second term is called the Laplace term. This Laplace term is responsible for the prior-volume effects: the volume in the nuisance parameter space when integrated over fixed Ω. In other words, this term corresponds to the shift in the maximum of the marginalised distribution with respect to the maximum of the full distribution, because the process of marginalisation favours regions of parameter space that cover a larger volume of the probability density in the direction of integration.

In Fig. 2.2 we demonstrate how the marginalised posterior distribution and the profile likelihood depend on the choice of the nuisance-parameter prior, σ_n, and the quality of the data (more constraining data has smaller uncertainty on the measurements, i.e., smaller σ). In the upper panel in green, we see that if the data is not constraining enough, the Laplace term becomes significant for larger nuisance-priors and is dragging the peak of the marginalised posterior distribution towards smaller and negative values of Ω. While in the lower panel we demonstrate the weak sensitivity to the prior-volume when data is well-constraining.

From the expression for the Laplace term, $\ln \mathcal{F}_*(\Omega)$, we can see that it also depends

on the specific parameterisation of the nuisance parameter. For instance, let us re-define our model to $\tilde{n}(k/k_0)^{\Omega}$ with some fixed quantity k_0 greater than any value of k_j. In this case, the first right-hand-side-term in the above definition of F_2 in Eq. 2.11 implies for the case of poorly constrained data, that the re-parameterisation leads to a negative Laplace term. As a consequence, it shifts the peak of the marginalised posterior towards higher values than $\Omega_{\rm fid}$. It also changes the width of the marginalised posterior distribution as we can see in the top right panel of Fig. 2.2 in dashed green.

Alternatively, we can apply Jeffreys prior [201] on the nuisance parameters, $\boldsymbol{n}$:

$$\Pi(\boldsymbol{n}) = \sqrt{\det\left(\frac{\partial M}{\partial n_i}\mathrm{Cov}^{-1}\frac{\partial M^T}{\partial n_j}\right)}\,, \tag{2.19}$$

which simplifies to $\Pi(n) = \sqrt{F_2}$ from Eq. 2.11 for a broad flat prior on the nuisance parameter with $\sigma_n \to \infty$ in our one-dimensional case. We can see from Eq. 2.12, the Jeffrey prior on n would cancel the impact of the prior-volume effects. Marginalisation with Jeffreys priors is equivalent to profiling the posterior over the same parameters for Gaussian data with parameter-independent covariance and linear nuisance parameters [200].

All in all, the prior-volume effects are an inescapable feature of the Bayesian method and depend on the choice of the nuisance-prior, parameterisation of the nuisance parameters, and covariance of the data. Assuming broad flat priors on nuisance parameters leads to a large Laplace term, while over-constrained priors are poorly physically motivated. One solution is to use Jeffreys prior or profile the full likelihood (which is constructed in such a way to peak at the best-fit values of the nuisance parameters). Ideally, we compute Jeffreys priors not only for nuisance parameters but for cosmological parameters as well. This will help with entangling degeneracies not only between nuisance but cosmological parameters too. However, analytical computation of the marginalised posterior in this case becomes already complicated even for our toy model. Auto-differentiable techniques [202] will become important for this issue in the future.

2.3.2 Cosmological Application

Marginalisation over nuisance parameters can be performed numerically or analytically. Here, we introduce analytical marginalisation of nuisance parameters that appear linearly in the model on the example of the EFTofLSS power spectrum multipoles (counter-terms, noise-terms and higher order bias parameters) [152, 203]. This analysis can be easily expanded to include other observables like BAO or bispectrum multipoles. We separate the power spectrum multipoles into analytically non-marginalised (nm) and marginalised

(m) parts:

$$P_l(k) = P_l^{\rm nm}(k) + \sum_i b_i^{\rm m} P_{i,l}^{\rm m}(k)\,, \tag{2.20}$$

with the bias parameters with superscript "m" appearing linearly in the model and having Gaussian priors. With Einstein notation and $\Delta_l(k) = P_l^{\rm nm}(k) - D_l(k)$ we find the posterior distribution marginalised over all nuisance parameters with Gaussian priors:

$$\mathcal{P}_{\rm m} = \Pi^{\rm nm} \int {\rm d}^n b^{\rm m} \exp\left[-\frac{1}{2}(b_i^{\rm m} F_{2,ij} b_j^{\rm m} - 2 b_i^{\rm m} F_{1,i})\right] \exp\left(-\frac{1}{2} F_0\right) \tag{2.21}$$

with $\Pi^{\rm nm}$ being the prior on the analytically non-marginalised parameters, Cov being the covariance matrix for the data, and C_{ij} being the covariance for the priors on nuisance parameters, that are Gaussian with the means μ_i. The terms above are defined as

$$F_0 = \Delta_l {\rm Cov}_{ll'}^{-1} \Delta_{l'} + \mu_i \mathrm{C}_{ij}^{-1} \mu_j\,, \tag{2.22}$$

$$F_{1,i} = -P_{i,l}^{\rm m} {\rm Cov}_{ll'}^{-1} \Delta_{l'} + \mathrm{C}_{ij}^{-1} \mu_j\,, \tag{2.23}$$

$$F_{2,ij} = P_{i,l}^{\rm m} {\rm Cov}_{ll'}^{-1} P_{j,l'}^{\rm m} + \mathrm{C}_{ij}^{-1}\,. \tag{2.24}$$

The integral can be solved analytically, which leads to the following χ^2:

$$\chi^2 = -2\ln \mathcal{P}_{\rm m} = -2\ln \Pi^{\rm nm} + \ln\det F_2 - n\ln 2\pi - F_{1,i} F_{2,ij}^{-1} F_{1,j} + F_0\,. \tag{2.25}$$

By minimising χ^2 we find the best-fit values for the marginalised nuisance parameters (as a function of all other parameters):

$$b_{i,*}^{\rm m} = F_{1,j} F_{2,ij}^{-1}\,, \tag{2.26}$$

with an uncertainty (unmarginalised over the cosmological parameters)

$$\tilde{\sigma}_i = \sqrt{{\rm diag}(F_{2,ij}^{-1})}\,. \tag{2.27}$$

The fact that we can analytically find the best-fit values for the nuisance parameters means that we can perform the likelihood profiling analytically too.

Similarly to the toy model example described above, the source of the projection effects is the Laplacian term $\ln\det F_2$, where from the definition of $F_{2,ij}$ we see that it depends on a) the modelling and parameterisation of $P^{\rm m}$; b) how constraining is the data via Cov; c) the size of the prior-volume in the marginalised nuisance parameters via C. Therefore, we can consider the following options to minimise the impact of the prior-volume effects: a) parameterise the model in terms of parameters with less degeneracy (e.g., sample in $\tilde{b}_1 = b_1 A_s$ or $\tilde{b}_1 = b_1 \sigma_8$) or vary the nonlinear scales parameters in the perturbative model

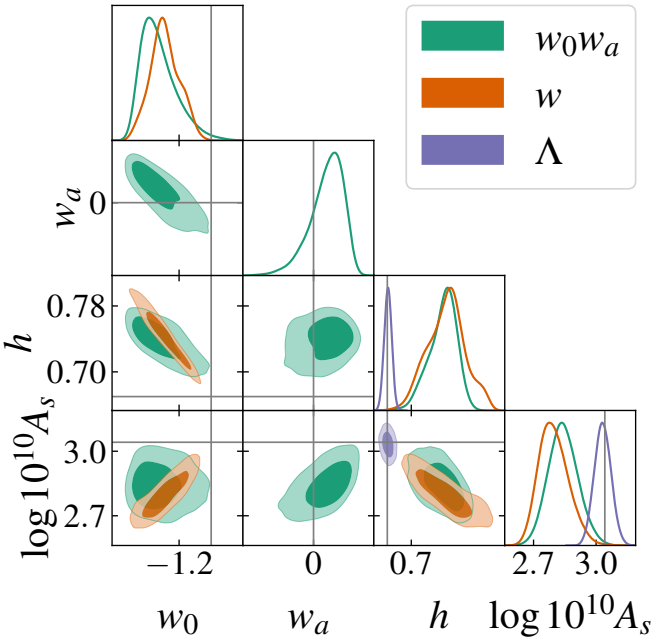

Figure 2.3 *Prior-volume effects in extended cosmologies for a Euclid-like spectroscopic setup. The standard cosmology is represented by purple contours, evolving dark energy – by the green ones, dark energy with a constant equation of state – by the orange ones. The solid gray lines denote the fiducial values of the cosmological parameters in the noiseless mock-data.*

analogously to k_0 in our toy model; b) decrease the size of the error bars with more data and larger survey volumes (e.g., Euclid's total effective volume will be ~ 10 times larger than the BOSS DR12 volume); c) constrain prior-volumes based on simulations or semi-analytical approaches (e.g., HOD inspired priors in Ref. [204, 205]); d) use profile likelihood or Jeffreys priors (synonymous in case of linear parameters, an approximation in case of nonlinear parameters), ideally we would use Jeffreys priors on all parameters, cosmological ones included. In Fig. 2.3 we show marginalised posterior distributions for a Euclid-like spectroscopic analysis on a noiseless mock-data. There we see that with Euclid-like observational error bars the projection effects in the standard cosmology are negligible: the inferred values of h and A_s are not biased with respect to their fiducial values. However, in this exemplary setup, the projection effects are severe for the DE models wCDM and w_0w_aCDM. The reason for these projections is in the degeneracies of the extended parameters, w and w_0w_a, with the standard cosmological parameters and their weak sensitivity to the probed redshifts (here the spectroscopic redshift bins are $z = [0.9, 1.2, 1.5, 1.8]$).

Weak lensing analyses are also affected by the projection effects, as they encompass a large number of nuisance parameters to model systematics (e.g., 10 z-bins for WL probes versus 4 bins for GC probes in Euclid). We briefly mention application cases

for analytical profile likelihood in the nuisance parameters for WL analyses: a) the photometric redshift distribution (linearised after calibration with external data); b) intrinsic alignment parameters; c) galaxy biases for photometric galaxy clustering (appear quadratically in the model, but still can be well-approximated [200]). Alternative solutions to overcome projection effects due to nuisance parameters are based on *a posteriori* comparisons: e.g., picking a simpler model for systematic effects [206] or restricting the prior-ranges [6]. However, in the case of Stage-III WL surveys, it is not only the nuisance parameters that cause prior-volume effects. There, the projection effects in the parameters of interest, Ω_m and S_8 (or σ_8), appear due to the marginalisation over poorly constrained cosmological parameters $h, n_s, \Omega_\mathrm{b}, \Omega_\nu$ that are correlated with the parameters of interest. By "poorly constrained" we mean that their posterior distributions are limited by the assumed priors. For example, see Ref. [207] with KiDS for a discussion of the impact of the A_s prior. Or in Refs. [208] and [209] with a DES setup the authors demonstrated how the projection bias also depends on the true value of the poorly constrained parameters and their displacement from the centre of the corresponding prior-range.

2.4 Posterior Sampling

In practice, we can rarely solve Eq. 2.1 analytically. Instead, we usually draw samples from the posterior distribution, reconstruct the complete density function or calculate its summary statistics. In the following section, we review the use of various Monte Carlo sampling methods for practical sampling from posterior densities important for our work. Namely, we will describe the principles of three samplers: `emcee` [210], `pocoMC` [211] and `Nautilus` [212]. There are many other samplers that are worth mentioning that we did not apply in our analyses, e.g., `dynasty` [213] and `PolyChord` [214].

2.4.1 Markov Chain Monte Carlo Methods

Markov Chain Monte Carlo (MCMC) methods provide us with an efficient technique of sampling regions of high probability density in a high-dimensional parameter space. The main idea of the method is to generate a Markov chain – a series of steps in the parameter space, where each step depends probabilistically only on the position of the previous step. The goal of each chain is to converge to the target density distribution, which in our case is the posterior distribution. To ensure convergence to the posterior distribution, a chain must satisfy two conditions:

- Detailed balance between the Markov chain and the posterior distribution: all points in the chain converge to the target distribution when the equilibrium (convergence) is achieved, i.e., the posterior distribution is a stationary distribution of the Markov chain.

- Ergodicity: any point in the chain can be reached from any other point, the stationary distribution does not depend on the starting point of the Markov chain.

Regarding the starting point, in case of it being in a region of low probability density, the random-walk in the parameter space will require some number of steps before a region with high probability density is reached. These initial steps are called the "burn-in" period and are usually removed from the final set of samples.

Regarding the equilibrium state, commonly, the Gelman-Rubin convergence test [215] is applied. The chains have to be independent and their variances (between-chains and within-chain) in agreement with $R < 1.03$, where R is a defined statistic computed on a parameter-by-parameter basis. For C chains and N number of steps, it depends on the variance of the individual chain means B, and the mean of the individual chain variances $\bar{V}$:

$$R = \sqrt{\frac{N-1}{N} + \frac{C+1}{CN}\frac{B}{\bar{V}}}\,. \tag{2.28}$$

In general, for different sampling strategies different convergence criteria are appropriate. There is no formal and ultimate definition of the convergence, careful comparison and adaptation to a problem of interest is always required.

2.4.2 Metropolis-Hasting

The Metropolis-Hasting (MH) algorithm [216–218] is a basic sampling scheme that follows the following iterative steps:

1. From a proposal distribution $Q(\theta_{i+1}|\theta_i)$ propose a next position in the parameter space θ_{i+1} given the current position θ_i;
2. Compute the probability $q = \min\left(1, \frac{\mathcal{P}(\theta_{i+1}|\boldsymbol{d})Q(\theta_i|\theta_{i+1})}{\mathcal{P}(\theta_i|\boldsymbol{d})Q(\theta_{i+1}|\theta_i)}\right)$;
3. Draw a random number r from the uniform distribution $\mathcal{U}(0,1)$;
4. If $r \leq q$ move to the proposed next step, otherwise remain at the current position.

The acceptance probability q satisfies the detailed balance condition, while a reasonable choice of proposal distribution Q (normally a multivariate Gaussian centered at the current position with a tuned or adaptive covariance tensor) leads to ergodicity. The fraction of proposed steps that are accepted is called the acceptance rate. As a rule of thumb, the optimal value of the acceptance fraction is between 0.2 and 0.5. The covariance tensor of the proposal distribution can be adapted to tune the acceptance rate.

2.4.3 Affine-Invariant Stretch Move

The standard MH algorithm is hardly efficient for problems with a large number of parameters. There are various extensions of this algorithm that we will apply in our

analyses. One is the so-called an affine-invariant ensemble sampling algorithm proposed in Ref. [219] and implemented in `emcee` [210]. In this method we specify a number of walkers and a maximum number of steps. The walkers are moving in the parameter space in such a way that the proposal distribution for one walker depends on the positions of all other walkers in the ensemble. For instance, for each walker k at the current position θ_i^k the following procedure is repeated in series:

1. From the ensemble pick a walker $j \neq k$ with the current position θ^j;
2. Propose a next position in the parameter space $\theta_{i+1}^k = z\theta_i^k + (1-z)\theta^j)$ where z is a scaling variable randomly drawn from a probability distribution with a symmetrical condition $g(z^{-1}) = zg(z)$:

$$g(z) \propto \begin{cases} \frac{1}{\sqrt{z}}, & \text{if } z \in \left[\frac{1}{a}, a\right], \\ 0 & \text{otherwise,} \end{cases} \tag{2.29}$$

   where usually $a = 2$ (but can be adapted to improve the acceptance rate);
3. Compute the probability $q = \min\left(1, z^{N_{\rm par}-1}\frac{\mathcal{P}(\theta_{i+1}^k|\boldsymbol{d})}{\mathcal{P}(\theta_i|\boldsymbol{d})}\right)$ with $N_{\rm par}$ being the dimension of the parameter space;
4. Draw a random number r from the uniform distribution $\mathcal{U}(0,1)$;
5. If $r \leq q$ move to the proposed next step, otherwise remain at the current position.

In order to parallelise this algorithm without violating the detailed balance condition, the full ensemble can be separated into two subsets. This allows to update all walkers from one subset based on the positions of walkers from the other subset in a parallel manner. In order to ensure ergodicity the minimum number of walkers must be $N_{\rm par} + 1$. A great advantage of this method is its affine invariance, meaning that it is insensitive to the linear transformations and covariances among parameters. Which implies the independence on the level of anisotropy in the density distribution.

The convergence criterion for this so-called stretch-move algorithm is controlled by the auto-correlation time[2]. In general, for any sampler the auto-correlation time quantifies the Monte Carlo error and quantifies the robustness of the MCMC analysis, i.e., the time it takes a chain to forget where it started. For a chain θ with N samples and means in parameters μ, the auto-covariance for a time-lag ΔT that corresponds to a discrete number of steps is given by

$$\mathrm{Cov}(\Delta T) = \frac{1}{N - \Delta T}\sum_{i=1}^{N-\Delta T}(\theta_i - \mu)(\theta_{i+\Delta T} - \mu)\,, \tag{2.30}$$

[2]We cannot apply the Gelman–Rubin criterion using multiple walkers in the same ensemble because the samples in the chain are not independent.

where with $\Delta T = 0$ we get the variance within the chain. The corresponding normalised auto-correlation function is expressed by

$$\rho_{\Delta T} = \frac{\mathrm{Cov}(\Delta T)}{\mathrm{Cov}(0)}\,, \tag{2.31}$$

where $+1$ would imply fully correlated states, -1 fully anti-correlated states, and 0 uncorrelated samples. The stronger correlated is the chain, the longer it takes for $\rho_{\Delta T}$ to reach zero. We can define the integrated auto-correlation time as

$$\tau_{\mathrm{I}} = 1 + 2\sum_{\Delta T=1}^{N} \rho_{\Delta T}\,, \tag{2.32}$$

which unfortunately becomes very noisy for large N. Instead, we evaluate

$$\tau_{\mathrm{I}}(M) = 1 + 2\sum_{\Delta T=1}^{M} \rho_{\Delta T} \tag{2.33}$$

with $M = \{M_1, M_2, ...\}$ being a number of steps in the chain dividable by 100, for instance. We stop a chain after M_j iterations if $50\tau_I(M_j) < M_j$ and $\left[\tau_{\mathrm{I}}(M_{j-1}) - \tau_{\mathrm{I}}(M_j)\right]/\tau_{\mathrm{I}}(M_j) < 0.01$. The smaller is the auto-correlation time, the less samples we must generate to produce a representative sampling of the target density – the more efficient is the analysis.

2.4.4 Sequential and Preconditioned Monte Carlo

The basic idea of Sequential Monte Carlo (SMC) is evolving a starting population of N_{live} particles drawn from a known distribution towards the target distribution via a number of intermediate steps [220]. In other words, we aim to bridge points selected from the prior distribution with the posterior distribution:

$$\mathcal{P}_t(\theta) \propto \mathcal{L}^{\beta_t}(\theta)\Pi(\theta), \quad 0 = \beta_1 < \beta_2 < ... < \beta_m = 1 \tag{2.34}$$

with β being the effective inverse temperature parameter. The ladder parameter β gets gradually increased in each iteration by a small step size, which is either fixed or adapted to maintain a constant number of effective particles. Number of effective particles correspond to a fraction of all particles, αN_{live}, inside the effective sample size (ESS) with a typical value $\alpha \sim 0.95$. ESS can be estimated as

$$\mathrm{ESS}_t = \frac{\left(\sum_{i=1}^{N_{\mathrm{live}}} w_i^{(t)}\right)^2}{\sum_{i=1}^{N_{\mathrm{live}}} \left(w_i^{(t)}\right)^2}\,, \tag{2.35}$$

where the importance weights are computed as

$$w_i^{(t)} = W_i^{(t-1)} \mathcal{L}^{\beta_t - \beta_{t-1}}(\theta_i^{(t-1)}) \tag{2.36}$$

with the normalised weights given by $W_i = w_i / \sum_{i=1}^{N_{\rm live}} w_i$. After drawing $(\theta_1^1, \theta_2^{(1)}, ..., \theta_{N_{\rm live}}^{(1)})$ from the prior with initial weights $W_i^{(1)} = 1/N_{\rm live}$ we repeat the following procedure before $\beta_t = 1$ is achieved:

1. Find β_t by solving $\mathrm{ESS}_t = \alpha N_{\rm live}$, re-weight the particles, update the evidence estimate;

2. Re-sample $\theta_i^{(t-1)}$ according to $w_i^{(t)}$: particles with small weight values are removed, particles with large weight values are multiplied in number proportionally; new weights are set to $1/N_{\rm live}$ again;

3. Update particles using MCMC (with, e.g., random Metropolis walk or using t-preconditioned Crank-Nicolson instead of Gaussian kernels in the proposed distribution): the chain stops when the mean correlation coefficient between the initial and current position of the particles in this iteration becomes lower than a threshold with a typical value of 0.75.

A novel Monte Carlo method that facilitates efficient sampling of probability distributions with non–trivial geometry was introduced in Refs. [211, 221] and implemented in `pocoMC`, a sampler we used in various projects (see Chapter 3 and Chapter 4). The basic idea is to 1) apply Normalising Flow (NF) to simplify complex correlations between parameters and continue sampling from the resulting latent space in which correlations are substantially reduced; 2) sample via an adaptive SMC scheme; 3) compute the model evidence, use it to control the convergence and compare models. The convergence is reached when $\beta_t = 1$.

2.4.5 Nested Sampling

The main idea of Nested Sampling (NS) [222] is to approximate the model evidence $\mathcal{Z}$ in shells of constant likelihood and provide weighted samples from the posterior distribution [223]. If the prior volume confined within the iso-likelihood contour of $\mathcal{L}(\theta) = \lambda$ is defined as

$$X(\lambda) = \int_{\mathcal{L}(\theta) > \lambda} \Pi(\theta) \mathrm{d}\theta, \tag{2.37}$$

then we can write the evidence integral as a one-dimensional integral

$$\mathcal{Z} = \int_0^1 \mathcal{L}(X) \mathrm{d}X \tag{2.38}$$

with $\mathcal{L}(X)$ being a monotonically decreasing function of X. Thus, we can compute the evidence integral numerically:

$$\mathcal{Z} = \sum_{i=1}^{m} \mathcal{L}_i \frac{X_{i-1} - X_{i+1}}{2} = \sum_{i=1}^{m} \mathcal{L}_i w_i \tag{2.39}$$

with discrete values of X: $0 < X_m < ... < X_2 < X_1 < X_0 = 1$. Of course, due to finite amount of steps, we deal with a truncation error, so we can estimate the remaining evidence with $\Delta\mathcal{Z} = \mathcal{L}_{\max} X_m$ (or with the mean of the likelihood among the live points instead of the maximum). In the context of parameter estimation, we find the normalised weights for samples in the posterior distribution are given by

$$p_i = \frac{\mathcal{L}_i w_i}{\mathcal{Z}} \,. \tag{2.40}$$

After drawing N_{live} points $(\theta_1^1, \theta_2^{(1)}, ..., \theta_{N_{\text{live}}}^{(1)})$ from the prior with initial volume $X = 1$ and evidence $\mathcal{Z} = 0$ we repeat the following procedure before the condition "$\Delta\mathcal{Z}/\mathcal{Z} <$ tolerance threshold" is satisfied:

1. Find the minimum likelihood out of all points ($\mathcal{L}^* = \mathcal{L}_1$ corresponding to X_1) and replace it with a new point of higher likelihood;

2. Update the weights, evidence and volume with the compression factor, e.g., $\exp(-1/N_{\text{live}})$.

The most difficult step is finding a replacement point with $\mathcal{L} > \mathcal{L}^*$ from the prior distribution. As the latter's volume shrinks exponentially with each iteration, it becomes hard to efficiently draw points. To find samples from the likelihood-constrained priors we can either use MCMC steps or apply region samplers. The later is implemented in `MultiNest`, which samples inside clustered ellipsoids based on mean and covariances of the live points [224]. In our projects (see Chapter 6) we used a novel sampler, `Nautilus` [212], which, during its exploration phase, follows a similar principle of sampling within an estimated boundary around the points with highest likelihood. However, it has the following improvements with respect to the standard NS techniques: a) the new proposal volume does not assume ellipsoidal shape, instead it uses neural networks to determine a part of the ellipsoidal where the predicted likelihood score corresponds to the edge of the live set. In other words neural networks help to find the iso-likelihood boundaries of the shells and improve the sampling efficiency; b) after the exploration phase, the evidence and posterior are refined with additional points in individual shells with the corresponding assigned importance weights.

Chapter 3

Interacting Dark Energy: Joint Power Spectrum and Bispectrum Analysis

This chapter is based on the following peer reviewed publication:

- **M. Tsedrik**, C. Moretti, P. Carrilho, F. Rizzo, A. Pourtsidou, 2023, *Interacting dark energy from the joint analysis of the power spectrum and bispectrum multipoles with the EFTofLSS*. Published in MNRAS: doi:10.1093/mnras/stad260, arXiv:2207.13011.

Here we aim to quantify the impact of the inclusion of the bispectrum multipoles on top of the power spectrum multipoles in redshift space, when constraining extended cosmological models. As examples of extended cosmologies we take a class of the interacting dark energy model and the wCDM model. Given a state-of-the-art large set of simulations, i.e., knowing the true cosmology, in this chapter we try to answer the following questions:

a) What are the optimal scale cuts for the power spectrum and bispectrum multipoles in a Stage-IV like setup with the Effective Field theory of the Large Scale Structure (EFTofLSS) model? By saying optimal, we mean the scales that lead to maximising information and minimizing uncertainty on the model parameters without causing biased results.

b) We focus on Dark Scattering, a phenomenologically interesting class of interacting dark energy models that is characterised by pure momentum exchange between dark energy and dark matter. This model extends the parameter space with respect to ΛCDM by two parameters, w and A, which define the dark energy equation of state and the strength of the coupling between dark energy and dark matter, respectively. How does the addition of the bispectrum monopole to the power spectrum multipoles improve constraints on the dark energy parameters, without introducing biases in the parameter estimation?

c) Can we achieve a similar level of improvement with more moderate scale cuts by applying bias relations, hence by decreasing the parameter number when some relations between nuisance parameters are imposed? Alternatively, can improvement be achieved by adding the bispectrum quadrupole?

d) When allowing the main cosmological parameters to vary as well, what are the degeneracies with the extended parameters, w and A, that are the driving force behind the corresponding projection effects? Does adding the bispectrum information impact the prior-volume (projection) effects?

Contributions

I led the main analysis for the project, which includes running all MCMC chains presented in the paper, interpreting results, and drafting the majority of the text. Chiara Moretti provided the likelihood pipeline, PBJ, and shared her expertise on the modelling part and simulation set used in this project. I modified PBJ to incorporate a new dark energy model and performed various checks (such as different samplers and binning schemes). Pedro Carrilho and Alkistis Pourtsidou made significant contributions in interpreting the results. Federico Rizzo provided power spectrum and bispectrum measurements, as well as the covariances from the simulations used in this work.

3.1 Interacting Dark Energy Modelling

In this work we focus on the subclass of Interacting Dark Energy (IDE) models which exhibits no coupling at the background level and introduces a pure momentum transfer at the level of linear perturbations. In general, non-gravitational interaction between dark matter and dark energy can be introduced either at the level of the action [225–227] or more phenomenologically at the level of the fluid equations [228, 229]. This leads to two different approaches for our model of interest.

The first approach corresponds to the "Type 3" class of models from the action-based derivation in Ref. [225]. There, the pure exchange of momentum is generated by a coupling between the dark matter velocity field and the covariant derivative of the dark energy scalar field. In this case, the two parameters describing the extension with respect to the standard cosmological model are given by the coupling strength β and the exponential factor of the quintessence potential λ. These parameters are included in the action as follows:

$$S_\phi = \int \mathrm{d}t\ \mathrm{d}^3x\ a^3 \left[\frac{1}{2}(1-2\beta)\dot{\phi}^2 - \frac{1}{2}|\nabla\phi|^2 - V_0 \mathrm{e}^{-\lambda\phi}\right], \tag{3.1}$$

where ϕ is the scalar field (quintessence), the last term is the quintessence potential of the single exponential form, the dot represents a derivative with respect to cosmic time and a is the scale factor. This model is explicitly studied in Refs. [230, 231] and has been

implemented into the CLASS [25, 232] and CAMB [24] Boltzmann codes. These analyses vary β and λ, while the quintessence potential normalisation, V_0, is varied automatically by the Boltzmann solver in order to match a given Ω_ϕ today.

The second approach is derived in the elastic scattering formalism in Ref. [229]. The main idea is that a dark matter particle moves through the isotropic dark energy fluid and experiences a drag-force proportional to the scattering cross-section between the particle and the fluid. Since a dark matter particle is more massive than the energy exchange with the dark energy fluid, they interact via elastic scattering, in a way that resembles Thomson scattering between non-relativistic electrons and photons in the radiation-dominated era.

Such interaction involves no energy transfer and hence it leaves the energy conservation equation unchanged with respect to the standard cosmology. Moreover, we assume that the dark energy density and velocity fields are homogeneous (i.e., $\delta_{\rm DE} = \theta_{\rm DE} = 0$), since dark energy perturbations are damped within the cosmic horizon. This follows from the assumption of the dark energy speed of sound being equal to the speed of light, and was confirmed numerically in Ref. [3]. While these fluctuations become non-negligible at super-horizon scales, even the most extreme modifications do not contradict the CMB measurements due to the presence of cosmic variance [230]. In presence of momentum exchange between the two components of the dark sector, and with the approximation of homogeneity in dark energy, this IDE model modifies only the Euler equation to

$$a\,\partial_a\Theta + \left(2 + (1+w)\,\xi\,\frac{\rho_{\rm DE}}{H} + \frac{a\,\partial_a H}{H}\right)\Theta + \frac{\nabla^2\Phi}{a^2H^2} = 0\,, \tag{3.2}$$

where $\xi = \sigma_{\rm D}/m_{\rm c}$ with $\sigma_{\rm D}$ is the cross-section of the dark energy - dark matter interaction and $m_{\rm c}$ the mass of dark matter particle, and $\Theta = \theta_{\rm c}/aH$ with $\theta_{\rm c}$ the dark matter velocity divergence. $H = \dot{a}/a$ is the Hubble rate and it describes the expansion history in the flat universe composed only of dark matter and dark energy by

$$H^2 = H_0^2\left(\Omega_{\rm c,0}\;a^{-3} + \Omega_{\rm DE,0}\;a^{-3(1+w)}\right)\,, \tag{3.3}$$

where as above w is the dark energy equation of state parameter. H_0, $\Omega_{\rm c,0}$, $\Omega_{\rm DE,0}$ are the values of Hubble parameter, dark matter density and dark energy density parameters today. Additionally, the gravitational potential stays unchanged and is given by the following Poisson equation:

$$\nabla^2\Phi = \frac{3}{2}a^2H^2\Omega_{\rm c}\delta_{\rm c}\,, \tag{3.4}$$

where $\Omega_{\rm c}$ is the background dark matter density parameter at the scale factor a and $\delta_{\rm c}$ is the corresponding density contrast.

Although there is no direct mapping between the elastic scattering and the "Type 3" models, a particular subclass of "Type 3" models can reproduce the drag-like behaviour [233]. In Ref. [234] the authors show how these models can be matched approximately.

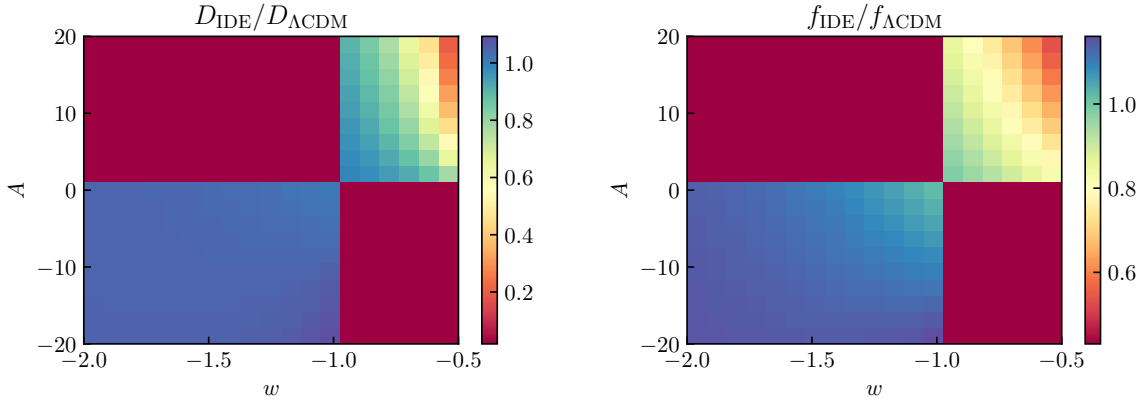

Figure 3.1 *Left panel: the linear growth factor fractional deviation relative to the ΛCDM case with* $D_{\Lambda\mathrm{CDM}} = 0.475$ *for varying values of IDE parameters,* w *and* A*. Right panel: the logarithmic growth rate fractional deviation from the ΛCDM value* $f_{\Lambda\mathrm{CDM}} = 0.861$*. Both growth parameters are computed at redshift* $z = 1$*. Parameter* A*, defining the coupling strength between dark energy and dark matter, is given in the units of* $b\ GeV^{-1}$*. The red patches in the upper left and the lower right corners denote the forbidden area of the IDE parameter space due to the condition* $A/(1+w) \geq 0$*.*

In this work we use the phenomenological approach with parameters w and $A = \xi(1 + w)$, which characterise the equation of state for dark energy and the coupling strength, respectively. We assume that w is constant, it affects the expansion history in Eq. 3.3 as well as structure formation in Eq. 3.2. At the same time, A impacts only the perturbation growth and is chosen in this form (i.e., a combination of ξ and w) for the purposes of parameter inference. This is particularly important for $w \approx -1$, where we can constrain A while ξ could take an arbitrary large value.

Parameters w and A modify the linear growth factor $D(a)$ and the logarithmic growth rate $f = \mathrm{d}\ln D/\mathrm{d}\ln a$. For a constant value of w in the late Universe with redshift $z \leq 10$, in the canonical (phantom) case of $w_{\mathrm{DE}} > -1\,(w_{\mathrm{DE}} < -1)$ the growth factor is decreased (increased) with respect to ΛCDM. The effect gets more prominent as the redshift decreases, and for larger values of ξ. This leads to a scale-independent suppression (enhancement) of the power spectrum at large scales. On smaller scales, the modification comes from the drag term in Eq. 3.2: for $w_{\mathrm{DE}} > -1\,(w_{\mathrm{DE}} < -1)$ there is a dissipation (injection) of kinetic energy within collapsed structures. In other words, for $w_{\mathrm{DE}} > -1\,(w_{\mathrm{DE}} < -1)$ particles inside collapsed objects experience additional friction (drag), hence it becomes harder (easier) for them to stream away, with a strong and scale-dependent enhancement (suppression) of the growth of structure in the nonlinear regime. This behaviour, anticipated from the theory, has been shown to hold true in N-body simulations in Refs. [3, 234] (see Fig. 1.4).

In this work we consider only one redshift $z = 1$, at which the impact of the IDE parameters is observable but not as prominent as at lower redshifts. In Fig. 3.1 we show

the impact of different values of w and A on the growth parameters at the redshift of our interest. The ratios are taken with respect to the ΛCDM values: $D_{\Lambda\mathrm{CDM}} = 0.475$ and $f_{\Lambda\mathrm{CDM}} = 0.861$ for our choice of cosmological parameters. The red patches in the upper left and the lower right corners denote the forbidden area of the IDE parameter space: the sign of A and $(1 + w)$ has to be the same, since $\xi = A/(1 + w)$ from Eq. 3.2 has to be non-negative. For $w < -1$ dark energy starts to dominate over matter at later times than in ΛCDM, hence with decreasing w the growth rate quickly becomes 1 (as in the matter-dominated epoch) nearly independent from the value of A. The linear growth factor is also independent of A and is slightly larger than the ΛCDM case for $w < -1$. For $w > -1$ the expected power suppression at linear scales is present, with a stronger effect for larger values of A.

3.2 Power Spectrum and Bispectrum Modelling

Halos and galaxies are biased tracers of the matter density field [145]. Their clustering properties up to mildly nonlinear scales can be described using the perturbative framework. The EFTofLSS formalism is based on perturbation theory, with the addition of counterterms to account for the impact of unknown small-scale physics, such as galaxy formation, on large-scale modes. The functional form of the counterterms is specified by the symmetries of the density field, while the nuisance parameters are determined by the data. We note that application to data would not be possible without huge effort in the development on the theoretical side (see, for example, Refs. [33, 34, 147, 235–240], and for a more comprehensive list for the development of the EFTofLSS see the footnote in Ref. [241]).

3.2.1 Bias Expansion

Both dark matter halos (the focus of this study) and galaxies are biased tracers of the underlying matter distribution. The halo overdensity can be expanded as $\delta_h = \sum_n b_n/n!\delta^n$, where δ^n are higher powers of the matter density contrast and b_n are the corresponding local bias terms [242]. Halos are formed by the gravitational collapse of matter from a spatially finite region. Anisotropies created by this process impact the local distribution of objects, and thus the bias parameters, with tidal effects [243, 244] and introduce scale dependency by breaking the local assumption [245]. Effects from an ellipsoidal gravitational collapse are encoded in the non-local operators, dubbed $\mathcal{G}_2$ and Γ_3[1]: the first one represents the tidal stress tensor produced by the gravitational potential, while the second one acts like a velocity tidal tensor. Effects due to the finite

[1]The exact expression for these operators as functions of gravitational and velocity potentials are $\mathcal{G}_2(\Phi_\mathrm{g}) = (\nabla_i\nabla_j\Phi_\mathrm{g})^2 - (\nabla^2\Phi_\mathrm{g})^2$ and $\Gamma_3 = \mathcal{G}_2(\Phi_\mathrm{g}) - \mathcal{G}_2(\Phi_v)$.

size of the collapsing region are taken into account by the higher-order derivative of the matter field $\nabla^2\delta$. Additionally, the relation between matter and galaxies is also affected by stochasticity, whose impact can be modeled as an additional contribution to Poisson shot noise on large scales [246, 247], while on small scales it can exhibit a scale-dependence due to the halo-exclusion effect [248, 249]. We consider the bias expansion given by [145, 250]

$$\delta_h = b_1\delta + \frac{b_2}{2}\delta^2 + b_{\mathcal{G}_2}\mathcal{G}_2 + b_{\Gamma_3}\Gamma_3 + b_{\nabla^2\delta}\nabla^2\delta + \epsilon + \epsilon_\delta\delta\,, \tag{3.5}$$

where b_1 and b_2 are the linear and quadratic bias, and the last two terms correspond to stochasticity contributions. Note that the higher derivative term gives rise to a $k^2P_L(k)$ correction, which is degenerate with one of the counterterms. Therefore, we omit $b_{\nabla^2\delta}$ in our analysis, as previously done in Ref. [8]. Moreover, we omit from Eq. 3.5 all operators that do not contribute to our chosen theoretical models for the power spectrum and bispectrum. Note that this bias expansion was derived in the context of ΛCDM cosmology. However, it is still applicable in our model, since IDE features a scale-independent linear growth, implies the same structure of the SPT kernels (see the next subsection) and obeys the same symmetries as in ΛCDM (for more information on bias expansion from symmetries see Refs. [251, 252]).

3.2.2 Power Spectrum and Bispectrum

The mildly nonlinear power spectrum and bispectrum in real space using the EFTofLSS can be modeled with three ingredients: a) the leading-order contribution in SPT at one-loop for the power spectrum with the addition of the EFTofLSS counterterms, and at tree-level for the bispectrum, b) a bias expansion, and c) an infrared-resummation routine to take the damping of the oscillatory features into account [253, 254]. In addition to that, to model redshift space quantities we should take the distortions due to peculiar velocities into consideration. This introduces an additional dependency of the observables on the direction of separation between the objects with respect to the line-of-sight, $\hat{\boldsymbol{s}}$. For the power spectrum this dependency is characterized by the cosine of the angle formed by the separation wave-number with the line-of-sight, $\mu = (\boldsymbol{k}\cdot\hat{\boldsymbol{s}})/k$. For the bispectrum we need two cosines, μ_1 and μ_2, of $\boldsymbol{k}_1$ and $\boldsymbol{k}_2$ with the line of sight $\hat{\boldsymbol{s}}$, with the condition $\boldsymbol{k}_1+\boldsymbol{k}_2+\boldsymbol{k}_3=\boldsymbol{0}$. However, it is more convenient to describe triangle configurations with three wave-numbers (k_1, k_2, k_3), and two angles, $\theta = \arccos\mu_1$ and ξ being the azimuthal rotational angle of $\boldsymbol{k}_2$ around $\boldsymbol{k}_1$ [255]. In total, the redshift space bispectrum depends on five variables, three of which determine the shape of the triangle while the remaining two define its orientation with respect to the line-of-sight.

The complete set of equations we use in this work will be detailed in a forthcoming paper by Chiara Moretti et al., where we also give a detailed description of the code used to perform the analysis. Here we briefly highlight the main formulae and techniques used.

These formulae are the same as in ΛCDM, as the interaction under consideration only modifies the linear growth factor, D (appearing below via P_L) and the linear growth rate of structure, f.

The expression for the halo power spectrum in redshift space that we adopt in our analysis is given by

$$P_{hh}(k,\mu) = P_{\rm SPT}(\boldsymbol{k}) + P_{\rm ctr}(\boldsymbol{k}) + P_{\rm stoch}(k)\,, \tag{3.6}$$

in which the first term equals

$$\begin{aligned} P_{\rm SPT}(\boldsymbol{k}) = P_{\rm Kaiser}(\boldsymbol{k}) + P_{\rm 1-loop}(\boldsymbol{k}) &= Z_1(\boldsymbol{k})P_L(k) \\ &+ 2\int {\rm d}^3\boldsymbol{q}[Z_2(\boldsymbol{q},\boldsymbol{k}-\boldsymbol{q})]^2 P_L(q)P_L(|\boldsymbol{k}-\boldsymbol{q}|) \\ &+ 6Z_1(\boldsymbol{k})P_L(k)\int {\rm d}^3\boldsymbol{q} Z_3(\boldsymbol{k},\boldsymbol{q},-\boldsymbol{q})P_L(q) \end{aligned} \tag{3.7}$$

with P_L being the linear power spectrum and $Z_1(\boldsymbol{k})$, $Z_2(\boldsymbol{k}_1,\boldsymbol{k}_2)$ and $Z_3(\boldsymbol{k}_1,\boldsymbol{k}_2,\boldsymbol{k}_3)$ the redshift space kernels for the loop corrections [255]:

$$Z_1(\boldsymbol{k}) = b_1 + f\mu^2 \tag{3.8}$$

$$\begin{aligned} Z_2(\boldsymbol{k}_1,\boldsymbol{k}_2) = b_1 F_2(\boldsymbol{k}_1,\boldsymbol{k}_2) + \frac{b_2}{2} + b_{\mathcal{G}_2} S(\boldsymbol{k}_1,\boldsymbol{k}_2) + f\mu^2 G_2(\boldsymbol{k}_1,\boldsymbol{k}_2) \\ + \frac{f\mu k}{2}\left[\frac{\mu_1}{k_1}Z_1(\boldsymbol{k}_2) + \frac{\mu_2}{k_2}Z_1(\boldsymbol{k}_1)\right] \end{aligned} \tag{3.9}$$

$$\begin{aligned} Z_3(\boldsymbol{k}_1,\boldsymbol{k}_2,\boldsymbol{k}_3) = b_1 F_3(\boldsymbol{k}_1,\boldsymbol{k}_2,\boldsymbol{k}_3) + b_2 F_2(\boldsymbol{k}_1,\boldsymbol{k}_2) + \frac{b_2 f\mu k}{2}\frac{\mu_1}{k_1} + 2b_{\mathcal{G}_2} S(\boldsymbol{k}_1,\boldsymbol{k}_{23})F_2(\boldsymbol{k}_2,\boldsymbol{k}_3) \\ + b_{\mathcal{G}_2} f\mu k \frac{\mu_1}{k_1} S(\boldsymbol{k}_2,\boldsymbol{k}_3) - \frac{4}{7} b_{\Gamma_3} S(\boldsymbol{k}_1,\boldsymbol{k}_{23})S(\boldsymbol{k}_2,\boldsymbol{k}_3) + f\mu^2 G_3(\boldsymbol{k}_1,\boldsymbol{k}_2,\boldsymbol{k}_3) \\ + \frac{(f\mu k)^2}{2} Z_1(\boldsymbol{k}_1)\frac{\mu_2\mu_3}{k_2 k_3} + f\mu k Z_1(\boldsymbol{k}_1)\frac{\mu_{23}}{k_{23}} G_2(\boldsymbol{k}_2,\boldsymbol{k}_3) \\ + f\mu k \frac{\mu_3}{k_3}\left[b_1 F_2(\boldsymbol{k}_1,\boldsymbol{k}_2) + f\mu_{12}^2 G_2(\boldsymbol{k}_1,\boldsymbol{k}_2)\right]\,. \end{aligned} \tag{3.10}$$

Where the symbols without subscripts in the n-th order kernel are $\boldsymbol{k} = \boldsymbol{k}_1 + ... + \boldsymbol{k}_n$ and $\mu = \hat{\boldsymbol{k}}\cdot\hat{\boldsymbol{z}}$, while $\boldsymbol{k}_{ij} = \boldsymbol{k}_i + \boldsymbol{k}_j$ and $\mu_{ij} = \hat{\boldsymbol{k}}_{ij}\cdot\hat{\boldsymbol{z}}$, F_n and G_n are SPT kernels, and Z_3 should be symmetrised with respect to Fourier momenta. Note that the computation is done under the assumption of the Einstein-de Sitter (EdS) approximation, i.e., the SPT kernels are computed with $\Omega_{\rm c,0} = 1$ in the absence of dark energy, while the time-dependence of density perturbations is captured by the linear growth factor from the IDE model. The scale-independent linear growth in IDE and the redshift of our interest being $z = 1$ allow us to conclude that EdS is a good approximation accurate at the sub-percentage level (for a detailed study of the EdS approximation in redshift space see Refs. [256, 257]).

We then apply IR-resummation [253, 254], following the procedure described in detail

in Ref. [258]. This gives us the re-summed version of the terms above:

$$P_{\rm Kaiser} \to (b_1 + f\mu^2)^2 \left[P_L^{\rm nw} + {\rm e}^{-k^2\Sigma_{\rm tot}^2} P_L^{\rm w}(1 + k^2\Sigma_{\rm tot}^2)\right] ,$$
$$P_{\rm 1-loop} \to P_{\rm 1-loop}^{\rm nw} + {\rm e}^{-k^2\Sigma_{\rm tot}^2} P_{\rm 1-loop}^{\rm w} , \tag{3.11}$$

where $\Sigma_{\rm tot}$ is given by [258]:

$$\Sigma_{\rm tot}^2(\mu) = (1 + f\mu^2(2 + f))\Sigma^2 + f^2\mu^2(\mu^2 - 1)\delta\Sigma^2 \tag{3.12}$$

that depends on

$$\Sigma^2 = \frac{1}{6\pi^2}\int_0^{k_s} {\rm d}q P^{\rm nw}(q)\left[1 - j_0(q\ell_{\rm osc}) + 2j_2(q\ell_{\rm osc})\right] \tag{3.13}$$
$$\delta\Sigma^2 = \frac{1}{2\pi^2}\int_0^{k_s} {\rm d}q P^{\rm nw}(q) j_2(q\ell_{\rm osc}) \tag{3.14}$$

with the spherical Bessel functions $j_{0,2}$, the separation scale $k_s = 0.2\ h/{\rm Mpc}$, the BAO scale $\ell_{\rm osc} = 102.707\ {\rm Mpc}/h$ and $P^{\rm nw} = P - P^{\rm w}$. The wiggle-no-wiggle splitting is performed using the Eisenstein-Hu (EH) fitting function [37]: the smooth no-wiggle component is computed from the convolution of the EH fit for the linear matter power spectrum with a Gaussian filter with width $\lambda = 0.25$. The redshift space loop corrections lead to 28 independent integrals, which we compute using the `FAST-PT` algorithm [158, 159].

The stochastic power spectrum is given by [249]

$$P_{\rm stoch}(k) = (1 + \alpha_P + \epsilon_{k^2}k^2)\bar{n}^{-1} , \tag{3.15}$$

with two free parameters, α_P and ϵ_{k^2}, describing a constant deviation from purely Poisson shot noise $\bar{n}^{-1}$, and higher-order scale dependent corrections generated to account for the short-range non-locality, respectively. The physical meaning of α_P can be explained with the halo exclusion effect [248, 259]; its value can be either positive (e.g., in galaxy populations with high satellite fractions) or negative (e.g., in central galaxies of massive halos) [248]. The term $(1 + \alpha_P)\,\bar{n}^{-1}$ corresponds to the noise parameter N usually used in the literature, which denotes a scale-independent noise power spectrum. In this work we include scale-dependency into the shot noise, a feature which is supported by numerical simulations [260]. Furthermore, as we show below, the data prefers a strong scale-dependence in the shot noise (see Subsection 3.3.1 and Fig. 3.2).

The EFTofLSS counterterms for this model are

$$P_{\rm ctr}(k,\mu) = -2\tilde{c}_0 k^2 \tilde{P}_L(k) - 2\tilde{c}_2 k^2 f\mu^2 \tilde{P}_L(k) \\ - 2\tilde{c}_4 k^2 f^2 \mu^4 \tilde{P}_L(k) + P_{{\rm ctr},\nabla^4\delta}(k,\mu)\,, \tag{3.16}$$

with the IR re-summed linear power spectrum

$$\tilde{P}_L(k) = P_L^{\rm nw} + {\rm e}^{-k^2\Sigma^2_{\rm tot}} P_L^{\rm w} \tag{3.17}$$

and an additional counterterm proportional to $\mu^4 k^4 \tilde{P}_L(k)$ to include higher-order contributions and model to some extent the Finger of God effect (FoG):

$$P_{{\rm ctr},\nabla^4\delta}(k,\mu) = c_{\nabla^4\delta} k^4 f^4 \mu^4 (b_1 + f\mu^2)^2 \tilde{P}_L(k)\,. \tag{3.18}$$

Overall, this power spectrum model includes in total 10 parameters: $\{b_1,\, b_2,\, b_{\mathcal{G}_2},\, b_{\Gamma_3},\, \tilde{c}_0,\, \tilde{c}_2,\, \tilde{c}_4,\, \alpha_P,\, \epsilon_{k^2},\, c_{\nabla^4\delta}\,\}$.

For the tree-level bispectrum the expression at tree-level is given by

$$B_g(\boldsymbol{k}_1,\boldsymbol{k}_2,\hat{\boldsymbol{s}}) = B_{\rm stoch}(\boldsymbol{k}_1,\boldsymbol{k}_2,\hat{\boldsymbol{s}}) \\ + \sum_{\boldsymbol{k}_1\leq\boldsymbol{k}_i\leq\boldsymbol{k}_j\leq\boldsymbol{k}_3} 2Z_1(\boldsymbol{k}_i)Z_1(\boldsymbol{k}_j)Z_2(\boldsymbol{k}_i,\boldsymbol{k}_j)\tilde{P}_L(k_i)\tilde{P}_L(k_j)\,, \tag{3.19}$$

with the stochastic contribution

$$B_{\rm stoch}(\boldsymbol{k}_1,\boldsymbol{k}_2,\hat{\boldsymbol{s}}) = (1+\alpha_B)\bar{n}^{-1}\sum_{i=1}^{3} Z_1^2(\boldsymbol{k}_i)\tilde{P}_L(k_i) + \bar{n}^{-2}\,, \tag{3.20}$$

where α_B describes a deviation from the Poisson limit. In contrast to Ref. [151], we do not include the FoG modelling and its corresponding parameter in our tree-level model, since such a contribution is expected only at 1-loop level and our data consists of halos only. This leaves the halo bispectrum to be described by 4 parameters: $\{b_1,\, b_2,\, b_{\mathcal{G}_2},\, \alpha_B\,\}$.

Overall, we express our theoretical prediction in terms of multipoles, in order to eliminate the μ-dependence. For the power spectrum we compute

$$P_l(k) = \frac{2l+1}{2}\int_{-1}^{1} {\rm d}\mu P_{hh}(k,\mu)\mathcal{P}_l(\mu) \tag{3.21}$$

where $\mathcal{P}_l(\mu)$ are the Legendre polynomials of order l and $P_{hh}(k,\mu)$ is the redshift space power spectrum given by Eq. 3.6. In this analysis we use the monopole ($l=0$), quadrupole ($l=2$), and hexadecapole ($l=4$). Studies have shown that these three multipoles contain most of the cosmological information (e.g., Refs. [34, 165, 261]).

An analogous expansion can be applied to the bispectrum, by expanding in terms of

spherical harmonics as

$$B_h(k_1, k_2, k_3, \theta, \xi) = \sum_l \sum_{m=-l}^{l} B_{lm}(k_1, k_2, k_3) Y_l^m(\theta, \xi) \tag{3.22}$$

with the same convention for triangle description as above [255]. The expansion coefficients are given by

$$B_{lm}(k_1, k_2, k_3) = \int_{-1}^{1} \mathrm{d}\cos\theta \int_0^{2\pi} \mathrm{d}\xi B_h(k_1, k_2, k_3, \theta, \xi) Y_l^m(\theta, \xi)\,. \tag{3.23}$$

As is typical in the literature, when we describe the redshift space multipoles of the bispectrum, we consider only the case with $m = 0$, as it has been shown that such seemingly strong compression does not lead to a significant loss of information [262]. This allows us to write the bispectrum version of Eq. 3.21, since the spherical harmonics reduce to Legendre polynomials in the $m = 0$ case:

$$B_l(k_1, k_2, k_3) = \frac{2l+1}{2} \int_{-1}^{1} \mathrm{d}\cos\theta \left[\frac{1}{2\pi} \int_0^{2\pi} \mathrm{d}\xi B_h(k_1, k_2, k_3, \theta, \xi) \right] \mathcal{P}_l(\cos\theta)\,. \tag{3.24}$$

Let us briefly list the known degeneracies, which follow from previous studies, our tests and theory directly:

1. $f - b_1$ are anti-correlated: both parameters control the amplitude on large scales, they occur combined with various powers in the model, hence if one gets larger the other should decrease.

2. The counterterms $\tilde{c}_0$, $\tilde{c}_2$, $\tilde{c}_4$ and $c_{\nabla^4\delta}$ are all slightly degenerate with one another, but especially strong is the anti-correlation between $\tilde{c}_4$ and $\tilde{c}_2$. This becomes clear after the projection of Eq. 3.16 into multipoles: for the monopole the first three terms in this equation yield $-1/2\,(2\,\tilde{c}_0 + 0.7\,\tilde{c}_2 f + 0.4\,\tilde{c}_4 f^2)\,k^2 P_L$, while for the quadrupole we obtain $-5/2\,(0.3\,\tilde{c}_2 f + 0.2\,\tilde{c}_4 f^2)\,k^2 f P_L$. For instance, for $f \approx 1$ the counterterm parameters $\tilde{c}_4$ and $\tilde{c}_2$ cancel each other out if $\tilde{c}_4 \approx -\tilde{c}_2$. In these ad-hoc calculations, we have neglected the angle-dependence in the linear power spectrum due to IR-resummation, which however will affect the counterterms in the same way and does not impact our argument. Additionally, $\tilde{c}_4$ cannot be constrained without the power spectrum hexadecapole data. This can be seen directly from Eq. 3.16 where there are three terms with coefficients $\tilde{c}_0$, $\tilde{c}_2$, $\tilde{c}_4$ that all of them have a form of $k^2 P_L(k)$. From this it follows that we need all three multipoles to constrain all three parameters.

3. The nonlinear bias parameters b_2, $b_{\mathcal{G}_2}$ and b_{Γ_3} are all degenerate: b_2 is correlated with $b_{\mathcal{G}_2}$, while $b_{\mathcal{G}_2}$ and b_{Γ_3} are strongly anti-correlated. The power spectrum model

includes overall 30 independent contributions (28 for the loop-corrections and 2 for the shot noise), in which the bias parameters come as products with various powers and various combinations: for instance, b_2 appears as $b_1 b_2$, b_2^2, $b_2 f$, so that it can be constrained with power spectrum data only, while b_{Γ_3} appears only twice and only linearly in combination with b_1 and f, which makes it harder to constrain. However, the inclusion of the tree-level bispectrum solves this issue, since the bispectrum model does not include b_{Γ_3}. Additionally, due to the absence of b_{Γ_3}, b_2 and $b_{\mathcal{G}_2}$ are better constrained since the strong degeneracy is not present anymore. Therefore, we expect measurements of b_2 and $b_{\mathcal{G}_2}$ to be more precise from bispectrum measurements only, although b_1 is better constrained by power spectrum only measurements.

4. The noise parameters are anti-correlated with one another since they both control the deviation from Poisson shot noise (constant and scale-dependent). They dominate on small scales together with other effects like FoG and the monopole counterterm, hence we expect correlations between α_P, ϵ_{k^2} and $\tilde{c}_0$, $c_{\nabla^4\delta}$.

3.3 MCMC Analysis

3.3.1 Data

In this work we analyse halo power spectrum and bispectrum measurements in redshift space from the large set of 298 Minerva N-body simulations [30, 263]. These follow the evolution of 1000^3 dark matter particles in a cubic box of side $L = 1500$ Mpc h^{-1}, corresponding to a total effective volume of $\sim 1,000$ Gpc^3 h^{-3}. The mass cut in the halo catalogues is set to $1.12 \cdot 10^{13}\, M_\odot\, h^{-1}$, with a resulting halo mean number density of $\bar{n} = 2.13 \cdot 10^{-4}\ h^3$ Mpc^{-3}. We limit this study to a single redshift $z = 1$. The binning scheme we apply is given by: $k_i = (2 + (i-1))k_f$, with the fundamental frequency $k_f = 2\pi L^{-1}$, the bin size is $\Delta k = k_f$, and the total number of bins is $N_k = 128$ for the power spectrum and $N_k = 29$ for the bispectrum (with a total number of triangles $N_t = 2766$). For a detailed description of the measurements, the halo catalog construction and the estimators, we refer the reader to Refs. [7–9].

The fiducial cosmology of the simulations is the ΛCDM best-fit of the combined analysis of WMAP and BOSS DR9 results [264] and is given by: $h = 0.695$, $\Omega_{\rm m} = 0.285$, $\Omega_{\rm b} = 0.046$, $n_s = 0.9632$, $\sigma_8 = 0.828$. This means that the fiducial IDE parameters we should recover are $w = -1$ and $A = 0$.

3.3.2 Covariance

The covariance matrix is constructed from 10,000 mock halo catalogues produced with the Pinocchio code [27, 265], 298 of which have initial conditions chosen to match the

initial conditions of the 298 Minerva simulations, while the rest have different initial seeds. The total halo power spectrum of the mock catalogs is matched to the one of the N-body simulations at large scales by adjusting the mass threshold [7]. The large number of mocks allows us to suppress the noise in the off-diagonal components, giving a more accurate covariance, which allows us to better assess the goodness of the fit of the theoretical models we study.

The uncertainties associated to a measurement inferred from this covariance correspond to the volume of a single realisation. However, in our analysis we fit the 298 realisations simultaneously by summing up their log-likelihoods (see Subsection 3.3.3), thus we effectively fit for the full simulation volume of $\sim$ 1000 Gpc^3 h^{-3}. This volume is unrealistically large when compared to a typical redshift survey, but can be used to study the theoretical systematics of the model. To perform a more realistic analysis, the volume can be decreased in two ways:

1. Fitting fewer measurements: it is sufficient to decrease the number of measurements (e.g., in our case 4 realisations correspond to 13.5 Gpc^3 h^{-3}), while using the same covariance for a single measurement. However, during various tests we found that the resulting parameters and the goodness-of-fit vary substantially depending on the particular set of simulations selected. We interpret this as a consequence of the fact that the volume of a single simulation is large, since we obtain large amount of low wave-number modes, which are heavily affected by cosmic variance.

2. Rescaling the covariance: this mimics the effect of analysing a subset of measurements, but with the same suppression in cosmic variance as if we were fitting all of them. Unfortunately, due to the artificial rescaling of the covariance we cannot use the traditional measure of goodness-of-fit, the χ^2-statistic, because the increased error bars do not match the scatter in the measurements.

In order to mimic the error budget of Stage-IV spectroscopic galaxy surveys, we rescale the measured covariance C_{ij} by a factor η:

$$C_{ij}^{\rm resc} = \frac{\eta}{N_{\rm R}+N_{\rm C}} \sum_{\alpha=1}^{N_{\rm R}+N_{\rm C}} (X_i^\alpha - \overline{X_i})(Y_j^\alpha - \overline{Y_j})\,, \tag{3.25}$$

where $N_{\rm R}$ and $N_{\rm C}$ are the number of measurements from the simulations and catalogs, $X, Y \in \{P_{l_1}, B_{l_2}\}$ with l being the multipole order, α is the realisation index, i and j denote indices of the wave-number or triangle configuration bin. This factor η is a ratio between the effective volumes of all simulation realisations and a typical Stage-IV survey with $V \sim 8$ Gpc$^3\,h^{-3}$ at $z = 1$, giving $\eta \approx 126$. The effective volume is computed as [266]

$$V_{\rm eff} = \left[\frac{\bar{n}P_{hh}(k^*)}{1+\bar{n}P_{hh}(k^*)}\right]^2 V\,, \tag{3.26}$$

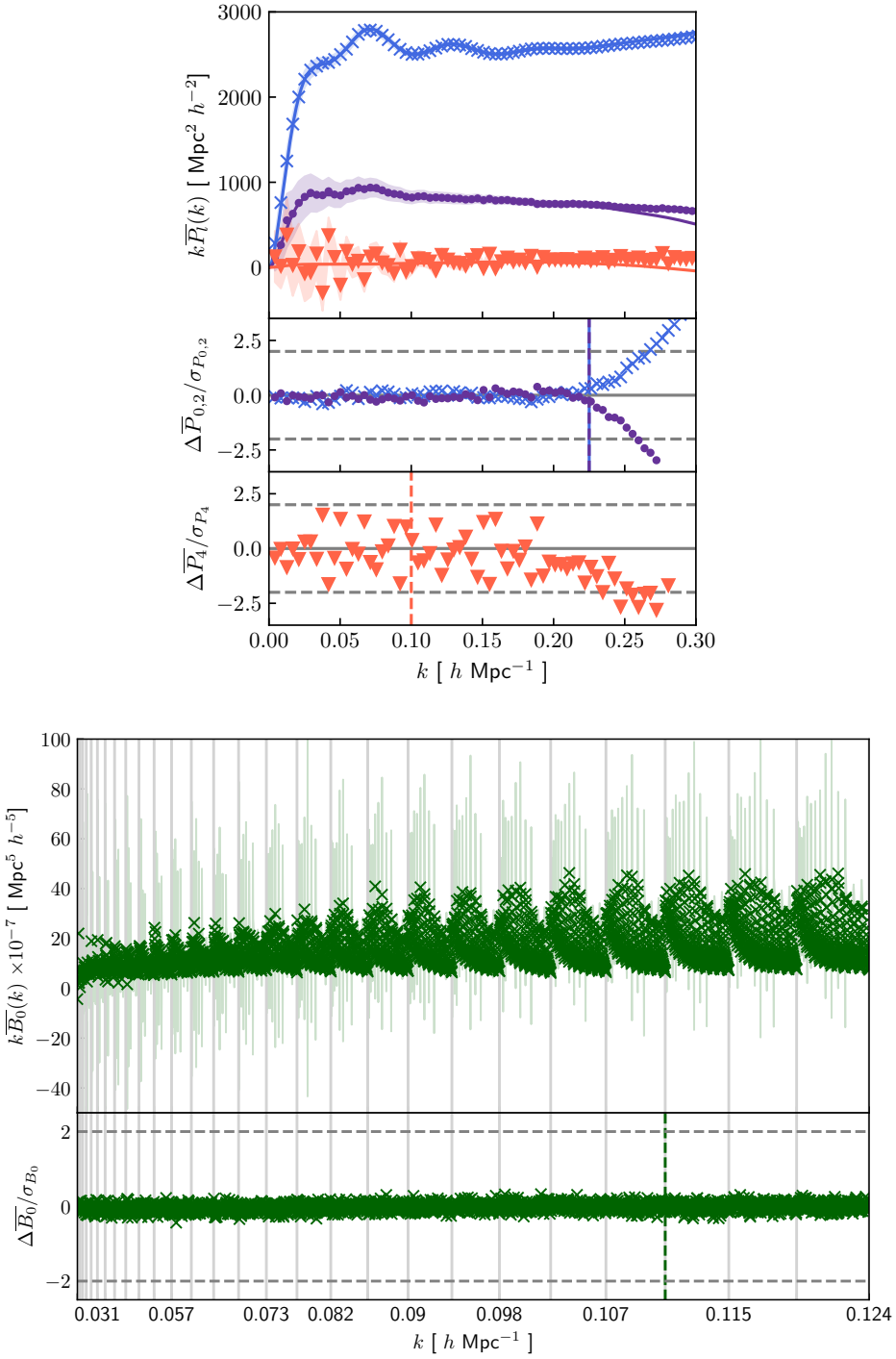

Figure 3.2 *Upper panel: measurements of the halo power spectrum multipoles – monopole ($l = 0$, blue crosses), quadrupole ($l = 2$, purple dots) and hexadecapole ($l = 4$, orange triangles). The solid curves correspond to the posterior-averaged theoretical predictions of the joint model with IDE for the following scale cuts (dashed vertical lines): $k^{l=0,2}_{\mathrm{max},P} = 0.225\ h\ \mathrm{Mpc}^{-1}$, $k^{l=4}_{\mathrm{max},P} = 0.1\ h\ \mathrm{Mpc}^{-1}$ and $k^{l=0}_{\mathrm{max},B} = 0.111\ h\ \mathrm{Mpc}^{-1}$. Lower panel: measurements of the halo bispectrum monopole (green crosses). Note that the Poisson shot noise contribution is not subtracted. Shaded areas denote the uncertainties on the mean of the observables. The lower panels show the ratio of residuals to errors on the mean of the observables.*

where $\bar{n}$ is the mean number density, V is the volume of the measured simulation and $k^* = 0.1\,h$ Mpc^{-1} is the reference scale. This allows us to roughly match our simulation data to that expected from future surveys, giving similar constraining power and signal-to-noise ratio. It also allows us to extend the range of validity of the theoretical model up to higher values of $k_{\rm max}$ with respect to the cuts we would have to adopt in the case of the non-rescaled covariance and the full volume of the simulations.

It is important to notice that shot noise is not subtracted from our measurements (both the Minerva and the Pinocchio ones). This is particularly prominent in the power spectrum monopole, as can be seen at small scales in Fig. 3.2. In this figure we show the average of the measurements with the corresponding error bars from the rescaled covariance, the chain averaged model from the joint Bayesian analysis (described below) and their residuals. Notice that the very small scatter in the residuals of the monopole and quadrupole (middle-left panel) is an artifact of our inflated error bars, while for the hexadecapole (bottom-left panel) we have some residual scatter due to the fact that we evaluate the model on the effective modes rather than performing the full average binning.

3.3.3 Likelihood Evaluation

In a Bayesian framework [189, 191], the probability of a model given some data is proportional to the product between the probability of obtaining the data under the assumption that the model is correct and the probability of the model parameters to have the corresponding values. In other words, the posterior distribution is proportional to the likelihood function multiplied by the prior distribution (Eq. 2.1).

In our analysis we choose the priors on nuisance parameters to be non-informative: they are uniform and very broad. We consider as fiducial values for these parameters the best fit values obtained in previous studies [8, 9]. Tests were performed to verify that the prior choice does not influence the parameter inference process. However, the priors on the IDE parameters w and A are informative and depend on each other. The equation of state parameter w has a flat prior with size $[-2, -0.5]$. For $w < -2$ dark energy starts to dominate over matter at a later epoch than our redshift of interest $z = 1$, so that the growth rate converges quickly to 1 independent from ξ as in the matter-dominated epoch. As for the upper bound, we have observational evidence of the late time acceleration, which implies $w < -1/3$. The parameter A also has a flat prior with size $[-20, 20]$, but with the additional condition that A must have the same sign as $1 + w$. The upper limit for A is given under the consideration of the upper bound for w and the most extreme value of $\xi = 50$ b GeV^{-1} tested out in simulations [3], while the lower limit is chosen to have a symmetric prior around the fiducial value of $A = 0$. Later, when varying additional cosmological parameters, we expand the prior on A to $[-500, 500]$ b GeV^{-1}. The additional condition on the sign is explained by the fact that

the parameter $\xi = A/(1+w)$ has to be non-negative, since it represents the ratio of two positive quantities: the cross section of dark sector interactions and the mass of dark energy particles (see discussion at the end of Section 3.1).

Given $N_{\rm R} = 298$ independent realisations, we evaluate the total likelihood as the product of individual likelihoods, under the assumption that each is well described by a multivariate Gaussian. As already mentioned, instead of fitting the mean of all realisations with the total volume covariance, we fit each individual simulation and compute

$$-2\ln\mathcal{L}_{\rm tot} = -2\sum_{\alpha}^{N_{\rm R}}\ln\mathcal{L}_{\alpha} = \sum_{\alpha=1}^{N_{\rm R}}\sum_{i,j=1}^{N_{\rm b}}\left(X_i^{\alpha}-X_i^{\rm theo}\right)C_{X,ij}^{-1}\left(X_j^{\alpha}-X_j^{\rm theo}\right)\,, \tag{3.27}$$

where X_i^{α} is the power spectrum or bispectrum multipole measurement from the α-realisation of the i-th Fourier bin from the total number of bins $N_{\rm b}$, $X_i^{\rm theo}$ is the theoretical prediction and C_{ij} is the rescaled covariance matrix from equation Eq. 3.25. We also test applying the correction to the likelihood function suggested in Ref. [267], which should take into account the finite number of mocks used in the construction of the covariance matrix:

$$-2\ln\mathcal{L}_{\alpha} = N_{\rm M}\ln\left(1+\frac{\chi_{\alpha}^2}{N_{\rm M}-1}\right), \tag{3.28}$$

where $N_{\rm M}$ is the number of mock catalogs. We found no impact on the posterior distributions, which confirms our expectation of a negligible effect given the large number of mocks catalogues used.

Our likelihood pipeline uses the `emcee` package [210] to sample the posterior distribution. We run the MCMC with 300 walkers, and assume them to have reached convergence after 30000 steps in the analysis which only includes the power spectrum multipoles, and after 15000 steps when the bispectrum multipole(s) is (are) included.

3.3.4 Model Evaluation

The evaluation of the theoretical model should in principle be performed on the same grid that is used for the measurements, and the model should be binned in the same way. This can be understood as the resolution of the following discrepancy: the theoretical prediction assumes an infinite universe with an infinite number of k-values, while in our case the measurements are performed in boxes with periodic boundary conditions, hence over a restricted number of k-bins. In general, there are four approaches to resolve this:

1. Full binning: compute an exact average of the theoretical predictions for the observables over each bin in Fourier space. In other words, calculate the theoretical model at each $q_i \in k_i$, with k_i being a Fourier bin and q_i denoting all discrete wavenumbers in a bin of size Δk_i, and then find a mean value. In our work the bin size equals the fundamental frequency $\Delta k = 2\pi/L$. Advantage: this is the most

consistent way; disadvantage: it is computationally demanding especially when re-computing the model at each step of the likelihood evaluation.

2. Effective binning: evaluate the theoretical predictions only at one "effective" wave-number, which is computed as the average over each bin centered at k for the power spectrum multipoles, while for the bispectrum the "effective" triplet is computed in a similar but hierarchical way (see equation B.2 in Ref. [9]). Advantage: less computationally expensive; disadvantage: it might introduce systematic errors comparable to the statistical uncertainties for the full volume of our data set [7].

3. Expansion approach [8]: this is an extension of the effective approach which includes a Taylor expansion of the theoretical model around the effective wave-number up to second order. Advantage: high accuracy, especially for the hexadecapole of the power spectrum; disadvantage: it can be computationally demanding if a large number of terms is involved.

4. Integration approach: similar to the averaging approach, but the integral is computed instead of building an average as a sum over the multipoles, divided by the number of all discrete vectors in a bin. This approach is popular in the literature [151, 268] but similarly to the effective binning it can introduce non-negligible systematic errors, especially for folded triangles. However, this issue can be bypassed by introducing "discreetness weights" as corrections [151].

In our study we choose the effective binning for power spectrum and bispectrum multipoles. Our tests show that this type of binning does not have an impact on the inferred parameters due to the enhanced size of our uncertainties after rescaling the covariance, while being the most computationally efficient.

We also note that in the bispectrum case we include all triangular configurations with $k_1 \geq k_2 \geq k_3$ in our analysis, and do not separate them into squeezed/equilateral/isosceles configurations as is common in the literature. Previous studies (e.g., Refs. [7, 268, 269]) show that the signal-to-noise ratio and the accuracy of a model increase for high $k_{\rm max}$ if nearly equilateral triangle bins are excluded, while still including elongated triangle configurations. Whether or not this selection improves our constraints of dark energy models when adopting realistic error bars is a subject of our future studies. However, we expect the effect to be minimal.

3.3.5 Model Selection

Our goal is to determine the appropriate scale cuts and forecast the constraining power of future surveys for the IDE parameters, w and A. It is crucial to determine the largest range of scales which can be used to extract information from the data in an unbiased

manner and tighten the cosmological constraints. This can be also achieved by removing or alleviating degeneracies between the parameters of the theoretical model. For instance, bias relations (i.e., the relations between bias parameters based on their connection due to the underlying physics of gravitational collapse) are able to reduce the parameter space without introducing bias in the estimated parameters. In order to evaluate whether a certain scale cut or a reduction of degeneracies in parameter space provide a better description of the observables we need a way to quantitatively compare the posterior distributions from our Markov chains. Since the χ^2-statistic is not valid anymore as a measurement of the goodness-of-fit, due to the rescaling of the covariance matrix (see discussion in Subsection 3.3.2), we make use of two performance metrics to select the best scale cut and/or reduced model (see a similar approach in Refs. [249, 270]):

1. the Figure of Bias (FoB) quantifies the relative separation of the measured parameters from their fiducial values in terms of the variance of the posterior distribution. We calculate the 68% - 95% percentile thresholds for the FoB by assuming the posterior distribution of the parameters of interest to be Gaussian. Hence, for one parameter the 68% threshold equals 1, while for two parameters the integration of two-dimensional Gaussian over an ellipse results in a FoB of 1.52. It is defined as

$$\mathrm{FoB} = \sqrt{(\theta_{\mathrm{fid}} - \bar{\theta}) S^{-1} (\theta_{\mathrm{fid}} - \bar{\theta})}\,, \tag{3.29}$$

   where $\bar{\theta}$ and θ_{fid} are vectors labeling, respectively, the posterior averages and fiducial values of the parameters we want to measure, and $S = \mathrm{cov}(\theta)$ is the covariance matrix of the parameters calculated from the chains. In our case, $\theta = [w, A]$ and $\theta_{\mathrm{fid}} = [-1, 0]$;

2. the Figure of Merit (FoM) shows the merit of the considered model with respect to the parameters varied in the fit. It is the inverse of the volume of the 68% contours of the parameters, effectively giving a global measure of the inverse size of the uncertainties obtained on the parameters [271]. This is given by

$$\mathrm{FoM} = \frac{1}{\sqrt{\det(S)}}\,. \tag{3.30}$$

3.4 Results

3.4.1 Joint Base Model

In total our base model contains 13 parameters: $\{w,\ A,\ b_1,\ b_2,\ b_{\mathcal{G}_2},\ b_{\Gamma_3},\ \tilde{c}_0,\ \tilde{c}_2,\ \tilde{c}_4,\ \alpha_P,\ \epsilon_{k^2},\ c_{\nabla^4\delta},\ \alpha_B\ \}$. Firstly, we aim to find the highest k_{max} at which the model parameters are not biased while the constraints on the dark energy parameters are the most informative (i.e.,

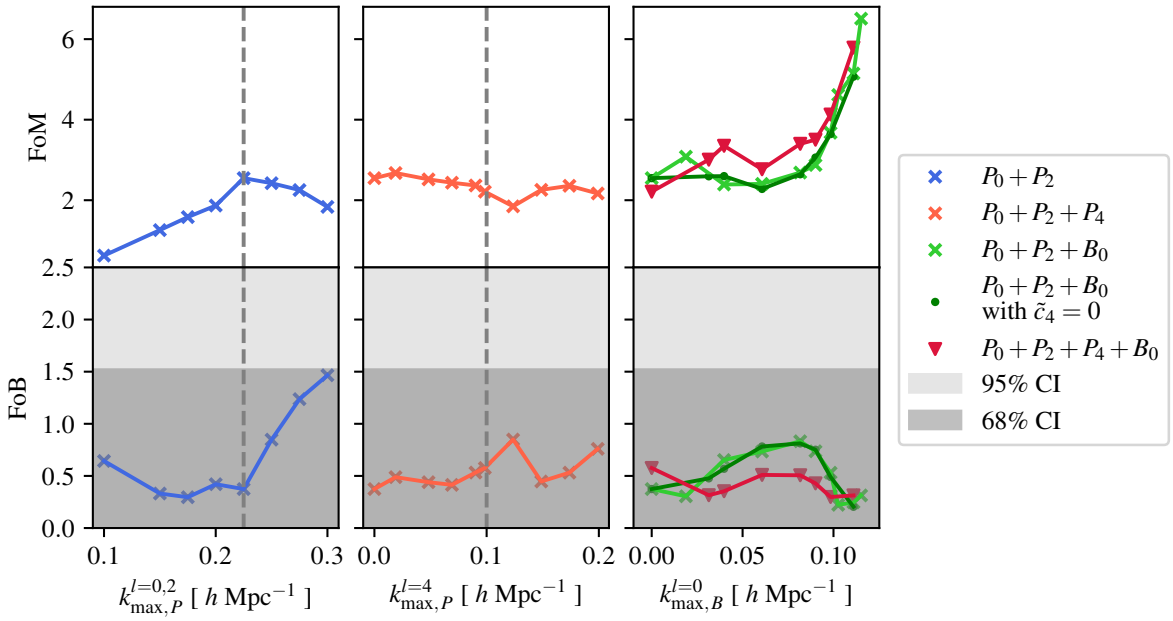

Figure 3.3 *Performance measures as a function of the maximum wave-number of the observable(s) for the following models. Left panel: the model includes only the monopole and quadrupole of the power spectrum (blue crosses). Middle panel: the hexadecapole (orange crosses) is added to the lower order power spectrum multipoles with their highest Fourier mode fixed to the best scale cut* $k^{l=0,2}_{\mathrm{max},P} = 0.225\ h\ \mathrm{Mpc}^{-1}$ *from the left panel. Right panel: the joint models — the power spectrum monopole and quadrupole with the bispectrum monopole (light-green crosses), the power spectrum monopole and quadrupole plus the bispectrum monopole and one counterterm parameter set to zero (dark-green dots), all power spectrum multipoles and the bispectrum monopole with the highest Fourier mode for the hexadecapole* $k^{l=4}_{\mathrm{max},P} = 0.1\ h\ \mathrm{Mpc}^{-1}$ *(dark-red triangles). The dashed grey lines correspond to the values of* k_{max} *used in the joint analyses: for the power spectrum monopole and quadrupole (left panel) and the hexadecapole (middle panel). The confidence intervals for FoB are calculated by direct integration of a two-dimensional Gaussian over an ellipse between* $\pm$ *FoB and equating the integral to the 68% and 95% percentile thresholds, which results in FoB equal to 1.52 and 2.49, respectively.*

FoM reaches its maximum). For this purpose we run our likelihood pipeline, calculate the performance metrics and check the posterior distributions for the nuisance parameters. The latter is done in order to avoid any deviation larger than two standard deviations from the fiducial values for b_1, b_2, $b_{\mathcal{G}_2}$, b_{Γ_3} α_P, ϵ_{k^2} and α_B as determined in the previous analyses of Refs. [7–9]. Note that the counterterms in real space and in redshift space are not the same.

We vary the value of k_{max} jointly for the power spectrum monopole and quadrupole, as is typically done in analyses of observational data [165]. The scale cut is varied in the range of $k^{l=0,2}_{\mathrm{max},P} \in [0.1, 0.3]\ h\ \mathrm{Mpc}^{-1}$ and is found to maximize the FoM while keeping the FoB within one standard deviation at $0.225\ h\ \mathrm{Mpc}^{-1}$. This can be seen in the left panel of Fig. 3.3, where blue crosses correspond to the joint analysis of the lower order

power spectrum multipoles. Keeping this value fixed, we then add the hexadecapole with $k^{l=4}_{\mathrm{max},\,P} \in [0, 0.2]$ h Mpc^{-1}. We expect our model to describe it less efficiently than the lower order multipoles, therefore the range of scales included for P_4 is smaller than for P_0 and P_2. Unsurprisingly the addition of the hexadecapole allows us to constrain $\tilde{c}_4$ and hence improve significantly the constraints on $\tilde{c}_2$, as well as on the other counterterms, though less significantly. However, we see in the middle panel of Fig. 3.3 no improvement in the constraints of the IDE parameters, the hexadecapole only slightly decreases the FoM and increases the FoB. This finding is in agreement with the conclusions of Ref. [272].

Next we include the bispectrum monopole, B_0. This is shown in the right panel of Fig. 3.3. We perform the analysis by adding it to $P_0 + P_2$, since the power spectrum hexadecapole does not contribute to the improvement of the constraints in the IDE parameters. The results are denoted by the light green crosses connected by a solid line. We observe an increase in the FoB and no improvement in the FoM for scales up to $k^{l=0}_{\mathrm{max},\,B} = 0.08$ h Mpc^{-1} for $P_0 + P_2 + B_0$. However, for $k^{l=0}_{\mathrm{max},\,B} > 0.08$ h Mpc^{-1} we notice a steep growth in the FoM as we add more k-bins. Clearly, inclusion of the small-scale information contained in the higher k-bins provides better constraining power, especially since the number of triangles increases significantly with each bin. The results do not show a bias in any of the parameters of the model, at least up to the 27-th k-bin (corresponding to $k^{l=0}_{\mathrm{max},\,B} = 1.12$ h Mpc^{-1}) from the total 29 bins of our measurements.

Additionally, we perform a joint analysis with the hexadecapole of the power spectrum included up to 0.1 h Mpc^{-1}, which is rather conservative and common in the literature. This model with all power spectrum multipoles and B_0 shows a mild but continuous improvement of the FoM in comparison to the model with only lower order power spectrum multipoles (see the dark red triangles in the right panel). Noticeably, adding the power spectrum hexadecapole in the joint analysis with the bispectrum monopole always results in a smaller FoB (and thus bias) of the IDE parameters. We check whether the same effect could be achieved by setting the otherwise unconstrained $\tilde{c}_4$ to zero in the model with the monopole and quadrupole only. As expected, the constraints of the $P_0 + P_2 + B_0$ model are not sensitive to this change. This is shown by the dark-green dots in the right panel, which overlap with the light-green crosses of the base model with $\tilde{c}_4 \neq 0$. We therefore conclude that the inclusion of the hexadecapole of the power spectrum, in combination with the bispectrum monopole, can help (especially at lower scale cuts) by breaking degeneracies between the counterterms and bias parameters.

The full posterior plot is shown in Fig. A.1 of Section A.1. Additionally, we present in Fig. 3.4 the triangle plot for the marginalized posterior distribution of the IDE parameters. The characteristic "butterfly" pattern, in which the posterior distribution is present only in two quadrants – upper-right and lower-left, is the consequence of the priors on the IDE parameters with the condition $A/(1 + w) \geq 0$, as described in Subsection 3.3.3. The $w - A$ contour shows a strong degeneracy: as argued in Section 3.1, a very negative value

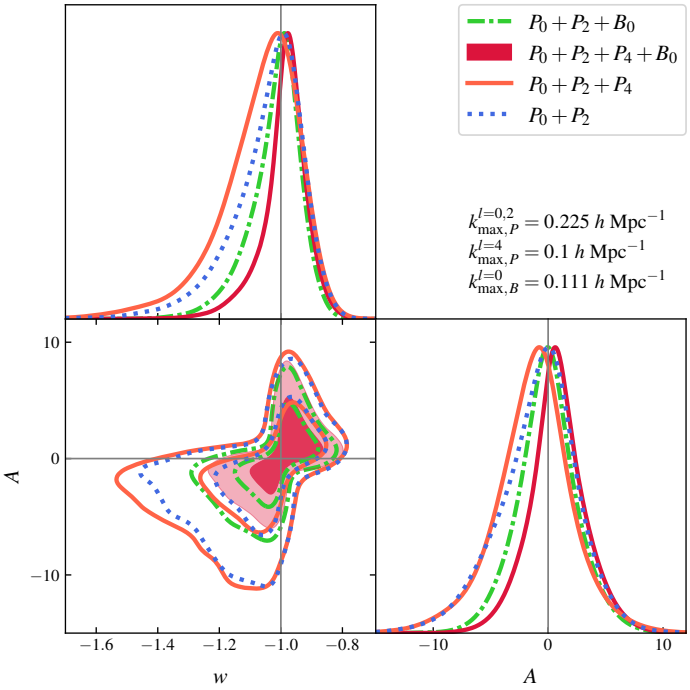

Figure 3.4 *Marginalized posterior distributions for the IDE parameters in the base model and with the scale cuts as specified on the plot. The power spectrum monopole and quadrupole analysis is denoted by the dotted blue line, constraints from all power spectrum multipoles are given by the solid orange line, the joint analysis of the power spectrum monopole plus quadrupole and bispectrum monopole is presented by the dotted-dashed light-green line, and the full joint analysis is shown with the dark-red line. Clearly, inclusion of the bispectrum monopole improves constraining power by* $\sim 30\%$*. The thin grey lines correspond to the fiducial values from the* ΛCDM *cosmology. Note that parameter* A *is given in the units of* $b\ GeV^{-1}$*. The fact that the contour shows non-vanishing values for the forbidden regions with* $A/(1+w) < 0$ *is an artifact of the smoothing used for plotting.*

of w leads to a later start of the dark energy dominated epoch, hence to a longer matter domination which is associated with increased growth of structures. A negative value of A leads to extra drag in Eq. 3.2, and thus to an enhancement of the growth of structures in the linear regime (the opposite is true for the nonlinear regime, as discussed in Section 3.1). On large scales the drag term acts in the same direction as the gravitational acceleration, since the velocity field is always aligned with the spatial gradient of the gravitational potential in the linear regime. The opposite happens for $w > -1$ and $A > 0$. This is in line with what can already be seen in Fig. 3.1 and its diagonal (from upper left to lower right) pattern in the growth rate f, and is particularly prominent in the upper right corner (for positive values of A and $(1+w)$). There we observe the same level of suppression for either a larger w value with A fixed, or for a larger A value with w fixed. It is therefore apparent how the two effects are strongly degenerate, which results in larger uncertainties on them, especially in biased cases. Such a conclusion is in agreement with the findings of Ref. [272].

In addition to the base model with 13 parameters, we run the joint analysis adopting some assumptions that are common in the literature: $b_{\Gamma_3} = 0$ and/or $\epsilon_{k^2} = 0$. Assuming that noise is scale-independent (as opposed to leaving the ϵ_{k^2} parameter free), results in no improvement and no bias in the constraints. This is a consequence of the rescaled error bars, since we know from the real space analysis with the full volume of the simulations by Ref. [8] that the scale-dependent term in shot noise is relevant at larger Fourier modes due to accounting for additional corrections beyond the assumed one-loop model. The assumption of $b_{\Gamma_3} = 0$ does not yield improved constraints, but it biases the noise parameters α_P, ϵ_{k^2} and α_B by more than 2σ with respect to the fiducial values. This is in line with the joint analysis performed on the same data set in real space, which measures $b_{\Gamma_3} = 0$ to be inconsistent with zero at more than 2σ [8]. The assumption of both conditions results in bias in the noise parameters and $b_{\mathcal{G}_2}$ at more than 2σ level, while α_B gets biased at more than 3σ level. From this we conclude that, when including the bispectrum monopole, b_{Γ_3} should not be set to zero.

3.4.2 Bias Relations

Although the strong degeneracy between $b_{\mathcal{G}_2}$ and b_{Γ_3} is broken by the inclusion of the bispectrum monopole in the analysis, we are still interested in the impact of bias relations for two reasons: firstly, to reduce the dimensionality of the parameter space; secondly, we know that both A and w are correlated with b_1, hence a tighter constraint on the latter will lead to tighter constraints on the IDE parameters.

We investigate the full joint analysis of $P_0+P_2+P_4+B_0$ for the following bias relations:

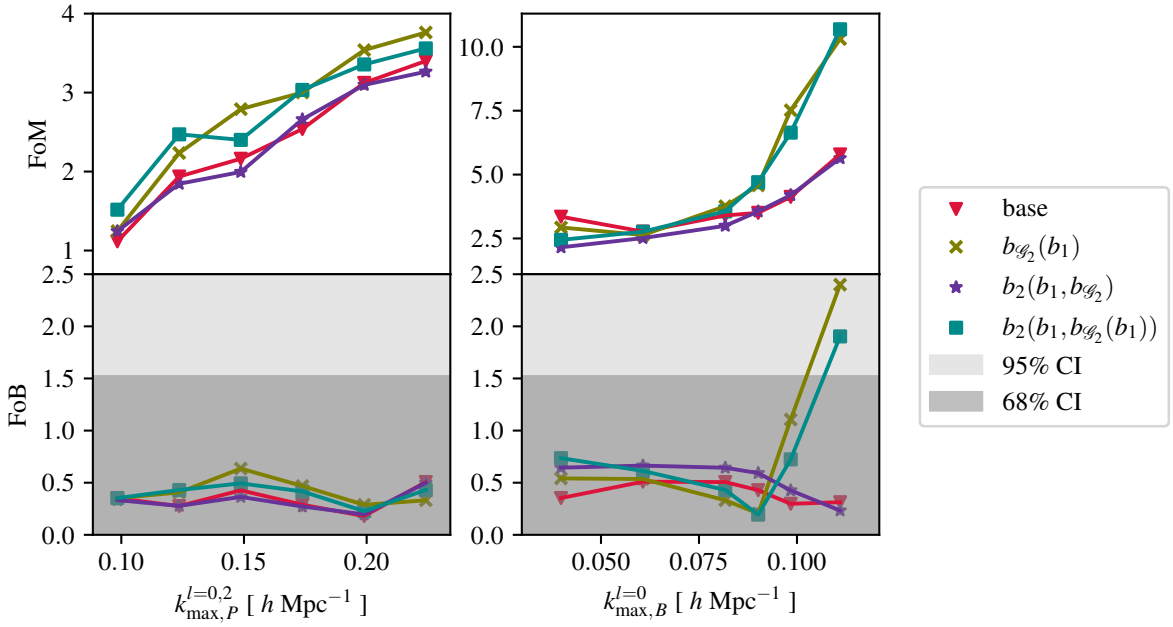

Figure 3.5 *Implementation of the bias relations into the joint analysis of all power spectrum multipoles with the bispectrum monopole. Left panel: performance metrics as a function of the maximum wave-number of the power spectrum monopole and quadrupole with the highest Fourier mode of the bispectrum monopole set to the moderate value of* $k^{l=0}_{\mathrm{max},B} = 0.08\ h\ \mathrm{Mpc}^{-1}$. *Right panel: performance metrics as a function of the maximum wave-number of the bispectrum monopole with the highest Fourier modes of the power spectrum multipoles set to* $k^{l=0,2}_{\mathrm{max},P} = 0.225\ h\ \mathrm{Mpc}^{-1}$ *and* $k^{l=4}_{\mathrm{max},P} = 0.1\ h\ \mathrm{Mpc}^{-1}$. *The dark-red triangles correspond to the base model with 13 parameters, the olive crosses denote the tidal bias relation, the purple stars represent the* b_2*-relation, the dark-cyan squares denote the combined relation of* b_2 *and* $b_{\mathcal{G}_2}$. *Note that the application of the combined or the tidal-bias relation leads to stronger constraining powers on the IDE parameters. This is especially prominent in the right panel for* $k^{l=0}_{\mathrm{max},B} \geq 0.09\ h\ \mathrm{Mpc}^{-1}$. *The confidence intervals for FoB are calculated as in Fig. 3.3.*

1. the fit from the separate universe simulations presented in Ref. [273][2] :

$$b_2(b_1, b_{\mathcal{G}_2}) = 0.412 - 2.143b_1 + 0.929b_1^2 + 0.008b_1^3 + \frac{4}{3}b_{\mathcal{G}_2}\,; \tag{3.31}$$

2. the fit from the excursion set approach of Ref. [249]:

$$b_{\mathcal{G}_2}(b_1) = 0.524 - 0.547b_1 + 0.046b_1^2\,; \tag{3.32}$$

3. the combination of both relations: $b_2(b_1, b_{\mathcal{G}_2}(b_1))$.

These relations have been shown to improve the fits of the power spectrum and bispectrum in Refs. [7–9]. Results for the individual relations as well as for the combined one are shown in Fig. 3.5 in terms of the FoM and FoB metrics. We notice that the $b_2(b_1, b_{\mathcal{G}_2})$ relation, denoted by purple stars, does not impact our constraints both when varying the maximum wave-number for the power spectrum (left panel) and for the bispectrum (right panel). This can be explained by a combination of two factors. Firstly, the fact that in our base model the b_2-relation always stays consistent with the fiducial value of b_2, that measured from the real space analysis of Refs. [7–9], which implies that we are not introducing any new information with the bias relation. Then, while a different behaviour has been seen in the analysis of Ref. [8] in Fig. 8 with very small error bars, the fact that ours are "realistic" (larger) for Stage-IV surveys means that we cannot detect this effect. On the other hand, the tidal bias relation (olive crosses) and its combination with the b_2-relation (dark-cyan squares) lead to a reduction in the constraints on w, A, b_1 and b_2. This improvement is particularly prominent in the right panel, where the number of modes in the bispectrum monopole is varied while the scale-range of power spectrum multipoles is fixed. At $k^{l=0}_{\mathrm{max},B} = 0.1\ h\ \mathrm{Mpc}^{-1}$ we see the $b_{\mathcal{G}_2(b_1)}$ has a higher value of FoM, which equals $\simeq 7.5$ and is larger than FoM$\simeq 4$ of the base model with the same largest Fourier mode. However, for $k^{l=0}_{\mathrm{max},B} > 0.1\ h\ \mathrm{Mpc}^{-1}$ cases (ii) and (iii) cause a continuous shift of the IDE parameters to the positive values of A and $(1+w)$. Nonetheless, even for $k^{l=0}_{\mathrm{max},B} = 0.111\ h\ \mathrm{Mpc}^{-1}$ all nuisance and IDE parameters stay within 2 standard deviations of their fiducial values (see the full posterior distribution in Fig. A.2), FoM reaches $\simeq 11$ for both relations. From the lower right panel we see that the combined bias relation results in the less biased dark energy parameters, in contrast to the tidal-relation only.

We note that the bias relations applied here are derived in the context of the ΛCDM cosmology. From the simulations performed in Ref. [3], we know that at the redshift of our interest deviations of the halo mass function from the standard cosmology are negligible. Moreover, the measurements in our analysis do not include modifications in

[2]The additional term $\frac{4}{3}b_{\mathcal{G}_2}$ is due to the difference in the definition of the tidal-bias operator in the reference and our notation.

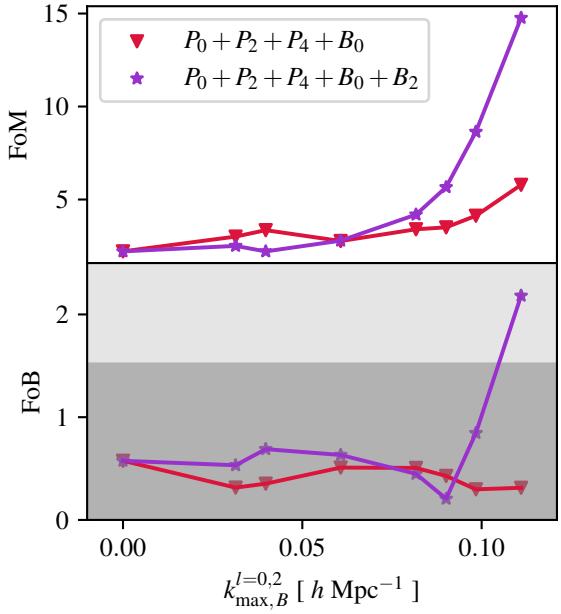

Figure 3.6 *Joint analysis of all power spectrum multipoles with the bispectrum monopole (dark-red triangles) and quadrupole (purple stars). The performance metrics, FoM and FoB, are presented as a function of the maximum wave-number on both multipoles of the bispectrum. Evidently, inclusion of the bispectrum quadrupole leads to tighter constraints on the IDE parameters for* $k^{l=0,2}_{\mathrm{max},B} \geq 0.09\ h\ \mathrm{Mpc}^{-1}$. *The confidence intervals for the FoB are calculated as in Fig. 3.3.*

the gravitational interaction. Therefore, the application of the bias relations is justified. Nevertheless, we aim to study the impact of the interactions between dark matter and dark matter on the bias relations in our future work.

3.4.3 Bispectrum Quadrupole

Recent progress in measuring the bispectrum multipoles from simulations [9] showed that, while the monopole constrains mostly the bias parameters b_1, b_2 and $b_{\mathcal{G}_2}$, the quadrupole can break the $b_1 - f$ degeneracy and can constrain the growth factor even in the case of a bispectrum only analysis. These constraints on the growth rate from the bispectrum multipoles are weaker than the ones that can be obtained from the power spectrum multipoles. The argument for the inclusion of higher order multipoles of the bispectrum is also discussed in Refs. [274, 275].

However, it raises the question: if including the bispectrum quadrupole improves the constraints on the growth rate, does it also do so for the IDE parameters, w and A? In particular, it is interesting to investigate if this holds also in the case of Stage-IV-like error bars, such as the ones we employ here. We run our likelihood pipeline for the base model and find that indeed, for $k^{l=0,2}_{\mathrm{max},B} > 0.09\ h\ \mathrm{Mpc}^{-1}$, the addition of the quadrupole improves

the constraints on the dark energy parameters. Our results are shown in Fig. 3.6, where dark-red triangles denote the power spectrum multipoles plus the bispectrum monopole, while the addition of B_2 is denoted by purple stars. We note that the FoB and FoM as functions of $k_{\rm max}$ resemble the trend obtained in the previous section with the bias relations, with the exception that in the present case the slope of the FoM in the upper panel is steeper at large wave-numbers. For instance, for $k^{l=0,2}_{{\rm max},B} = 0.1\ h\ {\rm Mpc}^{-1}$, we get FoM $\simeq 9$, while with the tidal bias relation from the previous section and without the bispectrum quadrupole we obtained FoM $\simeq 7.5$. The full posterior distribution for the $k^{l=0,2}_{{\rm max},B} = 0.111\ h\ {\rm Mpc}^{-1}$ can be seen in Fig. A.3. The increase in the FoM is the result of an improvement in the constraints on the IDE parameters and the linear bias. Moreover, because of the degeneracy between the linear bias and the other bias parameters, a tighter constraint on the former leads to the latter being more constrained too. This effect is more significant than in the case of the bias relations, and avoids resorting to such relations, which might not be valid in extended cosmological models. This is a hint that the bispectrum quadrupole might play a crucial role in constraining extended cosmological models with spectroscopic galaxy clustering data.

3.4.4 Forecast for wCDM

In addition to IDE, we repeat our analysis for the simplest extension to ΛCDM model in which $w = w_0$ is constant, but can assume values different from -1 (see Subsection 1.3.1). We assume the same flat prior of w as described in Subsection 3.3.3 without imposing any additional theoretical constraints (similar to Ref. [203]). However, $w < -1$ leads to gradient instabilities and should not be considered as a viable smooth quintessence theory in which the dark energy speed of sound equals the speed of light. See Ref. [276] for the analysis with the theoretical prior on w in smooth quintessence, as well as the case of $w < -1$ in clustering quintessence.

Based on what we have learned with the IDE model we perform the following analyses:

1. base model with $k^{l=0}_{{\rm max},B} = 0.111\ h\ {\rm Mpc}^{-1}$;
2. combined bias relations with $k^{l=0}_{{\rm max},B} = 0.095\ h\ {\rm Mpc}^{-1}$;
3. bispectrum monopole and quadrupole with $k^{l=0,2}_{{\rm max},B} = 0.09\ h\ {\rm Mpc}^{-1}$.

We obtain the following constraints on the dark energy equation of state parameter for the three runs respectively: $w = -0.99 \pm 0.10,\ -0.98 \pm 0.10,\ -0.99 \pm 0.09$. The full posterior is shown in Fig. A.4. All three cases result in similar level of uncertainty on the inferred parameters, except on the shot noise parameter of the bispectrum for which both the bias relations and the inclusion of B_2 yield tighter constraints. However, the improvement with respect to the analysis with the power spectrum only is apparent,

roughly 38%, demonstrating once again that the inclusion of the bispectrum does increase the cosmological information that can be extracted from the data.

With the same setup of $k^{l=0,2}_{\mathrm{max},P} = 0.225\ h\ \mathrm{Mpc}^{-1}$, $k^{l=4}_{\mathrm{max},P} = 0.1\ h\ \mathrm{Mpc}^{-1}$ and $k^{l=0}_{\mathrm{max},B} = 0.111\ h\ \mathrm{Mpc}^{-1}$ we obtain larger uncertainties on w for the wCDM cosmology than in the IDE case. This may seem counter-intuitive, since wCDM contains one fewer parameter. However, when we compare posterior distributions against each other, the contours in wCDM are always tighter or equal to the IDE case and the difference in σ_w can be explained by the non-Gaussian form of the posterior distribution and the corresponding projection effects in the IDE case (for more about projection effects of marginalisation see Ref. [277]).

3.4.5 Degeneracies with Cosmological Parameters

We discussed above the degeneracies between nuisance and IDE parameters in the case of fixed cosmology. Now we aim to understand the interplay between w, A and cosmological parameters. We first consider the scalar amplitude A_s with a flat prior $1 \leq \ln 10^{10} A_\mathrm{s} \leq 4$. Since w and A enter the model through the linear growth factor, they are degenerate with any parameter controlling the amplitude of the power spectrum (as argued above for the degeneracy with the linear bias b_1). Hence, there is a strong degeneracy between IDE parameters and the primordial amplitude A_s, which limits the measurement of those parameters individually in an analysis where the full cosmological parameter space is explored.

However, in such a realistic cosmological analysis, one should also take into account the Alcock-Paczynski effect (AP) [171], arising from the assumption of a particular cosmology when converting redshifts to distances in the measured data. This results in a re-scaling of the k-modes and angles, which is sensitive to w as well as to Ω_m and h (see Eq. A.11 in Ref. [258] and the *Observations* discussion in Section 1.4). Including that in the analysis, we find that, even when varying only the nuisance parameters in addition to the dark energy parameters, taking into account the AP-effect tightens the constraint on w by nearly 5 times (see Fig. A.5 in Appendix)[3].

We then perform the analysis with the inclusion of the AP-effect and varying A_s with the power spectrum multipoles only, and find a strong positive correlation between A_s and A and a negative one with b_1 (analogous to the findings of Ref. [99], e.g., Figure 7 and 18). This can be understood as follows: a very negative value of A corresponds to more

[3]The analysis in this section is performed with the `pocoMC` sampler [211, 221] with the standard convergence criterion, 10^3 live points and 3×10^4 additional sampling points. We switch to this MCMC sampler from `emcee` after reproducing results from the previous sections with the new sampler. This change is justified by the fact that this sampler is more computationally efficient and better suited to explore a parameter space with strong degeneracies. Moreover, we compute the linear power spectrum with the `bacco` linear emulator [31] instead of calling a Boltzmann solver at each step of the chain, which significantly speeds up the analysis.

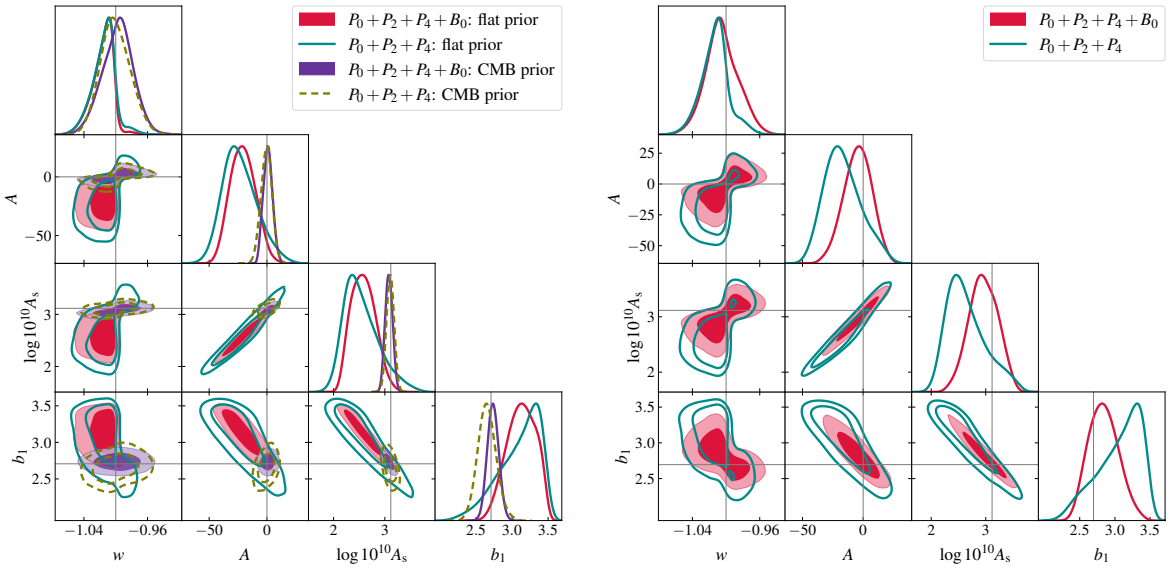

Figure 3.7 *Left panel: analysis with the simulated data. Dashed olive lines and purple contours show results with the Gaussian prior on A_s around its fiducial value with 3 standard deviations from the CMB analysis. Right panel: analysis with the synthetic data and flat priors. Grey lines denote the fiducial values. In both cases the AP-effect is mimicked by a tight Gaussian prior on w around its fiducial value and with $\sigma_w = 0.02$. Red contours represent the joint analysis, dark cyan lines represent the analysis with power spectrum multipoles only. Scale cuts are the same as in Fig. 3.4.*

power at linear scales, which requires a smaller value of the magnitude A_s and larger value of the linear bias b_1 to compensate. As a result, we find that the AP-effect confines the equation-of-state parameter to $w = -1.03 \pm 0.02$. We use this as a tight Gaussian prior on w in the following analysis. Note that a significant shift from the fiducial values is present only in w, A, A_s and b_1, while the rest of the nuisance parameters remain unbiased and are not dominated by priors.

Next we perform an analysis with a tight Gaussian prior on w around its fiducial value in order to mimic the AP-effect and study whether the addition of the bispectrum monopole can break the strong degeneracy between A and A_s. The reason for avoiding a direct implementation of the AP-effect for the bispectrum is the high computational demand when taking into account all possible triangle configurations, a solution for which we leave for future work. As can be seen in the left panel of Fig. 3.7, the addition of the bispectrum (red contours) to the power spectrum multipoles (dark cyan lines) makes the marginalised posterior distributions more Gaussian, reduces constraints on A and A_s by $25 - 27\%$, while bringing the mean and best-fit values closer to the fiducial values of these parameters. Constraints on the linear bias b_1 obtained with the power spectrum multipoles only are very broad, and prefer values close to the upper limit of its prior $[0.9, 3.5]$. Should this be increased, the degeneracy would drive b_1 to higher values, A_s to even lower values, and make A more negative. Analogous to findings from the previous

sections, the bispectrum improves constraints on all bias parameters, including b_1, and shifts its best-fit value closer to the fiducial one. As a consequence, it drives the peaks of the A and A_s distributions to their true values too. A similar effect is seen for fixed A_s in Fig. 3.4: with the power spectrum multipoles only, there is a clear asymmetry in the 2-D "butterfly" towards negative values of w and A, while adding the bispectrum monopole visibly improves the symmetry of the contour.

Although we recover the true values within 2 standard deviations, the degeneracy between A and A_s still leads to a preference of lower values for A_s and A. This degeneracy is decreased if one applies a Gaussian prior on A_s, centered on its fiducial value and with a size of 3σ from the WMAP+BOSS DR9 results [264]. We can impose a CMB-based prior because the IDE model introduces deviations to ΛCDM only in the late Universe, thus results obtained from CMB data assuming ΛCDM would still be valid. In this case, w fills in the prior without preferring values smaller than -1, A_s is fully defined by its prior as well, and the 16% improvement in constraints on A after adding the bispectrum monopole (purple contours) to the power spectrum multipoles (olive dashed lines) is explained by the 38% shrinking in the constraints on the linear bias b_1.

The fact that a strong degeneracy leads to a bias in the parameters hints at the existence of projection effects of the marginalisation. In order to verify this, we create synthetic data for the same fiducial cosmology, using the best-fit values obtained from the ΛCDM fits for the nuisance parameters. As before, we mimic the AP-effect by setting a tight prior on w around its true value. As can be seen from the results in the right panel of Fig. 3.7, a flat prior on the primordial scalar amplitude results in biases towards negative and smaller values in A and A_s respectively, which are similar to the biases appearing in the analysis of the simulated data on the left panel of the same figure. Also analogously to the results with data from the simulations, in the analysis with the power spectrum multipoles only, the linear bias b_1 tends to the upper limit of its prior range. However, the addition of the bispectrum monopole improves constraints of galaxy bias parameters, reduces the degeneracy between amplitude-controlling parameters, and decreases the shifts due to marginalisation in A and A_s. Thus it shows that the bispectrum is a promising tool for improving this type of projection effects.

It is important to note that, in spite of projection effects explaining some of the biases, the joint analysis on simulation data still favours a more negative value for A and w than the same analysis on synthetic data. We know that these biases are not caused by the invalidity of the model at the chosen scale cuts when the parameter space is opened to the additional cosmological parameters. Tests in ΛCDM and more importantly wCDM scenarios when A_s is varied do not demonstrate any significant deviations from the fiducial values. The actual reason for this is the following. As can been seen from the orange lines in Fig. 3.4, the model already slightly prefers the negative values of A and $w < -1$. This implies that the presence of a strong degeneracy on top of even slight theoretical errors

(discrepancies between a theory and data) amplifies the effects from the latter. Similar conclusions can be found in the analysis for DGP gravity in Ref. [278].

We now discuss the degeneracies appearing when varying additional cosmological parameters. Two other cosmological parameters enter the Euler equation (Eq. 3.2) and the AP-effect through the Hubble function: the fractional energy density of non-relativistic matter $\Omega_{\rm m}$ and the expansion rate h. Our tests with the power spectrum multipoles only, including the AP-effect (see Fig. A.6) agree with the results from Ref. [99], showing the degeneracy between these parameters and the IDE parameters is not as substantial as that with the scalar amplitude $A_{\rm s}$. Parameters w and h are strongly degenerate, since both of them affect the expansion history: smaller h or very negative w both lead to smaller value of the Hubble function; the same holds for w and $\Omega_{\rm m}$, though the degeneracy is less severe. We obtain an estimate of the expansion rate h biased towards higher values, which is a consequence of its degeneracy with w. For the same setup in the ΛCDM scenario this effect is not present. This degeneracy between w and h can be broken by combining data from different redshifts or from BAOs (e.g., as in Ref. [203]). BAO data also constrain $\Omega_{\rm m}h^2$, which breaks its degeneracy with the spectral index $n_{\rm s}$. We can achieve a similar effect by imposing a CMB prior on $n_{\rm s}$ (analogous to Refs. [46, 62]), essentially bringing both parameters closer to their fiducial values. Note that, in our case, degeneracies between $n_{\rm s}$ and other cosmological parameters are not as strong as in analyses of the BOSS data, since the largest scale we consider is $k_{\rm min} = 0.004\ h\ {\rm Mpc}^{-1}$, while for BOSS $k_{\rm min} = 0.01\ h\ {\rm Mpc}^{-1}$. In other words, due to the size of the simulation, we have more information from large-scale modes and can constrain the primordial slope better. We then impose a Planck prior on the scalar amplitude: separately as well as in combination with $n_{\rm s}$. The conclusion is that the unbiased cosmological parameters are reproduced only with the informative prior on the primordial parameter $A_{\rm s}$. Again, notice that the rest of nuisance parameters is only slightly affected by the choice of priors on $A_{\rm s}$ and $n_{\rm s}$: they remain unbiased and are not dominated by priors.

When varying all cosmological parameters, we expect the inclusion of the bispectrum monopole will tighten the constraints on $A_{\rm s}$, $n_{\rm s}$, A, $\Omega_{\rm m}h^2$, h, because a) all of them are degenerate with each other, and improvement on one of them shrinks the contours for the others, b) the bispectrum significantly improves constraints on b_1 and alleviates the w+A+$A_{\rm s}$+b_1 degeneracy coming from the amplitude of the power spectrum, c) in contrast to the previous analyses in the literature, we include information from smaller scales, since our model is still valid up to $k^{l=0}_{{\rm max},B} = 0.111\ h\ {\rm Mpc}^{-1}$, hence the improvement of constraints on cosmological parameters in the case of our joint analysis will be more prominent than in the previous studies (e.g., $\sim (5-15)\%$ improvement relative to the power spectrum analysis after the addition of the bispectrum monopole with $k^{l=0}_{{\rm max},B} = 0.08\ h\ {\rm Mpc}^{-1}$ in Ref. [151]). Additionally, we expect the bispectrum monopole to reduce the role of the choice of priors and decrease the effects of marginalisation by making the probability

distribution closer to a multivariate Gaussian. A proper investigation of these effects is the topic of our future work.

3.5 Conclusions

In this chapter we have performed a detailed analysis of the role of the bispectrum multipoles in constraining an interacting dark energy model. This is relevant for Stage-IV spectroscopic surveys, as a validation test and a comprehensive case study for the joint power spectrum and bispectrum analyses of extended cosmological models.

We modelled the power spectrum and bispectrum multipoles with the EFTofLSS at one-loop and tree-level, respectively. We computed the linear growth factor and the logarithmic growth rate by solving the growth equation for the IDE model. As input data (the fiducial data vector in our likelihood pipeline) we used a large set of simulations at a single redshift $z = 1$, complemented with a rescaled numerical covariance constructed from $10,000$ mock catalogues. Our fits used an effective volume that mimics the error budget of Stage-IV spectroscopic galaxy surveys, and we run our MCMC analyses with a Gaussian likelihood function.

Using this setup, we first added more observables in sequence and studied them in terms of their ability to constrain the IDE parameters w and A without introducing a bias in the dark energy and nuisance parameters of the model. For the latter, we adopted as fiducial values the best fit values from previous studies performed in the context of standard ΛCDM [7–9]. We found that the tree-level model for the bispectrum monopole is still valid up to $k \simeq 0.11\ h\ \mathrm{Mpc}^{-1}$, close to the largest value available in our measurements. In contrast to adding the hexadecapole to the lower-order multipoles of the power spectrum, the addition of the bispectrum monopole improved the constraints on the IDE parameters by $\sim 30\%$ for the equation of state parameter w, and $\sim 26\%$ for the coupling parameter A. We also found that the $P_0 + P_2 + P_4 + B_0$ combination yields better constraints and less bias in the inferred parameters than $P_0 + P_2 + B_0$.

In general, the large number of triangular configurations over which the bispectrum model has to be evaluated when including such nonlinear scales results in a rather computationally expensive analysis. Hence, we studied two approaches, which could allow us to get the same level of constraints but at smaller scales. The first approach aims at reducing the parameter space, which in our base case included 13 parameters, by means of bias relations. We tested the validity of two bias relations, and found that the tidal bias relation and its combination with the b_2 relation are the most suitable for this goal. In the second approach we added the bispectrum quadrupole to our Bayesian analysis. We found that either applying the bias relations or including the bispectrum quadrupole allows us to efficiently constrain the IDE parameter at more moderate values of k_{max} than in the base model $P_0 + P_2 + P_4 + B_0$. For instance, to achieve the same level of constraints with

FoM ~ 6 one can use either of the following: a) use only the bispectrum monopole in the base model, but include it up to high Fourier mode of $k^{l=0}_{\mathrm{max},B} = 0.111\ h\ \mathrm{Mpc}^{-1}$, b) apply the tidal bias relation in the scale range with the highest mode $k^{l=0}_{\mathrm{max},B} = 0.095\ h\ \mathrm{Mpc}^{-1}$, c) add the quadrupole measurements and evaluate the model up to $k^{l=0,2}_{\mathrm{max},B} = 0.09\ h\ \mathrm{Mpc}^{-1}$.

We then forecasted the constraining power of Stage-IV spectroscopic galaxy surveys on the IDE parameters and the dark energy equation of state parameter in wCDM for fixed cosmological parameters. At $z = 1$ we found $\sigma_w = 0.08$ and $\sigma_A = 2.51$ b GeV^{-1} for the IDE case, while for the wCDM case, we found $\sigma_w = 0.1$. The first values are in a good agreement with the results of Ref. [272] for the same redshift, where $\sigma_w = 0.06$ and $\sigma_A = 2$ b GeV^{-1} were found when only power spectrum multipoles were used in the MCMC analysis. However, in Ref. [272] the simulated data contained more than one order of magnitude less shot noise in comparison to our case, while the volume of the measurements was smaller with $V \sim 4$ Gpc^3 h^{-3}. Additionally, the covariance in the previous work was computed analytically up to the linear order, while the one used in this work is based on mocks, which is more realistic and contributes to larger uncertainties on the inferred parameters.

For comparison, we cite here the results of the full-shape analyses (FS) with the EFTofLSS from the BOSS survey of Refs. [99, 203]. We stress that the analysis of BOSS data takes advantage of two redshift bins and four different sky cuts (three cuts in Ref. [203]), with the addition of BAO measurements, while the total volume of 6.5 Gpc^3 h^{-3} and mean number density of 2.2×10^{-4} h^3 Mpc^{-3} are very comparable with our values. In Ref. [203], the authors mention that FS analysis with the power spectrum alone is not sufficient to constraint w, due to strong degeneracies. They measure $w = -1.101^{+0.14}_{-0.11}$, which is still a stronger limit than the one obtained from Planck2018 data with lensing [279] alone: $w = -1.57^{+0.16}_{-0.33}$. These values of w from the power spectrum analysis are in agreement with our forecast with fixed cosmological parameters without inclusion of the Alcock-Paczynski effect, when the bispectrum is not included (see Fig. A.4). They also agree with the recent findings of Ref. [99] with $w = -1.17^{+0.12}_{-0.11}$ for wCDM without a CMB prior in the FS+BAO analysis. For IDE the authors of Ref. [99] find it necessary to include the CMB prior on A_s and n_s (without BAOs), their analysis produces the following constraints: $w = -0.954^{+0.024}_{-0.046}$ and $A = 4.8^{+2.8}_{-3.8}$ b GeV^{-1} in the base model. In our setup for the analysis with power spectrum multipoles we find (see Fig. A.6) $w = -1.14 \pm 0.09$ and $A = -4.45 \pm 3.9$ b GeV^{-1}. The discrepancy in the error on w can be explained by the fact that the base model in Ref. [99] assumes informative priors on the nuisance parameters, when this assumption is alleviated and the priors are broader by 3 times (10 times) they find $w = -0.985^{+0.081}_{-0.038}$ ($w = -0.994^{+0.083}_{-0.046}$), which is closer to our uncertainties, despite them using BAO data in Table 8. In this work we assume broad flat priors on the nuisance parameters, hence our results are more in agreement with the BOSS analysis for uninformative priors on the nuisance parameters.

Without a CMB prior on the primordial parameters the model fails to accurately reproduce the true values used in the simulations in the case of the dark scattering model, while we do not observe similar behaviour in the case of the standard cosmological model or wCDM. The reason for that is a strong degeneracy between A_s and IDE parameters that drives the model prediction towards negative values of w and A, small values in the scalar amplitude A_s, and large values for the linear bias b_1. This hints to the presence of projection effects due to marginalisation of a strongly non-Gaussian posterior distribution. We demonstrate with synthetic data that such projection effect disappears when we include the bispectrum monopole to the analysis. Unfortunately, this is less prominent in the analysis with simulated data, since they already prefer more negative values of w, and hence of A. The fragile symmetry around $A = 0$ and $w = -1$ is restored if the amplitude A_s is fixed to the fiducial value with an informative CMB prior. However, even in this case the addition of the bispectrum improves the constraints on A. This suggests that a joint power spectrum and bispectrum analysis can lead to improved constraints also on the other cosmological parameters, even when adopting informative priors on the primordial parameters. This will be the next step in our ongoing investigation.

A number of interesting questions remain to be answered. The first natural step would be to perform this analysis with the data from the BOSS survey to improve the constraints from the power spectrum analysis of Ref. [99] with the bispectrum. Additionally, it would be interesting to study the time-dependent dark energy equation of state, for example, in the CPL parameterisation [85, 86], which would allow for different effects of the interaction. This study requires data at different redshift bins, in order to constrain w_0 and w_a. In the case of IDE, the time-dependent equation of state promises to have weaker impact on the nonlinear scales than the constant-w models [234]. Another potential direction of our study is the inclusion of one-loop effects in the bispectrum model, as was recently done for ΛCDM cosmology in Refs. [241, 280]. In the latter the authors show that the one-loop corrections for the bispectrum start to be significant already at $k^{l=0}_{\mathrm{max},B} > 0.1\,h\,\mathrm{Mpc}^{-1}$. This is also expected to extend the reach of the model and therefore its constraining power.

Chapter 4

Growth Index Parameterisation: BOSS DR-12 Analysis

This chapter is based on the following peer reviewed publication:

- C. Moretti, **M. Tsedrik**, P. Carrilho, A. Pourtsidou, 2023, *Modified gravity and massive neutrinos: constraints from the full shape analysis of BOSS galaxies and forecasts for Stage-IV surveys.* Published in JCAP: doi:10.1088/1475-7516/2023/12/025, arXiv:2306.09275.

Here, we constrain the growth index γ by performing a full-shape analysis of the power spectrum multipoles measured from the BOSS DR12 data. We adopt a theoretical model based on the Effective Field theory of the Large Scale Structure (EFTofLSS) and focus on two different cosmologies: γCDM and $\gamma\nu$CDM, where we also vary the total neutrino mass. We explore different choices for the priors on the primordial amplitude A_s and spectral index n_s, finding that informative priors are necessary to alleviate degeneracies between the parameters and avoid strong projection effects in the posterior distributions. Despite the model being purely phenomenological, a measurement of γ inconsistent with its ΛCDM prediction would provide a clear detection of deviations from the standard cosmological model.

Precise measurement of the growth index γ is among the key objectives of ongoing Stage-IV surveys [10, 80, 281]. In addition to testing the theory of gravity, a key science goal of Stage-IV galaxy surveys is a measurement of the neutrino mass. It is well known that massive neutrinos can suppress structure formation below a specific free streaming scale, thus leaving a distinct signature on cosmological observables (see Ref. [282] for a review, or our discussion in Subsection 1.3.2). However, current LSS data alone are not sufficiently accurate to constrain the neutrino mass, or even provide competitive upper bounds with respect to CMB measurements. This picture is expected to change with Stage-IV measurements of the LSS, that promise to achieve sufficient precision to allow

for a detection of the neutrino mass. With this in mind, we produce forecasts for a Stage-IV spectroscopic galaxy survey (DESI-like). We fit synthetic data-vectors for three different galaxy samples generated at three different redshift bins, both individually and jointly.

Contributions

The main analysis and drafting for this paper was led by Chiara Moretti, using her modelling code PBJ and including massive neutrinos. I co-led the main analysis, which consisted of coding an independent likelihood pipeline for comparison with Chiara's results, running all MCMC chains from the paper without massive neutrinos, testing different samplers and effects of analytical marginalisation, running profile likelihood analysis, producing and analysing BOSS-like and DESI-like synthetic data (noiseless and with noise). Pedro Carrilho and Alkistis Pourtsidou made significant contributions to discussions and the draft.

4.1 Theoretical Model

We model the nonlinear galaxy power spectrum in redshift space using the EFTofLSS [239, 283–285], which allows to model the effects of unknown small-scale physics on mildly nonlinear scales with the introduction of scale-dependent terms in the theoretical model. In particular, we follow a prescription analogous to the one of Ref. [150], but employ an independent implementation [7–9], whose redshift space modelling for the power spectrum has been validated on N-body simulations [272, 286]. The model features several ingredients, including loop corrections, EFTofLSS counterterms, a bias prescription and an infrared-resummation routine; we outline these below, but refer to Ref. [99] and Subsection 3.2.2 for a more detailed description.

4.1.1 Nonlinear Power Spectrum

The modelling we apply here is similar to the previous chapter. The bias expansion we adopt is based on a perturbative expansion of the galaxy density field δ_g [145, 245, 250, 287], which includes contributions from the underlying matter density field and large-scale tidal fields. Here we only consider terms up to third order in perturbations of δ:

$$\delta_g = b_1\delta + \frac{b_2}{2}\delta^2 + b_{\mathcal{G}_2}\mathcal{G}_2 + b_{\Gamma_3}\Gamma_3 + \epsilon\,, \tag{4.1}$$

where b_1 and b_2 are respectively the linear and quadratic local bias parameters, $\mathcal{G}_2$ and Γ_3 are non-local functions of the density field and ϵ is a stochastic contribution. The one

loop anisotropic galaxy power spectrum can then be written as:

$$P_{gg}(\boldsymbol{k}) = P_{\rm SPT}(\boldsymbol{k}) + P_{\rm ctr}(\boldsymbol{k}) + P_{\epsilon\epsilon}(\boldsymbol{k})\,, \tag{4.2}$$

with the one-loop power spectrum $P_{\rm SPT}$ from Eq. 3.7[1], the EFTofLSS counterterms contribution $P_{\rm SPT}$ from Eq. 3.16, and the stochastic power spectrum $P_{\epsilon\epsilon}$. Following Ref. [150], we re-define the k^2-counterterm parameters in order to have separate contributions to each multipole: $\tilde{c}_i \to c_i$ for $i \in \{0, 2, 4\}$. We model the noise contribution as:

$$P_{\epsilon\epsilon}(k, \mu) = N + e_0 k^2 + e_2 k^2 \mu^2\,, \tag{4.3}$$

where μ is the cosine of the angle between the wavevector $\boldsymbol{k}$ and the line of sight, N is a constant that includes deviations from pure Poisson shot noise, and we have two additional scale-dependent terms. We account for the nonlinear evolution of the BAO peak [235, 236, 289] by means of an infrared-resummation routine, applied by splitting the linear power spectrum in a smooth broadband component (computed using the fit of Ref. [37]) and a wiggle part. Full details of the approach we use can be found in Sec. 2.2.2 of Ref. [99] and in Subsection 3.2.2 with additional variation of $\ell_{\rm osc}$ as a function of cosmology given in Eq. 1.66. In total we have a set of 11 nuisance parameters *per redshift bin*:

$$\theta = \{b_1,\ b_2,\ b_{\mathcal{G}_2},\ b_{\Gamma_3},\ N,\ e_0,\ e_2,\ c_0,\ c_2,\ c_4,\ c_{\nabla^4\delta}\}\,. \tag{4.4}$$

In our baseline analysis we keep the total neutrino mass fixed to its fiducial value $M_\nu = 0.06$ eV. We model the scale-dependent suppression induced by massive neutrinos by computing the CDM+baryon linear power spectrum and using it as input for the theoretical model (instead of the total matter one, which also includes the neutrino contribution). Additionally, we consider a cosmology with free neutrino mass, and we modify the theoretical model as described in more detail in Subsection 4.1.3.

In order to include the impact of the fiducial cosmology assumed when converting redshifts to distances in the data, we correct wavenumbers and angles by applying Alcock-Paczynski distortions [171] (see the corresponding discussion in Section 1.4):

$$\bar{k}^2 = k^2 \left(\frac{H_0^{\rm fid}}{H_0}\right)^2 \left(\left(\frac{H}{H^{\rm fid}}\right)^2 \mu^2 + \left(\frac{D_A^{\rm fid}}{D_A}\right)^2 (1-\mu^2)\right)\,, \tag{4.5}$$

$$\bar{\mu}^2 = \mu^2 \left(\frac{H}{H^{\rm fid}}\right)^2 \left(\left(\frac{H}{H^{\rm fid}}\right)^2 \mu^2 + \left(\frac{D_A^{\rm fid}}{D_A}\right)^2 (1-\mu^2)\right)^{-1}\,, \tag{4.6}$$

[1]For all analyses performed here we consider a massive neutrino component, even when we do not vary the total neutrino mass as a free parameter. Motivated by Refs. [131, 288], we always use the Cold Dark Matter (CDM) + baryon as linear power spectrum in Eq. 4.2 and following equations.

as well as re-scaling the power spectrum by a factor

$$A_{\rm AP} = \left(\frac{H_0^{\rm fid}}{H_0}\right)^3 \frac{H}{H^{\rm fid}} \left(\frac{D_A^{\rm fid}}{D_A}\right)^2 , \tag{4.7}$$

where H_0 is the Hubble factor today, D_A is the angular diameter distance, and $^{\rm fid}$ refers to quantities evaluated in the fiducial cosmology. Finally, we project the anisotropic power spectrum to multipoles in the usual way:

$$P_\ell(k) = \frac{2\ell+1}{2} \int_{-1}^{1} {\rm d}\mu \, P_{gg}\left(\bar{k}(k,\mu), \bar{\mu}(k,\mu)\right) \mathcal{P}_\ell(\mu) , \tag{4.8}$$

where $\mathcal{P}_\ell(\mu)$ is the Legendre polynomial of order ℓ.

As before, our implementation allows for bypassing the `CAMB` Boltzmann solver [290] in order to use linear power spectrum emulators, namely `bacco` [133] and/or `CosmoPower` [291]. We note that this speeds up the model evaluations by roughly two orders of magnitude.

4.1.2 The Growth Index γ Parameterisation

In order to check for deviations from ΛCDM, we adopt the phenomenological parameterisation proposed in Refs. [292, 293]. Specifically, we compute the growth rate $f = {\rm d}\ln D / {\rm d}\ln a$ as:

$$f_\gamma(a) = \Omega_m(a)^\gamma , \tag{4.9}$$

where $\Omega_m(a) = \Omega_{m,0} a^{-3}/E^2(a)$ is the time dependent matter density parameter, with $E(a)$ the dimensionless Hubble factor. Eq. 4.9 has been shown to be 0.2% accurate for ΛCDM scenarios, with $\gamma = 0.55$ [293]. We compute the linear growth factor D by numerically integrating Eq. 4.9:

$$D_\gamma(a) = \exp\left[-\int {\rm d}a' \, \frac{f_\gamma(a')}{a'}\right] . \tag{4.10}$$

We normalise the growth rate to its ΛCDM value at high redshift, i.e., during matter domination. The growth functions from Eq. 4.9 and Eq. 4.10 are then used to re-scale the linear power spectrum computed at redshift $z = 0$ and construct the redshift space multipoles as described in Subsection 4.1.1. An analysis of the behaviour of γ over cosmic history can be found in Refs. [294, 295], while Ref. [296] proposes an alternative parameterisation, that extends γ to be a function of redshift.

4.1.3 Massive Neutrinos

The scale-dependent suppression in growth induced by massive neutrinos free streaming (see a review in Ref. [282] as well as the discussion in Subsection 1.3.2) is modelled

following the prescription of Ref. [288], which consists in using the CDM + baryon power spectrum P_{cb} instead of the total matter $P_m = P_{cb+\nu}$ to compute the galaxy power spectrum multipoles. While not exact, this approach was shown to be sufficiently accurate for survey volumes similar to that of BOSS in Ref. [297], especially for small neutrino masses. For our baseline analysis with fixed $\sum m_\nu \equiv M_\nu = 0.06$ eV we modify the model described in Subsection 4.1.1 by substituting δ with δ_{cb} in Eq. 4.1, and thus P_L with P_{cb} in what follows.

For the case where the neutrino mass is varied as a free parameter, given the bigger impact that neutrino masses larger than the minimal one have on the power spectrum, we perform the following modifications to the model:

- we compute the linear P_{cb} twice, once for each effective redshift of the galaxy sample, in order to properly model the scale-dependent suppression introduced by massive neutrinos;
- we modify our infrared-resummation routine, since the Eisenstein-Hu prescription we adopt for the broadband power spectrum does not include a dependence on massive neutrinos. We use instead a discrete sine transform approach to perform the wiggle-no wiggle decomposition [298, 299];
- we compute the growth rate of Eq. 4.9 using only the CDM+baryon density Ω_{cb} [300];
- the resulting growth factor is normalised to its ΛCDM counterpart at the effective redshift, so that differences in the amplitude only come from the γ parameter.

In principle, a more accurate modelling of the impact of massive neutrinos would require a modification of the perturbation theory kernels and the use of a scale dependent growth rate (see, e.g., Refs. [301–305]). However, we do not expect any relevant effect for the case of BOSS measurements given the size of the error bars [297].

4.2 Data and Analysis Setup

Our main analysis setup and dataset follow the ones described in Ref. [99]. We summarise here the main points, but refer to that work for more details.

4.2.1 Dataset

We use the galaxy power spectrum multipoles of BOSS DR12 [306–308], which is split in two galaxy samples (CMASS and LOWZ) and covers two different sky cuts (NGC and SGC). The measurements are performed by splitting the sample into two redshift bins, with effective redshift $z_1 = 0.38$ and $z_3 = 0.61$ and widths $\Delta z = 0.3$ and 0.25, respectively.

In particular, we use the windowless measurements provided in Ref. [62], based on the windowless estimator [168, 169]. The power spectrum measurements are complemented with BAO measurements of the Alcock-Paczynski parameters $\alpha_\perp$, $\alpha_\parallel$ obtained from the same BOSS data release and also provided by Ref. [62], as well as pre-reconstruction BAO measurements at low redshift (6DF survey [309] and SDSS DR7 MGS [310]) and high redshift measurements of the Hubble factor and angular diameter distance from the Ly-α forest auto and cross-correlation with quasars from eBOSS DR12 [311]. We model them with Eq. 1.64 and Eq. 1.65. For BOSS power spectrum multipoles and BAOs we use a numerical covariance matrix computed from 2048 "MultiDark-Patchy" mock catalogs [312, 313], also provided in its windowless form [62].

4.2.2 Analysis Setup

We fit all three multipoles of the galaxy power spectrum up to $k_{\rm max} = 0.2\ h\ {\rm Mpc}^{-1}$. The nonlinear power spectrum is modelled with the EFTofLSS as described in Subsection 4.1.1, with a custom implementation which takes advantage of the `FAST-PT` algorithm [158, 159] to compute the convolution integrals of Eq. 4.2 in $\mathcal{O}(10^{-2})$ seconds. The theoretical prediction is then combined with an independently developed likelihood pipeline, where we sample the parameter space by means of the affine-invariant sampler implemented in the `emcee` package [210], using the integrated auto-correlation time[2] as convergence diagnostic for our MCMC chains [219]. For the Stage-IV forecasts presented in Subsection 4.3.3 we use the pre-conditioned MonteCarlo method discussed in Subsection 2.4.4 and implemented in `pocomc` [211, 221], which allows for a speed up in the sampling of parameters. We check the two samplers give consistent results.

We marginalise analytically over the nuisance parameters that enter the model linearly [152, 203], namely the EFT counterterm parameters, the noise parameters, and $b_{\Gamma 3}$. The parameter space is thus restricted to 18 free parameters (19 when we also vary the total neutrino mass):

$$\{\omega_c,\ \omega_b,\ h,\ n_s,\ A_s,\ \gamma,\ (M_\nu);\ \mathbf{b_1},\ \mathbf{b_2},\ \mathbf{b_{\mathcal{G}_2}}\}\,, \tag{4.11}$$

where the bias parameters assume different values in each redshift bin and sky cut (e.g., $\mathbf{b_1} = \left[b_1^{\rm NGC,z1},\ b_1^{\rm SGC,z1},\ b_1^{\rm NGC,z3},\ b_1^{\rm SGC,z3}\right]$).

Concerning priors[3], we impose a Gaussian BBN prior on ω_b[4], and broad, flat priors on the cosmological parameters, matching the ranges of parameters allowed by the `bacco`

[2] In particular, we compute τ every 100 steps of the chain and check that, for each parameter, two conditions are satisfied: $\tau <$ nstep/50 and $\Delta\tau/\tau < 0.01$, with $\Delta\tau$ the difference between the current value of τ and its value at the previous check. For more details see Subsection 2.4.3.

[3] We denote the uniform distribution with edges a, b as $\mathcal{U}(a, b)$, and the normal distribution with mean a and standard deviation b as $\mathcal{N}(a, b)$.

[4] We use the results of Refs. [184, 185, 314], so that $\omega_b \in \mathcal{N}(0.02268, 0.00038)$

linear emulator:

$$\Omega_{cb} \in \mathcal{U}(0.06, 0.7)\,,\ h \in \mathcal{U}(0.5, 0.9)\,, M_\nu \in \mathcal{U}(0, 1)\,, \tag{4.12}$$

where and $\Omega_{cb} = \Omega_c + \Omega_b$. We impose no prior on the other cosmological parameters in our baseline analysis, but we also explore the impact of including Planck priors on the primordial parameters A_s and n_s. In particular, for each cosmology explored (γCDM, $\gamma\nu$CDM), we have three options:

- one with no priors on A_s, n_s (labelled *baseline*);
- one with a 3σ Gaussian Planck prior on A_s: $\ln(10^{10}\ A_s) \in \mathcal{N}(3.044, 0.042)$ (labelled *prior* A_s);
- and one with a 3σ Gaussian Planck prior on both A_s and n_s: $\ln(10^{10}\ A_s) \in \mathcal{N}(3.044, 0.042)$ and $n_s \in \mathcal{N}(0.9649, 0.0126)$ (labelled *prior* A_s,n_s).

For both parameters, the Gaussian priors are centered on the best-fit values from Planck 2018 [22] and have width corresponding to the 3σ error from the same work. For the nuisance parameters, we adopt those of Ref. [62]:

$$\begin{gathered} b_1 \in \mathcal{U}(0, 4)\,,\ b_2 \in \mathcal{N}(0, 1)\,,\ b_{\mathcal{G}_2} \in \mathcal{N}(0, 1)\,,\ b_{\Gamma_3} \in \mathcal{N}\left(\frac{23}{42}(b_1 - 1), 1\right)\,, \\ N \in \mathcal{N}\left(\frac{1}{\bar{n}}, \frac{2}{\bar{n}}\right)\,,\ e_0 \in \mathcal{N}\left(0, \frac{2}{\bar{n}k_{\rm NL}^2}\right)\,,\ e_2 \in \mathcal{N}\left(0, \frac{2}{\bar{n}k_{\rm NL}^2}\right)\,,\ \frac{c_0}{[{\rm Mpc}/h]^2} \in \mathcal{N}(0, 30)\,, \\ \frac{c_2}{[{\rm Mpc}/h]^2} \in \mathcal{N}(30, 30)\,,\ \frac{c_4}{[{\rm Mpc}/h]^2} \in \mathcal{N}(0, 30)\,,\ \frac{c_{\nabla^4\delta}}{[{\rm Mpc}/h]^4} \in \mathcal{N}(500, 500)\,. \end{gathered} \tag{4.13}$$

4.3 Results

4.3.1 BOSS Analysis

Here we present the main results of the analysis of the galaxy power spectrum multipoles measured from the BOSS DR12; we cover the two extensions of the base ΛCDM scenario discussed in the previous sections: γCDM and $\gamma\nu$CDM. For each cosmology, we explore the three options for priors described in Subsection 4.2.2. We show the posterior distributions for the γCDM case with fixed neutrino mass $M_\nu = 0.06$ eV in Fig. 4.1 and summarise the 68% c.l., mean and best-fit values for the cosmological parameters in Tab. 4.1. Plots for the full parameter space can be found in Appendix B.1. We obtain $\gamma = 0.007^{+0.170}_{-0.229}$ (0.149) for the baseline priors, shown by green contours, $\gamma = 0.617^{+0.098}_{-0.110}$ (0.614) (prior on A_s, orange contours) and $\gamma = 0.647 \pm 0.085$ (0.655)

Parameter	baseline	prior on A_s	prior on A_s, n_s
ω_c	$0.1208^{+0.0076}_{-0.0086}$ (0.1216)	$0.1157^{+0.0072}_{-0.0090}$ (0.1165)	$0.1186^{+0.0052}_{-0.0058}$ (0.1196)
ω_b	0.02267 ± 0.00039 (0.02298)	0.02265 ± 0.00038 (0.02292)	0.02266 ± 0.00038 (0.02275)
h	0.680 ± 0.010 (0.682)	0.675 ± 0.011 (0.682)	0.678 ± 0.010 (0.681)
$\ln(10^{10}\, A_s)$	$2.030^{+0.248}_{-0.371}$ (2.190)	3.034 ± 0.042 (3.055)	3.033 ± 0.042 (3.065)
n_s	0.973 ± 0.057 (0.970)	$0.996^{+0.072}_{-0.062}$ (0.994)	0.966 ± 0.012 (0.970)
γ	$0.007^{+0.170}_{-0.229}$ (0.149)	$0.617^{+0.098}_{-0.110}$ (0.614)	0.647 ± 0.085 (0.655)
σ_8	$0.498^{+0.047}_{-0.096}$ (0.534)	0.796 ± 0.030 (0.807)	0.801 ± 0.029 (0.819)

Table 4.1 *Mean values and 68% c.l. values for γCDM with fixed neutrino mass $M_\nu =$ 0.06 eV for the three prior choices. We show the best-fit values in parentheses, and include derived constraints on σ_8.*

(prior on A_s and n_s, purple contours), where values in parentheses refer to the best-fit values, obtained as the maximum of the analytically marginalised posterior.

We first note that our baseline analysis is affected by strong projection effects (also known as prior-volume effects), in particular involving the parameters regulating the amplitude of the power spectrum, A_s and γ: when no CMB priors are imposed, the two-dimensional marginalised posteriors are shifted towards extremely low values of A_s and γ, along the degeneracy between the two. In fact, lowering the primordial amplitude A_s or introducing a low value for γ, which effectively increases the growth factor, result in two opposite effects which can balance out and give the same power spectrum. An analogous behaviour for extensions of the standard model was highlighted in Ref. [99], especially for the case of exotic (interacting) dark energy cosmology (see their Fig. 7). Other works focusing on the full-shape analysis of the same dataset also highlighted issues when trying to constrain extended parameter models [154, 278]. In particular in Ref. [278] the authors provide constraints on nDGP modified gravity [107] using a similar EFTofLSS-based model, and discuss the presence of projections due to the degeneracy between the primordial amplitude A_s and the nDGP $\Omega_{\rm rc}$ parameter (see Subsection 1.3.1). We study the presence of prior-volume effects in more detail in Subsection 4.3.2 by generating and fitting synthetic data, adopting the same covariance matrix used for our main BOSS analysis, and by profiling the posterior.

Imposing a prior on A_s breaks these degeneracies and shifts the two-dimensional

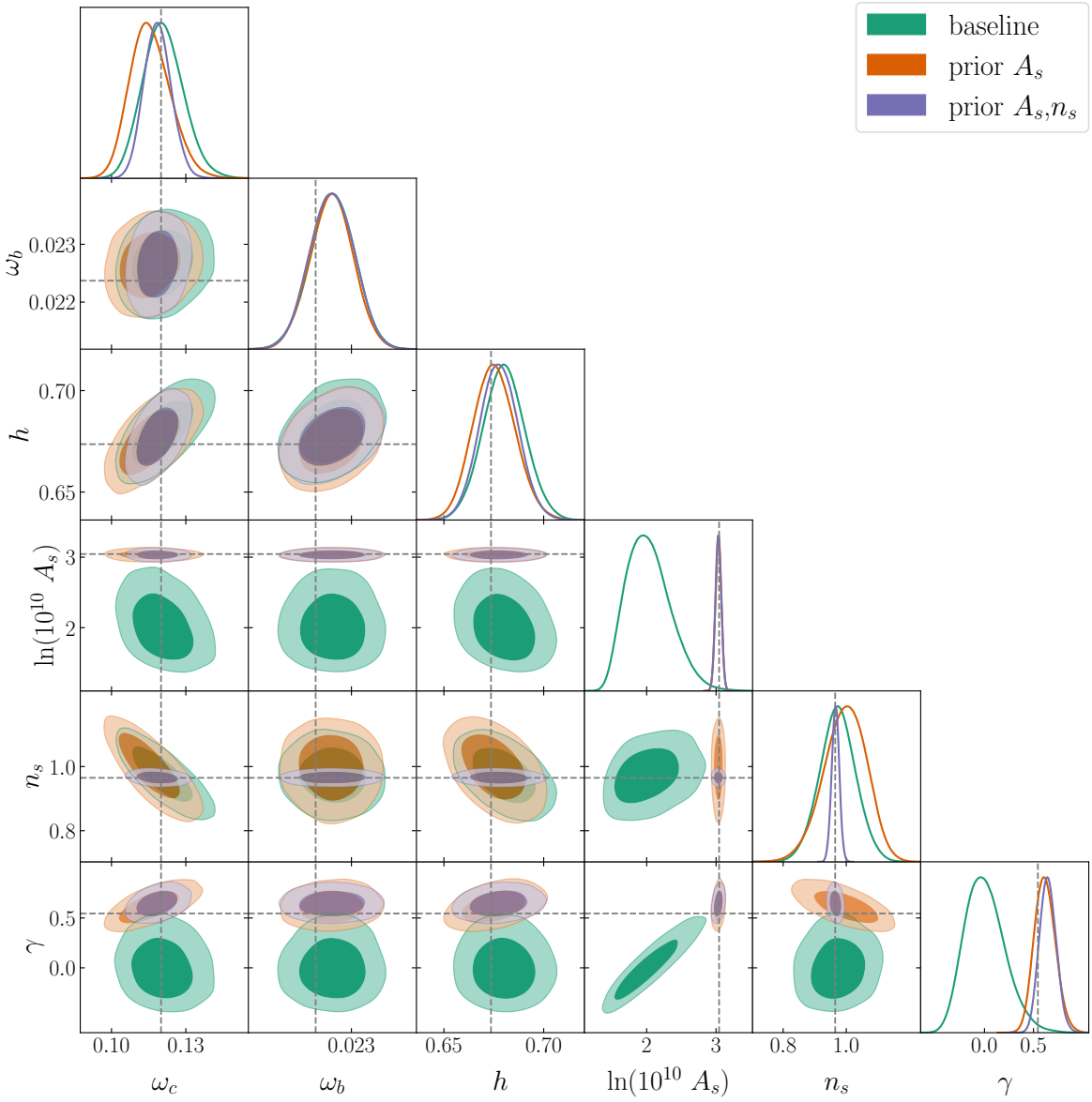

Figure 4.1 *Marginalised posterior distribution for the cosmological parameters for the γCDM cosmology and the three prior choices, as detailed in the legend. We fit all three multipoles and use $k_{\rm max} = 0.2\ h\ {\rm Mpc}^{-1}$. Grey dashed lines mark the Planck best-fit values (ΛCDM prediction for γ).*

marginalised posterior closer to the Planck best-fit and ΛCDM values, as can be seen in the orange contours of Fig. 4.1. In fact, the other cosmological parameters are mostly unaffected, but the error on γ is reduced by $\sim 48\%$. Moreover, adopting a prior on n_s yields an additional $\sim 18\%$ improvement on γ. Both the mean and best-fit values obtained in these cases are slightly larger than the ΛCDM prediction of $\gamma = 0.55$, though still $\sim 1\sigma$ consistent. This slight deviation is likely equivalent to the finding in previous full-shape BOSS analyses of a low value of A_s[5] [99, 152, 258] ($\ln(10^{10}\ A_s) \simeq 2.8$ as opposed to the Planck value $\ln(10^{10}\ A_s) = 3.044$): when we impose a prior on A_s the model tries to compensate by lowering the amplitude with a larger value for γ. We also notice that the degeneracy with A_s was masking a degeneracy between γ, ω_c and n_s, which emerges when we impose a prior on A_s and is then broken when we apply a Planck prior on n_s.

We then open up the parameter space and allow the neutrino mass to vary as a free parameter. It is worth noting that we do not expect to obtain tight constraints on the neutrino mass, as previous analyses already highlighted the inability of BOSS data alone to do so [152, 315, 316]; in fact, as discussed in Ref. [152] the precision of BOSS data does not allow to detect the step in the power spectrum which marks the free streaming length of massive neutrinos, restricting detectable signatures only to changes to the overall amplitude. Nevertheless, our goal is to study possible degeneracies between γ and M_ν, and the impact of massive neutrinos on the constraints on γ. We modify the theoretical model as described in Subsection 4.1.3, and explore the same three options for priors as for the γCDM case. The marginalised posteriors for $\gamma\nu$CDM are shown in Fig. 4.2, and the 68% c.l., mean and best-fit values for the cosmological parameters are listed in Tab. 4.2.

We first note that the baseline shows a similar shift in the two-dimensional marginalised posteriors for γ and A_s as the one of Fig. 4.1. This is again due to the presence of strong degeneracies between the parameters that control the amplitude of the power spectrum. However, the error on γ is not affected by the introduction of M_ν, and in fact there seems to be no degeneracy between the two. This is actually due to the fact that such degeneracy is mild compared to the others and to the size of the error bars on BOSS data (see, e.g., Fig. 4.12 where we perform forecasts for Stage-IV surveys, an anti-correlation between γ and M_ν can clearly be seen).

When we impose Planck priors on the primordial parameters on the other hand we can see a mild degeneracy emerge between γ and M_ν, which leads to marginally lower values for γ with respect to γCDM. Concerning neutrinos, as expected the data are not very constraining, and we only provide (somewhat large) upper limits. It is worth commenting on the case with a CMB prior on A_s, where the model seems to be picking up a large

[5] This low amplitude is possibly arising due to prior-volume/projection effects as seen in Refs. [99, 154, 241]. We explore some of these effects in Subsection 4.3.2, but leave a more complete analysis for future work.

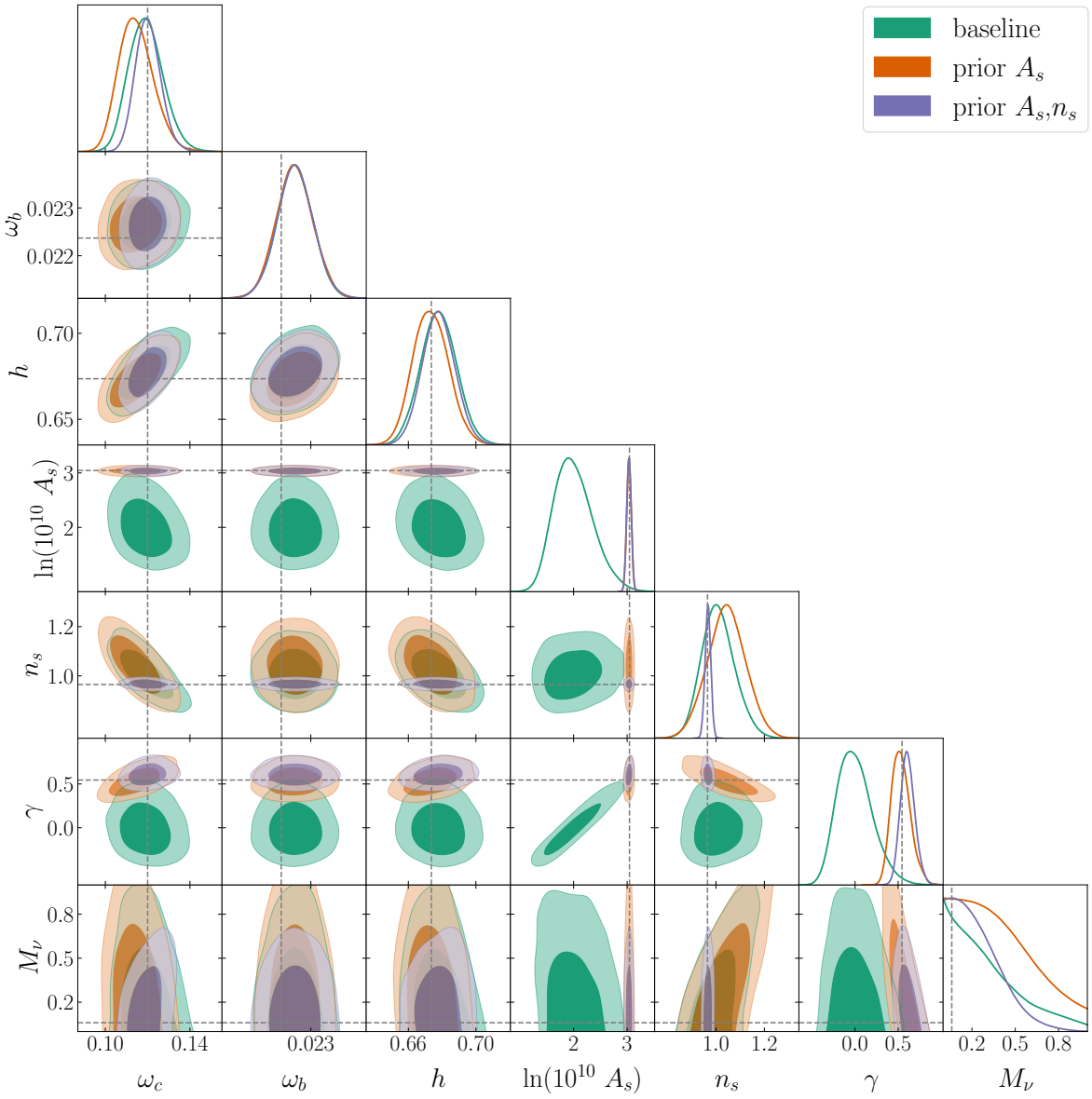

Figure 4.2 *Marginalised posterior distribution for the cosmological parameters for $\gamma\nu$CDM for the three prior choices. We use $k_{\max} = 0.2\ h\ \mathrm{Mpc}^{-1}$ and a flat prior $M_\nu \sim \mathcal{U}(0,1)$ eV for the neutrino mass. Grey dashed lines mark the Planck best-fit values (with the ΛCDM prediction for γ and minimal neutrino mass $M_\nu = 0.06$ eV).*

Parameter	baseline	prior on A_s	prior on A_s,n_s
ω_c	$0.1193^{+0.0072}_{-0.0088}$	$0.1146^{+0.0070}_{-0.0090}$	$0.1202^{+0.0054}_{-0.0063}$
	(0.1173)	(0.1184)	(0.1195)
ω_b	0.02266 ± 0.00038	0.02265 ± 0.00039	0.02267 ± 0.00038
	(0.02284)	(0.02292)	(0.02264)
h	0.678 ± 0.011	0.673 ± 0.011	0.6779 ± 0.010
	(0.675)	(0.683)	(0.681)
$\ln(10^{10}\, A_s)$	$2.004^{+0.298}_{-0.412}$	3.035 ± 0.042	3.034 ± 0.042
	(2.290)	(3.028)	(3.040)
n_s	$1.009^{+0.061}_{-0.074}$	1.043 ± 0.079	0.967 ± 0.012
	(0.977)	(1.028)	(0.957)
γ	$0.001^{+0.165}_{-0.232}$	$0.534^{+0.091}_{-0.12}$	$0.612^{+0.075}_{-0.090}$
	(0.183)	(0.526)	(0.61)
M_ν	< 0.372	< 0.478	< 0.298
	(0.038)	(0.362)	(0.016)
σ_8	$0.496^{+0.054}_{-0.108}$	$0.806^{+0.031}_{-0.034}$	0.809 ± 0.031
	(0.550)	(0.818)	(0.806)

Table 4.2 *Mean values and 68% c.l. values for $\gamma\nu$CDM for the three prior choices. We show the best-fit values in parentheses, and include derived constraints on σ_8.*

value for M_ν: we argue that this is to be ascribed to the model trying to lower the amplitude by exploiting the degeneracy between M_ν and n_s. More specifically, in the baseline case the amplitude is mostly controlled by A_s; when that is fixed by the prior, other parameters change to compensate: mostly γ, but also the neutrino mass, resulting in a looser constraint on M_ν in that case. However, this is only possible if the change in the shape of the power spectrum due to massive neutrinos is compensated by a change in n_s. When n_s is also fixed by the Planck prior, there is less freedom in the shape and thus the constraint on M_ν tightens again.

In Fig. 4.3 we plot the one-dimensional marginalised posterior distributions for γ for all cases described in this section, to allow for an easier comparison between the constraints we get for this parameter. We mark the best-fit values with dashed lines, following the same color scheme of Fig. 4.1 and Fig. 4.2, and the ΛCDM prediction with solid grey lines. As we can see, adopting CMB priors on the primordial parameters shifts the peak of the posterior from (projection affected) negative values to values consistent with the ΛCDM prediction, albeit slightly larger. Moreover, the difference between the peak of the posterior and the best-fit for the case without CMB-based priors is a hint of the projection which affects the marginalised posteriors.

Our results are broadly consistent with previous analyses of the BOSS data, although

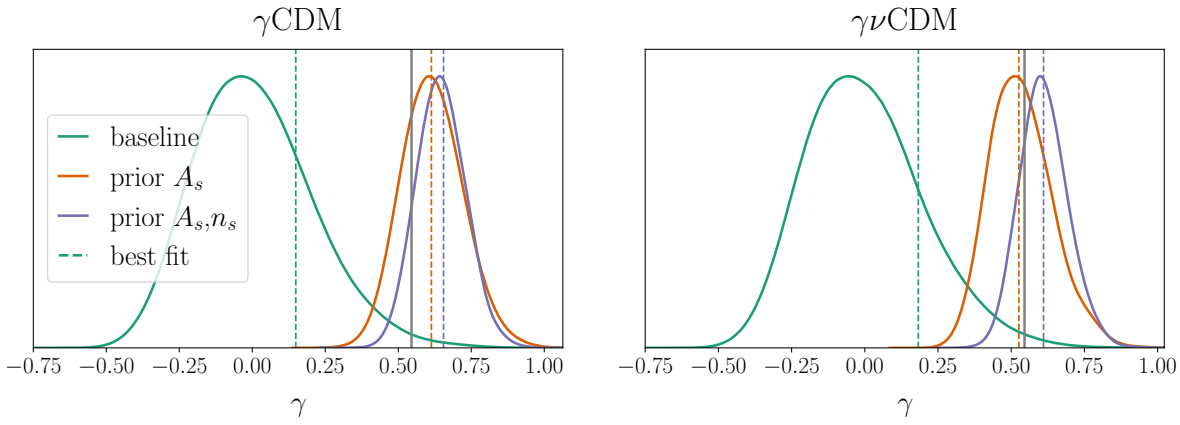

Figure 4.3 *Marginalised one-dimensional posterior distribution for the γ parameter for γCDM (left) and $\gamma\nu$CDM (right), for the three prior choices as stated in the legend. Dashed vertical lines mark the best-fit values corresponding to the maximum of the marginalised posterior distribution; the solid grey line corresponds to the ΛCDM prediction.*

an exact comparison is difficult due to different choices in the analysis setup and datasets included. The main novelty of this work is the use of a full-shape approach, as opposed to template fitting adopted in the official BOSS analysis, and the exploration of the impact of priors on the inferred parameters. Moreover, most previous works take advantage of a joint analysis with CMB data, which results in generally tighter constraints. Nevertheless, we report here some of the recent measurements of γ that used BOSS galaxies as the main dataset for comparison, highlighting the main differences with respect to this work: Ref. [317] found $\gamma = 0.566 \pm 0.058$ combining BOSS DR12 galaxies with Planck CMB data and SNIa data. Additionally, Ref. [318] provides joint constraints on γ and the neutrino mass M_ν, although they used a previous data release (DR11) and again performed a joint fit with CMB data: they found $\gamma = 0.67 \pm 0.14$, $M_\nu = 0.25^{+0.13}_{-0.22}$. A joint analysis with the galaxy bispectrum was performed in Ref. [319], finding $\gamma = 0.733^{+0.068}_{-0.069}$. All these works are official analyses from the BOSS collaboration, and adopt a fixed template for the power spectrum multipoles. More recently, Ref. [66] performed a similar analysis combining data from BOSS, DES and Planck, finding $\gamma = 0.633^{+0.025}_{-0.024}$. Also in this case the power spectrum was fitted using a fixed template, as opposed to the full-shape fit we perform in this work.

Overall, our strongest constraints (those where we impose CMB-based priors on the primordial parameters) show a marginal preference for a high value of γ, consistent for example with Ref. [66]. However, in our case the deviation from the ΛCDM prediction is $\sim 1\sigma$, as opposed to the $\sim 4\sigma$ discrepancy found in that work. In general, our constraints are weaker than those obtained in previous works. This can be attributed to the fact that we only rely on LSS data and include CMB information merely in terms of priors on the primordial parameters: given the degeneracies between the additional parameters

of γCDM and $\gamma\nu$CDM and the other parameters, some of which are tightly constrained by the CMB, it is no surprise that performing a joint analysis with Planck data can yield tighter constraints. This can also be approximated by including Gaussian priors derived from Planck on all cosmological parameters, see Appendix F of Ref. [320] for a comparison.

Another possible way of gaining in constraining power without resorting to CMB information would be to use higher-order statistics such as the galaxy bispectrum. Indeed, the tree-level bispectrum does not depend on b_{Γ_3}, and its inclusion in the analysis can therefore break the degeneracy between $b_{\mathcal{G}_2}$ and b_{Γ_3}, leading to improved constraints on the linear bias b_1 (see Refs. [62, 152] for a full-shape joint analysis of BOSS data). While the impact on cosmological parameters is somewhat marginal in the context of ΛCDM and Stage-III surveys, it can become significant for extended models where there are strong degeneracies between parameters controlling the amplitude: a tighter constraint on b_1 implies a more precise measurement of A_s and therefore of γ. Some work towards quantifying the impact of including the bispectrum for beyond-ΛCDM models has already been done in Chapter 3 in the context of simulations, where a $\sim 30\%$ improvement was found for a power spectrum and bispectrum joint analysis for an interacting dark energy model. We leave a proper exploration of the impact of the bispectrum in the context of γCDM and $\gamma\nu$CDM to a future work.

4.3.2 Projection Effects

In this section we study in more details the prior-volume effects found for γCDM and $\gamma\nu$CDM when no CMB priors are applied (green contours in Fig. 4.1 and Fig. 4.2, in particular the A_s–γ plane). The presence of projection effects is already highlighted by the shift between the peak of the one-dimensional marginalised posterior and the best-fit point, see Fig. 4.3. To better investigate this we adopt two approaches: first we perform a consistency check using synthetic data, then we carry out profiling of the posterior. For the consistency check we perform the same analysis described in Subsection 4.3.1 on a synthetic datavector generated with a fiducial cosmology and set of nuisance parameters. We note that the ability of our pipeline to recover the cosmological parameters correctly has been validated with N-body simulations, and we are using the same theoretical model to generate the datavector and fit it, which should lead to perfect agreement between the input and inferred parameters. We use the same covariance computed from the "MultiDark-Patchy" mock catalogues adopted in the BOSS analysis, and include (synthetic) BAO information. As fiducial parameters we adopt the best-fit values of Planck [22], while the nuisance parameters are determined by maximising the BOSS likelihood with cosmology fixed to the Planck values. Our results are plotted in Fig. 4.4 (purple contours and lines), where we also include the baseline result of Fig. 4.1 for

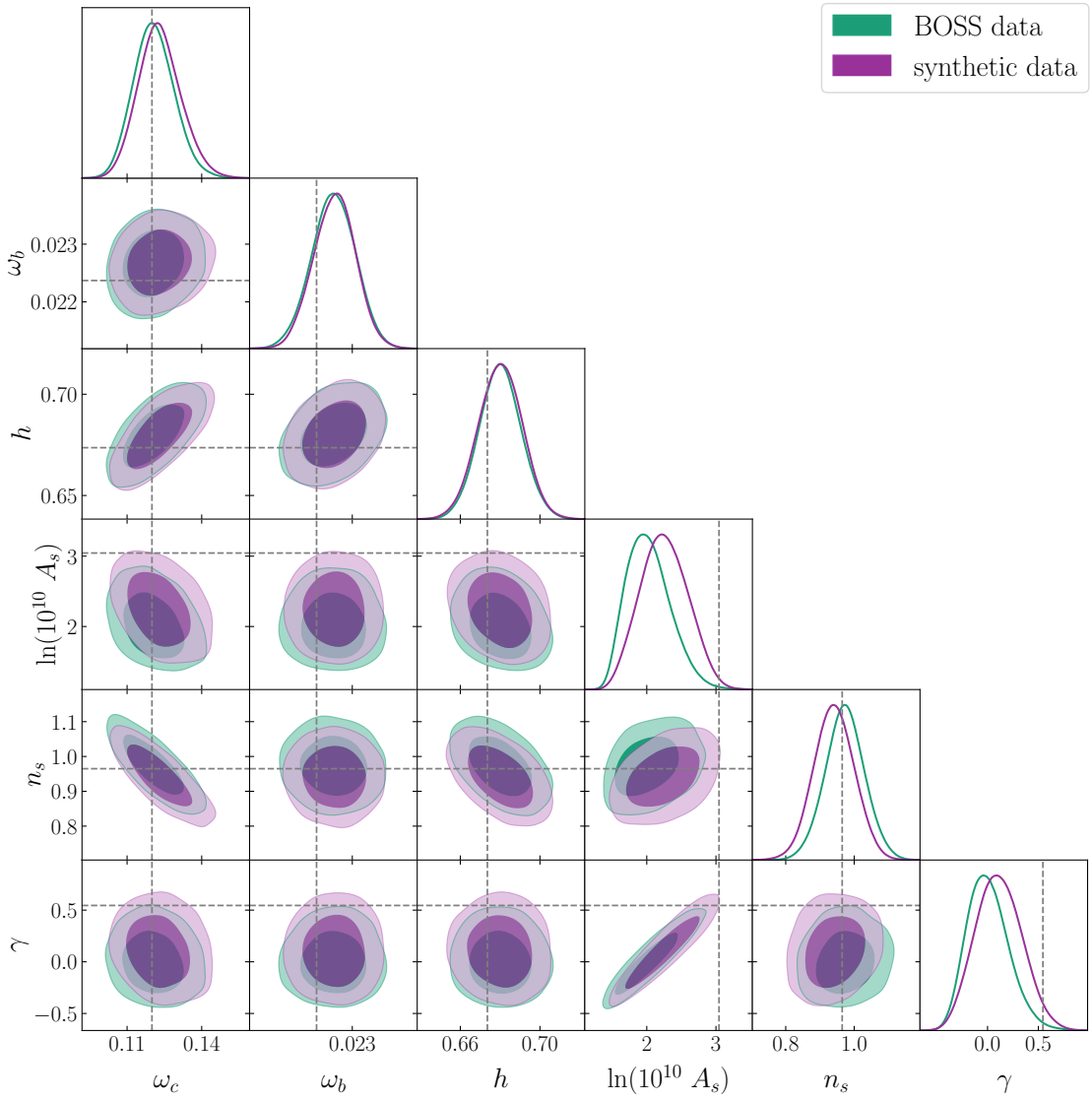

Figure 4.4 *Posterior distribution for the cosmological parameters for the BOSS data (green) and synthetic data generated with the Planck fiducial cosmology (purple). We fix the total neutrino mass to* $M_\nu = 0.06$ eV *and use a scale-cut of* $k_{\rm max} = 0.2\ h\ {\rm Mpc}^{-1}$. *Grey dashed lines mark the fiducial cosmology used to generate the synthetic data.*

comparison (green contours and lines).

The two-dimensional marginalised posteriors for the synthetic data exhibit a very similar behaviour as the one we observed in the BOSS data, with a strong shift in the posterior towards low values of A_s and γ and almost perfect overlap with the posterior obtained from BOSS data. As discussed above, this effect can be ascribed to the presence of extreme degeneracies in the extended parameter space, which lead to a highly non-Gaussian posterior. As a consequence, the marginalisation process can result in apparent biases in the two-dimensional confidence regions, as discussed thoroughly in Ref. [277].[6] In that work, the author proposes to use profile distributions to assess the impact of marginalisation. As opposed to marginalisation, this profile likelihood (PL) approach allows one to obtain a one-dimensional distribution by evaluating the posterior over a scan of a parameter of interest, θ_i, while maximising the posterior with respect to all other parameters θ_k, $k \neq i$. This profile distribution is not biased by projection effects, since it is centred on the maximum of the full posterior. For non-Gaussian posteriors, as is the case here, the resulting distribution will be different than the usual marginalised distribution obtained via integration over the marginalised parameters. Depending on the type of non-Gaussianity, this distribution can be broader or narrower over the parameter of interest. This difference between integration and maximisation of the posterior is approximately given by the so-called Laplace term, which accounts for volume effects as explained in Ref. [200].

Ref. [277] suggests performing this profiling step directly on the MCMC samples. However, in addition to resulting in noisy distributions, this is not ideal in our case, since we sample over the analytically marginalised posterior and we therefore expect additional projection due to that pre-marginalisation step. We profile instead the full posterior using the MINOS algorithm implemented in the `iminuit` package [195]. Our parameter of interest is the growth index γ, for which we plot the PL in the left panel of Fig. 4.5, and compare to the one-dimensional marginalised posterior from the MCMC in the right panel. Additionally, we compare the confidence intervals obtained from the MCMC to those obtained from the profiling in Fig. 4.6.

Fig. 4.5 shows a clear shift of the PL towards the ΛCDM prediction with respect to the marginalised posterior. Moreover, the confidence intervals are larger in the case of the PL, making the results consistent with ΛCDM. We also note how the best-fit points from the MCMC (orange crosses in Fig. 4.6) are close to the PL results, though still somewhat lower in A_s. This demonstrates the presence of additional projection effects due to the analytic marginalisation of linear nuisance parameters in the posterior sampled in the MCMC. Overall, the use of the profile likelihood shows a more conservative result, which appears, at least in this case, to reflect better the effect of the large degeneracy between the amplitude parameters on the final one-dimensional constraint on γ. Note that

[6] See also Ref. [200] for further explanation of the origin of these biases and our discussion in Section 2.3.

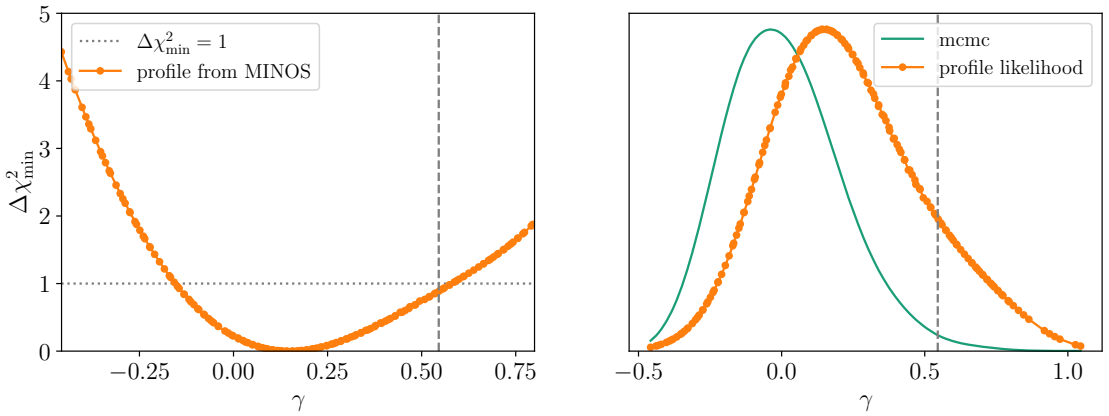

Figure 4.5 *Left: $\Delta\chi^2_{\text{min}}$ for a set of values for γ obtained from profiling the likelihood with MINOS. The horizontal dotted line marks $\Delta\chi^2_{\text{min}} = 1$, which is used to determine confidence intervals. Right: comparison between the marginalised posterior obtained from the mcmc (green curve) and the PL (orange curve and datapoints). The dashed vertical line marks the ΛCDM prediciton.*

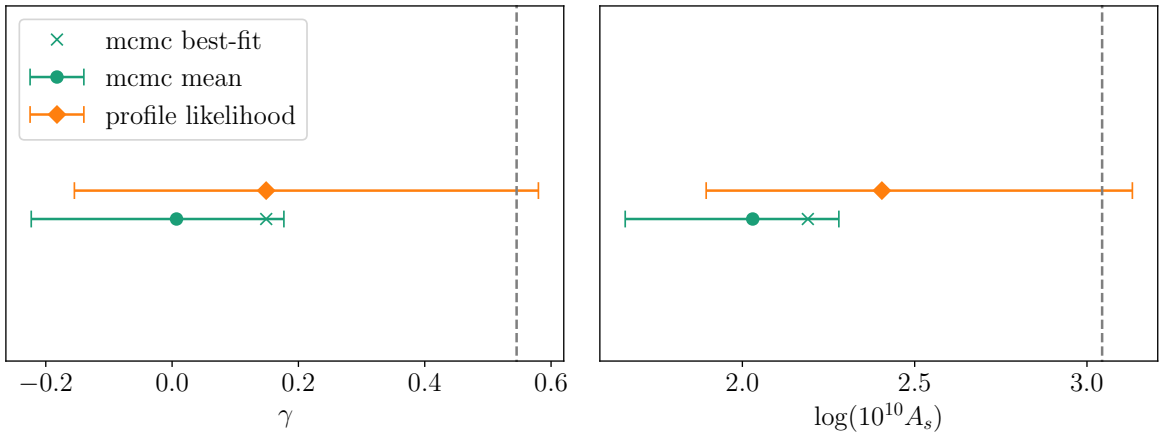

Figure 4.6 *Comparison between the mean values and confidence intervals obtained from the marginalised posterior (green points and error bars) and the PL (orange points and error bars) for γ (left) and $\ln(10^{10}\ A_s)$ (right). We show the best-fit points obtained from the MCMC with crosses. The dashed vertical line marks the ΛCDM prediciton.*

should the posterior be closer to the Gaussian case, the difference between marginalising and profiling would disappear, so we expect projection effects to disappear with more constraining data.

As mentioned already in Section 4.3, the presence of volume (or projection) effects was already highlighted in a number of recent works performing the full-shape analysis of BOSS data in the context of beyond-ΛCDM models [99, 154, 278, 321]. It is expected that the higher precision of forthcoming data will mitigate this effect, as also suggested by the forecasts we present in Subsection 4.3.3. However, projections can also be alleviated by the combination with additional probes or the inclusion of higher order correlation functions. In general, we recommend extreme care in the choice of priors, especially when constraining beyond-ΛCDM models.

4.3.3 Forecasts for Stage-IV Surveys

In this section we present forecasts for a Stage-IV spectroscopic galaxy survey, focusing in particular on DESI-like galaxies. Similarly to what described in Subsection 4.3.2, we generate and fit synthetic datavectors with the same EFTofLSS theoretical model. The aim is twofold: on one hand, we wish to provide forecasted constraints on γ and jointly on γ and M_ν, on the other hand, we can assess the ability of the higher precision measurement of reducing the projection effects. Despite a number of approximations we make in our forecasting strategy, which we highlight below, we expect the results to give a more realistic picture of the outcome of future surveys, as opposed to the standard Fisher matrix approach. The latter, while extremely useful due to its low computational cost, has been shown to be unable to capture complex features in the likelihood, which can arise in the context of strong degeneracies between parameters and highly non-Gaussian posteriors (see, e.g., Refs. [322–325]).

We generate three sets of synthetic datavectors, assuming Planck values for the cosmological parameters and simulating the three galaxy samples that are the target of DESI: the bright galaxy sample (BGS), luminous red galaxies (LRGs), and star-forming emission line galaxies (ELG). We follow Ref. [10] and compute expected values for the linear bias and number density of the samples, which we list in Tab. 4.3 together with the respective effective volume. Specifically, we assume constant values for the combination $b_1(z)D(z)$, where $D(z)$ is the linear growth factor evaluated at the central redshift of each bin, and use $b_{\rm LRG}(z)D(z) = 1.7$, $b_{\rm ELG}(z)D(z) = 0.84$, and $b_{\rm BGS}(z)D(z) = 1.34$.

All redshift bins have size $\Delta z = 0.4$ and are centered on the $z_{\rm eff}$ values listed in the table. We compute an analytic covariance matrix, assuming no cross correlation between

Galaxy sample	$z_{\rm eff}$	V_s [Gpc$^3/h^3$]	b_1	$\bar{n}$ [h^3/Mpc^3]
BGS	0.2	1.8	1.135	0.013
LRGs	0.8	12	2.56	3.2×10^{-4}
ELG	1.2	17	1.51	3.7×10^{-4}

Table 4.3 *Parameters used to generate the synthetic DESI-like datavectors for the forecasts. We follow Ref. [10] in computing the effective redshift $z_{\rm eff}$, the volume V_s and number density $\bar{n}$, and determine the linear bias b_1 assuming constant, sample-specific values for the combination $b_1(z)D(z)$ as specified in the text.*

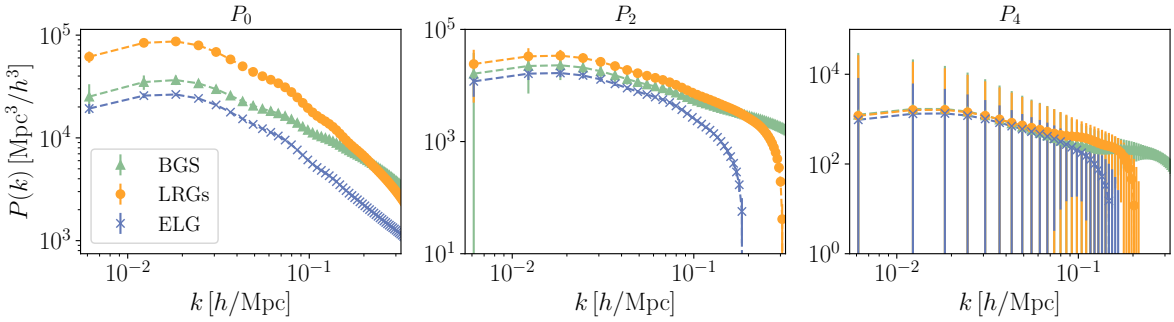

Figure 4.7 *Power spectrum multipoles for the three galaxy samples in our synthetic DESI-like dataset: BGS (green, triangle markers), LRGs (orange, round markers) and ELGs (blue, crosses). The error bars are the square roots of the diagonal elements of the analytic covariance matrix.*

the redshift bins / samples. Specifically, we use the following [34]:

$$C_{\ell_1\ell_2}(k_i, k_j) = \frac{(2\ell_1+1)(2\ell_2+1)}{N_k} \int_{-1}^{1} \mathrm{d}\mu \; \mathcal{L}_{\ell_1}(\mu_i)\mathcal{L}_{\ell_2}(\mu_j) \left[P(\boldsymbol{k}_i) + \frac{1}{\bar{n}}\right] \left[P(\boldsymbol{k}_j) + \frac{1}{\bar{n}}\right] , \tag{4.14}$$

where μ_i is the cosine between $\boldsymbol{k}_i$ and the line of sight, $\mathcal{L}_\ell$ is the Legendre polynomial of order ℓ, $\bar{n}$ is the number density and $N_k = 4\pi k^2 \Delta k \; V_s/(2\pi)^3$ is the number of Fourier modes within a given k-bin of size Δk, V_s being the survey volume. For the power spectrum $P(\boldsymbol{k})$ in Eq. 4.14 we use the Kaiser approximation [140]:

$$P(\boldsymbol{k}) = \left(b_1 + f\mu^2\right)^2 P_L(k) \, . \tag{4.15}$$

As for priors, we use the same ones we adopted for the baseline BOSS analysis of Subsection 4.2.2, specifically we impose no prior on the primordial parameters A_s and n_s, both to showcase the constraining power of LSS alone and to assess potential projection effects in the context of Stage-IV surveys. The resulting power spectrum multipoles for the three samples, with corresponding error bars, are shown in Fig. 4.7.

We fit the three galaxy samples separately and then combine them, and explore two options for the scale cuts: a pessimistic one with $k_{\rm max} = 0.15 \; h$ Mpc^{-1} and an optimistic

one with $k_{\rm max} = 0.25\ h\ {\rm Mpc}^{-1}$. Our results for γCDM are shown in Fig. 4.9 (Fig. 4.8) for the optimistic (pessimistic) case, and summarised in Tab. 4.4. Moreover, we perform the same analysis for $\gamma\nu$CDM and show the results in Fig. 4.11 (Fig. 4.10) for the optimistic (pessimistic) case, while the constraints are listed in Tab. 4.5.

For the joint analysis in γCDM we find $\sigma(\gamma) = 0.058$ (0.072) for the optimistic (pessimistic) case, which represents an improvement of $\sim 85\%$ with respect to the BOSS results when no CMB priors are imposed. For $\gamma\nu$CDM we find the same values, despite the introduction of M_ν as a free parameter. As for massive neutrinos, we get $M_\nu < 0.27$ (< 0.314) at 68% c.l. for the optimistic (pessimistic) case, with a very modest improvement with respect to the constraints obtained from BOSS data. Such a dramatic improvement in the constraints on γ is due to the combination of the different samples: each sample features a slightly different orientation of the degeneracy between A_s and γ, which is then broken when we perform the joint fit.

Focusing on the projection effects which heavily affected the BOSS analysis, we can clearly see how they are strongly mitigated by the increased precision of the mock data and the combination of multiple samples at different redshifts. In fact, for the joint analysis of the three galaxy samples the deviation between the input and best-fit values for γ is $\sim 0.1\sigma$, with the exception of the $\gamma\nu$CDM cosmology in the optimistic case where the deviation is $\sim 0.4\sigma$. On the other hand, some projection is still present in the fits for the single samples, although we can always recover the input value at the 1σ level. It is also worth noting how the inclusion of more nonlinear modes can further alleviate the projection. For example, from the BGS sample we obtain $\gamma = 0.43^{+0.25}_{-0.22}$ (0.37) in the pessimistic case and $\gamma = 0.68^{+0.22}_{-0.19}$ (0.521) in the optimistic case, with the shift between the best-fit point and the input value reduced from 0.37σ to 0.06σ.

A proper comparison to other forecasts in the literature is complicated, because the results depend strongly on the forecasting strategy. Nonetheless, we try to summarise previous results and highlight the differences with this work. Overall we find weaker constraints on γ, which can mainly be attributed to the following reasons:

- most works rely on the Fisher matrix formalism, known to be unable to properly describe the likelihood in presence of strong degeneracies in the parameter space;
- most works use a linear model for the power spectrum, with a significantly smaller number of nuisance parameters;
- most works perform a joint analysis with CMB information, which, as discussed above, can tightly constrain some of the parameters which are most degenerate with γ.

Forecasts for the γ parameterisation for Stage-IV surveys can be found in Ref. [326]. The authors use a Fisher matrix approach and a linear model for the power spectrum,

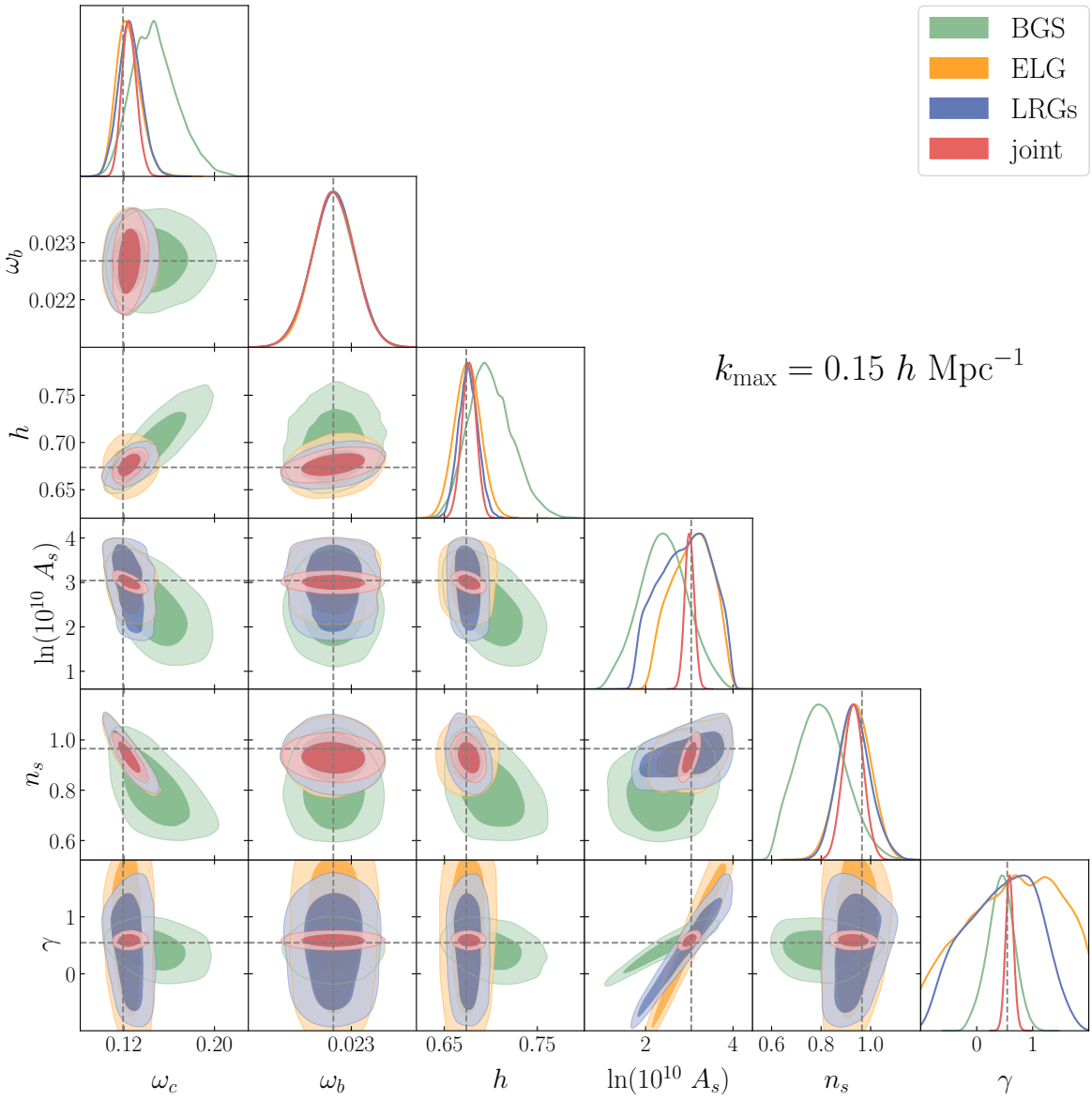

Figure 4.8 *Marginalised posterior for γCDM for the pessimistic case with $k_{\rm max} = 0.15\ h\ {\rm Mpc}^{-1}$. We fit the three samples separately and jointly, as detailed in the legend. Dashed grey lines mark the fiducial values.*

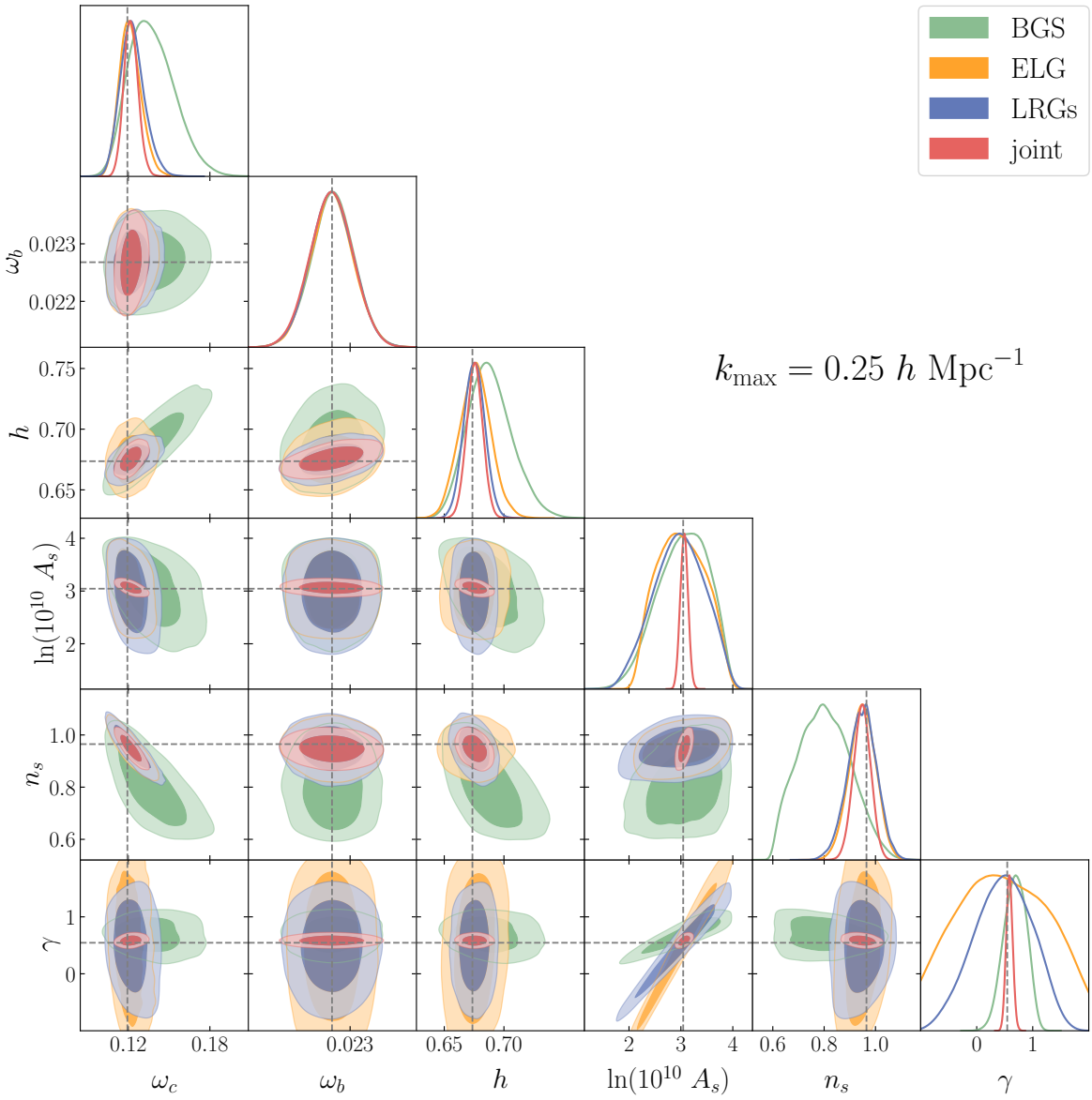

Figure 4.9 *Marginalised posterior for γCDM for the optimistic case with $k_{\rm max} = 0.25\ h\ {\rm Mpc}^{-1}$. We fit the three samples separately and jointly, as detailed in the legend. Dashed grey lines mark the fiducial values.*

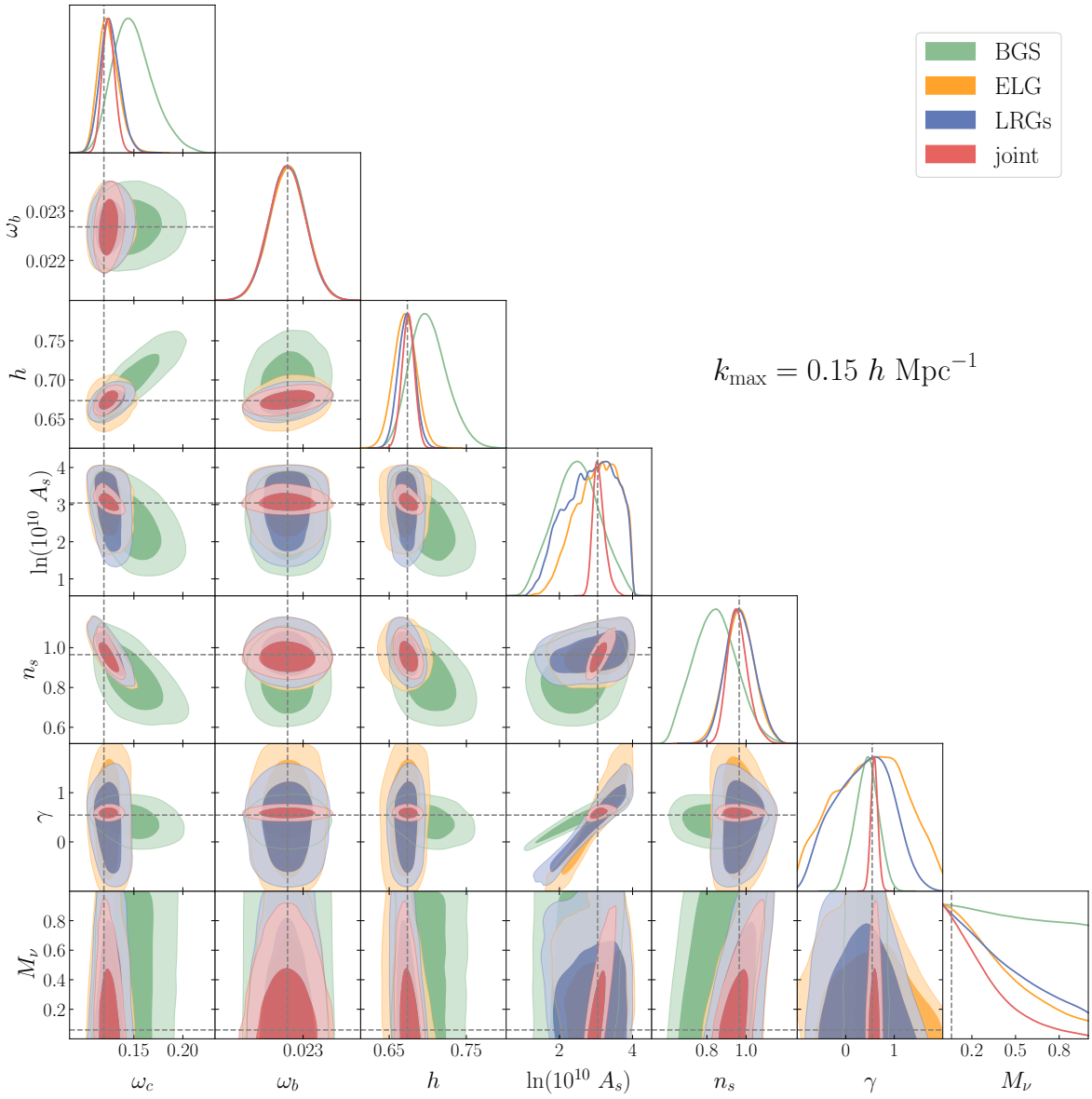

Figure 4.10 *Marginalised posterior for $\gamma\nu$CDM for the pessimistic case with $k_{\rm max} = 0.15\ h\ {\rm Mpc}^{-1}$. We fit the three samples separately and jointly, as detailed in the legend. Dashed grey lines mark the fiducial values.*

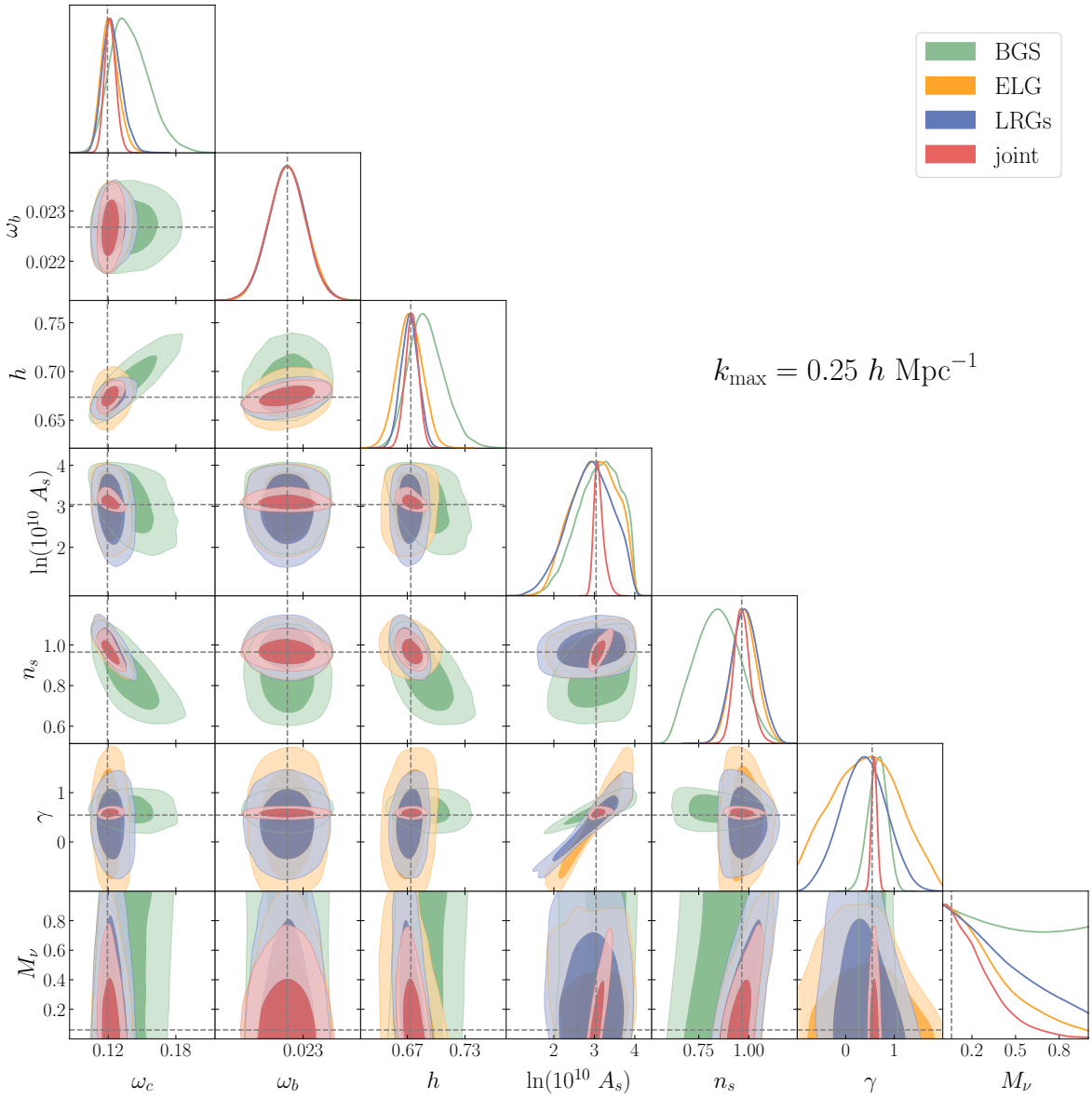

Figure 4.11 *Marginalised posterior for $\gamma\nu$CDM for the optimistic case with $k_{\rm max} = 0.25\ h\ {\rm Mpc}^{-1}$. We fit the three samples separately and jointly, as detailed in the legend. Dashed grey lines mark the fiducial values.*

Parameter	BGS	ELGs	LRGs	joint
Pessimistic $k_{\rm max} = 0.15\ h\ {\rm Mpc}^{-1}$				
ω_c	$0.148^{+0.016}_{-0.023}$	$0.1242^{+0.0088}_{-0.012}$	$0.1256^{+0.0095}_{-0.011}$	$0.1250^{+0.0059}_{-0.0069}$
	(0.1352)	(0.1202)	(0.1228)	(0.1212)
ω_b	0.02268 ± 0.00038	0.02269 ± 0.00037	0.02268 ± 0.00038	0.02268 ± 0.00038
	(0.02255)	(0.02230)	(0.02306)	(0.02303)
h	$0.700^{+0.020}_{-0.027}$	0.675 ± 0.014	0.676 ± 0.011	0.6765 ± 0.0078
	(0.688)	(0.671)	(0.679)	(0.676)
$\ln(10^{10}\ A_s)$	2.41 ± 0.55	$3.06^{+0.56}_{-0.43}$	$2.90^{+0.71}_{-0.55}$	3.00 ± 0.11
	(2.27)	(3.26)	(3.27)	(3.04)
n_s	$0.801^{+0.090}_{-0.11}$	0.935 ± 0.066	$0.933^{+0.060}_{-0.069}$	0.930 ± 0.041
	(0.752)	(0.955)	(0.950)	(0.950)
γ	$0.43^{+0.25}_{-0.22}$	$0.64^{+1.1}_{-0.63}$	$0.45^{+0.76}_{-0.58}$	0.587 ± 0.072
	(0.37)	(0.94)	(0.81)	(0.57)
σ_8	$0.65^{+0.11}_{-0.19}$	$0.84^{+0.15}_{-0.25}$	$0.80^{+0.15}_{-0.31}$	0.804 ± 0.037
	(0.55)	(0.903)	(0.912)	(0.809)
Optimistic $k_{\rm max} = 0.25\ h\ {\rm Mpc}^{-1}$				
ω_c	$0.137^{+0.014}_{-0.019}$	$0.1216^{+0.0068}_{-0.0088}$	$0.1231^{+0.0076}_{-0.0098}$	$0.1221^{+0.0048}_{-0.0055}$
	(0.1298)	(0.1175)	(0.1176)	(0.1135)
ω_b	0.02269 ± 0.00038	0.02268 ± 0.00038	0.02268 ± 0.00037	0.02267 ± 0.00038
	(0.02205)	(0.02245)	(0.02196)	(0.02139)
h	$0.688^{+0.016}_{-0.021}$	0.676 ± 0.013	0.6752 ± 0.0087	0.6755 ± 0.0067
	(0.679)	(0.676)	(0.669)	(0.662)
$\ln(10^{10}\ A_s)$	$3.04^{+0.57}_{-0.42}$	$3.01^{+0.46}_{-0.51}$	2.96 ± 0.48	3.063 ± 0.074
	(2.81)	(2.91)	(3.51)	(3.10)
n_s	0.80 ± 0.10	0.949 ± 0.052	0.947 ± 0.056	0.947 ± 0.034
	(0.872)	(0.975)	(0.965)	(0.982)
γ	$0.68^{+0.22}_{-0.19}$	0.47 ± 0.75	$0.47^{+0.57}_{-0.50}$	0.584 ± 0.058
	(0.521)	(0.287)	(1.016)	(0.549)
σ_8	$0.85^{+0.17}_{-0.21}$	$0.82^{+0.12}_{-0.25}$	$0.81^{+0.15}_{-0.23}$	0.822 ± 0.026
	(0.737)	(0.754)	(1.015)	(0.816)

Table 4.4 *Mean values and 68% c.l. values for γCDM with fixed neutrino mass $M_\nu =$ 0.06 eV for the three DESI-like galaxy samples fitted separately and jointly. We show the best-fit values in parentheses, and include derived constaints for σ_8.*

Parameter	BGS	ELG	LRGs	joint
		Pessimistic $k_{\rm max} = 0.15\ h\ {\rm Mpc}^{-1}$		
ω_c	$0.149^{+0.016}_{-0.024}$	$0.1243^{+0.0086}_{-0.012}$	$0.1257^{+0.0091}_{-0.011}$	$0.1242^{+0.0060}_{-0.0069}$
	(0.1431)	(0.1171)	(0.1181)	(0.1212)
ω_b	0.02269 ± 0.00038	0.02269 ± 0.00038	0.02268 ± 0.00037	0.02268 ± 0.00038
	(0.02322)	(0.02274)	(0.02261)	(0.02273)
h	$0.701^{+0.020}_{-0.027}$	0.670 ± 0.015	0.672 ± 0.011	0.6745 ± 0.0081
	(0.698)	(0.676)	(0.675)	(0.68)
$\ln(10^{10}\ A_s)$	2.47 ± 0.61	$3.02^{+0.79}_{-0.41}$	$2.85^{+0.96}_{-0.46}$	$3.08^{+0.12}_{-0.19}$
	(1.25)	(3.32)	(3.25)	(2.99)
n_s	0.84 ± 0.11	0.967 ± 0.075	$0.971^{+0.068}_{-0.079}$	$0.958^{+0.043}_{-0.058}$
	(0.816)	(0.969)	(0.979)	(0.95)
γ	0.43 ± 0.23	0.51 ± 0.71	$0.36^{+0.66}_{-0.55}$	0.590 ± 0.072
	(-0.07)	(0.04)	(0.81)	(0.563)
M_ν	—	< 0.434	< 0.494	< 0.314
	(0.017)	(0.024)	(0.026)	(0.032)
σ_8	$0.63^{+0.11}_{-0.22}$	$0.79^{+0.22}_{-0.25}$	$0.74^{+0.19}_{-0.30}$	$0.801^{+0.037}_{-0.046}$
	(0.351)	(0.925)	(0.900)	(0.798)
		Optimistic $k_{\rm max} = 0.25\ h\ {\rm Mpc}^{-1}$		
ω_c	$0.1398^{+0.0137}_{-0.0198}$	$0.1216^{+0.0065}_{-0.0087}$	$0.1237^{+0.0072}_{-0.0095}$	$0.1219^{+0.0046}_{-0.0054}$
	(0.1308)	(0.1197)	(0.1208)	(0.1203)
ω_b	0.02268 ± 0.00038	0.02269 ± 0.00038	0.02268 ± 0.00037	0.02267 ± 0.00037
	(0.02265)	(0.02278)	(0.02325)	(0.02207)
h	$0.690^{+0.016}_{-0.021}$	0.672 ± 0.013	0.673 ± 0.009	0.675 ± 0.007
	(0.684)	(0.678)	(0.683)	(0.671)
$\ln(10^{10}\ A_s)$	$3.106^{+0.666}_{-0.393}$	$2.989^{+0.644}_{-0.496}$	$2.893^{+0.615}_{-0.516}$	$3.116^{+0.084}_{-0.145}$
	(2.87)	(3.12)	(3.26)	(3.07)
n_s	0.844 ± 0.110	$0.978^{+0.058}_{-0.065}$	0.983 ± 0.067	$0.968^{+0.035}_{-0.045}$
	(0.877)	(0.958)	(0.979)	(0.962)
γ	$0.655^{+0.202}_{-0.180}$	0.405 ± 0.668	0.366 ± 0.462	0.588 ± 0.058
	(0.539)	(0.748)	(0.795)	(0.598)
M_ν	—	< 0.368	< 0.489	< 0.270
	(0.214)	(0.039)	(0.052)	(0.082)
σ_8	$0.817^{+0.181}_{-0.205}$	$0.776^{+0.174}_{-0.250}$	$0.738^{+0.166}_{-0.239}$	$0.815^{+0.026}_{-0.031}$
	(0.732)	(0.841)	(0.910)	(0.822)

Table 4.5 *Mean values and 68% c.l. values for $\gamma\nu$CDM for the three DESI-like galaxy samples fitted separately and jointly. We show the best-fit values in parentheses, and include derived constraints for σ_8.*

limiting their analysis at $k_{\rm max} < 0.1\ h\ {\rm Mpc}^{-1}$, and find an overly optimistic $\sigma(\gamma) = 0.0096$ for the case with fixed neutrino mass and dark energy parameter. This result is mainly driven by the differences in the dimensionality of the parameter space considered: their modelling only involves six parameters (nine when they also consider massive neutrinos and evolving dark energy), with only one (linear) bias, and no parameter controlling the overall amplitude of the power spectrum, whose inclusion can undermine the ability to measure γ.

A more comprehensive collection of forecasts for future experiments can be found in Ref. [327], that however still relies on a Fisher matrix approach. All forecasts presented there include Planck CMB and are limited to a linear model for the power spectrum, and can therefore be expected to be more constraining than our analysis. Nonetheless, the authors find $\sigma(\gamma) = 0.025$, which is closer to our forecasted $\sigma(\gamma) = 0.058$ than the results of Ref. [326].

We note that lifting some of the simplifications we make when generating the synthetic dataset could improve our constraints. For example, considering several redshift bins per sample can yield more precise measurements of the cosmological parameters, including γ [328, 329], but it also leads to an increased number of nuisance parameters and increased shot-noise per redshift bin. Moreover, some of the effects we are not accounting for are expected to result in reduced constraining power, for example the assumption of a Gaussian covariance, neglecting the convolution with the survey window function and in general additional observational systematics which can increase the size of the error bars on the measurements [330, 331].

We finally comment on our forecasts on massive neutrinos. A measurement of the neutrino mass is one of the main goals of Stage-IV surveys, with predicted errors well below the detection threshold (e.g., Refs. [320, 327, 332]). In this sense, our forecasts might seem too pessimistic, given our best case scenario gives $M_\nu < 0.27$ eV at 68% c.l. Once again, most previous forecasts take advantage of a combined analysis with CMB data from Planck, able to put tight constraints on the primordial parameters A_s and n_s. The latter are degenerate with the neutrino mass M_ν, as can be seen in Fig. 4.11 (or equivalently and more clearly in the green contours of Fig. 4.12): we therefore expect a joint analysis to be extremely beneficial. We do not perform such an analysis here, but we can get a sense of the impact by imposing a 3σ Planck prior on the primordial parameters, as done in Subsection 4.3.1 for the BOSS analysis. We only focus on the combination of the three redshift bins for the optimistic case with $k_{\rm max} = 0.25h\ {\rm Mpc}^{-1}$. Our results are shown in Fig. 4.12 and Tab. 4.6. As expected, the CMB prior on A_s and n_s breaks the degeneracies and brings the upper limit on the neutrino mass down to $M_\nu < 0.175$ eV at 68% c.l., with a 35% improvement over the case with no priors.

Despite being quite large in the context of a detection of the neutrino mass, our results are generally compatible with Ref. [297]; there, the authors performed a validation against

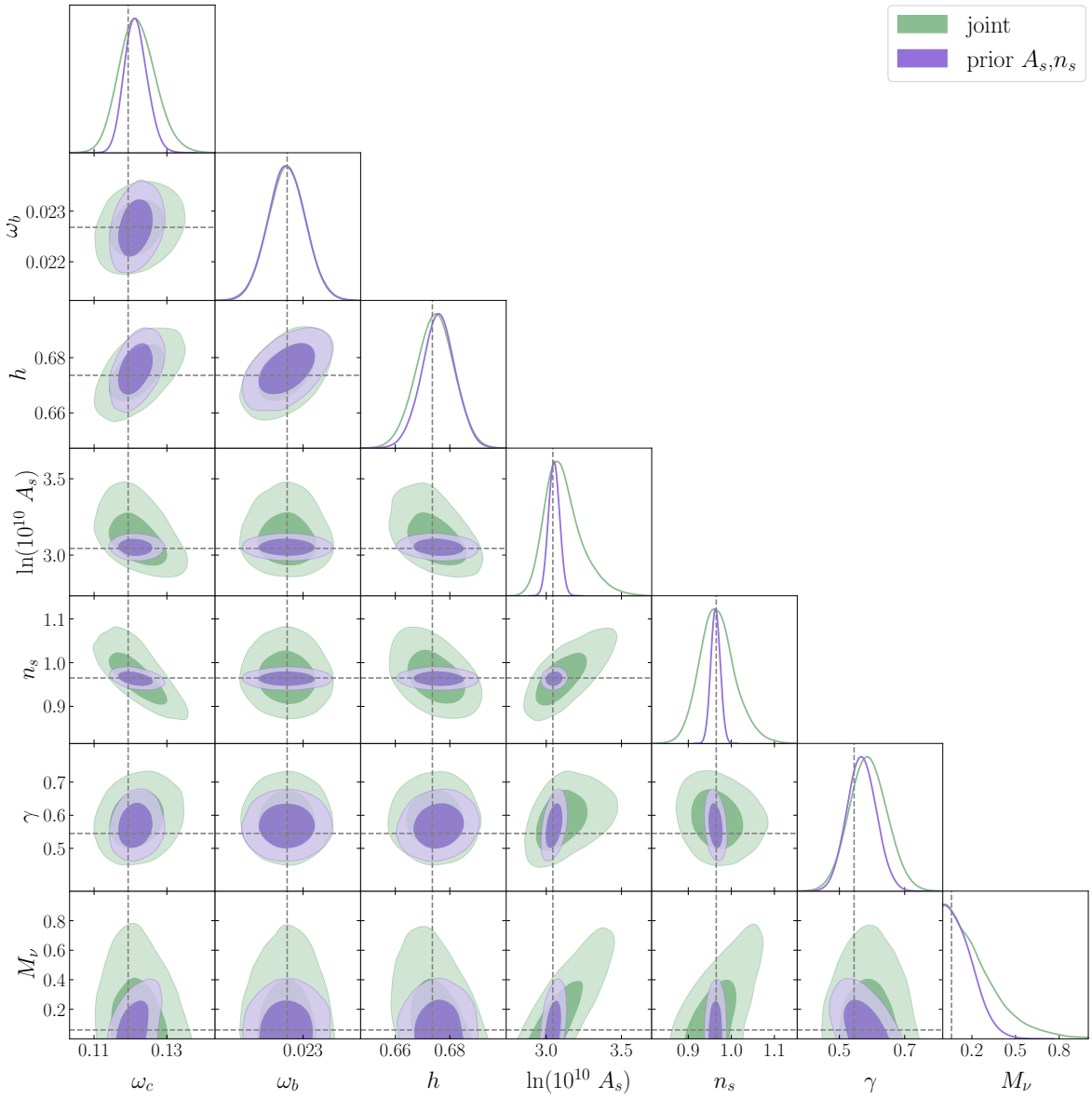

Figure 4.12 *Comparison between the forecast when no CMB prior is imposed (green lines and contours) and the case with 3σ Planck priors on A_s and n_s (purple lines and contours). We use $k_{\rm max} = 0.25\ h\ {\rm Mpc}^{-1}$.*

Parameter	baseline	prior on A_s,n_s
ω_c	$0.1219^{+0.0046}_{-0.0054}$	$0.1215^{+0.0028}_{-0.0034}$
	(0.1203)	(0.1211)
ω_b	0.02267 ± 0.00037	0.02268 ± 0.00037
	(0.02207)	(0.02266)
h	0.6746 ± 0.0069	0.6758 ± 0.0062
	(0.6712)	(0.6767)
$\ln(10^{10}\, A_s)$	$3.116^{+0.084}_{-0.14}$	3.052 ± 0.037
	(3.074)	(3.016)
n_s	$0.968^{+0.035}_{-0.045}$	0.963 ± 0.011
	(0.962)	(0.957)
γ	0.588 ± 0.058	0.568 ± 0.045
	(0.598)	(0.554)
M_ν	< 0.270	< 0.175
	(0.082)	(0.033)
σ_8	$0.815^{+0.026}_{-0.031}$	0.804 ± 0.020
	(0.822)	(0.807)

Table 4.6 *Best-fit and 68% c.l. values for the DESI forecasts with 3σ Planck priors on A_s,n_s. We use $k_{\rm max} = 0.25\ h\ {\rm Mpc}^{-1}$.*

N-body simulations of a similar 1-loop model for the power spectrum as the one adopted here. For a 25 Gpc^3/h^3 survey, similar in volume to our combined DESI-like mocks, they found $M_\nu < 0.49$ eV at 68% c.l. and conclude that 2-point summary statistics from spectroscopic clustering alone might not be sufficient detect the neutrino mass. Beside the combination with CMB data, we expect the combination with higher order statistics such as the bispectrum to bring significant improvements [333, 334]. We leave the study of the impact of the bispectrum on the determination of the neutrino mass scale to a future work. Further improvement should come from using photometric probes, namely cosmic shear and galaxy-galaxy lensing [281].

4.4 Conclusions

In this chapter, we presented the full-shape analysis of the power spectrum multipoles measured from BOSS DR12 galaxies with the inclusion of post-reconstruction BAO data. We used the windowless measurements of Ref. [62] combined with BAO measurements obtained from a variety of data-sets [62, 309–311]. We provided constraints on a single parameter extension of ΛCDM which allows for deviations from the standard scenario in the growth functions, the so-called growth index (or γ) parameterisation. We also explored the case with the total neutrino mass as a free parameter, and provided joint constraints for γ and M_ν. Our theoretical model for the power spectrum is based on the EFTofLSS and takes advantage of the `bacco` emulator for the linear power spectrum and the `FAST-PT` algorithm for a fast evaluation of the likelihood.

We explored different options for the priors on the parameters that determine the primordial power spectrum, A_s and n_s, finding that strong degeneracies in the extended parameter space result in large projection effects, especially concerning the parameters which regulate the amplitude of the power spectrum. For this reason, we applied a 3σ Planck prior on A_s and on both A_s and n_s, and obtained $\gamma = 0.647 \pm 0.085$ and $\gamma = 0.612^{+0.075}_{-0.090}$, respectively, $\sim 1\sigma$ consistent with the ΛCDM prediction $\gamma = 0.55$. For neutrinos we found $M_\nu < 0.478$ eV (Planck prior on A_s) and $M_\nu < 0.298$ eV (Planck prior on A_s, n_s), consistent with previous EFTofLSS-based studies of the BOSS dataset that did not perform a full joint analysis with CMB data [152, 315].

To assess the presence of projection effects in the case when no priors are imposed on the primordial parameters we generated synthetic datavectors with a fiducial set of cosmological and nuisance parameters, and then fitted them using the same numerical covariance used for the BOSS analysis. We found a similar shift of the posterior in the A_s–γ plane as the one found in our baseline BOSS analysis. Additionally, we performed a profile likelihood analysis, finding the maximum of the PL to be closer to the ΛCDM prediction than the peak of the marginalised posterior, and the confidence intervals derived from the PL to be larger and consistent with $\gamma = 0.55$ at 68% c.l..

Overall, we find the EFTofLSS model complemented with Planck priors to provide constraints on γ that are only $\sim 30\%$ larger than the official BOSS analysis [317], despite the fact that we did not perform a full joint analysis with CMB data. Additionally, our theoretical model features a significantly larger number of parameters, which is expected to degrade the constraints to some extent. On the other hand, the full-shape approach allows to provide direct constraints on the cosmological parameters.

In the second part of this work we presented forecasts for a Stage-IV spectroscopic survey, focusing on a DESI-like galaxy sample. We generated three synthetic datavectors at three redshifts using different values for the nuisance parameters, to match the expected BGS, LRGs and ELGs samples that are the target of DESI. We computed Gaussian covariance matrices neglecting the cross-correlation between samples, and adopted two different scale-cuts: $k_{\rm max} = 0.15\ h\ {\rm Mpc}^{-1}$ (pessimistic) and $k_{\rm max} = 0.25\ h\ {\rm Mpc}^{-1}$ (optimistic). We performed separate fits for each sample and then combined them in a joint analysis, finding the combination to provide significantly tighter constraints, yielding $\sigma(\gamma) = 0.058$ (0.072) in the optimistic (pessimistic) case, with a $\sim 85\%$ improvement with respect to our baseline BOSS analysis without CMB-based priors. Concerning neutrinos, we found that the improvement with respect to Stage-III constraints is only marginal, $M_\nu < 0.27$ eV ($M_\nu < 0.314$ eV) in the optimistic (pessimistic) case at 68% c.l..

In order to reduce the error bars on γ and M_ν, but also to keep the projection effects under control, we advocate the combination with additional observables. For example, a joint analysis with Planck data (or the inclusion of CMB-based priors, at least on the primordial parameters), can have a significant impact on the constraints. We explored this by performing a fit of the synthetic DESI-like data where we adopted 3σ Planck priors on A_s and n_s. We obtained a $\sim 20\%$ improvement in the measurement of γ, and $\sim 35\%$ for M_ν with respect to the case with no priors. Similarly, a combination with weak lensing can alleviate the degeneracies and yield tighter constraints [281]. However, an optimal exploitation of galaxy clustering data alone can already go in this direction: as shown in Chapter 3, the ability of the bispectrum to better determine the bias parameters can prove crucial in the context of extended models. We leave the study of the impact of the bispectrum for γCDM and $\gamma\nu$CDM to a future work.

Chapter 5

Model-Independent Approach for Dark Energy and Modified Gravity

This chapter is based on the following peer reviewed publication:

- B. Bose, **M. Tsedrik**, J.Kennedy, L. Lombriser, A. Pourtsidou, A. Taylor, 2023, *Fast and accurate predictions of the nonlinear matter power spectrum for general models of Dark Energy and Modified Gravity.* Published in MNRAS: doi:10.1093/mnras/stac3783, arXiv:2210.01094.

Here we introduce linear and nonlinear parameterisations of beyond standard cosmological physics in the halo model reaction framework, providing a model-independent prescription for the nonlinear matter power spectrum. As an application, we focus on Horndeski theories, using the Effective Field Theory of Dark Energy (EFTofDE) to parameterise linear and quasi-nonlinear perturbations. In the nonlinear regime we investigate both a nonlinear parameterised-post Friedmannian (nPPF) approach as well as a physically motivated and approximate phenomenological model based on the error function (Erf).

The main focus is modelling the nonlinearities, as well as testing and justifying the assumptions made. We compare the parameterised approaches' predictions of the nonlinear matter power spectrum to the exact solutions, as well as to state-of-the-art emulators, in an evolving dark energy scenario and two popular modified gravity models. We also suggest a minimal model parameterisation that is expanded into the nonlinear regime and is valid for a broad class of dark energy and modified gravity models.

Contributions

Benjamin Bose and I co-led this paper. Benjamin implemented new parameterisations into the `ReACT` code, performed thorough comparison tests, and drafted the paper. My contribution consists of a comprised literature review on EFTofDE, drafting various sections of the paper, reproducing calculations, investigating the optimal functional form

of the screening term, and performing validation checks of the code. I also produced a pedagogical Jupyter notebook to replicate the results from the paper. Lucas Lombriser and Andrew Taylor contributed to this project via valuable comments and discussions. Alkistis Pourtsidou and Joe Kennedy greatly contributed to the final draft of the paper.

5.1 Introduction

Fundamental models of nature generally begin with an action, which when combined with the principle of least action, gives us the temporal and spatial dynamics of the system. For the physical system that is our Universe (U), the action is widely accepted to be the action associated with general relativity (GR), the Einstein-Hilbert (EH) action, together with a matter contribution and cosmological constant:

$$S_U = S_{\rm EH} + S_{\rm M} = \int d^4x\sqrt{-g}\left[\frac{R}{2\kappa^2} - \frac{\Lambda}{\kappa^2}\right] + S_{\rm M}\,, \tag{5.1}$$

where $\kappa^2 = 8\pi G_{\rm N}$, $G_{\rm N}$ being Newton's gravitational constant and R is the 4-dimensional Ricci scalar that gauges the curvature of spacetime. $S_{\rm M}$ is the action of the matter content of the Universe, usually approximated by a perfect, pressureless fluid, but in general will contain all standard model fields. Λ is the cosmological constant that can appear naturally in a 4-dimensional action without violating preferred symmetries [335]. This constant is measured to be non-zero by a suite of cosmological probes such as the CMB radiation [22], SNIa [42, 69], and optical galaxy surveys (see, for example, Ref. [70]). This has led to the standard model of cosmology, ΛCDM, where CDM stands for cold dark matter[1]. We introduce the basic concepts of the standard cosmological model in Section 1.2.

The dark energy and cosmological constant problems (see Section 1.3) motivate a minimal extension of Eq. 5.1 to include a single extra scalar degree of freedom, ϕ. It is both physically and theoretically acceptable, i.e., not allowing for negative energies for example, and can encapsulate one or more cosmological constant problem solutions. Such an extension is found in the well studied Horndeski (H) scalar-tensor theory [336]. This is the most general, Lorentz-covariant scalar-tensor theory in 4 spacetime dimensions that yields second-order equations of motion, a basic condition for the physical viability of the theory, i.e., it is ghost-free. A universe described by Horndeski gravity is given as

$$\begin{aligned} S_U = S_{\rm H} + S_{\rm M} = \int {\rm d}^4x\sqrt{-g}\big[&G_2(\phi,X) - G_3(\phi,X)\Box\phi + G_4(\phi,X)R \\ &+ G_{4,X}(\phi,X)[(\Box\phi)^2 - (\nabla_\mu\nabla_\nu\phi)^2] + G_5(\phi,X)G_{\mu\nu}\nabla^\mu\nabla^\nu\phi \\ &- \frac{1}{6}G_{5,X}(\phi,X)[(\Box\phi)^3 - 3\Box\phi(\nabla_\mu\nabla_\nu\phi)^2 + 2(\nabla_\mu\nabla_\nu\phi)^3]\big] + S_{\rm M}\,, \end{aligned} \tag{5.2}$$

[1] CDM is the primary matter component in this model, outweighing baryonic matter five fold according to cosmological and astrophysical measurements such as the CMB.

where each $G_i(\phi, X)$, $i = 2, 3, 4, 5$ is a free function of the scalar field ϕ and its canonical kinetic term $X = -(\partial\phi)^2/2$, and $G_{i,X}(\phi, X) = \partial G_i/\partial X$.

This opens up a very large theory space which needs to be trimmed down with observational data. We have very strong data constraints at small spatial scales, i.e., within the Solar System and at astrophysical scales [104, 337], showing gravity is highly consistent with GR in this regime. We also have high quality observational data from cosmology, primarily from the CMB which is associated with early cosmological times. This allows new theoretical models most phenomenological freedom at large temporal and spatial scales as they must recover CMB and solar system observations. The small spatial scale constraints can be evaded using so called screening mechanisms (for reviews see Refs. [106, 338], also see Subsection 1.3.1) that force predictions of modified gravity models back to those of GR locally, while early time measurements like the CMB can easily be recovered through appropriate time evolution of ϕ.

An obvious late time cosmological data set directly related to gravity is the Large Scale Structure (LSS). A key summary statistic of this is the two point correlation function or power spectrum (in Fourier space) of the cosmological matter field. A prime science goal then becomes the production of accurate predictions of the matter power spectrum in general theories beyond-ΛCDM. For the Horndeski class of models, this is a nontrivial task as there are an additional four free functions of space and time to contend with, beyond the matter content and metric freedoms. Of course, one can always choose particular forms for the $G_i(\phi, X)$ and then produce predictions for the 2-point correlations of matter. This approach allows one to fully specify how matter should cluster at all physical scales, and there are many tools and models that do just that to varying degrees of accuracy [4, 130, 339–347].

If, on the other hand, we choose not to specify a particular model, we are required to parameterise both the linear and nonlinear scales i.e., the large and small physical scales of LSS respectively. At linear scales and for the Horndeski class of models, we can opt to perform a Taylor expansion of the G_i functions and truncate at some order. Linear theory can then be characterised by a small number of free functions of time but with no unique specification in the nonlinear regime. This describes the approach of the Effective Field Theory of Dark Energy (EFTofDE) [348, 349] (also see Ref. [350] for a great review). Note that if we wish to be even more general than Horndeski we can directly parameterise the linear relation between matter and the gravitational potential (see Eq. 1.38 and the corresponding discussion in Subsection 1.3.1).

On nonlinear scales, a parameterisation framework one can consider is the nonlinear parameterised post-Friedmannian (nPPF), which captures modified gravity or dark energy effects [351]. Both linear and nonlinear parameterisations then need to be consistently embedded in some more comprehensive predictive framework in order to be able to confront theory with LSS observations.

For past galaxy surveys the precision of the data did not call for high accuracy in the power spectrum modelling, as argued in Refs. [352, 353]. This changes with the next generation of Stage-IV surveys such as Euclid [354] and the Vera C. Rubin Observatory's Legacy Survey of Space and Time (VRO/LSST) [355]. These surveys will provide a significant reduction in statistical errors, errors which will be lowest in the nonlinear regime. With such precision, we have the opportunity to greatly constrain deviations to ΛCDM, including the well defined model space within Eq. 5.2. This is contingent on whether or not we can accurately and efficiently map these deviations to the matter power spectrum. Typically, to remain unbiased in our cosmological constraints, $\mathcal{O}(1)\%$ is quoted as being the target accuracy for theoretical predictions (see, for example, Ref. [281]). But this is not sufficient. We also require this map to be computationally efficient enough to perform data analyses. Without accuracy, we forfeit trust in our constraints. Without conciseness and efficiency we face major computational issues.

This work provides a balance that satisfies these criteria. We mainly focus on the Horndeski class of models, embedding the EFTofDE and nPPF approaches into the halo model reaction framework [4, 130, 299, 356–358], which is able to predict the nonlinear power spectrum for specified theories beyond-ΛCDM at $\mathcal{O}(1)\%$-level accuracy. We also present a completely model independent parameterisation of beyond-ΛCDM physics at nonlinear scales, which can be combined with similar parameterisations for the Universe's background expansion history and linear structure formation, giving a parameterisation for general deviations to ΛCDM.

5.2 Halo Model Reaction

We begin at the observational end and look how to model the halo model reaction. The leading order moment of the cosmological matter distribution is the nonlinear matter power spectrum, $P_{\rm NL}(k,z)$. This Fourier space quantity captures most of the matter clustering information at all scales (for a review see Ref. [33]). Following the halo model (see Ref. [359] for a review) based approach of Ref. [4], in a target theory of cosmology and gravity this quantity can be modelled as

$$P_{\rm NL}(k,z) = \mathcal{R}(k,z) P_{\rm NL}^{\rm pseudo}(k,z)\,, \tag{5.3}$$

where $P_{\rm NL}^{\rm pseudo}(k,z)$ is called the pseudo power spectrum. This is defined as the power spectrum of a ΛCDM universe but whose initial conditions have been set so as to match the target, beyond-ΛCDM, theory's linear total matter power spectrum $P_L(k,z)$ at some target redshift, z. The reason for making such a definition is that it guarantees the halo mass functions in the target and pseudo universes are similar since they will have the same linear clustering by definition. This results in a smoother transition between the

clustering statistics in the inter- and intra-halo regimes. This quantity can be modelled in a number of ways, for example, by using existing halo model based fitting functions such as `HMCode` [360–362] or for target theories that only predict a redshift dependent, but scale independent rescaling of the linear spectrum, ΛCDM-based emulators such as `EuclidEmulator2` [32] or `bacco` [31] can be used by tuning the spectrum amplitude parameter to match the modified cosmology's linear spectrum.

The reaction function $\mathcal{R}(k,z)$ represents all the corrections to the pseudo spectrum coming from nonlinear beyond-ΛCDM physics. Following Refs. [356, 363] (where the halo model reaction is derived and discussed in detail, as well as tested against numerical simulations) we can write this as

$$\mathcal{R}(k) = \frac{(1-f_\nu)^2\, P_{\rm hm}^{\rm (cb)}(k) + 2f_\nu\,(1-f_\nu)\, P_{\rm hm}^{\rm (cb\nu)}(k) + f_\nu^2 P_{\rm L}^{(\nu)}(k)}{P_{\rm hm}^{\rm pseudo}(k,z)}\,, \tag{5.4}$$

with the subscript 'hm' standing for halo model, (m) ≡ (cb + ν), cb for CDM and baryons, ν for massive neutrinos and $f_\nu = \Omega_{\nu,0}/\Omega_{m,0}$ being the massive neutrino energy density fraction at $z = 0$. The effects of massive neutrinos are included linearly through the weighted sum of the nonlinear cb halo model and linear massive neutrino spectra following the findings of Ref. [364]. We note that we do not consider massive neutrino effects in this work, but have included them in the expressions to highlight the generality of this approach (for a study with massive neutrinos see Ref. [363]).

The individual components are given by

$$P_{\rm hm}^{\rm (cb\nu)}(k) \approx \sqrt{P_{\rm hm}^{\rm (cb)}(k) P_{\rm L}^{(\nu)}(k)}\,, \tag{5.5}$$

$$P_{\rm hm}^{\rm (cb)}(k) = \left[(1-\mathcal{E})e^{-k/k_\star} + \mathcal{E}\right] P_{\rm L}^{\rm (cb)}(k) + P_{\rm 1h}^{\rm (cb)}(k)\,, \tag{5.6}$$

$$P_{\rm hm}^{\rm pseudo}(k,z) = P_{\rm L}(k,z) + P_{\rm 1h}^{\rm pseudo}(k,z), \tag{5.7}$$

where the parameters are given by

$$\mathcal{E}(z) = \lim_{k\to 0} \frac{(1-f_\nu)^2 P_{\rm 1h}^{\rm (cb)}(k,z)}{P_{\rm 1h}^{\rm pseudo}(k,z)}, \tag{5.8}$$

$$k_\star(z) = -\,\bar{k}\left(\ln\left[\frac{T_1(\bar{k},z) \pm T_2(\bar{k},z)}{(1-f_\nu)^2 P_{\rm L}^{\rm (cb)}(\bar{k},z)(1-\mathcal{E}(z))}\right]\right)^{-1}. \tag{5.9}$$

We take the "+" root if $\mathcal{E} > 1$, otherwise we take the "-" root. The T_i terms are given by

$$\begin{aligned} T_1(k,z) =& f_\nu^2 P_{\rm L}^{(\nu)}(k,z) + P_{\rm hm}^{\rm pseudo}(k,z)\mathcal{R}_{\rm SPT}(k,z) \\ & - (1-f_\nu)^2[\mathcal{E}(z) P_{\rm L}^{\rm (cb)}(k,z) + P_{\rm 1h}^{\rm (cb)}(k,z)]\,, \end{aligned} \tag{5.10}$$

$$T_2(k,z) = 2\sqrt{f_\nu^2 P_{\rm hm}^{\rm pseudo}(k,z) P_{\rm L}^{(\nu)}(k,z)\mathcal{R}_{\rm SPT}(k,z)}\,, \tag{5.11}$$

where $\mathcal{R}_{\rm SPT}(k,z)$ is the 1-loop Standard Perturbation Theory (SPT) [33] prediction for the reaction given by Eq. 5.4-Eq. 5.7 but with the replacements $P_L(k,z) \to P_{1-\rm loop}(k,z)$ and $P_L(k,z)^{\rm (cb)} \to P_{1-\rm loop}(k,z)^{\rm (cb)}$ and $\mathcal{E} = 1$. As in Ref. [4] the default scale where we calculate $k_\star$ is set to $\bar{k} = 0.06\ h\ {\rm Mpc}^{-1}$.

We see that Eq. 5.4 depends on three general predictions for beyond-ΛCDM theories: the 2-halo term which we have approximated by the linear power spectrum $P_{\rm L}$, the quasi-nonlinear power spectrum given by the 1-loop perturbation theory power spectrum $P_{1-\rm loop}$, and the highly nonlinear power spectrum given by the 1-halo term $P_{\rm 1h}$. The computation of these quantities requires the specification of the matter density fluctuations at different physical scales. The first two regimes (linear and quasi-nonlinear) are perturbatively derived up to 3rd order in the linear density fluctuation δ_L, while the fully nonlinear quantity, $\delta_{\rm NL}$, can be obtained using the assumptions of spherical collapse [359]. Both these routes require us to solve differential equations representing energy and momentum conservation on a cosmological background. Our Universe's spacetime metric is well described by the Friedman-Lemaître-Robertson-Walker (FLRW) metric, whose background expansion is described by the Hubble parameter $H(a) \equiv \dot{a}/a$, where a is the scale factor and an over-dot represents a derivative with respect to the metric time t.

Further, the conservation equations rely on the relation between the gravitational potential and the matter density fluctuation: the Poisson equation. In particular, we consider the Poisson equation in the perturbative limit, only valid up to quasi-nonlinear scales, as well as the fully nonlinear expression, valid at all scales

$$-\left(\frac{k}{aH(a)}\right)^2 \hat{\Phi}_{\rm QNL}(\boldsymbol{k},a) = \frac{3\Omega_{\rm m}(a)}{2}\mu(k,a)\,\hat{\delta}_{\rm QNL}(\boldsymbol{k},a) + S(\boldsymbol{k},a)\,, \tag{5.12}$$

$$-\left(\frac{k}{aH(a)}\right)^2 \hat{\Phi}_{\rm NL}(\boldsymbol{k},a) = \frac{3\Omega_{\rm m}(a)}{2}[1+\mathcal{F}(k,a)]\,\hat{\delta}_{\rm NL}(\boldsymbol{k},a)\,, \tag{5.13}$$

where $\Omega_{\rm m}(a) = \Omega_{\rm m,0}H_0^2/(H(a)^2a^3)$, $\Omega_{\rm m,0}$ being the total matter fraction today. Φ is the gravitational potential in the time-time component of the perturbed FLRW metric. This can be identified with the Newtonian gravitational potential in the non-relativistic limit, valid for the curvatures and velocities we consider. The subscripts QNL and NL denote "quasi-nonlinear" and "nonlinear" respectively. One should further note that Eq. 5.12 and Eq. 5.13 also assume a spherically symmetric density distribution.

The additional functions in Eq. 5.12 and Eq. 5.13 are as follows: $\mu(k,a)$ characterises the linear modification to GR, $\mathcal{F}(k,a)$ is the nonlinear modification and $S(\boldsymbol{k},a)$ is a source term capturing modifications at 2nd and 3rd order in the linear matter density

perturbations. The source term is given by [365]

$$S(\boldsymbol{k},a) = \int \frac{d^3\boldsymbol{k}_1 d^3\boldsymbol{k}_2}{(2\pi)^3}\,\delta_{\rm D}(\boldsymbol{k}-\boldsymbol{k}_{12})\gamma_2(\boldsymbol{k}_1,\boldsymbol{k}_2,a)\hat{\delta}(\boldsymbol{k}_1)\,\hat{\delta}(\boldsymbol{k}_2) + \int \frac{d^3\boldsymbol{k}_1 d^3\boldsymbol{k}_2 d^3\boldsymbol{k}_3}{(2\pi)^6}\delta_{\rm D}(\boldsymbol{k}-\boldsymbol{k}_{123})\gamma_3(\boldsymbol{k}_1,\boldsymbol{k}_2,\boldsymbol{k}_3,a) \times \hat{\delta}(\boldsymbol{k}_1)\,\hat{\delta}(\boldsymbol{k}_2)\,\hat{\delta}(\boldsymbol{k}_3)\,, \tag{5.14}$$

introducing two additional functions γ_2 and γ_3 characterising quasi-nonlinear modifications to the Poisson equation (for explicit expressions for these in the Horndeski class of models see Ref. [365]). The functions γ_2, γ_3 and $\mathcal{F}$ all encode details regarding the potential screening mechanism of the theory under consideration. On this point, it is worth noting that for general theories beyond-ΛCDM such mechanisms may not be present, in which case the spherical density distribution approximation assumed in Eq. 5.12 and Eq. 5.13 may break down [366]. For the modified gravity models considered in this work, which have some method of screening, this appears to be a reasonable approximation [367]. For a study of screened and unscreened models in the Horndeski class see Ref. [368].

In total, the halo model reaction, and so the nonlinear power spectrum, requires specification of four functions of space and time - one for the background $H(a)$, one for the linear regime $\mu(k,a)$, two for the quasi-nonlinear regime $\gamma_2(\boldsymbol{k}_1,\boldsymbol{k}_2,a)$ and $\gamma_3(\boldsymbol{k}_1,\boldsymbol{k}_2,\boldsymbol{k}_3,a)$ and finally one for the fully nonlinear regime $\mathcal{F}(k,a)$. In principle these functions are not completely independent, and one should have $\mathcal{F}\to\mu$ in the linear limit. We investigate the importance of respecting this limit in Section 5.5. Finally, we remind the reader that all these functions are required to compute the key ingredients of $\mathcal{R}$ (and hence $P_{\rm NL}$): $P_{\rm L}$, $P_{1-\rm loop}$ and $P_{\rm 1h}$.

The right half of Fig. 5.1 summarises the map from background and Poisson equations to the halo model reaction as described in this section. The left half of the figure will be the focus of the next section.

5.3 Parameterisations

We now move away from the observational end and return to the starting point, the fundamental action. In particular, here we mostly focus on the Horndeski action given in Eq. 5.2, but the approach can be trivially extended to further generality.

As pointed out, given a specific form of the G_i functions, the explicit functional forms of H, μ, γ_2, γ_3 and $\mathcal{F}$ can be directly derived. But rather than specifying the full covariant theory, i.e., 4 free functions of space and time, we ultimately wish to parameterise the action's predictions for cosmological matter clustering in terms of a few free constants.

To do this, we split LSS into three regimes: the *background* and *linear*, *quasi-nonlinear* and the *nonlinear*. The background, linear and quasi-nonlinear regimes will follow the

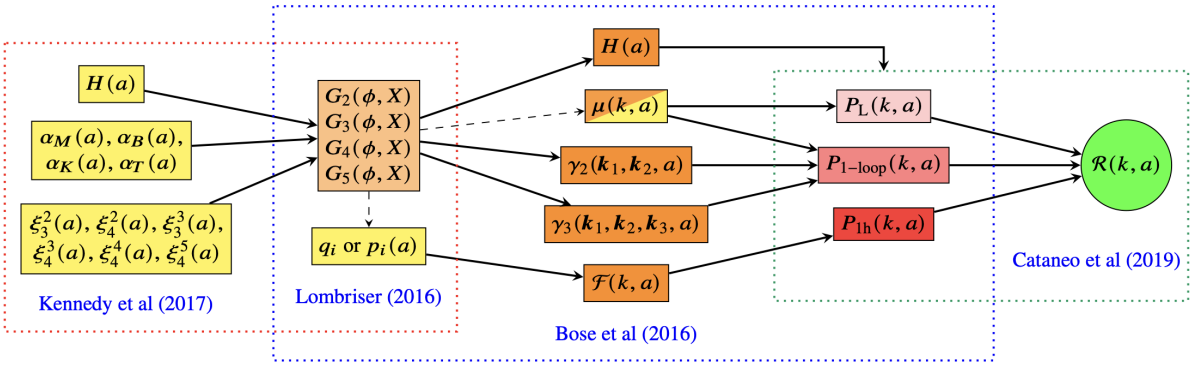

Figure 5.1 *A rough schematic of the map from the Horndeski action in the EFTofDE parameterisation (H, α_i, ξ_i^j) and nonlinear parameterisations (p_i or q_i) to $\mathcal{R}(k,t)$. The yellow rectangles indicate the input functions of time (here parameterised by the scale factor a) or constants. The orange rectangles indicate the modifications to the Poisson equation. $\mu(k,a)$ is bi-coloured indicating we may choose to parameterise it directly instead of starting at the action level. We provide the main sources in the literature for each piece of the map along with a dotted box roughly indicating their associated piece. Note that the solid arrows can only reconstruct G_i to the linear and quasi-nonlinear levels, which can in turn inform choices for p_i. The p_i provide the nonlinear complement in the G_i.*

well studied EFTofDE program [348, 349]. For the nonlinear regime we will consider two different parameterisations. One is the established nonlinear parameterised post-Friedmannian (nPPF) approach [351]. The other parameterisation we propose here is phenomenological and is based on some well known screening mechanisms. We begin by parameterising the background and linear regime.

5.3.1 Background and Linear: Effective Field Theory of Dark Energy

Among the methods to generically parameterise beyond-ΛCDM physics on cosmological scales, the methods of Effective Field Theory (EFT) have proven to be particularly useful. It is simply necessary to determine which symmetries one wishes the action to have before constructing various operators out of the fields and derivatives of the fields. One can trust the predictions made with an EFT as long as it is made at an energy scale below the "cutoff" of the theory, beyond which the validity of the EFT breaks down.

While not being an EFT in this strict sense, the EFTofDE is constructed in a similar manner and is capable of describing the dynamics of the cosmological background and perturbations in Horndeski theory in a generic manner. The EFTofDE approach breaks time diffeomorphism invariance of the cosmological background by choosing a particular gauge. By doing this one is able to form a theory out of operators which only respect spatial diffeomorphism invariance.

In constructing the EFTofDE action one begins by foliating spacetime with constant-time hypersurfaces. Utilising the complete freedom one has in choosing the coordinates of the theory we can set the scalar field to be only a function of time such that $\phi(x,t) \to \phi(t)$. In particular, we can choose

$$\phi = t/\kappa^2 \,. \tag{5.15}$$

This choice is called the unitary gauge and in this gauge the scalar field perturbations vanish, being absorbed into the time-time component of the metric. The operators in the EFTofDE are the cosmological perturbations themselves. In the unitary gauge we are free to include operators in the EFT which are only spatially diffeomorphism invariant, such as g^{00}.

Let us denote the normal vector to each spatial hypersurface as

$$n_\mu = -\frac{\partial_\mu \phi}{\sqrt{-(\partial\phi)^2}} \,. \tag{5.16}$$

The induced spatial metric of each hypersurface is then given by $h_{\mu\nu} = g_{\mu\nu} + n_\mu n_\nu$. This allows us to include the extrinsic curvature which is given by the projection of the derivative of the normal vector along the the hypersurface, onto the hypersurface $K_{\mu\nu} = h_{\mu\sigma}\nabla^\sigma n_\nu$. With the induced metric, one can also compute the intrinsic curvature of each hypersurface given by the three-dimensional Ricci scalar $R^{(3)}$.

Collecting relevant combinations of the invariants under residual spatial diffeomorphism symmetry gives the EFTofDE action, which is capable of describing the dynamics of the background and linear perturbations of Horndeski theory. The action is given by [101]

$$S_{U,L} = S^{(0,1)} + S^{(2)} + S_M[g_{\mu\nu}, \Psi_m] \,, \tag{5.17}$$

$$S^{(0,1)} = \int d^4x\sqrt{-g}\left[\frac{\Omega(t)}{2\kappa^2}R - \Lambda(t) - c(t)\delta g^{00}\right] \,, \tag{5.18}$$

$$\begin{aligned} S^{(2)} = \int d^4x\sqrt{-g}\Big[&\frac{M_2^4(t)}{2}(\delta g^{00})^2 - \frac{\bar{M}_1^3(t)}{2}\delta K \delta g^{00} \\ &- \bar{M}_2^2(t)\Big(\delta K^2 - \delta K^{\mu\nu}\delta K_{\mu\nu} - \frac{1}{2}\delta R^{(3)}\delta g^{00}\Big)\Big] \,. \end{aligned} \tag{5.19}$$

where $S_{U,L}$ represents the action of a Horndeski-universe that describes field dynamics up to the linear level in the matter and velocity perturbations. The $(0,1,2)$ represent the order in the perturbed quantities. The action is reduced to the standard cosmology from Eq. 5.1 for $\Omega(t) = 1$, $\Lambda(t) = \Lambda/\kappa^2$ and $c = M_2^4 = \bar{M}_1^3 = \bar{M}_2^2 = 0$.

In front of each term we include a free function of time called an EFT coefficient, giving a total of six free functions, $\{\Omega(t), \Lambda(t), c(t), M_2^4(t), \bar{M}_1^3(t), \bar{M}_2^2(t)\}$. Once we specify a metric, we also introduce any metric degrees of freedom. For FLRW this is the scale factor a, or equivalently the Hubble parameter $H(a)$. We can then employ the field

equation constraints, which in the FLRW are the Friedmann equations:

$$0 = \kappa^2(2c - \Lambda + \rho_{\rm m}) - 3H^2(\Omega + a\Omega')\,, \tag{5.20}$$

$$0 = \kappa^2\Lambda + H[aH'(2\Omega + a\Omega') + H(3\Omega + 3a\Omega' + a^2\Omega'')]\,, \tag{5.21}$$

where we have dropped the time dependence in constituent parameters for compactness, and use the scale factor to parameterise time. A prime denotes a scale factor derivative and $\rho_{\rm m}$ is the matter density at a. The Friedmann equations reduce the number of free functions describing the background and linear perturbations to five. Solving these equations yields

$$c(a) = -\frac{\rho_{\rm m}}{2} - \frac{aH[H'(2\Omega + a\Omega') + aH\Omega'']}{\kappa^2}\,, \tag{5.22}$$

$$\Lambda(a) = -\frac{H[aH'(2\Omega + a\Omega') + H(3\Omega + 3a\Omega' + a^2\Omega'')]}{\kappa^2}\,. \tag{5.23}$$

This means the free functions of the scale factor defining the background and linear theory would be $\{\Omega, H, M_2^4, \bar{M}_1^3, \bar{M}_2^2\}$, which we will refer to as the M-basis. We can alternatively write the Hubble function as the solution to

$$H(a):\ 0 = (2\Omega + a\Omega')H' + aH\Omega'' + \frac{\kappa\rho_{\rm m}}{aH} + \frac{2\kappa c}{aH}\,, \tag{5.24}$$

if we wish to specify c instead of H, for example.

Common in the literature is the α-basis $\{H, \alpha_M, \alpha_B, \alpha_K, \alpha_T\}$ which has a clearer physical interpretation of the effects of each function (see, for example, Ref. [100] and Subsection 1.3.1). We provide the map between the α- and M-bases[2]

$$\alpha_M = \frac{a(M^2)'}{M^2}\,, \tag{5.25}$$

$$\alpha_B = -\frac{aH\Omega' + \kappa^2\bar{M}_1^3}{HM^2\kappa^2}\,, \tag{5.26}$$

$$\alpha_K = \frac{2c + 4\bar{M}_2^4}{M^2H^2}\,, \tag{5.27}$$

$$\alpha_T = -\frac{\bar{M}_2^2}{M^2}\,, \tag{5.28}$$

where $M^2 = \Omega\ \kappa^{-2} + \bar{M}_2^2$. Note that one can alternatively specify M^2 and solve for H.

To end this section, another basis worth considering is the basis introduced in Ref. [370]: $\{H, M^2, c_s^2, \alpha, \alpha_{B0}\}$ (also see Ref. [371]), which implicitly assumes $\alpha_T = 0$ (see Subsection 5.4.3 for motivation). This basis allows for some simple priors on the functions that ensure the theory has no ghost or gradient instabilities, i.e., negative energies or

[2]Note the factor of "$-1/2$" difference in α_B between our expression and that of `EFTCAMB` [369] or [370], for instance.

imaginary sound speeds. We will refer to this basis as the s-basis. The priors to ensure stability on these functions are then simply $M^2, c_s^2, \alpha > 0$, and α_{B0} is constant[3]. The map between the s- and α-bases is given by

$$c_s^2 = \frac{2}{\alpha}\Big[\frac{a\alpha_B'}{2} - (1+\alpha_T)\left(1-\frac{\alpha_B}{2}\right)^2 + \left(1+\alpha_M - \frac{aH'}{H}\right)\left(1-\frac{\alpha_B}{2}\right) - \frac{\rho_{\rm m}}{2H^2M^2}\Big]\,, \tag{5.29}$$

$$\alpha = \alpha_K + \frac{3}{2}\alpha_B^2\,, \tag{5.30}$$

where c_s is the speed of sound, while $\alpha_{B0} = \alpha_B(a=1)$ is the boundary condition (α_B's value today) specified to solve the differential equation given by Eq. 5.29.

In what follows we will stick with the α-basis and implement this as the default basis in the accompanying code `ACTio et ReACTio`. We provide the explicit form of the linear modification to the Poisson equation in this basis in Subsection C.1.1. We leave it to the user to perform the transformation from their preferred basis to the α-basis, and provide an accompanying notebook `GtoPT.nb` that performs some of these transformations.

5.3.2 Quasi-Nonlinear: Covariant Theory Map

To fully specify the halo model reaction, we need to go beyond the linear matter perturbations. In particular, we also require the 2nd and 3rd order density perturbations to solve for the 1-loop power spectrum entering $\mathcal{R}_{\rm SPT}$ in Eq. 5.10-Eq. 5.11. This requires us to expand to fourth order in the metric perturbation δg^{00} and extrinsic curvature $\delta K^{\mu\nu}$ in Eq. 5.17. This has been done in Ref. [102] and has been used to calculate the 1-loop spectrum in Ref. [373]. Further, in Ref. [101] the authors relate the EFTofDE functions up to a given order to the corresponding covariant theory's Lagrangian G_i functions as

$$G_i(\phi, X) = g_i(\phi, X) + \Delta G_i(\phi, X)\,, \tag{5.31}$$

where g_i, $i \in \{2,3,4,5\}$, are well-defined functions of ϕ, X and the lower order EFTofDE parameters, e.g., $\{H, \alpha_M, \alpha_B, \alpha_K, \alpha_T\}$. The other terms are given as

$$\Delta G_{2,3} = \sum_{n>2} \xi_n^{(2,3)}(\phi)\Big(1 + X\kappa^4\Big)^n\,, \tag{5.32}$$

$$\Delta G_{4,5} = \sum_{n>3} \xi_n^{(4,5)}(\phi)\Big(1 + X\kappa^4\Big)^n\,, \tag{5.33}$$

where ΔG_i are higher order corrections to the covariant action and $\xi_n^i(\phi)$ are higher order EFTofDE functions, X again being the scalar field canonical kinetic energy term.

[3] We note that this basis does not ensure the absence of a tachyonic instability [372].

A particular covariant theory is specified once ξ_n^i are given for all $n \in \mathbb{N}$, but if we truncate at some order n_t, we specify the subset of Horndeski theories which are identical on scales described by the EFTofDE up to $\xi_{n_t}^i$. Up to 3rd order in the matter density perturbation, we introduce 6 new functions with $n_t = 4$. Together with the background and linear order functions, this gives a total of 11 free functions of time for the quasi-nonlinear scales. The G_i given in Eq. 5.31 can then be related to μ, γ_2 and γ_3 by the map provided in the Appendices of Refs. [365, 374].

In Section C.1 we provide the map between the 5 linear EFTofDE functions in the α-basis and the linear modification to the Poisson equation, μ, used in Eq. 5.12. The 2nd and 3rd order functions γ_2 and γ_3 (see Eq. 5.14) are significantly more complicated but can be derived by using the map from the EFTofDE to $G_i(\phi, X)$ provided in Ref. [101] and then the $G_i(\phi, X)$ to γ_2 and γ_3 given in Ref. [365]. The map, although not reproduced here in full, is given in detail in a `Mathematica` notebook provided in the `ACTio et ReACTio` repository, `GtoPT.nb`. This being said, in Section 5.4 we give support for the omission of γ_2 and γ_3 in the calculation of $\mathcal{R}$ for moderate to low modifications to gravity, and given the additional degrees of freedom we will introduce in the nonlinear regime.

Having specified a route between the Horndeski action and the linear and 1-loop power spectra, $P_{\rm L}(k, a)$ and $P_{\rm 1-loop}(k, a)$, we now look at two methods of parameterising clustering in the highly nonlinear regime, characterised by the 1-halo term, $P_{\rm 1h}(k, a)$. This will then specify a full parameterisation of the halo model reaction $\mathcal{R}$, and consequently the nonlinear power spectrum, $P_{\rm NL}(k, a)$.

5.3.3 Nonlinear

The effects of modified gravity on the nonlinear cosmic structure formation are captured by the effective deviation $\mathcal{F}$ from the gravitational constant in the nonlinear Poisson equation given in Eq. 5.13 and the cosmological background evolution. Specifically, the modified Poisson equation alters the evolution equation for the halo top-hat radius $R_{\rm TH}$ [375]. This quantity gives an estimate for $\delta_{\rm NL}$, needed to compute the 1-halo power spectrum. Here we discuss two parameterisations of $\mathcal{F}$.

Nonlinear Parameterised Post-Friedmannian Framework

Following the nPPF approach in Ref. [351], the effective gravitational coupling for generic screening mechanisms and other suppression effects can be decomposed as a function of scale r

$$1 + \mathcal{F}(a, r) = A + \sum_i^{N_0} B_i \prod_j^{N_i} \mathcal{F}_{ij} \,, \tag{5.34}$$

where $\mathcal{F}_{ij}$ are some transition functions encapsulating screening or other suppression effects such as a Yukawa suppression. N_0 and N_i characterise their respective number.

In the fully screened limit, the effective coupling reduces to A, typically unity, whereas it becomes B_i in the fully unscreened limit, matching linear theory. To parameterise these transitions, Ref. [351] adopted a generalised form of the Vainshtein screening effect in the DGP braneworld model [107]

$$\mathcal{F} \sim b \left(\frac{r}{r_{\rm scr}}\right)^{a_f} \left\{ \left[1 + \left(\frac{r_{\rm scr}}{r}\right)^{a_f}\right]^{1/b} - 1 \right\} , \tag{5.35}$$

where $r_{\rm scr}$ denotes the screening scale, which in general can be time, mass, and environment dependent. The parameter a_f (not to be confused with the scale factor) determines the radial dependence of the coupling in the screening limit along with b that characterises an interpolation rate between the screened and unscreened limits.

Screening effects such as the chameleon [376–378] symmmetron [379, 380], k-mouflage [345, 381], and Vainshtein [107, 339, 382] mechanisms as well as other suppression effects such as the linear shielding mechanism [383] or Yukawa suppression, can be analytically mapped onto Eq. 5.35 by matching expressions in the limits of large and small r and $r \to r_{\rm scr}$. The relevant expressions may be found in Ref. [351]. It is worth highlighting that the parameters of Eq. 5.35 for a given screening model may in principle be directly read off from Eq. 5.2 by employing the scaling method of Refs. [384, 385] and counting the powers of second and first spatial derivatives and the scalar field potential. Note that the parameter b may be understood as the choice of transition template used to approximately cast the screening effect into. Alternatively to Eq. 5.35, one could also adopt other transition functions such as a hyperbolic tangent, a sigmoid or an error function as we will propose in Subsection 5.3.3. For DGP, the choice of Eq. 5.35 with $b = 2$ becomes exact.

To implement Eq. 5.35 in the spherical collapse model, one replaces $r/r_{\rm scr} \to y/y_{\rm scr}$, where y is the normalised top-hat radius (Eq. C.44). A single general element $N_0 = N_1 = 1$ can then be described by seven parameters (or functions) p_{1-7} in addition to $p_0 = A$ (typically $= 1$). The first three, p_{1-3}, determine a_f, b, and B. The other four are used to generally capture possible time, mass, and environmental dependencies of the dimensionless screening scale, which can be modelled as [351]

$$y_{\rm scr} = p_4 a^{p_5} \left(2 G_N \, H_0 M_{\rm vir}\right)^{p_6} \left(\frac{y_{\rm env}}{y_{\rm h}}\right)^{p_7} , \tag{5.36}$$

where $y_{\rm h}$ and $y_{\rm env}$ refer to the normalised radii of the the halo and the environment respectively, H_0 is the Hubble constant and $M_{\rm vir}$ is the virial mass of the halo[4]. In this

[4]Note that in `ReACT` we use the initial comoving top-hat radius, $R_{\rm th}$ (see Subsection C.2.4), as an input parameter instead of mass, related as $M_{\rm vir} = 4\pi\bar{\rho}_{{\rm m},i}(1+\delta_i)(a_i R_{\rm th})^3/3 \approx 4\pi\Omega_{{\rm m},0}\rho_{\rm crit}R_{\rm th}^3/3$ with the critical density $\rho_{\rm crit}$ and $1+\delta_i \approx 1$.

way, we can simplify Eq. 5.35 to [351]

$$\mathcal{F}_{\rm nPPF} = p_1 p_2 \frac{(1+s^{a_f})^{\frac{1}{p_1}} - 1}{s^{a_f}}\,, \tag{5.37}$$

where

$$a_f = \frac{p_1}{p_1 - 1} p_3 \tag{5.38}$$

and $s = y_{\rm scr}/y_{\rm h}$. Note we have set $p_0 = 1$. The parameters p_{1-7} can be computed from theory and in many cases take on trivial values (see Subsection C.2.2). It is worth highlighting here that the nPPF formalism has also been implemented in N-body simulations and cast into Fourier space [386], where it was shown to accurately match simulations of exact model implementations.

Finally, we consider the large, linear scale limit of $\mathcal{F}$. Eq. 5.39 provides a parameterised function for the screening regime, where we have a transition to GR from some large scale modification. In this form, it does not capture any additional effects coming from say Yukawa suppression, typical of chameleon theories. Such phenomena may become relevant for the spherical collapse calculation at early times or for very large halo masses. In order to correctly capture this, we could either model the Yukawa suppression as another transition cast into Eq. 5.37 or simply augment Eq. 5.37 with the linear modification $\mu(k, a)$ as

$$\mathcal{F}_{\rm nPPF} = p_1 p_2 \frac{(1+s^{a_f})^{\frac{1}{p_1}} - 1}{s^{a_f}} \times (1 - \mu(\tilde{k}, a))\,. \tag{5.39}$$

In this case we also need to perform the Fourier transform of $\mu(\tilde{k}, a)$, which is non-trivial. As a first order approximation, we parameterise this with a simple scaling of the inverse of the comoving initial top-hat radius $R_{\rm th}$ as

$$\tilde{k} = \frac{10^{p_8}}{a^2 y_{\rm h} R_{\rm th}}\,, \tag{5.40}$$

where the dimensionless constant p_8 calibrates the Yukawa suppression. The Fourier transform can be made more sophisticated [386] but in Section 5.5 we find the impact of Yukawa suppression is negligible for the $f(R)$ models we consider, and so only include this augmentation for completeness. Further, Eq. 5.39 would only be meaningful for a non-trivial scale dependent $\mu(k, a)$. For scale-independent theories one can absorb the scaling provided by $\mu(a)$ in the $p_2(a)$ parameter of Eq. 5.37.

Phenomenological Parameterisation

With its full freedom, the nPPF parameterisation is a very flexible way of modelling the nonlinear scales. It is able to capture various specific covariant theories exactly or to high accuracy (see Subsection C.2.2 and Section 5.5), and given a covariant theory,

say from the Horndeski class, we can map its nonlinear Poisson modification to the p_i parameters. On the other hand, if we remain agnostic about the covariant theory, 8 additional parameters, some of which may also be time dependent, poses computational issues as well as degrades the amount of cosmological and gravitational information we can extract due to degeneracies between these nuisance and the physical parameters of interest.

With this in mind, we propose the following general and reduced parameterisation of $\mathcal{F}$ based on the error function (Erf). We have found this mimics the general profile of the effective gravitational constant in various modified gravity theories. Essentially we wish to capture a basic transition from unscreened to screened regimes. The simple form we adopt is given by

$$\mathcal{F}_{\rm Erf} = {\rm Erf}[a y_{\rm h} 10^{\bar{J}}] \times (1 - \mu(\tilde{k}, a)) \,, \tag{5.41}$$

where as in the nPPF case, we use

$$\tilde{k} = \frac{10^{q_4}}{a^2 y_{\rm h} R_{\rm th}} \,, \tag{5.42}$$

and

$$\bar{J} = q_1 - q_2 \log(R_{\rm th}) + q_3 \log(a y_{\rm env}) \,. \tag{5.43}$$

μ is the linear modification to gravity. In the EFTofDE parameterisation μ is given in Eq. C.1, but this can also be parameterised more generally [370, 387, 388].

The Erf model introduces 4 free constants:

$\mathbf{q_1}$: This parameterises the screening scale and goes as its inverse.

$\mathbf{q_2}$: This gives the halo mass dependency of the screening scale.

$\mathbf{q_3}$: This gives the environment dependency of the screening scale.

$\mathbf{q_4}$: This calibrates any existing Yukawa suppression scale.

The time dependence of $\mathcal{F}_{\rm Erf}$ is fixed and so for a specified cosmology and set of EFTofDE parameters, we only need to adjust the constants $\{q_1, q_2, q_3, q_4\}$. To provide some insight, we note the following limits

$$\lim_{q_1 \to \infty} 1 + \mathcal{F}_{\rm Erf} = \mu \to \textbf{Unscreened limit} \,, \tag{5.44}$$

$$\lim_{q_1 \to -\infty} 1 + \mathcal{F}_{\rm Erf} = 1 \to \textbf{GR limit} \,, \tag{5.45}$$

$$\lim_{q_2, q_3 \to 0} 1 + \mathcal{F}_{\rm Erf} \to \textbf{Vainshtein type models} \,, \tag{5.46}$$

$$\lim_{q_3 \to 0} 1 + \mathcal{F}_{\rm Erf} \to \textbf{k} - \textbf{mouflage type models} \,, \tag{5.47}$$

$$q_3 > 0 : \; 1 + \mathcal{F}_{\rm Erf} \to \textbf{chameleon type models} \,, \tag{5.48}$$

where we refer to the main types of screening mechanisms typical of scalar-tensor theories (see Subsection 5.3.3). Note that all parameters lose their meaning as $\mu(k,a) \to 1$, which in the EFTofDE case is when the relevant parameters assume their GR values.

Given this, we can take q_2 and q_3 to be positive. Being exponents of the top-hat radius and environment parameter, they are also not expected to be very large, and as we will see in Section 5.5, they turn out to be $\mathcal{O}(1)$. Further, since in the GR limit $\mu \to 1$, and so $\mathcal{F}_{\rm Erf} \to 0$ irrespective of the value of q_1, we can also take q_1 to be positive. We also find q_1 to be an $\mathcal{O}(1)$ parameter.

Parameter q_4, which calibrates the Yukawa suppression scale, is generally only relevant for theories where the linear growth factor, or Poisson modification μ, is scale-dependent. As we will show in Subsection 5.5.3, q_4 does not appear to be relevant for the scales associated with spherical collapse. We note q_4 can in principle take on negative values, pushing the Yukawa suppression to smaller scales. As $q_4 \to \infty$ the Yukawa suppression scale also goes to infinity. We leave its relevance for more general theories for a future work.

We provide a `Mathematica` notebook, `Nonlinear.nb`, with all the forms of $\mathcal{F}$ considered in this chapter along with comparisons. Finally, the left half of Fig. 5.1 summarises the map from the parameterised action, together with additional parameters, to the Poisson equation modifications as described in this section, completing the map from action to reaction.

5.4 Approximations and Overview

We have outlined a map that goes from the parameterised action and structure formation $\{H\}_b$,$\{\alpha_M, \alpha_B, \alpha_K, \alpha_T\}_{\rm L}$,$\{\xi^2_3, \xi^2_4, \xi^3_3, \xi^3_4, \xi^4_4, \xi^5_4\}_{\rm QNL}$,$\{p_1, p_2, p_3, p_4, p_5, p_6, p_7, p_8\}_{\rm NL}$ or $\{q_1, q_2, q_3, q_4\}_{\rm NL}$ to the nonlinear effects on the power spectrum $\mathcal{R}(k,a)$, where "b" stands for background, "L" for linear, "QNL" for quasi-nonlinear and "NL" for nonlinear. A schematic of this map is given in Fig. 5.1. An important point worth stressing is that our nonlinear parameterisations are completely general, and not specific to the Horndeski class of theories. They do however rely on $\mu(k,a)$, which one can always choose to parameterise in a model independent way.

Considering the Horndeski class for concreteness, the EFTofDE and nonlinear parameterisations constitute a very large set of arbitrary functions of time and constants. Despite it being significantly less than the infinite number of theories contained within the Horndeski class, it is still arguably too many for statistical data analyses, both on computational and scientific grounds. Thankfully, as we will shortly motivate, these sets can be yet reduced significantly.

To reduce or optimise the parameter space without sacrificing accuracy for the forthcoming surveys, we consider the following:

(**1**) We assume the quasi-static approximation (QS) for all perturbative calculations (see, for example, Ref. [389, 390]). In other words, we ignore the effects from time derivatives in the Einstein equations for perturbations at scales larger than the cosmological horizon.

(**2**) We assume $\gamma_2 = \gamma_3 = 0$, i.e., no loop-corrections.

(**3**) Existing observational and theoretical constraints.

(**4**) Time parameterisations of EFTofDE functions, $\alpha_i(a)$.

(**5**) The parameterised nPPF (see Eq. 5.39) or phenomenological (see Eq. 5.41) form of $\mathcal{F}$ is flexible enough to capture general modifications to gravity.

In this section we will motivate approximations **(1)** - **(4)** with direct reference to the accompanying code `ACTio et ReACTio`. Assumption **(5)** will be addressed separately in Section 5.5.

5.4.1 Quasi-Static Approximation

We begin by noting that the QS in linear theory can be easily avoided by using a Boltzmann code such as `EFTCAMB` [391, 392] to calculate the linear input spectrum or transfer function[5]. This option is available in our code, but the default setting assumes a ΛCDM linear spectrum or transfer function at $z = 0$ and rescales it using the internally calculated growth functions of the desired theory. This is done using the linear form of Eq. 5.12 (see Eq. C.1) which assumes the quasi-static approximation. Being able to use a ΛCDM linear spectrum enhances the computational efficiency of our code as it avoids a call to `EFTCAMB`. `EFTCAMB` is significantly slower than `CAMB` [290], which already takes $\mathcal{O}(1)$ seconds to produce a linear spectrum. In this case one can also use a linear spectrum emulator like `CosmoPower` [291] or `bacco` [133], which takes $\mathcal{O}(0.1)$ seconds to produce the linear spectrum. Note that one can also employ `CosmoPower` to construct an emulator for the linear power spectrum in the EFTofDE based on `EFTCAMB` output, overcoming the QS and computational inefficiency issues.

Given the utility in using the QS, we want to get an idea of its validity. In Fig. 5.2 we show the effects of the QS at $z = 0$ and $z = 1$ for models with non-zero α_K and α_B KGB [393], on the nonlinear spectrum as given by Eq. 5.3. We use the halofit [394] formula for $P_{\rm NL}^{\rm pseudo}$ and assume a ΛCDM background expansion, $H(a) = H_{\Lambda\rm CDM}(a)$ as well as no screening effects, i.e., $\mathcal{F} = \mu - 1$ and $\gamma_2 = \gamma_3 = 0$.

We find that the QS is valid for these mild to moderate parameter choices on scales of $k \geq 0.1h/\text{Mpc}$. Upcoming surveys will probe scales larger than this which may be

[5]The QS can be partly circumvented in the nonlinear regime, Eq. 5.39 and Eq. 5.41, by also using the prediction of $\mu(k, a)$ taken from say `EFTCAMB`.

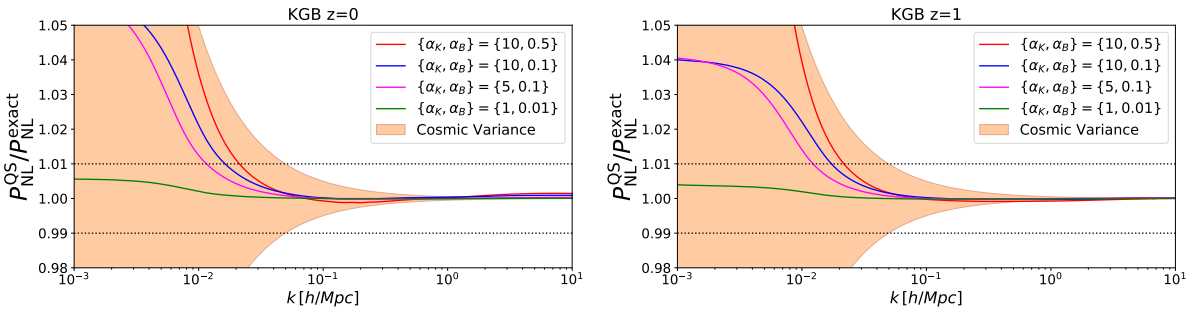

Figure 5.2 *Ratio of the quasi-static approximated (QS) nonlinear spectrum to the exact calculation. We show the results for four EFTofDE models with* $\{\alpha_K, \alpha_B\}$ *non-zero and all other* α *parameters set to 0 and a* Λ*CDM background expansion, at* $z = 0$ *(left) and* $z = 1$ *(right). The exact calculation uses Eq. 5.4 with an* `EFTCAMB` *linear spectrum while the QS uses Eq. 5.4 with a rescaled* Λ*CDM linear spectrum using the modified growth equations, making use of Eq. C.1. The orange band represents the error coming from cosmic variance assuming an effective survey volume of* $V_{\rm eff} = 20\ {\rm Gpc}^3/h^3$*. We assume* $\mathcal{F} = \mu - 1$ *and* $\mathcal{E} = 1$ *in all nonlinear computations. The dotted lines mark 1% deviations which is an optimistic estimate on the modelling errors of the halo model reaction framework.*

an issue. Taking into account cosmic variance assuming a galaxy survey volume similar to the effective volume of forthcoming surveys, $V_{\rm eff} = 20\ {\rm Gpc}^3/h^3$ [10, 354, 395], the QS is still a sub-dominant source of error for even extreme choices of α_B and α_K (see Subsection 5.4.3). Note that time derivatives of the fields drop out from the calculation of μ for $k \to \infty$ in Horndeski theories [390, 396]. We note at small scales, modelling inaccuracies and shot noise errors will arguably dominate any inaccuracies incurred from using the QS.

We do however warn that the QS begins to break significantly for beyond Horndeski theories [396]. For large modifications to GR within Horndeski, we advise comparing the resulting nonlinear spectrum with and without the QS against the predicted errors on the specific data that is being analysed. Further, we have implemented the following necessary condition for the QS to hold in our code [110]

$$\frac{k}{aH(a)} > c_s^2(a)\,, \tag{5.49}$$

where c_s^2 is given by Eq. 5.29, with its violation producing a warning prompt.

5.4.2 Loop-Corrections Approximation

We begin by noting that setting $\gamma_2 = \gamma_3 = 0$ implies we have $R_{\rm SPT} \approx 1$ in Eq. 5.10 as the 1-halo terms are subdominant. This forces the argument of the logarithm in Eq. 5.9 to be very close to unity, giving a very large $k_\star$. Effectively, this is the same as setting $\mathcal{E} = 1$ in Eq. 5.6. This is the choice we take when adopting this approximation. We should remark

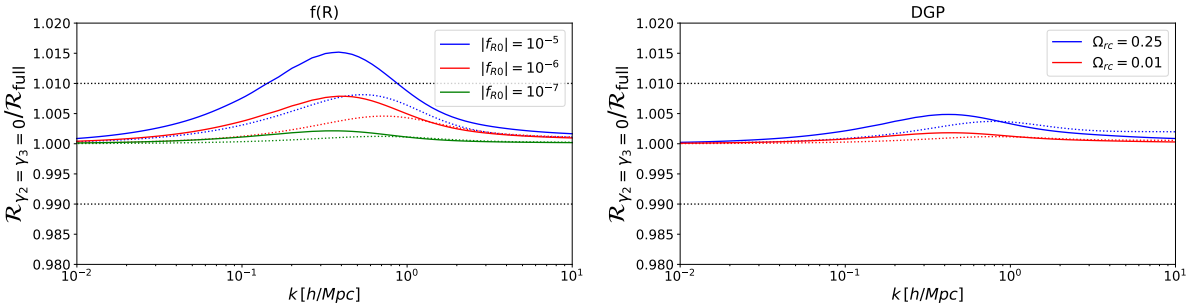

Figure 5.3 *Ratio of the approximated reaction to the full calculation. The approximation assumes $\mathcal{E} = 1$ in Eq. 5.6 which is approximately equivalent to no higher order perturbative, screening terms i.e, $\gamma_2 = \gamma_3 = 0$. We show Hu-Sawicki $f(R)$ gravity on the left and the normal branch of DGP on the right for varying modifications to GR. For $f(R)$ we show predictions for when the model parameter takes the value of $|f_{R0}| = 10^{-5}$ (moderate modification, blue), $|f_{R0}| = 10^{-6}$ (low modification, red) and $|f_{R0}| = 10^{-7}$ (very low modification, green). For DGP we show predictions for when the model parameter is $\Omega_{\rm rc} = 0.25$ (moderate modification, blue) and $\Omega_{\rm rc} = 0.01$ (low modification, red). We also show the comparison over two redshifts, $z = 0$ (solid lines) and $z = 1$ (dotted lines).*

that simply setting $\gamma_2 = \gamma_3 = 0$ leaves one slightly sensitive to the $k_\star$ correction through the 1-halo terms and consequently on the particular choice of halo mass function.

Using the exact forms of γ_2 and γ_3 as described in Subsection 5.3.2 is a big challenge. This is primarily for computational reasons as it involves numerical time derivatives. Smoothness of such derivatives is difficult to ensure and can affect results. In particular, the exponential dependence of $\mathcal{R}$ on $k_\star$ (see Eq. 5.4) makes it very sensitive to inaccuracies in the 1-loop calculation. Further, the full map to γ_2 and γ_3 from the EFTofDE would increase computational time significantly, degrading our code's ability to perform statistical analyses on data.

To test the impact of setting $\gamma_2 = \gamma_3 = 0$ we compare Eq. 5.4 with and without these terms switched on for two different theories of gravity, DGP and the Hu-Sawicki $f(R)$ model [109]. The former is an instance of derivative or Vainshtein screening and the latter of potential or chameleon screening, covering two main types of screening mechanism.

This comparison is shown in Fig. 5.3. We find that in the case of DGP, the correction coming from the 1-loop computation is negligible for small and moderate modifications to GR at all scales. On the other hand, the corrections to the $f(R)$ theory can be up to 1.5% at $z = 0$ for moderate modifications to GR. This may be acceptable if these inaccuracies can be partially absorbed into the nonlinear degrees of freedom. We explore this in Section 5.5.

		scalar	tensor	
	no ghost	$\alpha_K + \frac{3}{2}\alpha_B^2 > 0$	$M^2 > 0$	[100]
Low	gradient stability	$c_s^2 \geq 0$	$\alpha_T \geq -1$	
Energy	(sub)luminality	large α_K	$\alpha_T \leq 0$	[397]
	no GW-induced instability	$\lvert\alpha_M + \alpha_B\rvert \leq 10^{-2}$		[398]
High	scalar-scalar scattering	$\alpha_B \leq \frac{2\alpha_T}{1+\alpha_T}$		[399]
Energy	scalar-matter scattering	$\alpha_T \geq 0$		[400]
Data	GW propagation speed	$\lvert\alpha_T\rvert \leq 10^{-15}$		[401]
	CMB and LSS	$\lvert\alpha_M\rvert, \lvert\alpha_B\rvert \leq \mathcal{O}(0.1)$		[352]

Table 5.1 *Theoretical and observational constraints on α-parameters from references in the right column. Theoretical constraints are coming from low-energy (EFT) and high-energy (positivity bounds) physics. Note that α_K is not constrained by data, hence the subluminality condition does not impose any constraining power on the scalar mode perturbations. Also note the contradiction in the condition for GW propagation: subluminal versus superluminal speed. The positivity bounds do not hold in general, they are derived for a quadratic subclass of Horndeski theories with $G_3 = G_5 = G_{5,X} = 0$ in Eq. 5.2. Data driven constraints strongly depend on the imposed theoretical priors and time-dependent parameterisation of α-functions. Here we mention only two prior-independent observational constraints.*

5.4.3 Observational and Theoretical Constraints

Firstly, we want to eliminate a range of α-parameter values that lead to two pathological instabilities: ghost (i.e., negative kinetic energy) and gradient (i.e., imaginary speed of sound). These constraints for the Horndeski theories were first derived in Ref. [402]. In terms of the α-functions, Ref. [100] found that the stability of the background requires

$$\alpha > 0\,, \quad c_s^2 \geq 0\,, \tag{5.50}$$

from Eq. 5.29 and Eq. 5.30 for scalar modes, and

$$M^2 > 0\,, \quad c_T^2 = 1 + \alpha_T \geq 0\,, \tag{5.51}$$

for tensor modes of perturbations. An additional theoretical constraint is the stability of scalar modes in the presence of gravitational waves of large amplitude, for instance, sourced by massive binary systems [398]. Mapped to the parameterisation used in this work this requires the following bound [403]:

$$\lvert\alpha_M + \alpha_B\rvert \leq 10^{-2}\,. \tag{5.52}$$

Previously, it was argued that the constraining power of upcoming cosmological surveys will allow us to pin down the α-parameters at the $\mathcal{O}(0.1)$-level [404]. For the condition above this implies that $\alpha_M \approx -\alpha_B$. However, in such forecasts nonlinear scales were ignored with a typical highest mode around $k_{\rm max} \approx 0.15\ h\ {\rm Mpc}^{-1}$. We speculate that this constraint may be improved upon by inclusion of the nonlinear scales. Therefore, in our code we treat α_B and α_M independently.

Secondly, one may consider that the new physics should not modify the speed of gravitational wave propagation [397, 401, 405–412], and so $\alpha_T = \bar{M}_2^2 = 0$. This luminality condition has been argued to not be as clear cut a constraint through EFT considerations [397, 413] as well as through the positivity bounds from high energy physics [400], so in our code we keep the α_T dependence in μ. Subluminality, stated in the former references, follows from the existence of a Wilsonian UV completion [414] and dependence on the theory's "cutoff" scale. From Eq. 5.29 it can be seen that subliminality of scalar modes is guaranteed for large values of α_K, while for tensor modes subluminality requires $\alpha_T < 0$. Superluminality, stated in Ref. [400], is a consequence of the positivity bounds for scattering between scalar and matter fields. Such positivity bounds require a unitary, causal, local UV completion of our low-energy EFT theory. However, superluminality does not necessary result in casual paradoxes [415, 416]. In general, the notion of causality in terms of the low-energy EFT is a rather subtle topic (for instance, see Refs. [417, 418]).

Thirdly, in the QS α_K does not enter the equations of motion [100]. Therefore, it is completely unconstrained in our approach, or for any model with $c_s^2 \approx 1$. However, in the exact computation α_K affects only the largest scales (see Fig. 5.2), which are dominated by cosmic variance. This can be a motivation to not consider α_K in data analyses, leaving only α_M and α_B in a "bare-bones" case. We do not impose any of these reductions in our code and leave it to the user to specify well motivated priors on the full set of EFTofDE parameters in their analyses.

Lastly, we note that there are a host of data driven constraints that one can put on the EFTofDE parameters [352, 399, 400, 403, 419–421]. Such constraints strongly depend on the imposed theoretical priors and time-dependent parameterisation of the α-functions (see Subsection 5.4.4). However, they all agree that the uncertainties and values of the α-parameters are of order $\mathcal{O}(0.1)$. The future CMB and LSS surveys promise to improve the constraints up to at least one order of magnitude $\sigma(|\alpha_i|) \sim \mathcal{O}(0.01)$ (see, for example, Ref. [422]). One may also assume a ΛCDM background, well motivated by CMB data [22], and so set $H(a) = H_{\Lambda{\rm CDM}}({\rm a})$[6]. We summarize the constraints discussed above in Tab. 5.1.

[6]Our code defaults to this assumption, but there is the option to parameterise the background too.

5.4.4 Parameterising Time Dependence

Here, we look at how one can parameterise the time dependence of the EFTofDE functions. To first order this can be approximated by a Taylor expansion, $\theta_i(a) \approx \theta_{i,0} + \theta_{i,p}(1-a)$, leaving at least 6 free constants characterising deviations from ΛCDM. In typical data analyses, only a 1-parameter time dependence is considered. For example, in Ref. [421] the authors consider the following three parameterisations for the α_i, $i \in \{M, B, K, T\}$

$$(\mathbf{1}) : \alpha_i(a) = c_i \Omega_\Lambda(a)\,, \tag{5.53}$$

$$(\mathbf{2}) : \alpha_i(a) = c_i a\,, \tag{5.54}$$

$$(\mathbf{3}) : \alpha_i(a) = c_i a^{n_i}\,, \tag{5.55}$$

where c_i and n_i are free constants and $\Omega_\Lambda(a)$ is the ΛCDM cosmological constant energy density fraction as a function of time. For a comprehensive list of various other time parameterisations see Appendix B of Ref. [350]. These all draw on the motivation that modifications should only become relevant at late times. In our code, the default is set to **(2)** for all α_i. We note that such parameterisations may exclude well-known theories as shown in Ref. [370], which motivated the s-basis introduced in Subsection 5.3.1.

We can also adopt similar parameterisations for the background $H(a)$, but a more general choice would be, for example, the Chevalier-Polarski-Linder (CPL) parameterisation [85, 86], which parameterises the dark energy equation of state $w(a)$ in terms of two free constants, $\{w_0, w_a\}$ as

$$w(a) = w_0 + w_a(1-a)\,, \tag{5.56}$$

which gives the following form for $H(a)$

$$H^2(a) = H_0^2 \left(\Omega_{\mathrm{m},0} a^{-3} + \Omega_\Lambda e^{-3\int(1+w(a))\mathrm{d}\log a}\right)\,. \tag{5.57}$$

5.4.5 Nonlinear Parameterisation

The nPPF form for $\mathcal{F}$ given in Eq. 5.39 captures dependencies of the nonlinear modification to the Poisson equation on the relevant variables, namely $\{y_\mathrm{h}, a, M_{vir}, y_\mathrm{env}\}$. Being motivated by the form of $\mathcal{F}$ in DGP (Eq. C.41), it can recover the DGP form given appropriate choices for p_i albeit with a non-trivial dependency of p_2 on a (see Eq. C.49). Eq. 5.39 becomes approximate when moving beyond DGP. On the other hand, the Erf form, Eq. 5.41, is completely phenomenological and is an approximation even in DGP.

Note that the nPPF is also more directly relatable to specific actions and gravity models, in which case its degrees of freedom can be significantly restricted. It is thus far more suitable when particular models are being targeted for analysis. The Erf model

	Maximal	Reduced	Minimal (Horndeski)	Minimal
Background	$H(a)$	$H(a)$	$H(a)$	w_0, w_a
Linear	$\alpha_M(a), \alpha_B(a)$ $\alpha_K(a), \alpha_T(a)$	$\alpha_M(a), \alpha_B(a),$ $\alpha_K(a), \alpha_T(a)$	$\alpha_M(a), \alpha_B(a)$	γ
Quasi-nonlinear	$\xi_3^2(a), \xi_4^2(a), \xi_3^3(a),$ $\xi_4^3(a), \xi_4^4(a), \xi_4^5(a)$	-	-	-
Nonlinear	$p_{1-7}(a) + p_8$	$p_{1-7}(a)$	q_1, q_2, q_3	q_1, q_2, q_3
Total	18+1	12	3 + 3 constants	6 constants

Table 5.2 *A maximal, reduced and minimal set of parameters needed for a comprehensive nonlinear power spectrum analysis of the unrestricted theory space of Eq. 5.2, together with a proposed minimal set for more general theories. The Horndeski minimal set assumes $\alpha_T = \alpha_K = 0$ and Eq. 5.43, while the maximal and the reduced assume full freedom of Eq. 5.39. Both reduced and minimal assume $\gamma_2 = \gamma_3 = 0$. The totals show the number of free functions of time plus any free constants. We note q_4 and p_8 are found in Section 5.5 to be likely irrelevant for the 1-halo computation, and so we do not consider them in the reduced or minimal cases. We also note very tight constraints on $\alpha_B - \alpha_M$ (see Subsection 5.4.3) relevant to the minimal case.*

on the other hand is completely general and has no direct relation to specific actions of gravity. It is thus more suitable when no specific model is being targeted and we want to place constraints on general models of gravity. In Section 5.5 we test these two approximations in both DGP and $f(R)$ gravity.

5.4.6 Overview

With all these approximations and constraints, the arguable minimal parameter space characterising deviations to ΛCDM is 3 free functions of time and 4 constants. Without approximations or constraints, the maximal is 18 free functions of time and a constant. Of course we can also find intermediate reduced sets, such as using the nPPF but with $\gamma_2 = \gamma_3 = 0$. Given we need to parameterise these functions of time, the maximal set is currently an unfeasible parameter space to probe comprehensively, both in terms of data processing as well as parameter degeneracies which limits the amount of useful physical information one can extract from the data.

Finally, we have focused on the Horndeski class of models, but one can extend this to larger generality by considering, for example, the growth index γ parameterisation for $\mu(a)$ [292, 423] explicitly, see Eq. 47 in Ref. [370] and Eq. 5.57 for $H(a)$. Combined with the Erf model, this would constitute a minimal set of 6 free constants for general modifications to ΛCDM. This minimal model-independent parameterisation has also been implemented into the code.

We summarise these parameterisations in Tab. 5.2.

5.5 Testing the Nonlinear Parameterisations

In this section we compare the predictions for the halo model reaction $\mathcal{R}$, using the various nonlinear parameterisations of modifications to the Poisson equation outlined in Subsection 5.3.3, to exact solutions as well as state-of-the-art emulators within an evolving dark energy scenario (wCDM), DGP and Hu-Sawicki $f(R)$ gravity (see Subsection 1.3.1 and Subsection 1.3.1 for more details on these models). Note that the exact solutions for the reaction have in turn been themselves compared to full N-body simulations in other works (see, for example, Ref. [4]), exhibiting $\mathcal{O}(1)\%$ agreement. These models cover a fair range of theoretical and phenomenological features typical of modified gravity and dark energy models, making them good representatives and test cases.

We look to test predictions for $\mathcal{R}$ using Eq. 5.39 (nPPF) and Eq. 5.41 (Erf) with $\gamma_2 = \gamma_3 = 0$ against the full calculation which computes $\mathcal{R}$ using exact forms for γ_2, γ_3 and $\mathcal{F}$ (see Appendices of Ref. [130] for all relevant expressions). We further employ the `EuclidEmulator2` emulator [32] and the fofr emulator [424] for the wCDM and $f(R)$ cases respectively. These emulators have been trained on high quality N-body simulations and are 1-2% accurate within the scales we examine, providing a good benchmark for our predictions. One should keep in mind that the halo model reaction approach's accuracy is limited by the pseudo power spectrum employed. For example, if we use `HMCode2020` [362] for the pseudo, which is claimed to be 2.5% accurate down to $k \leq 10\ h/\text{Mpc}$, we then expect any power spectrum comparisons to then be $\sim 4.5\%$ consistent with N-body at $k \leq 3\ h/\text{Mpc}$, which assumes the result of Ref. [425], i.e., that the exact solution for $\mathcal{R}$ is $\sim 2\%$ accurate at these scales. In the wCDM and DGP cases, both ΛCDM and $P_{\rm NL}^{\rm pseudo}$ are computed using the halofit fitting function [394], but the $f(R)$ case uses `HMCode2020`.

The computation of $\mathcal{R}$ requires us to solve the evolution equations for the spherical top-hat radius parameterised by $y_{\rm h}$ (Eq. C.44). This necessitates the specification of $\mathcal{F}$ at all redshifts up to the target redshift. We then should test approximations for $\mathcal{F}$ even at high redshifts, which is done in Subsection C.2.3, where we compare $\mathcal{F}$ at $z = 0, 1, 4$. For comparisons of the halo model reaction, we only consider $z = 0, 1$ which are more observationally relevant.

We fit $\{q_1, q_2, q_3, q_4\}$ for the Erf model, $\mathcal{F}_{\rm Erf}$. In the nPPF case, we do not fit all the 8 free parameters of $\mathcal{F}_{\rm nPPF}$, and only consider p_1 and p_8, treating both as constants. In principle, and indeed for unspecified theories of gravity, all 8 parameters will be fit to the data. For the comparisons made here, p_{2-7} are fixed to the theoretically predicted values quoted in Section C.2. Fitting such a high dimensional parameter space is beyond the scope of this work.

In what follows we fit the free parameters by performing a least square fit to the exact

	nPPF		Erf		
$\Omega_{\rm rc}$	p_1	p_8	q_1	q_2	q_3
0.25	-	-	0.76	0	0
0.01	-	-	0.71	0	0
$\lvert f_{\rm R0}\rvert$	p_1	p_8	q_1	q_2	q_3
10^{-5}	3	-0.8	0.9	0.35	0.65
10^{-6}	8.5	-0.5	1.65	0.7	2.45
10^{-7}	5.65	-0.45	0.6	0.8	2.15

Table 5.3 *Best fit parameter values for the DGP and $f(R)$ models. The fit is performed to the exact solution for $\mathcal{R}$ in the range $0.1\ h/\text{Mpc} \leq k \leq 3\ h/\text{Mpc}$ and at $z = 0, 1$ as described in the main text. For the Erf model, we do not fit q_2, q_3 and q_4 for DGP and for $f(R)$ we find the quality of fit with and without q_4 is similar. For all fits we thus set $q_4 = 0$. The nPPF is exact for DGP and so we only consider $f(R)$, fixing all p_{2-7} to the values given in Eq. C.50.*

$\mathcal{R}$ prediction. We choose to fit our parameterised models to the exact predictions for $\mathcal{R}$, rather than the emulator predictions for $P_{\rm NL}(k)$ for two reasons. First so as to test the ansatz for the phenomenological screening and the consistency of the predictions (see Section C.2). Second, we do not want to assume anything about the pseudo spectrum in these fits. To fit we minimise the following merit function

$$s^2 = \sum_{j=\min}^{\max} \sum_{i=\min}^{\max} \frac{[\mathcal{R}_{\rm exact}(k_i, z_j) - \mathcal{R}_{\rm approx}(k_i, z_j)]^2}{\sigma^2_{i,j}}\,, \tag{5.58}$$

where we assume error bars on $\mathcal{R}_{\rm exact}$ coming from cosmic variance [281, 426, 427] and a constant systematic error added in quadrature

$$\sigma^2_{i,j}(k, z) = \frac{4\pi^2}{k_i^2 \Delta k_i V_{s,j}} + \sigma^2_{\rm sys}\,, \tag{5.59}$$

where $V_{s,j} \in \{0.3, 8\}\ \text{Gpc}^3/h^3$ is taken to be a Stage-IV survey-like volume for each bin $z_j \in \{0, 1\}$ respectively [10, 354, 395, 427]. We fit in the range $k_{\rm min} = 0.1 \leq k_i \leq 3 = k_{\rm max}$ which is the range over which the exact computation of $\mathcal{R}$ is 2% accurate [4], sampling logarithmically, with Δk_i being the bin width. We take $\sigma_{\rm sys} = 0.02$ to reflect the systematic error in the parameterised reaction when compared to simulations by proxy of the exact solution. The best fit parameter values are shown in Tab. 5.3.

5.5.1 Evolving Dark Energy Example: wCDM

Here we perform a sanity check that the general minimal model outlined in Tab. 5.2 produces consistent results for a wCDM cosmology, and is at least as accurate as the exact solution. To do this we compare a minimal model with CPL parameters $w_0 = -1.2$ and $w_a = 0.4$, and a growth index of $\gamma = 0.55$ to the exact solution as well as predictions from `EuclidEmulator2` using the same CPL parameters. We further set the nonlinear parameters of the Erf model (q_i) to unity, but check that they have no impact on the results as expected from Eq. 5.41 ($\mu \approx 1$ for $\gamma = 0.55$).

We show our results in Fig. 5.4. We see that the minimal model is both completely consistent with the exact solution which has no nonlinear or linear modification to the Poisson equation, as well as 1% consistent with the emulator down to $k \leq 2$ h/Mpc and 2% down to $k \leq 3$ h/Mpc. The minimal general model could feasibly outperform the exact solution given its degrees of freedom. In a future work we plan to check forecasted constraints and possible biases on cosmological parameters for the minimal general model, in full posterior estimation analyses employing N-body simulation measurements.

5.5.2 Vainshtein Example: DGP

For DGP the nPPF parameterisation reproduces the exact form of $\mathcal{F}$ (Eq. C.41) for specific choices of the p_i parameters (Eq. C.49). On the other hand, the Erf parameterisation (Eq. 5.41) is approximate and we fit the associated parameters. We note that DGP has no Yukawa suppression at large scales and produces a constant enhancement of the ΛCDM linear growth factor. This enhancement is controlled by the DGP degree of freedom $\Omega_{\rm rc} \equiv 1/(4H_0^2 r_c^2)$ where r_c is the cross-over scale dictating where gravity goes from behaving 4-dimensionally to 5-dimensionally. We consider two levels of deviation to ΛCDM: a moderate modification given by $\Omega_{\rm rc} = 0.25$ and a small modification given by $\Omega_{\rm rc} = 0.01$.

We only fit q_1 as we do not have any mass, environment or Yukawa-suppression scale dependence, and so we set $q_2 = q_3 = q_4 = 0$ in this case. The best fit values of q_1 are given in Tab. 5.3. Further, we employ the exact form of $\mu(a)$ in Eq. 5.41 for the explicit expression see Appendix in Ref. [130].

In the top panels of Fig. 5.5 we show the ratio of a DGP power spectrum to a ΛCDM spectrum with the same background expansion history, normalised to unity at linear scales for easier comparisons of nonlinear effects. The DGP spectrum is given by Eq. 5.3. We see the moderate modification gives up to a 6% deviation from ΛCDM (above the linear growth enhancement) for $k \leq 3h$/Mpc while the small modification can reach 2% over the same range of scales. Reassuringly, in the bottom panels we find sub-percent agreement between the Erf and exact predictions down to $k = 5$ h/Mpc, with a smaller disagreement for the smaller deviation from ΛCDM.

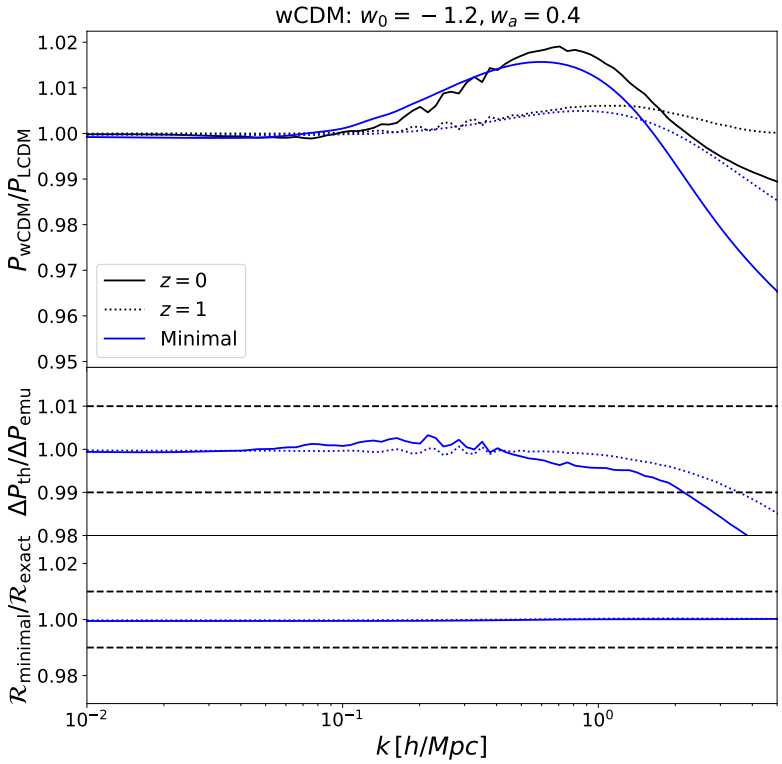

Figure 5.4 *Top panel: The ratio of the wCDM nonlinear power spectrum to the ΛCDM nonlinear power spectrum computed using the* `EuclidEmulator2` *(black) and halofit together with the halo model reaction (see Eq. 5.3) for the minimal general model (blue) as outlined in the right most column of Tab. 5.2. Middle panel: The ratio between theoretical and emulator predictions for the ratio between wCDM to ΛCDM spectra, i.e., the ratio of blue to black top panels curves. Bottom panel: The ratio of the exact halo model reaction to the minimal general model. We plot the ratio for two observationally relevant redshifts, $z = 0$ (solid) and $z = 1$ (dotted). We show these results for $w_0 = -1.2$ and $w_a = 0.4$. The minimal general model also has $\gamma = 0.55$ and $q_1 = q_2 = q_3 = q_4 = 1$.*

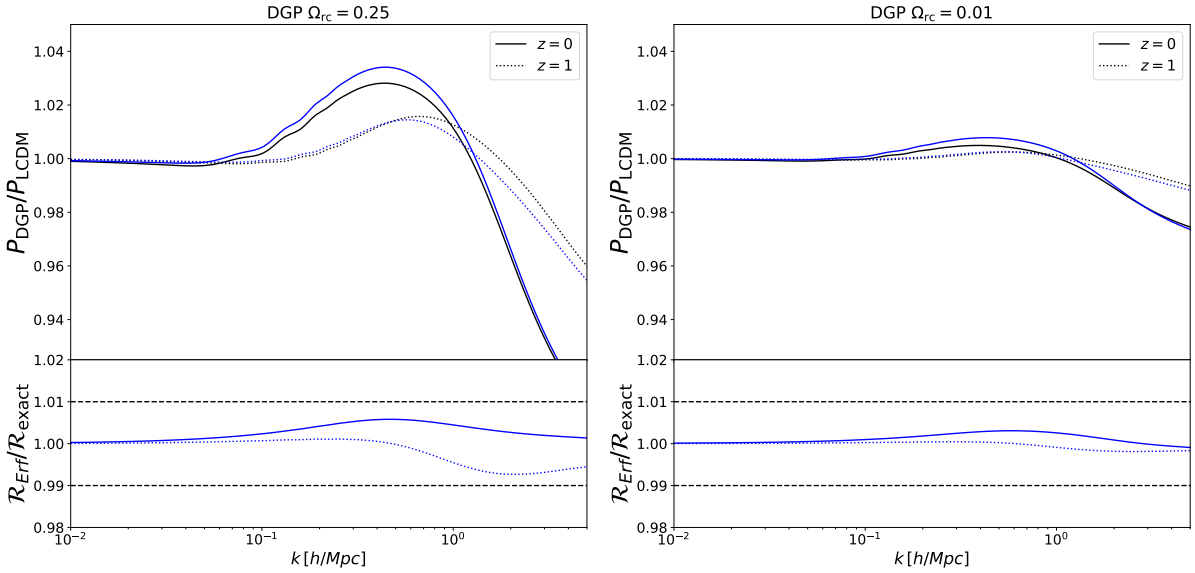

Figure 5.5 *Top panels: The ratio of the DGP nonlinear power spectrum to the ΛCDM nonlinear power spectrum computed using halofit and the halo model reaction (see Eq. 5.3) for the exact (black) and Erf (blue) cases. We do not show the nPPF case as it reduces to the exact solution for specific choices of its parameters. The Erf model assumes* $\gamma_2 = \gamma_3 = 0$. *We have normalised the ratio to unity at large scales for easier comparisons. Bottom panels: The ratio of halo model reactions; the Erf model* $\mathcal{R}_{\rm Erf}$ *to the exact solution. This is equivalent to the ratio of the top panel blue to black curves. We show these results for a moderate modification,* $\Omega_{\rm rc} = 0.25$ *(left) and a low modification,* $\Omega_{\rm rc} = 0.01$ *(right). We plot the ratio for two observationally relevant redshifts,* $z = 0$ *(solid) and* $z = 1$ *(dotted).*

One can further parameterise the time dependence of q_1 which would alleviate some of these deviations, but we find these differences to be more than acceptable given the relative size compared to the modification to ΛCDM shown in the top panels. Moreover, a large number of additional degrees of freedom will be introduced in real data analyses such as intrinsic alignments and parameterisations of baryonic physics. These will be degenerate to some level with modified gravity effects [428], allowing lower accuracy demands in the modelling of $\mathcal{R}$.

This additional time dependence is highlighted in Fig. C.1, where we find that the Erf model can match the exact form of $\mathcal{F}$ extremely well at a fixed redshift. Upon investigation, we found this dependence to be highly degenerate with q_2 which prompted us to not introduce new freedom to the model, especially because we can achieve very good fits already, even without q_2.

Note we have not compared the parameterised model to an emulator nor simulations in this case. Given the excellent agreement with the exact solution we can infer its accuracy is at least as good as the exact solution, given it employs 3 additional degrees of freedom. We remind the reader that the exact reaction was found to be 2% accurate when compared to N-body simulations in Ref. [4].

5.5.3 Chameleon Example: Hu-Sawicki $f(R)$

For this theory we consider both the nPPF and Erf models for $\mathcal{R}$, and compare them to the exact solution (Eq. C.46) as well as at the power spectrum level to the fofr emulator [424]. This model makes use of the chameleon screening mechanism which exhibits an environmental and mass dependence. It also has a Yukawa suppression which returns it to GR at large scales. The additional degree of freedom is the value of the background scalar field at $z = 0$, $f_{\rm R0}$, which controls the level of deviation from GR. We consider three levels of deviation from ΛCDM, $|f_{\rm R0}| = 10^{-5}$ (moderate modification), $|f_{\rm R0}| = 10^{-6}$ (low modification) and $|f_{\rm R0}| = 10^{-7}$ (very low modification). We note that the moderate $f(R)$ modification is already ruled out by data (for example, see Refs. [340, 429–431]), but provides a good flexibility test of the parameterisation.

In the nPPF case, we choose the theoretically motivated parameters given in Eq. C.50. These emerge from a parameterised form of $f(R)$ gravity [378] and so are approximate. p_1 and our new parameter p_8 remain free. Treating them both as constants, we fit them in the same way that we fit the Erf model's parameters, by minimising Eq. 5.58. We note that the other nPPF parameters, $p_2 - p_7$, take on different forms for the chameleon screening and Yukawa suppression regimes. We only consider the screening regime which is more relevant for the spherical collapse calculation, and rely on $\mu(\tilde{k}, a)$ appearing in Eq. 5.39 to take care of the Yukawa suppression.

Yukawa suppression is relevant for large masses, large $y_{\rm env}$ or small values of $f_{\rm R0}$. Given

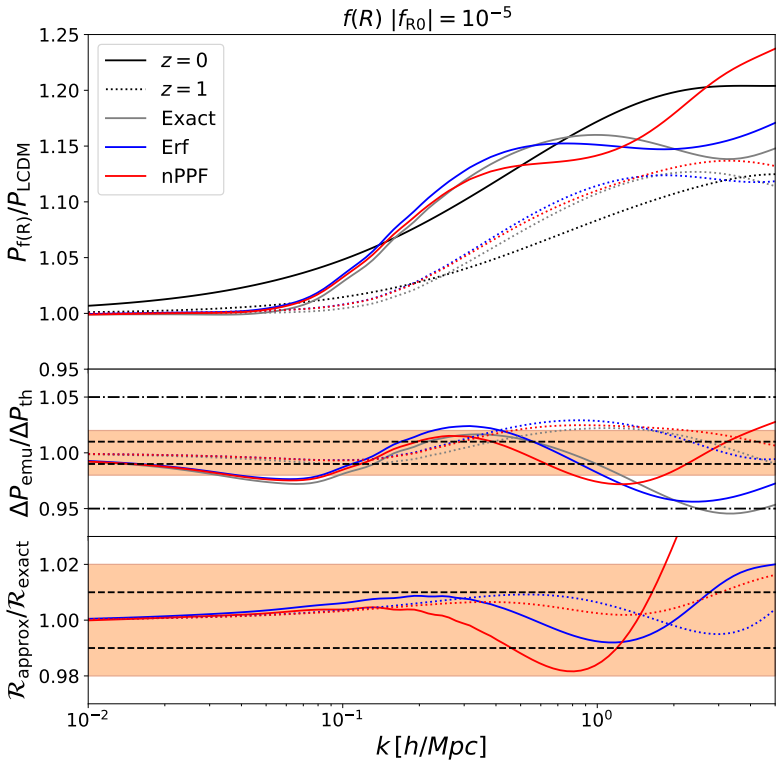

Figure 5.6 *Top panel: The ratio of the $f(R)$ nonlinear power spectrum to the ΛCDM nonlinear power spectrum computed using* `HMCode2020` *and the halo model reaction (see Eq. 5.3) for the exact (grey), Erf (blue) and nPPF (red) cases. The fofr emulator is also shown in black. Middle panel: The ratio between theoretical and emulator predictions for the ratio between $f(R)$ to ΛCDM spectra, i.e., the ratio of grey, blue and red to black top panels curves. Bottom panel: The ratio of halo model reactions; the parameterised models to the exact solution. This is equivalent to the ratio of the top panel coloured curves to the gray curves. Note that both parameterised models have $\gamma_2 = \gamma_3 = 0$. We plot the ratio for two observationally relevant redshifts, $z = 0$ (solid) and $z = 1$ (dotted). We show these results for a moderate modification, $|f_{R0}| = 10^{-5}$. The orange bands indicate the 2% region which is the current absolute accuracy of the exact $\mathcal{R}$.*

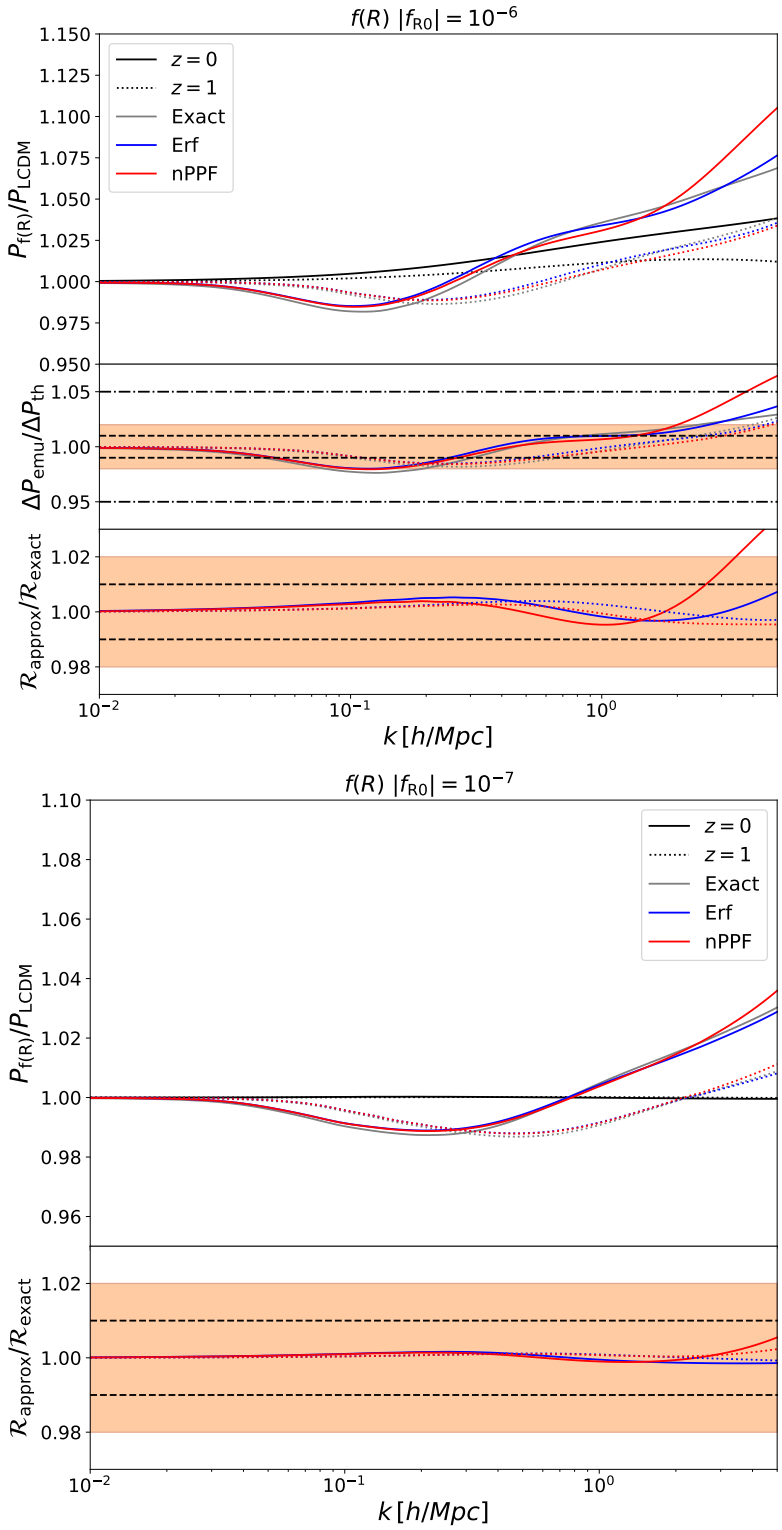

Figure 5.7 *Same as Fig. 5.6 for a low modification, $|f_{R0}| = 10^{-6}$ (top) and a very low modification, $|f_{R0}| = 10^{-7}$ (bottom). Note that the fofr emulator for $|f_{R0}| = 10^{-7}$ gives the ΛCDM prediction and so we omit the middle panel.*

this, we do not expect p_8 or q_4 to be relevant for spherical collapse where $y_\mathrm{h} \leq y_\mathrm{env} \leq 1$, and even less for the 1-halo spectrum where the Sheth-Torman mass function down-weights large masses (see, for example, Ref. [375]). We verify this by performing two separate fits: the first only including the parameter sets $\{p_1\}$ and $\{q_1, q_2, q_3\}$ for the nPPF and Erf model respectively, while the second extending these sets to include p_8 and q_4 respectively.

We find that values of $q_4, p_8 \geq 0$ negligibly change the goodness of fit for the low and very low modification strengths, while sufficiently negative values degrade the fit, which is expected as the Yukawa scale begins to overlap with the screening scale. Further, we observe only a marginal improvement at $z = 0$ for $|f_{\mathrm{R}0}| = 10^{-5}$ in the Erf case. Given this, all fits shown and quoted here set $q_4 = 0$ for the Erf case. In the nPPF case, we observe a moderate improvement for $|f_{\mathrm{R}0}| = 10^{-5}$ and so keep p_8. We report the best-fit parameters in Tab. 5.3.

The $f(R)$ results are shown in Fig. 5.6 and Fig. 5.7. We see the moderate modification can reach a 20% deviation from ΛCDM for $k \leq 3h/\mathrm{Mpc}$ while the low and very low modifications reach 10% and 3% respectively. Both parameterisations do well in modelling the moderate modification case $|f_{\mathrm{R}0}| = 10^{-5}$, shown in Fig. 5.6. The Erf model prediction for $\mathcal{R}$ stays within 1% of the exact solution for $k \leq 3h/\mathrm{Mpc}$. Similarly, the nPPF remains within 2% for $k \leq 2h/\mathrm{Mpc}$. The situation improves for the lower modification cases, shown in Fig. 5.7. These comparisons exhibit sub-1% agreement between the Erf (nPPF) model and exact solution for $k \leq 5(3)\ h/\mathrm{Mpc}$ at $z = 0$ and $z = 1$.

All power spectra predictions are $\sim 3\%$ consistent with the fofr emulator which mainly demonstrates the accuracy of `HMCode2020`. Interestingly, we find that the additional degrees of freedom within the nPPF and Erf models are degenerate with possible inaccuracies in the pseudo, even down to $k = 5\ h/\mathrm{Mpc}$. Again, we leave it to a future work to see if these additional degrees of freedom can improve constraining power on cosmological and gravitational parameters while remaining unbiased.

Our comparisons indicate that for the Erf model, degeneracies between q_{1-3} and q_4 make the latter parameter unnecessary. We note that the fit of q_{1-3} becomes insensitive to the value of q_4 if it is sufficiently large, here found to be $q_4 = 0$. For the nPPF model, the additional freedom provided by p_8 is necessary to improve the fit, but it does not help substantially for observationally viable values of $f_{\mathrm{R}0}$. Further, we remind the reader that we do not know p_{2-7} a priori for unspecified theories of gravity, and so the importance of p_8 is likely to be minimal when considering these additional degrees of freedom.

Lastly, we remark that the Erf model gives a good fit for a range of values for q_{1-3}[7]. The values quoted in Tab. 5.3 are only the best fit values, which are also very dependent on Eq. 5.59. This makes it hard to extract any further dependence on $f_{\mathrm{R}0}$ in Eq. 5.41 (note this already depends on $\mu(k, a)$), which is also beyond the scope of this parameterisation which aims to be general in terms of gravitational degrees of freedom.

[7]Similar fits were found for $\mathcal{O}(0.1)$ values for these parameters.

5.6 Summary

In this chapter we have presented a significant extension of the code described in Ref. [130] which produces nonlinear corrections to the matter power spectrum coming from beyond-ΛCDM physics in the form of the halo model reaction $\mathcal{R}$. In particular, we have focused on implementing parameterisations of key equations, such as the background expansion history and the linear and nonlinear Poisson equations.

For the linear scales and background we have considered the effective field theory of dark energy (EFTofDE) while for the nonlinear scales we have considered two distinct parameterisations, a nonlinear parameterised post-Friedmannian (nPPF) based model and a more phenomenological model based on the error function (Erf). Together, these give a general parameterisation of the nonlinear matter power spectrum in Horndeski models. We neglect loop corrections in these parameterisations but leave these as viable additions and we provide theoretical and numerical means of deriving these for the Horndeski class of theories. This being said, we remark that the nonlinear parameterisations are completely general, and so to move beyond the Horndeski class it is sufficient to parameterise only the background expansion history and the linear modification to the Poisson equation. Further, the nonlinear parameterisations also have unscreened limits, and so we are not restricted to theories exhibiting screening. In summary, this work presents a fast, accurate and highly general nonlinear power spectrum predictor for non-standard models of gravity and cosmology including massive neutrinos, parameterised with a minimal set of free, physically meaningful constants.

We have tested these parameterisations against the full solutions for $\mathcal{R}$ in three beyond-ΛCDM models, wCDM, Hu-Sawicki $f(R)$ and DGP gravity. This has identified a minimal set of 3 free functions of time and 3 dimensionless, positive, $\mathcal{O}(1)$ dimensionless constants, which can replicate the exact solutions to within 1% at $k \leq 5h/\text{Mpc}$ and at $z \leq 1$ for modifications to GR within current data constraints and within the Horndeski class. This level of imprecision is sub-dominant to the 2% accuracy currently achieved by the reaction method at these scales [4, 356], and further to the inaccuracies in current pseudo spectrum prescriptions [358, 363]. We have seen that the additional parameters have some degree of degeneracy with pseudo spectrum inaccuracies, which may improve the scales of validity for the nonlinear power spectrum, P_{NL}, as predicted within the halo model reaction framework. We thus suspect that this minimal parameterisation is acceptable for upcoming Stage-IV cosmic shear analyses given the flexibility of the nonlinear parameterisation and the many other nuisance degrees of freedom entering a real data analyses, such as those characterising baryonic physics or intrinsic galaxy alignments [432].

The Erf model is also highly model independent, capturing the basic phenomenology of screening mechanisms. It can thus be suitable for analyses targeting general deviations

from ΛCDM. For example, one may perform a model independent analysis combining the Erf parameterisation with the linear theory growth index γ-parameterisation [292, 423] (also see Eq. 47 of Ref. [370]) and say the background parameterisation of Refs. [85, 86], giving 6 free constants characterising general deviations from ΛCDM in the matter power spectrum at a wide range of scales. On the other hand, the nPPF approach is complementary as it can be directly related to specific actions, making it very suitable when we look to constrain more specific classes of theories. Both approaches have a clearly defined unscreened limit.

In future work we will test the robustness of the minimal parameterisation, and forecast constraints on deviations to ΛCDM by performing full Markov chain Monte Carlo (MCMC) analyses on mock data of the cosmic shear spectrum. Consistency and accuracy checks can also be performed using recently developed parameterised modified gravity simulations [386, 388, 433–435]. On this note, our code is as fast as the original `ReACT` and so is capable of running MCMC analyses. Despite its appreciable baseline speed, we aim to make this even faster by creating emulators based off halo model reaction predictions using the recently released `CosmoPower` code [291] which will highly optimise such analyses. It is a future plan to also perform real data analyses on currently available cosmic shear data to constrain deviations to ΛCDM using the general minimal parameterisation given in Tab. 5.2.

It is currently an ongoing project to also extend the halo model reaction to redshift space and biased tracers in a vein similar to Ref. [357]. We also plan to include interacting dark energy parameterisations [436, 437] from Chapter 3, a scenario where essentially one decouples the baryons from ΛCDM modifications, contrary to the scenario considered in this chapter where all matter is coupled to the scalar field.

Chapter 6

Growth Index Parameterisation with Cosmic Shear

This chapter is based on the following peer reviewed publication:

- **M. Tsedrik**, B. Bose, P. Carrilho, A. Pourtsidou, S. Pamuk, S. Casas, J. Lesgourgues, 2024, *Stage-IV cosmic shear with modified gravity and model-independent screening*. Published in JCAP. doi:10.1088/1475-7516/2024/10/099, arXiv:2404.11508.

Here we apply the minimal parameterisation introduced in the previous chapter. This phenomenological parameterisation was developed with galaxy clustering probes in mind and has been used to look for deviations from standard cosmology [66, 153, 438]. In Ref. [439] it was demonstrated that γ can be constrained with weak lensing probes as well. Constraining the growth index is one of the main objectives of Stage-IV surveys. We should note that this parameterisation assumes that the linear growth factor and rate are scale-independent which is not the case for some Modified Gravity (MG) models, such as $f(R)$.

The novelty is the implementation of the screening. To our knowledge, attempts to take the screening effects into account have been made in Refs. [352, 440–442]. Therein, screening was modeled as an exponential cut-off in the α-parameters with a characteristic screening scale at which the screening mechanism becomes effective. This scale was either varied as a free parameter or fixed to the value motivated by simulations [443]. However, the performance of this approximation across various MG scenarios remains to be tested, in order to understand if the corresponding accuracy suffices for Stage-IV surveys.

In this chapter, we investigate whether we could provide constraints on the minimal model-independent parameterisation of MG, including nonlinear scales with forthcoming Stage-IV cosmic shear data. We investigate the importance of including the screening scale, the degeneracy between the screening scale and baryonic feedback, and the effects from massive neutrinos. For acceleration of our analysis we emulate our models of interest,

trained with `CosmoPower` on power spectra generated using the halo model reaction. We have made a public repository for this and related emulators.

Contributions

I led the main analysis of the paper, including writing a new likelihood pipeline, adding a new model to `MGCAMB` and `ReACT`, emulating models of interest with `CosmoPower`, running all MCMC chains, interpreting the results, and drafting the majority of the paper. Alkistis Pourtsidou, Benjamin Bose and Pedro Carillho contributed to the interpretation of the results. Benjamin Bose provided his pipeline for data production. Part of Sefa Pamuk's and Santiago Casas's original code was used in the development of my pipeline. They and Julian Lesgourgues provided comments for the final version of the draft.

6.1 Modelling

For a generic theory of gravity, the cosmic shear power spectrum can be derived from the lensing potential, also known as the Weyl potential. The Weyl potential is intricately linked to the underlying matter density fluctuations via a corresponding Poisson equation. Therefore, we can obtain the cosmic shear power spectrum by integrating the nonlinear matter power spectrum along the line-of-sight under the Limber approximation [1] [441]:

$$C_{ij}^{\gamma\gamma}(\ell) = \int_{z_{\rm min}=0}^{z_{\rm max}} {\rm d}z \frac{W_i^{\gamma}(z) W_j^{\gamma}(z)}{H(z)\chi^2(z)} \Sigma^2[k_\ell(z), z] P_{\rm NL}[k_\ell(z), z] \,, \tag{6.1}$$

where we set the speed of light to $c = 1$, $k_\ell = (\ell + 1/2)/\chi(z)$, $\chi(z)$ signifies the radial comoving distance from an observer at $z = 0$ to an object at redshift z, $H(a)$ represents the Hubble function, $\Sigma(k, z)$ denotes the modification to the Poisson equation for the Weyl potential in MG theories, and $z_{\rm max}$ stands for the maximum redshift of the source distribution in a survey. The weighting functions W_i^{γ} are defined as:

$$W_i^{\gamma}(z) = \frac{3}{2} H_0^2 \Omega_{\rm m} \chi(z)(1+z) \int_{z_{\rm min}=0}^{z_{\rm max}} {\rm d}z' n_i(z') \left[1 - \frac{\chi(z)}{\chi(z')}\right] \,, \tag{6.2}$$

where $\Omega_{\rm m} = \Omega_{\rm m}(z = 0)$ denotes the total matter density fraction today, H_0 represents the Hubble constant in Mpc^{-1}, and n_i is the redshift distribution for bin i. The observed lensing signal $C_{ij}^{\rm WL}(\ell)$ is contaminated by the intrinsic alignment contribution (IA, see Ref. [444] for a recent review). IA represent correlations in the orientation between galaxies which are not caused by lensing but rather by the same gravitational field in which these galaxies evolve. We model this using the redshift-dependent nonlinear alignment

[1] As we have discussed in Section 1.5, the Limber approximation might be insufficient for Stage-IV surveys. The goal of this chapter is to study nonlinear effect at scales not strongly affected by this approximation. In a real data analysis the model must be computed without employing the Limber approximation (e.g., with BLAST [18]).

(zNLA) model [445, 446]. Additionally, we account for the shape-noise contribution due to the intrinsic ellipticity field (unlensed). These effects introduce the following additional contribution to the signal:

$$C_{ij}^{\mathrm{WL}}(\ell) = C_{ij}^{\gamma\gamma}(\ell) + C_{ij}^{I\gamma}(\ell) + C_{ij}^{II}(\ell) + \frac{\sigma_\epsilon^2}{\bar{n}}\delta_{ij}^{\mathrm{K}}\,, \tag{6.3}$$

where δ_{ij}^{K} is the Kronecker's delta, σ_ϵ stands for the variance of the intrinsic ellipticity distribution, $\bar{n} = n/N_{\mathrm{bins}}$ with n being number of galaxies per radians squared, and the superscript I denotes the contribution from the IA with the following kernel:

$$W_i^I(k,z) = -A_{\mathrm{IA}}C_{\mathrm{IA}}(1+z)^{\eta_{\mathrm{IA}}}\frac{\Omega_{\mathrm{m}}}{D(k,z)/D(k,0)}n_i(z)H(z)\,, \tag{6.4}$$

where $D(k,z)$ denotes the growth factor[2] – the general definition for MG theories includes a scale dependence, but in this work we only study models with scale-independent linear growth. We set $C_{\mathrm{IA}} = 0.0134$ (its conventional value[3], as it is degenerate with A_{IA}), while A_{IA} and η_{IA} are additional nuisance parameters in our modelling. A_{IA} is called the alignment amplitude. It quantifies the strength of the IA signal given the underlying matter density distribution. The IA signal evolves with redshift and depends on galaxy type [448, 449]. The redshift evolution of the IA amplitude is controlled by the redshift scaling parameter η_{IA}. We also assume that the redshift at which we observe the IA signal is lower than the redshift at which the alignment was initiated. In this framework, the ellipticity of a galaxy is linearly related to the gravitational potential at the time when the IA signal is set. Therefore, it is related to the density perturbations and the matter power spectrum via the Poisson equation. In zNLA, we extend this connection into the nonlinear regime by using the full nonlinear matter power spectrum. It has been widely applied to Stage-III galaxy survey measurements (see, for instance, Refs. [450–453]) that seem to prefer simpler IA models. The zNLA model allows for amplitude and redshift dependence of the IA signal from any MG model through $D(k,z)$ in Eq. 6.4 and P_{NL} in Eq. 6.1. Unlike other IA models where tidal physics is taken into account and perturbatively re-derived for MG scenarios, this does not affect NLA [115]. While there is still debate on whether or not zNLA captures all IA effects sufficiently well for Stage-IV surveys [447, 454], we leave a detailed exploration of more complex models for future work. In general, IA occurs on small astrophysical scales, where we assume that all modifications of gravity are screened [350]. However, a more complex IA model may introduce degeneracies with cosmological and MG parameters, and, hence, degrade the inferred constraints. We note that by choosing a simpler IA model, our forecasts may underestimate uncertainties of

[2]This is found by solving the linearised growth equation in the cosmological scenario of interest, which we compute using `MGrowth`: github.com/MariaTsedrik/MGrowth.

[3]The definition of this constant includes critical density and another normalisation constant frequently set to $\bar{C} = 5\times10^{-14}M_\odot^{-1}h^{-2}\mathrm{Mpc}^3$ in the literature (e.g., Ref. [447]): $C_{\mathrm{IA}} = \bar{C}\rho_{\mathrm{crit}}$.

the inferred parameters.

The main component from Eq. 6.1 that we model and modify in our analysis is the nonlinear power spectrum:

$$P_{\rm NL}(k,z) = P_{\rm NL}^{\rm MG+\nu}(k,z) \times B^{\rm baryons}(k,z) = B^{\rm MG+\nu} \times B^{\rm baryons} \times P_{\rm NL}^{\Lambda\rm CDM}\,, \tag{6.5}$$

where the nonlinear ΛCDM power spectrum without neutrinos, $P_{\rm NL}^{\Lambda\rm CDM}$, is combined with the emulated boosts due to effects from baryonic feedback, $B^{\rm baryons}$, and MG with massive neutrinos, $B^{\rm MG+\nu} = P_{\rm NL}^{\rm MG+\nu}/P_{\rm NL}^{\Lambda\rm CDM}$. This prescription is described in detail in the following subsections.

6.1.1 Nonlinear Power Spectrum Modelling

We model the nonlinear power spectrum similar to the prescription from Chapter 5. In the halo model reaction framework[4] [4], based on the halo-model approach (see Ref. [35] for a recent review), we can compute the nonlinear power spectrum in a modified theory of gravity including massive neutrinos as (see a discussion on massive neutrinos in Subsection 1.3.2):

$$P_{\rm NL}^{\rm MG+\nu}(k,z) = \mathcal{R}(k,z) P_{\rm NL}^{\rm pseudo}(k,z)\,, \tag{6.6}$$

where $P_{\rm NL}^{\rm pseudo}(k,z)$ is called the pseudo power spectrum. This is defined as a nonlinear power spectrum, evolved in a ΛCDM universe with adjusted initial conditions in order to match the linear clustering of the MG model of interest at the target redshifts, i.e., $P_{\rm L}^{\rm pseudo}(k,z_j) = P_{\rm L}^{\rm MG}(k,z_j)$. In the context of N-body simulations it can be understood as follows: initial conditions are generated from a power spectrum computed as $P_{\rm L}^{\rm pseudo}(k,z_{\rm ini}) = D^2_{\Lambda\rm CDM}(z_{\rm ini})/D^2_{\Lambda\rm CDM}(z_j)\ P_{\rm L}^{\rm MG}(k,z_j)$ while the evolution up to z_j is done with standard gravity and ΛCDM expansion. In the context of `HMcode` it can be understood as using $D^2_{\Lambda\rm CDM}(z=0)/D^2_{\Lambda\rm CDM}(z_j)\ P^{\rm MG}(k,z_j)$ as input linear power spectrum at redshift $z = 0$. Since in our case the re-scaling of the initial conditions is scale-independent (as we are dealing with MG theories with scale-independent linear growth), one can also compute a pseudo power spectrum at the target redshift simply by re-scaling the primordial amplitude as $A_s^{\rm pseudo} = D^2_{\rm MG}(z_j)/D^2_{\Lambda\rm CDM}(z_j)A_s$. Instead of utilising a ΛCDM nonlinear power spectrum with the same cosmological parameters and modelling the reaction as an expected ratio $P_{\rm NL}^{\rm MG+\nu}/P_{\rm NL}^{\Lambda\rm CDM}$ with halo model, we opt for the pseudo cosmology, which implies the halo mass functions of both MG and pseudo cosmologies are similar. As a consequence, the transition between 2- and 1-halo terms becomes smoother.

[4]The series of papers "On the road to percent accuracy" covers the developments of the framework including the basic foundation [4], an emulator for the pseudo power spectrum [299], inclusion of massive neutrinos [356], the first forecasts for an LSST-like survey and the `ReACT` code release [130], a comparison with simulations and simulation-based emulators including baryonic contribution in [363], and interactions between dark matter and dark energy [358].

For example, in Fig. 5 and 7 of Ref. [4], when comparing $P_{\rm NL}^{\rm MG}/P_{\rm NL}^{\Lambda{\rm CDM}}$ and $P_{\rm NL}^{\rm MG}/P_{\rm NL}^{\rm pseudo}$, the latter clearly appears as a smoother function.

We compute the pseudo power spectrum using `HMCode` [360, 361, 455, 456], in particular its 2020-version. Alternatively, the pseudo power spectrum can be computed with `HaloFit` [457] or for MG theories with scale-independent linear growth, ΛCDM-based emulators such as `EuclidEmulator2` [32, 458] or `bacco` [31] can be used by adjusting the spectrum amplitude parameter, A_s or σ_8, to match the modified cosmology.

The reaction function $\mathcal{R}(k,z)$ contains all nonlinear corrections to the pseudo spectrum coming from modifications of gravity and massive neutrinos. We refer the reader to Refs. [4, 130] and Section 5.2 for more details on how to model the reaction function. In a nutshell, similar to the halo-model approach, there are three distinct regimes in scale: linear (2-halo term), quasi-nonlinear (1-loop corrections and smoothing), and nonlinear (1-halo term). For each we need to follow a certain prescription within our framework. These three regimes are demonstrated clearly in the Poisson equations 5.12-5.13.

In the linear regime, the enhancement or suppression of structure formation relative to ΛCDM is controlled by $\mu_{\rm L}(k,a)$. In the quasi-nonlinear regime, the modifications at second and third orders are captured by a source term $S(\boldsymbol{k},a)$ (see Eq. 5.14). Within the reaction function, two parameters guarantee a smooth transition between the 2- and 1-halo terms in the quasi-nonlinear regime: $\mathcal{E}$ and $k_\star$. The first parameter corresponds to the 1-halo power spectrum ratio in the modified and pseudo cosmologies at very large scales, tuning the similarities in their halo mass functions. The second parameter controls the rate of the transition, and for that parameter the one-loop corrections given by $S(\boldsymbol{k},a)$ are essential.

In the nonlinear regime, the modification to gravity is governed by $\mu_{\rm NL}(k,a)$, which should recover GR at very nonlinear scales ($k \gg 10\,h/{\rm Mpc}$) in the screened MG theories $\mu_{\rm NL} \to 1$ or $\mu_{\rm NL} = \mu_{\rm L}$ in the unscreened MG theories. This function is then considered when solving the gravitational collapse equation for the top-hat radius. From the solution of the gravitational collapse equation and Virial theorem, we derive the density at the collapse, virial scale factor and virial density, which are then used for computing the halo-mass function [459, 460] and halo density profile [461] – two essential properties of the 1-halo term power spectrum.

All in all, to fully describe $P^{{\rm MG}+\nu}$ we require the following information: the total neutrino mass M_ν (or equivalently the neutrino density parameter, related to the mass by $M_\nu \approx 93.14\,\Omega_\nu h^2$ eV), and 5 functions – the expansion history $H(a)$, the modification of gravity on linear scales $\mu_{\rm L}(k,a)$, two functions γ_2 and γ_3 included in the source term $S(\boldsymbol{k},a)$ that modifies quasi-nonlinear scales, and the modification of gravity in the nonlinear regime $\mu_{\rm NL}(k,a)$. In the subsequent subsection, we discuss these functions for the MG theories of interest.

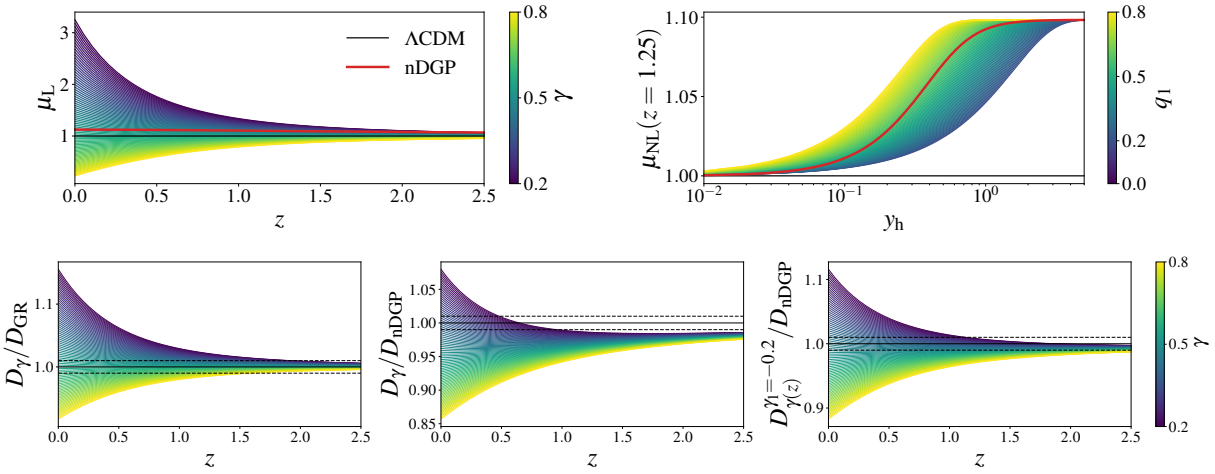

Figure 6.1 *Upper panel: left – linear modification to the Poisson equation for nDGP gravity with strong modification of $\Omega_{rc} = 0.25$ (red solid line), GR (black line) and different growth index values specified in the colour-bar; right – nonlinear modification to the Poisson equation for the same nDGP scenario, and growth index with $\gamma = 0.4$ and various values of the screening scale q_1 at $z = 1.25$ as a function of the normalised halo radius y_h, defined in Eq. C.44. Lower panel: ratio between the growth factors computed for various values of γ; left – with respect to the growth in GR, middle and right – with respect to nDGP for time-independent and time-dependent growth index respectively. Dashed black lines denote the 1% range.*

6.1.2 Modified Gravity Scenarios

In the previous Chapter 5, we studied Horndeski theories employing the Effective Field Theory of Dark Energy (EFTofDE). Horndeski theories [462] encompass the most general class of scalar-tensor theories of gravity in 4 dimensions that are Lorentz-covariant, ghost-free and have second-order equations of motion. However, in this work, we specifically focus on a popular example of scalar-tensor theories with Vainshtein screening [382] – the normal branch of DGP theories (nDGP, [107]). We aim to recover its main features with the phenomenological growth index parameterisation [292, 293, 423] extended to the nonlinear regime (see the "minimal parameterisation" in Tab. 5.2).

For our theories of interest the modification of the Weyl potential from Eq. 1.40 is $\Sigma_L = 1$, i.e., lensing is not affected: for nDGP this is derived in Refs. [463, 464] and for the γ-parameterisation we set it by hand. Therefore, in this work, in Eq. 6.1 we set $\Sigma(k, z) = 1$ and modify P_{NL} only.

Below is a summary of the functions required for the reaction calculations and our assumptions:

1. The background expansion is set to be equal the standard cosmology: $H(a) = H_0\sqrt{\Omega_m a^{-3} + (1 - \Omega_m)}$.

2. Modifications in the linear regime:

$$\mu_{\rm L}(a) = \begin{cases} 1 + \frac{1}{3\beta(a)} & \text{for nDGP} \\ \frac{2}{3}\Omega_{\rm m}^{\gamma-1}(a)\left[\Omega_{\rm m}^{\gamma}(a) + 2 - 3\gamma + 3(\gamma - 1/2)\Omega_{\rm m}(a)\right] & \text{for } \gamma = const \\ \frac{2}{3}\Omega_{\rm m}^{\gamma-1}(a)\gamma_1(a-1/a)\log\Omega_{\rm m}(a) + \mu_{\rm L}^{\gamma=const}(a) & \text{for } \gamma(a) \end{cases} \tag{6.7}$$

with $\beta(a)$ defined as

$$\beta(a) = 1 + \frac{H(a)}{H_0}\frac{1}{\sqrt{\Omega_{rc}}}\left(1 + \frac{\dot{H}(a)}{3H^2(a)}\right), \tag{6.8}$$

where dot denotes a derivative with respect to the time coordinate and Ω_{rc} corresponds to the strength of modification in the nDGP cosmology ($\Omega_{rc} = 0$ in GR). The derivation of $\mu_{\rm L}$ for nDGP can be found in Ref. [463], while for the growth index parameterisations one inserts the growth rate, $f(a) = [\Omega_{\rm m}(a)]^{\gamma(a)}$, into the linearised growth equation

$$f'(a) + f^2(a) + \left(2 + \frac{H'(a)}{H(a)}\right) f(a) = \frac{3}{2}\mu_{\rm L}(a)\Omega_{\rm m}(a) \tag{6.9}$$

with $' = {\rm d}/{\rm d}\ln a$, to find the expression for $\mu_{\rm L}$. In addition to the standard (constant) growth index parameter, we consider a time-dependent version of the form $\gamma(a) = \gamma_0 + \gamma_1(a + 1/a - 2)$ from the recent work of Ref. [296]. We add this model to our `MGCAMB` branch. The latter parameterisation was recently proposed because it captures the time-evolution of growth in Horndeski theories better than the constant growth index. We demonstrate this in the lower right panel of Fig. 6.1. Additionally, in the same figure, we illustrate the impact different choices of $\mu_{\rm L}$ have on the growth factor D for the time-independent growth index. Indeed, for nDGP the time-dependent parameterisation of the growth index provides a better fit than the constant one. However, for the standard cosmology, the growth index parameterisation remains excellent, whereas, for a scalar-tensor theory like nDGP, it does not. Further discussion on the correspondence between the constant growth index and DGP theories is provided in Appendix D.1. In all models, we ensure a match with General Relativity at high redshifts. In other words, we introduce modifications of the standard cosmology only in the late universe, while the early universe remains ΛCDM.

3. In the quasi-nonlinear regime for nDGP γ_2- and γ_3-functions[5] within $S(\boldsymbol{k}, a)$ are specified in Ref. [365], while for the scale-independent growth index parameterisation

[5]Note that the γ_2- and γ_3-functions are not related with the growth index parameterisation despite having similar notation. These functions, $\gamma_2(\boldsymbol{k}_1, \boldsymbol{k}_2, a)$ and $\gamma_3(\boldsymbol{k}_1, \boldsymbol{k}_2, \boldsymbol{k}_3, a)$, characterise quasi-nonlinear modifications to the Poisson equation.

we set them to zero. In Subsection 5.4.2 we demonstrated that the 1-loop corrections impact the reaction function very weakly for nDGP, less than 1%. However, this might become a consideration when scale-dependency in the linear growth is present.

4. Modifications in the fully nonlinear regime:

$$\mu_{\rm NL}(a) = \begin{cases} \frac{2}{3\beta(a)}\frac{\sqrt{1+s^3}-1}{s^3} + 1 & \text{for nDGP} \\ (\mu_{\rm L}^{\gamma}(a) - 1)\text{erf}(a\, y_{\rm h} 10^{q_1}) + 1 & \text{for } \gamma \text{ parameterisations}\,. \end{cases} \tag{6.10}$$

The expression for nDGP is derived in Ref. [339] following the solution of a spherically symmetrical overdensity with

$$s = \left[\frac{2\Omega_{\rm m}(\delta+1)}{9a^3\beta(a)^2\Omega_{rc}}\right]^{\frac{1}{3}}, \tag{6.11}$$

and δ being the nonlinear over-density given by

$$\delta = y_{\rm h}^{-3}(1+\delta_{\rm ini}) - 1\,, \tag{6.12}$$

with $\delta_{\rm ini}$ being the initial over-density and

$$y_{\rm h} \equiv \frac{R_{\rm TH}/a}{R_i/a_{\rm ini}}\,, \tag{6.13}$$

$R_{\rm TH}$ and R_i being the physical halo top-hat radius at the target scale factor a and at the initial scale factor $a_{\rm ini}$, respectively. The second expression is phenomenological and was demonstrated in Subsection 5.5.2 to reproduce the Vainshtein screening behaviour within 1% up to $k = 5\ h/$Mpc when compared against the exact solution. By the exact solution we mean the halo-based reaction computation for the exact expression of $\mu_{\rm NL}$ in nDGP from Eq. 6.10. This exact `ReACT` solution, in turn, shows percent-level agreement when tested against numerical simulations in Ref. [4]. The error function form in $\mu_{\rm NL}$ guarantees a smooth transition from the modified into the screened regime: on large scales in the linear regime $\mu_{\rm NL} \to \mu_{\rm L}$, while on small scales $\mu_{\rm NL} \to 1$. The parameter q_1 corresponds to the screening scale, and its impact is demonstrated in the right upper panel of Fig. 6.1 (for a case of $\gamma = 0.4$ that matches the linear modification of nDGP with $\Omega_{rc} = 0.25$ at redshift $z = 1.25$). From this figure, we see that the higher q_1 the deeper into the halo the transition from modification to no modification happens. The opposite is also true, the lower q_1 the farther outside the halo $\mu_{\rm NL} = 1$. The GR-limit is fully recovered at all scales when $q_1 \to -\infty$. Values of $q_1 \gtrsim 2$ correspond to a screening scale deep within a halo, indicating that we will observe no effect of screening in the nonlinear power spectrum at the scales of our interest.

6.1.3 Baryonic Effects

The last missing component from Eq. 6.6 is the boost from the baryonic feedback, B^{baryons}. It is well-known that astrophysical processes significantly impact the matter power spectrum in the nonlinear regime. For instance, active galactic nuclei (AGN), supernovae, and stellar winds repulse matter from clustered centralised clumps into intergalactic medium, causing a suppression of the observed structures on small scales. On even smaller astrophysical scales, the observed structures get boosted by gas cooling and star formation. The effects of baryonic processes have been extensively studied in various hydrodynamical simulations, including BAHAMAS [465], Illustris-TNG [466], and more recent FLAMINGO [467], among others. However, these effects are sensitive to the sub-grid physics and can vary significantly between different simulations (as depicted in Fig. 9 of Ref. [468]).

Instead of running computationally expensive hydro-simulations and fine-tuning them to match observations, the impact of baryons can be modelled using a baryonification model [468, 469]. In this approach, halo profiles, the outputs of a dark-matter-only simulations, are modified by slightly displacing particles around halo centres in a spherically symmetric way. This displacement is characterised by 7 baryonic parameters: $\{\log_{10} M_c, \theta_{\text{ej}}, \mu_{\text{bar}}, \gamma_{\text{bar}}, \delta_{\text{bar}}, \eta_{\delta\text{bar}}, \eta_{\text{bar}}\}$ (the first five describe the gas distribution, while the last two are related to the stellar abundances)[6], along with one cosmological parameter, the baryonic fraction $f_{\text{b}} = \Omega_{\text{b}}/\Omega_{\text{cdm+b}}$. In our analysis we use the baryonic emulator `BCEMU` [470], which accurately reproduces the power spectra of state-of-the art hydrodynamical simulations even with a reduced number of parameters. This emulator has been employed to analyse cosmic shear data in Ref. [471], and provides a robust and flexible tool for incorporating baryonic effects into our analyses. In Subsection 6.3.3 we discuss the cosmology dependence in the context of MG theories for the baryonification approach.

The importance of baryonic feedback becomes evident on scales comparable to the size of a halo, which coincides with the scales where screening is crucial for MG theories. In this work, we aim to investigate whether an independent parameterisation of the screening scale can be decoupled from the effects of baryons. To achieve this, when exploring the generalised parameterisation in Subsection 6.3.3 and Subsection 6.3.5, we only vary $\log_{10} M_c$ (similarly to the DES Y3 shear analysis in Ref. [472]), while keeping the

[6] $\log_{10} M_c$ defines the characteristic mass scale where the slope of the gas profile becomes shallower than -3 (i.e., shallower than the Navarro-Frenk-White profile) for small halos with $M_{\text{vir}} \ll M_{\text{c}}'$. The critical mass M_c is given in the solar mass units $M_{\text{c}} := M_{\text{c}}'/\left(M_\odot\, h^{-1}\right)$. μ_{bar} defines how fast the slope of the gas profile becomes shallower towards small halo masses. θ_{ej} specifies the maximum radius of gas ejection relative to the virial radius. γ_{bar} and δ_{bar} control the slope of the gas profile falling beyond the virial radius. η_{bar} specifies the total stellar fraction within a halo (including central galaxy, satellites, and halo stars). $\eta_{\delta\text{bar}}$ defines the difference between the total stellar fraction and the one of the central galaxy.

others fixed at their fiducial values. Exploring degeneracies with the full set of baryonic parameters will be explored in future work. The $\log_{10} M_c$ parameter controls the slope of the gas density distribution: smaller haloes with masses less than M_c have shallower profiles. Both the screening and baryonic feedback effects display weak cosmological dependence and result in the suppression of growth on approximately the same scales. Already from this fact alone we can highlight the urgency of accurately measuring baryonic parameters.

Fortunately, there exists a well-established connection between the baryonic effects on the power spectrum and the gas and stellar fractions in haloes [469]. This suggests that additional secondary CMB observables and/or X-ray measurements of galaxy groups and clusters can help constrain these parameters or impose physically motivated priors. For instance, in Ref. [473] authors measured $\log_{10} M_c = 14.53 \pm 0.20$ with a compilation of Bayesian population studies of galaxy groups and clusters and with cluster gas density profiles derived from deep, high-resolution X-ray observations. While Ref. [471] found $\log_{10} M_c \approx 13.2 \pm 0.4$ from the combination of the KiDS-1000 cosmic shear data with the gas profiles from kinematic Sunyaev–Zeldovich (kSZ) observations and X-ray data. Recently, Ref. [474] found a significantly stronger baryonic feedback suppression than in previous studies with $\log_{10} M_c = 13.22^{+0.42}_{-0.29}$ using the DES Y3 cosmic shear and CMASS + ACT DR5 kSZ observations. In these three works all 7 parameters of the model were varied. Interestingly, it has been demonstrated in Ref. [428] that with the addition of mock gas fractions from eROSITA a Euclid-like setup finds $\sigma_{\log_{10} M_c} / \log_{10} M_c \sim \mathcal{O}(0.001)$ when $\log_{10} M_c$ is varied together with $\mu_{\rm bar}$ and $\theta_{\rm ej}$. This implies that future surveys can decrease baryonification model errors by more than an order of magnitude. However, whether or not the model with only 3 baryonic parameters, $\{\log_{10} M_c, \mu_{\rm bar}, \theta_{\rm ej}\}$, qualifies for Stage-IV surveys without introducing biases is still under investigation. Additionally, the percent and sub-percent level of precision assumes that the baryonification model is correct and complete. This as well requires further exploration, especially for the newest generation of surveys.

Alternative approaches to mitigate the baryonic effects include a) a slightly different model of baryonification called Baryon Correction Model [475, 476] that was applied to DES Y3 data [64, 472], b) halo model [456, 477], and c) Principal Component Analysis (PCA) [478–480].

6.2 Analysis Setup

The survey specifications in our pipeline are chosen to mimic Stage-IV specifications: sky fraction $f_{\rm sky} = 0.4$, number density of galaxies per arcminute squared $n = 30$ arcmin^{-2}, and per-component dispersion in the intrinsic galaxy ellipticities $\sigma_\epsilon = 0.3$. We take 10 equipopulated tomographic bins between redshifts $z \in [0.001, 2.5]$. The photometric

redshift distribution of galaxies is following $n_i(z) \propto (z/z_0)^2 \exp -(z/z_0)^{3/2}$ with $z_0 = 0.9/\sqrt{2}$ [481] . The uncertainty on the photometric redshift is modeled as the sum of two Gaussian distributions: one for the well determined photometric redshifts and another for the outliers (we follow the prescription in Section 3.3.1 of Ref. [281]).

As input we use synthetic data, namely angular power spectra, C_ℓ, computed according to Eq. 6.3, with the fiducial cosmology in three scenarios:

1. ΛCDM scenario in Subsection 6.3.1: nonlinear power spectrum is calculated with `HMcode2020` in which linear input is computed with `bacco`;

2. nDGP scenario in Subsections 6.3.2 and 6.3.5 with strong deviation from the standard cosmology $\Omega_{rc} = 0.25$: nonlinear power spectrum computed with reaction from `ReACT` and pseudo-power spectrum from `HMcode2020`;

3. minimal parameterisation in Subsections 6.3.3 and 6.3.4 with $\gamma = 0.4$, $q_1 = 0.76$: nonlinear power spectrum computed with reaction from `ReACT` and pseudo-power spectrum from `HMcode2020`.

We use these scenarios to validate the pipeline and then test the performance of the growth index parameterisation. We model the angular power spectra from Eq. 6.3, where the background remains unaffected and the MG modification impacts the linear growth parameter and the nonlinear power spectrum. In total, we emulate 3 models for $B^{\mathrm{MG}+\nu}$ from Eq. 6.5 using `cosmopower` [482]: nDGP[7], $\gamma + q_1$ and $\gamma(z) + q_1$ in the ranges specified in Table 6.2 and the accuracy of emulators provided in the corresponding code repository[8]. We compute our models for the nonlinear matter power spectrum boost in the wavenumber range of $k \in [0.01, 5]\, h/\mathrm{Mpc}$. For smaller k-values we extrapolate the boost to be constant and equal to its value at $k = 0.01\, h/\mathrm{Mpc}$, while for larger k-values we extrapolate the boost as a power law. For the ΛCDM nonlinear power spectrum from Eq. 6.5 we use `HMcode2020`. Finally, the baryonic boost, B^{baryons}, in Eq. 6.5 is computed with `BCEMU`.

The likelihood is computed as (see Appendix B.2 of Ref. [332]):

$$\log \mathcal{L} = -\frac{1}{2} \sum_{\ell=10}^{\ell_{\max}} (2\ell + 1) f_{\mathrm{sky}} \left(\frac{d_\ell^{\mathrm{mix}}}{d_\ell^{\mathrm{model}}} + \ln \frac{d_\ell^{\mathrm{model}}}{d_\ell^{\mathrm{data}}} - N_{\mathrm{bins}} \right) \tag{6.14}$$

where N_{bins} is the number of photometric bins and d_ℓ denote the determinants of C_ℓ^{ij}: the mock data and model are both computed with Eq. 6.3, and d_ℓ^{mix} is defined as

$$d_\ell^{\mathrm{mix}} = \sum_{k=1}^{N_{\mathrm{bins}}} \det \left[\begin{cases} C_{ij}^{\mathrm{model}}(\ell) & \text{if } j \neq k \\ C_{ij}^{\mathrm{data}}(\ell) & \text{if } j = k \end{cases} \right] . \tag{6.15}$$

[7] Alternative emulators for nDGP trained on numerical simulations: BRIDGE [483] and github.com/BartolomeoF/nDGPemu [484].

[8] github.com/nebblu/ReACT-emus/emulators/Accuracy Plots

The modelling and likelihood function we use were validated in Ref. [485]. The priors are given in Tab. 6.1, and the fiducial values for the fixed baryonic parameters are: $\theta_{\rm ej} = 4.235$, $\mu_{\rm bar} = 0.93$, $\gamma_{\rm bar} = 2.25$, $\delta_{\rm bar} = 6.4$, $\eta_{\delta \rm bar} = 0.14$, $\eta_{\rm bar} = 0.15$.

Effect	Parameter	Prior	Fiducial
Cosmological	ω_c	$\mathcal{U}(0.11, 0.13)$	0.12
	ω_b	$\mathcal{N}(0.02268, 0.00038)$	0.02268
	h	$\mathcal{U}(0.63755, 0.7305)$	0.68
	$\log\left(10^{10}\ A_s\right)$	$\mathcal{U}(2.7081, 3.2958)$	3.044
	n_s	$\mathcal{N}(0.97, 0.004)$	0.97
Intrinsic Alignments	$A^{\rm IA}$	$\mathcal{U}(0, 12.1)$	1.72
	$\eta^{\rm IA}$	$\mathcal{U}(-7, 6.17)$	-0.41
Modified Gravity	$\log_{10}\Omega_{rc}$	$\mathcal{U}(-3, 2)$	0.25
	γ, γ_0	$\mathcal{U}(0, 1)$	-
	γ_1	$\mathcal{U}(-0.7, 0.7)$	-
	q_1	$\mathcal{U}(-2, 2)$	-
Baryonic	$\log_{10} M_c$	$\mathcal{U}(11.4, 14.6)$	13.32
Massive Neutrinos	M_ν	$\mathcal{U}(0, 0.1576)$	0.06

Table 6.1 *Sampling parameters, prior ranges and fiducial values in the model and mock data respectively. The spectral index n_s has tight Planck prior and the baryonic density component has a BBN-prior, both motivated by weak constraints on these parameters from cosmic shear data [11].*

	$\Omega_{\rm m}$	$\Omega_{\rm b}$	Ω_ν	h	n_s	A_s	γ, γ_0	γ_1	q_1	$\log_{10}\Omega_{rc}$	z
lower	0.2899	0.04044	0.	0.629	0.9432	1.5×10^{-9}	0.	-0.7	-2	-3	0.
upper	0.3392	0.05686	0.00317	0.731	0.9862	2.7×10^{-9}	1.	0.7	3	2.	2.4

Table 6.2 *Prior ranges for the emulators.*

The posterior distribution is sampled with `Nautilus` [212] for 3×10^3 live points. This sampler is based on the importance nested sampling (INS) technique combined with deep learning via neural network regression. Nested sampling-based samplers tend to under-predict the size of the posterior contours when compared to much slower but more accurate samplers (see, for example, Appendix D of Ref. [453]). However, `Nautilus` does not suffer from this tendency (see Appendix H of Ref. [486]). We varied the number of live points to guarantee the convergence and to control the differences in posterior-volumes when comparing between models with different number of parameters.

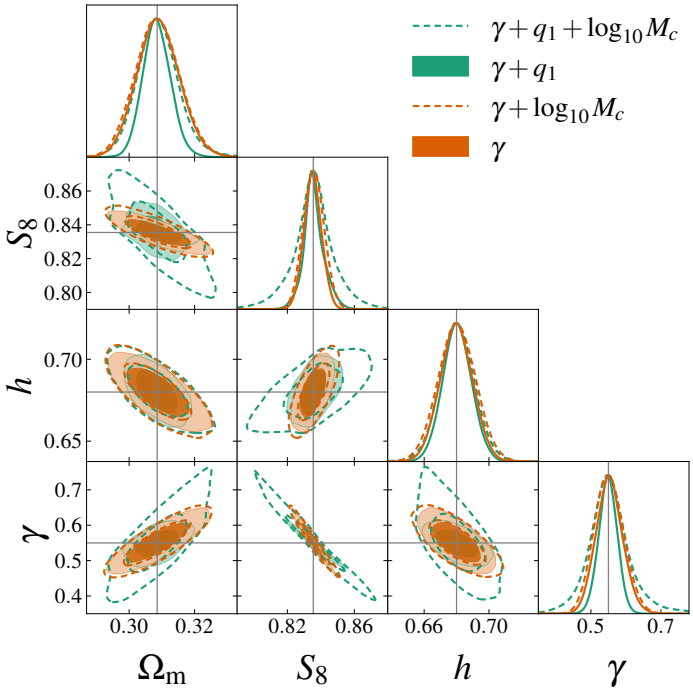

Figure 6.2 *Marginalised posterior distribution for the cosmological parameters. Mock data: ΛCDM scenario (see Subsection 4.2.2). Models: the time-independent growth index parameterisation with screening (green) and without screening (orange). We fit the cosmic shear power spectra with* $\ell_{\max} = 3000$. *Solid lines and filled contours correspond to* $B^{\text{baryons}} = 1$ *from Eq. 6.5 (for both – data and models), while dashed lines and empty contours correspond to the baryonic feedback contribution with varying* M_c *and fixed values of the other baryonic parameters as detailed in the main text. Grey lines mark the true values of the synthetic data.*

6.3 Results

We first validate our models on synthetic data in ΛCDM, i.e., data with GR as the model of gravity. Then we test how the index growth models – with and without screening – perform when the true cosmology is nDGP, i.e., with enhancement of structure on large scales and recovering of GR on small-scales via Vainshtein screening. After that, we produce synthetic data with the screened $\gamma + q_1$ model, and study degeneracies between the screening scale and baryonic feedback, and massive neutrinos. Finally, we compare the performance of the exact nDGP model versus the model-independent growth index approach on a mock data vector assuming nDGP gravity, baryonic feedback and massive neutrinos.

6.3.1 Validation with GR

In order to validate our likelihood pipeline, we perform MCMC analyses on mock data in the standard cosmology (without massive neutrinos). For the scale-cut we take

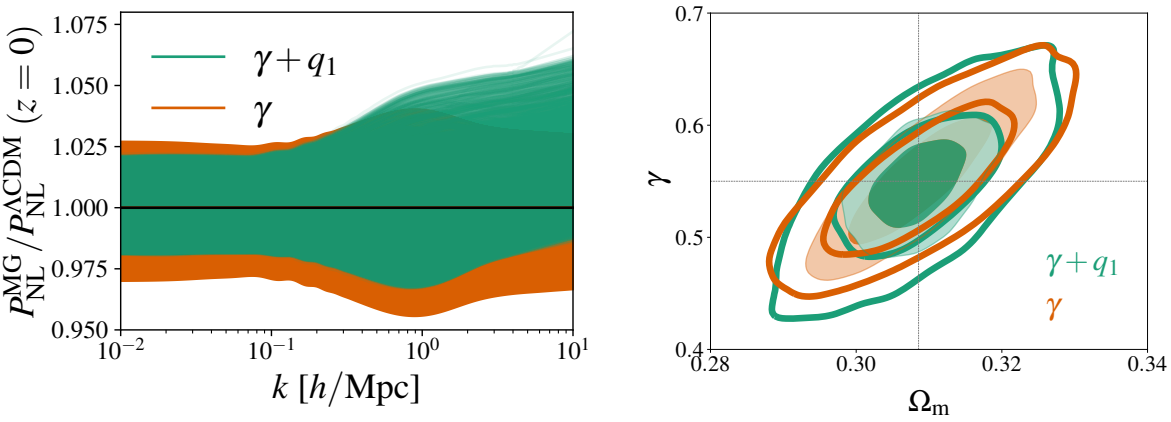

Figure 6.3 *Left panel: the variation in the ratio* $P_{\rm NL}^{\rm MG}/P_{\rm NL}^{\Lambda{\rm CDM}}$ *at redshift zero for the screened,* $\gamma + q_1$*, and unscreened,* γ*, models drawn from the posterior distributions in Fig. 6.2 within a* 1σ *deviation around the posterior maximum for* γ*. Right panel: marginalised posterior distribution in* $\Omega_{\rm m} - \gamma$ *for the same models on the mock GR data with* $\ell_{\rm max} = 3000$ *(filled contours) and* $\ell_{\rm max} = 1000$ *(unfilled contours).*

$\ell_{\rm max} = 3000$, which is considered a middle value between "pessimistic" ($\ell_{\rm max} = 1500$) and "optimistic" ($\ell_{\rm max} = 5000$) scenarios for Stage-IV surveys [281]. We test two models – the growth index parameterisation without screening via a pseudo-power spectrum (γ) and with screening ($\gamma + q_1$). In Fig. 6.2 we show posterior distributions for the main parameters of interest in weak lensing as well as the expansion rate today, h. The latter is added to demonstrate its anti-correlation with the extended parameter γ, while the h degeneracy with ω_b and n_s is broken by informative priors on the latter two parameters. The full posterior distribution is demonstrated in Fig. D.1 of Appendix D.2 together with a detailed discussion on the various degeneracies and the parameters controlling the amplitude[9].

In Fig. 6.2, both models recover all cosmological parameters correctly, and the value of the growth index is ~ 0.55 as expected, with uncertainties $\sigma_\gamma = 0.03$ for $\gamma + q_1$ and $\sigma_\gamma = 0.04$ for γ without screening. The fact that a model with more parameters results in tighter constraints is explained by the functional form of $\mu_{\rm NL}$ (see Eq. 6.10): any deviation from $\gamma \sim 0.55$ or $\mu_{\rm L} = 1$ opens the possibility of constraining q_1, which leads to a worse fit or smaller likelihood due to nonlinear signatures that are very different from the GR predictions. We illustrate this in the left panel of Fig. 6.3, where we plot the power spectra ratio $P_{\rm NL}^{\rm MG}/P_{\rm NL}^{\Lambda{\rm CDM}}$ at $z = 0$ from the posterior distribution's 1σ γ-constraints. We see that broader uncertainty on γ in the pseudo model manifests on linear scales, however for $k > 1\ h/{\rm Mpc}$ the variation in the power spectrum becomes larger for $\gamma+q_1$ than for γ only.

[9]For the amplitude of the power spectrum we present both – the sampled parameter of the primordial amplitude A_s, and its derived late-Universe counterpart $\sigma_8 = D_\gamma(z=0)/D_{\Lambda{\rm CDM}}(z=0)\,\sigma_8^{\Lambda{\rm CDM}}$, with σ_8 being the r.m.s. density variation when smoothed with a top-hat filter of radius 8 Mpc$/h$, and $S_8 = \sigma_8\sqrt{\Omega_{\rm m}/0.3}$. We also show the derived matter density parameter $\Omega_{\rm m} = (\omega_c + \omega_b)/h^2$.

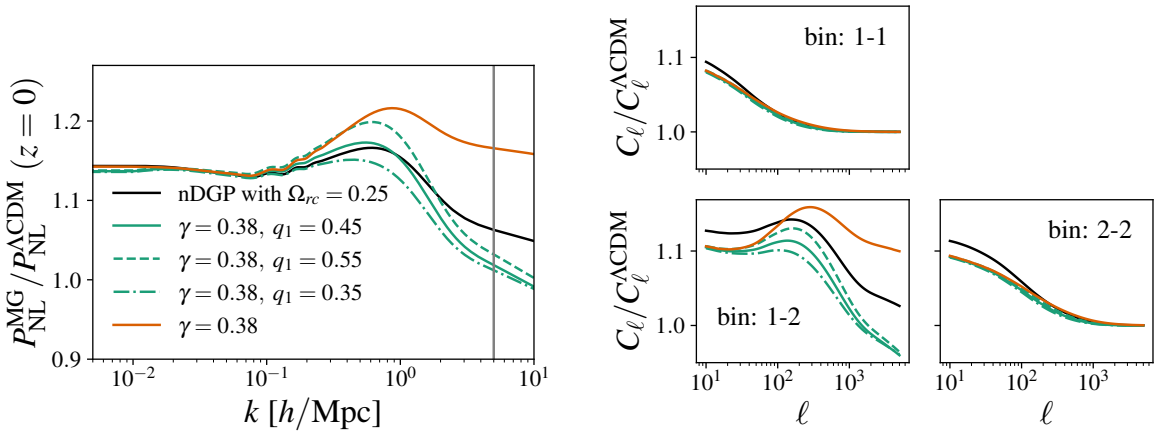

Figure 6.4 *Left panel: power spectrum ratios at redshift $z = 0$ for the screened (green lines) and unscreened (orange line) models with nonlinear prescriptions described in the text. Grey line denotes $k_{\rm max} = 5\ h/{\rm Mpc}$ that we compute and emulate with* `ReACT`*, for higher values we extrapolate the MG boost as a power law. Right panel: corresponding ratios of the shear angular power spectra. Central redshifts: for bin 1 $z_c = 0.21$, for bin 2 $z_c = 0.49$. We fix all cosmological parameters to the fiducial values.*

This also implies that for more conservative scale-cuts we should not obtain differences in σ_γ, this effect is purely due to the inclusion of nonlinear scales and high sensitivity to these scales in a Stage-IV-like setup. As an additional proof of this conclusion we demonstrate the $\Omega_{\rm m} - \gamma$ contours for stricter scale-cuts of $\ell_{\rm max} = 1000$ in the right panel of Fig. 6.3. The 1σ ranges are visibly in better agreement between the models now. The inclusion of a baryonic feedback model increases the errors for the pseudo model to $\sigma_\gamma = 0.04$ and $\sigma_\gamma \approx 0.05$ for the screened model. In this case the strong degeneracy between the screening scale and baryonic parameters explains a more significant broadening of the contours. We study this degeneracy in detail in Subsection 6.3.3.

6.3.2 Screening Scale with nDGP Gravity

Next we validate our model on a theory with the Vainshtein screening mechanism on nonlinear scales and a strong deviation from GR on linear scales ($\sim 14\%$ more structure than in GR on linear scales at lower redshifts). In the left panel of Fig. 6.4 we show the ratio of power spectra $P_{\rm NL}^{\rm MG}/P_{\rm NL}^{\Lambda{\rm CDM}}$ at $z = 0$ for the nDGP model with $\Omega_{rc} = 0.25$ (black solid line). For the same fiducial cosmological parameters, we show also this ratio for the screened (green line) and pseudo (orange line) growth index models. The pseudo approach captures the bump-feature in the range of $k \sim 0.2 - 0.9\ h/{\rm Mpc}$ but overpredicts its amplitude. The screened model reproduces this feature extremely well, at the percent level for $k \lesssim 3\ h/{\rm Mpc}$. In the right panel, we show ratios of the corresponding angular power spectra, C_ℓ, for the three models with respect to GR for the same set of cosmological

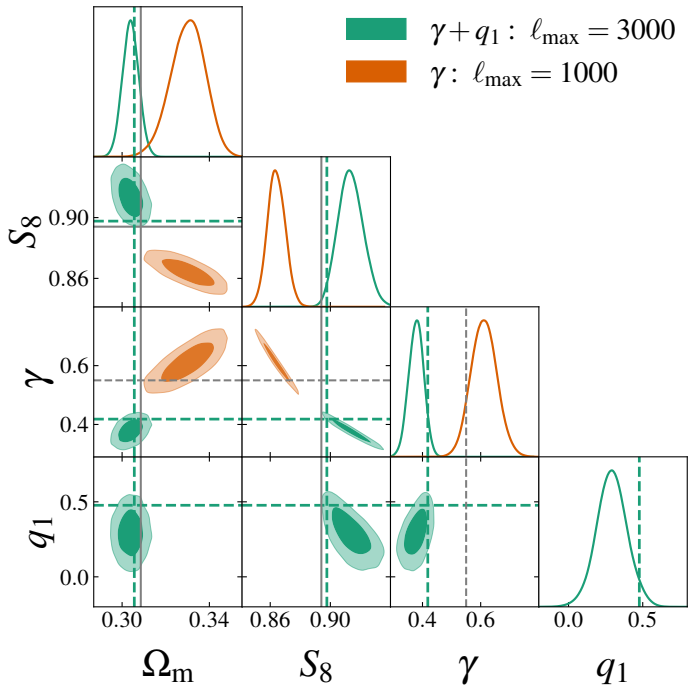

Figure 6.5 *Marginalised posterior distribution for the cosmological and extended parameters analysed with $\ell_{\rm max} = 3000$. Mock data: nDGP cosmology with $\Omega_{rc} = 0.25$ (see Subsection 4.2.2). Models: the time-dependent growth index parameterisation with screening when both γ-parameters are varied (green) and with γ_1 fixed (orange). Grey solid lines mark the true values of the synthetic data, grey dashed lines mark the GR-limit. Orange dashed lines denote the best fit values from the plotted MCMC chain for the second model.*

parameters. The bump-feature in the nonlinear regime is visible in the cross-correlated redshift-bins, while in the auto-correlated bins we see characteristic curves that tightly converge for all models at smaller scales. However, we notice a shift at linear scales for the γ-models. The reason for this shift is the difference in the time evolution between nDGP and the growth index parameterisation as discussed in Subsection 6.1.2: while the growth modification is matched between different models at $z = 0$, this is no longer the case for higher redshifts.

We consider the same two models: models with screening in the reaction function ($\gamma + q_1$) and without screening via a pseudo-power spectrum (γ) and repeat our analysis on the mock nDGP data with $\ell_{\rm max} = 3000$ and using the same setup. We show the marginalised posterior distribution in Fig. 6.5. The full posterior distribution for the sampled cosmological parameters is shown in Fig. D.4 of Appendix D.4 with a more detailed description. Overall, our model with screening (green contours and lines) correctly captures the fiducial cosmology, detects a γ-value lower than its GR-limit as expected, namely $\gamma = 0.38 \pm 0.03$, and detects a screening transition with $q_1 = 0.29 \pm 0.10$. We notice a 1σ-bias in $\Omega_{\rm m}$ and a 2σ-bias in S_8. Both shifts are consequences of fitting a model, $\gamma + q_1$, to data with small error bars, while there is no accurate mapping of the

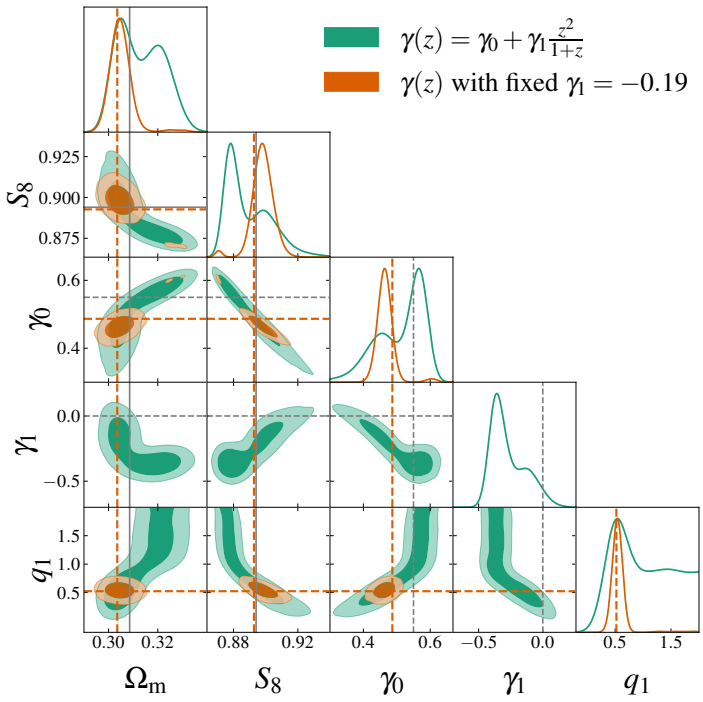

Figure 6.6 *Marginalised posterior distribution for the cosmological and extended parameters analysed with* $\ell_{\rm max} = 3000$. *Mock data: nDGP cosmology with* $\Omega_{rc} = 0.25$ *(see Subsection 4.2.2). Models: the time-dependent growth index parameterisation with screening when both* γ*-parameters are varied (green) and with* γ_1 *fixed (orange). Grey solid lines mark the true values of the synthetic data, grey dashed lines mark the GR-limit. Orange dashed lines denote the best fit values from the plotted MCMC chain for the second model.*

time-evolution of linear growth between the growth index parameterisation and nDGP. We check whether this can also be connected to projection effects [153]. In other words whether the likelihood maxima (green dashed lines) are at the true values of cosmological parameters and not at the posterior maximum values. From the MCMC chain, we derive the best-fit value $\Omega_{\rm m}^{\rm best-fit} \approx 0.306$, which is closer to the fiducial value of $\Omega_{\rm m}^{\rm fid} \approx 0.309$ than the posterior mean of $\Omega_{\rm m}^{\rm mean} \approx 0.304$. Also the best-fit values for $\gamma^{\rm best-fit} \approx 0.42$ and $S_8^{\rm best-fit} \approx 0.898$ very close to the true value of $S_8^{\rm nDGP} \approx 0.895$. We use the likelihood minimiser `iminuit` [195] and obtain similar values for the best-fit parameters. This implies a presence of projection or prior-volume effects. Lastly, we note that this bias vanishes when more parameters are varied and the contours are broadened (see Subsection 6.3.5). Overall, the agreement within 2σ satisfies the "precision versus accuracy" test for our model.

In Fig. 6.5, we notice that even for scale-cuts below the pessimistic scenario for Stage-IV surveys, namely for $\ell_{\rm max} = 1000$, there is a significant bias in S_8 and $\Omega_{\rm m}$ for the model without screening (orange contours and lines), with S_8 being closer to its GR value. Moreover, the value of γ does not correspond to the expected behaviour on large scales but rather points towards suppression of structure formation relative to the standard

cosmology. This signals that ignoring a correct screening implementation will result in the wrong extracted cosmology.

In the nonlinear regime our model-independent screening scale seems to be in a good agreement with nDGP theory which includes Vainshtein screening mechanisms. The disadvantage of this model is the inaccurate representation of time evolution of growth on linear scales. We can improve this by introducing the time-dependent γ-parameterisation from Ref. [296] (also see Subsection 6.1.2). The results are shown in Fig. 6.6 and Fig. D.5 for the same setup as before. From the green contours in Fig. 6.6 we see that while fiducial values lay within 1σ of all parameters, the screening scale is not properly constrained with cosmic shear information alone. Note how in general, extended parameters make the posterior distribution non-Gaussian by bringing additional degeneracies with cosmological parameters and with each other. Two extended parameters γ_0 and γ_1 are strongly anti-correlated, so we can aim to break degeneracies by fixing γ_1. We find from fitting to the boost at lower redshifts that $\gamma_1 = -0.19$ is a good fit and it breaks the degeneracy and allows us to constrain the screening parameter $q_1 = 0.57^{+0.07}_{-0.12}$ with $\gamma_0 = 0.47 \pm 0.02$ (orange contours and lines). In Fig. 6.6, we clearly see that while Ω_m is still 1σ-biased towards lower values, the bias in S_8 towards higher values decreases to 1σ contrary to the time-independent growth index. We again compute and plot best-fit values (dashed orange lines) from the MCMC chain, for fixed γ_1 they are $\Omega_\mathrm{m}^{\mathrm{best-fit}} \approx 0.304$ (0.306 from `minuit`), $\gamma^{\mathrm{best-fit}} \approx 0.49$, and $S_8^{\mathrm{best-fit}} \approx 0.894$. The model with more accurate time-evolution of growth seems to decrease the projection effects. The necessity of tight constraints on γ_1 implies that additional measurements from clustering will improve our constraints. We aim to investigate probe combinations in future work.

6.3.3 Screening Scale versus Baryons

Here we explore the degeneracy between the suppression due to the screening mechanism and baryonic feedback effects. In the left panel of Fig. 6.7 we demonstrate the comparison between MG and baryonic boosts for different parameters. The larger the value of q_1, the less is the suppression due to screening. The larger the value of $\log_{10} M_c$, the stronger is the suppression due to baryonic feedback at nonlinear scales. It is clear that both effects become noticeable at scales $k \gtrsim 1\, h/\mathrm{Mpc}$, since they demonstrate similar scale-dependence and overall amplitude. Already from this we can conclude that our model-independent screening scale, q_1, is highly degenerate with the baryonic suppression parameter $\log_{10} M_c$.

In order to avoid biases due to different time evolution of growth structure on linear scales, we perform an MCMC analysis on the mock data computed with the $\gamma + q_1$ model directly with $\gamma^{\mathrm{fid}} = 0.4$ and $q_1^{\mathrm{fid}} = 0.76$. We show the marginalised posterior distribution for $\gamma - q_1 - \log_{10} M_c$ in the right panel of Fig. 6.7, while the corresponding full posterior distribution is shown in Fig. D.6. The unbiased determination of γ, as

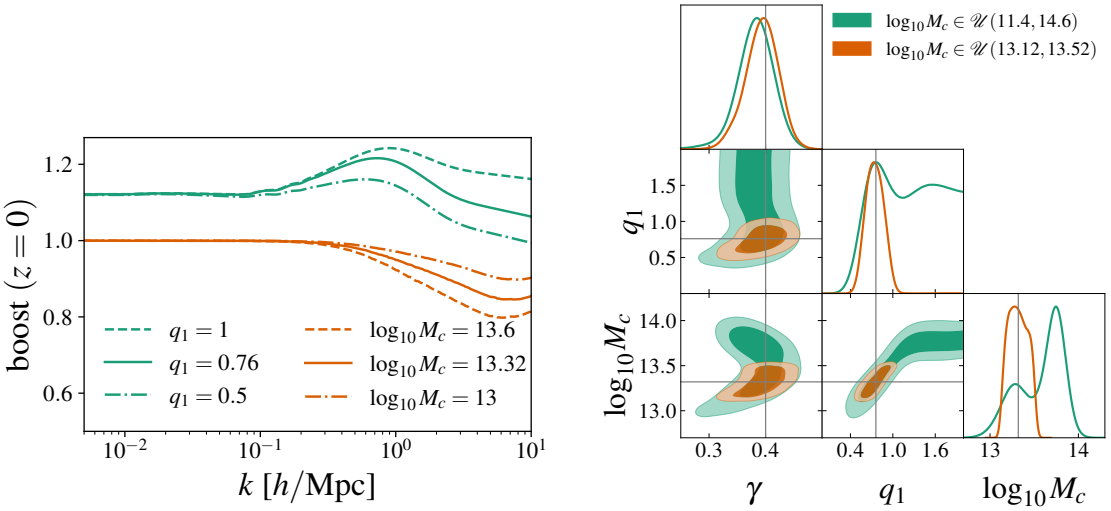

Figure 6.7 *Left panel: power spectrum boost at redshift zero for the MG contribution, $\gamma = 0.4$ and varying q_1 (green lines), and baryonic feedback (orange lines). Right panel: marginalised posterior distributions using cosmic shear power spectra with $\ell_{\max} = 3000$ for the MG and baryonic parameters with different priors on the latter, as detailed in the legend. Mock data and model: minimal parameterisation with the time-independent growth index (see Subsection 4.2.2). Grey lines mark the true values of the synthetic data.*

well as other cosmological parameters, is not affected by the inclusion of the baryonic feedback. However, the screening scale demonstrates a very strong positive correlation with the baryonic parameter and prefers the unscreened regime of $q_1 > 1.5$. The baryonic parameter absorbs the suppression due to screening and, as a result, gets biased towards higher values with respect to the fiducial value. This degeneracy persists, when testing variations in the fiducial values of $\log_{10} M_c$ within the same $\gamma + q_1$ model, while also examining different fiducial values of $\gamma + q_1$ while keeping $\log_{10} M_c$ constant. We perform these checks to mitigate potential coincidences in the choice of fiducial parameters. However, we find that when we impose a tight flat prior on $\log_{10} M_c$, the screening scale is recovered unbiased. This means we require a good understanding of baryonic physics for the detection of the model-independent screening transition: for instance, tight priors on baryonic parameters of the order $\sigma_{\log_{10} M_c} = 0.1$ or $\sigma_{\log_{10} M_c} / \log_{10} M_c \approx 1\%$.

Note that an incorrectly inferred prior imposed on baryonic feedback would bias MG parameters due to their strong degeneracy. Instead of imposing priors, for example, based on independent galaxy cluster X-ray observations, a better approach will be the cross correlation or the joint analyses of weak lensing and X-ray/kSZ probes like in the works mentioned in Subsection 6.1.3. We also highlight the importance of non-standard hydro-dynamical simulations. The `BCEMU` emulator we use in this work was trained for standard cosmologies. Despite the flexibility of the baryonification model with 7 or 3 parameters, we still do not know whether this is accurate enough to model nonlinear baryonic physics in beyond-ΛCDM cosmologies. Reassuringly, Refs. [361, 487] show

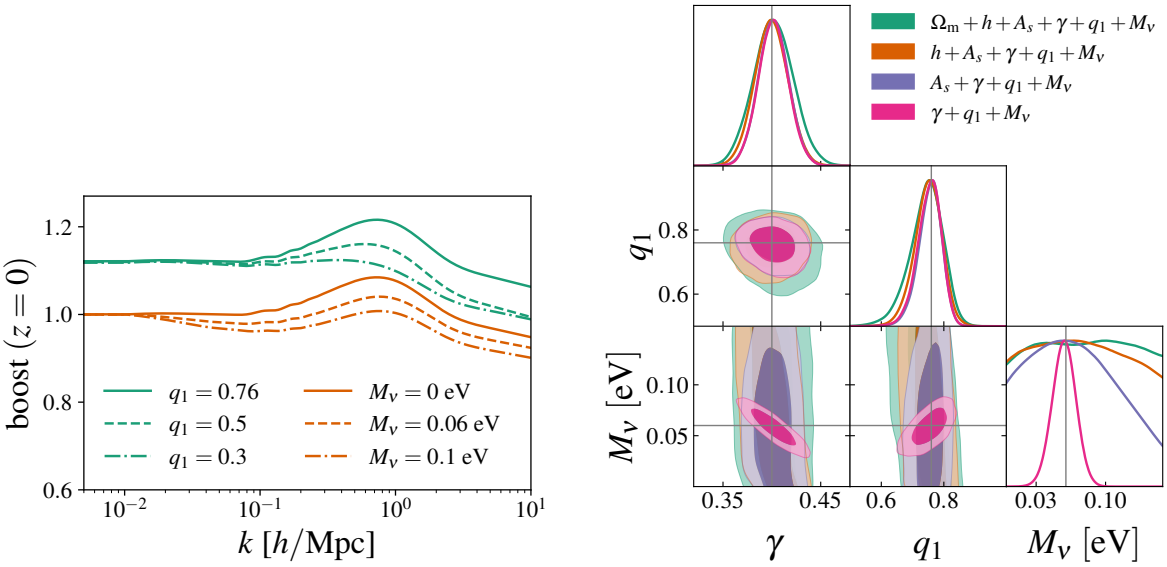

Figure 6.8 *Left panel: power spectrum boost at redshift zero for the MG contribution with $\gamma = 0.4$, $M_\nu = 0$ and q_1 varied (green lines), and $\gamma = 0.4$, $q_1 = 0.76$, M_ν varied (orange lines). The boosts for various neutrino masses are normalised to the value at the largest scales computed. Right panel: marginalised posterior distributions using the cosmic shear power spectrum with $\ell_{\max} = 3000$ for models with different cosmological parameters varied, as detailed in the legend. Mock data and model: minimal parameterisation with the time-independent growth index (see Subsection 4.2.2). Grey lines mark the true values of the synthetic data.*

both within the halo model and in N-body simulations that baryons and MG physics can be modelled independently to a large extent. For our fiducial nDGP model with $\Omega_{rc} = 0.25$ or N1, Ref. [488] demonstrates with full-physics hydrodynamical simulations a percent level agreement between separate and combined responses of the nonlinear matter power spectrum to MG and baryons. A promising argument for this would be that the astrophysics responsible for baryonic effects is happening on the scales in the screened regime, hence there is no reason to believe that it is significantly different from the standard baryon feedback processes. Especially since these are only weakly cosmology dependent (up to several percent for small variations in cosmology) and mainly depend on the fraction of baryons to the total matter according to various studies (e.g., Refs. [489, 490]). However, more work is needed to confirm whether these assumptions satisfy the requirements of Stage-IV surveys [491].

6.3.4 Screening Scale versus Neutrinos

The last nonlinear effect to consider is the suppression of structure growth due to the contribution of massive neutrinos (see Subsection 1.3.2). In the left panel of Fig. 6.8 we demonstrate the comparison between MG boosts for different values of screening and

neutrino mass parameters. The larger the value of q_1, the smaller the suppression due to screening. The larger the value of M_ν, the stronger is the suppression due to massive neutrinos. However, massive neutrinos lead to suppression of growth already at mildly nonlinear scales $k \gtrsim 0.1$ h/Mpc. Furthermore, the scale-dependency in the suppression due to massive neutrinos is drastically different form the suppression due to screening: there is no clear feature in the power spectrum in a constrained scale range. We still expect a positive correlation between q_1 and M_ν, but this will be in addition to noticeable degeneracies with other cosmological parameters controlling the amplitude and slope of the power spectrum at all scales, and not only in the nonlinear regime. For instance, the primordial amplitude A_s, the expansion rate h, and the matter density Ω_m. In the right panel of Fig. 6.8, for the same fiducial $\gamma + q_1$ cosmology as in the previous section with the addition of massive neutrinos with $M_\nu^\mathrm{fid} = 0.06$ eV, we showcase how the more parameters we vary the more sensitivity to the neutrino mass we are losing. For example, the prominent and expected negative correlation between γ and M_ν (pink contour) disappears even if just one additional parameter is varied (purple contour). We conclude that Stage-IV cosmic shear measurements alone are not sufficient to put any constraints on the neutrino mass, which is in agreement with the findings of other works, for example, Ref. [492].

6.3.5 Combined Nonlinear Effects

Finally, we combine our findings in the previous sections to demonstrate how our model-independent approach performs if the underlying cosmology is nDGP with massive neutrinos (with $M_\nu = 0.06$ eV) and known baryonic feedback effects (within some prior). All background properties and the growth factor in the IA terms are computed with the total matter density including neutrinos via Ω_m, while for the baryonification, since it was trained without neutrinos and is relevant on nonlinear scales, we exclude the neutrinos contribution in $f_b = \Omega_\mathrm{b}/(\Omega_\mathrm{m} - \Omega_\nu)$.

In our main result of this work, Fig. 6.9 (the full posterior distribution can be found in Appendix D.5), we compare our model independent approach (green colour for time-independent γ, orange colour for time-dependent γ) against the exact MG model (purple colour). Overall, for the fiducial value of $\log_{10}\Omega_{rc} = -0.6$, we get the mean value of $\log_{10}\Omega_{rc} = -0.86^{+0.69}_{-0.36}$, which corresponds to $\gamma = 0.44^{+0.06}_{-0.05}$ with $q_1 = 0.33^{+0.21}_{-0.17}$ or $\gamma_0 = \gamma = 0.47^{+0.03}_{-0.04}$ with $\gamma_1 = -0.2$ and $q_1 = 0.58^{+0.08}_{-0.14}$. The differences in the S_8 uncertainties between models are due to the strong γ-dependence of the growth at lower redshifts (this is discussed in Appendix D.2). However, the inferred value of S_8 agrees between all models. This shows that the growth index parameterisation seems to be a reasonable approximation in the late universe. It is in the connection to the earlier universe where we see discrepancies in the primordial amplitude, due to different growth evolution. For the

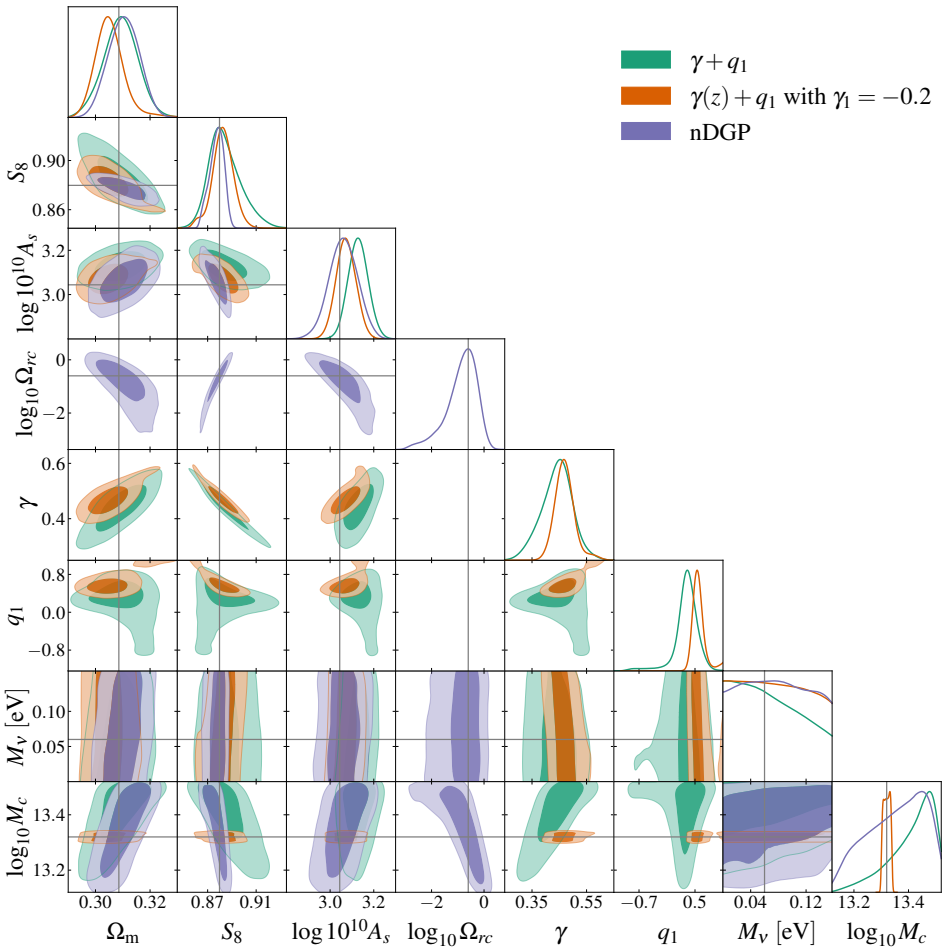

Figure 6.9 *Marginalised posterior distribution for the cosmological and MG parameters with massive neutrinos and baryonic feedback with a tight uniform prior on the baryonic parameter, using cosmic shear power spectra up to* $\ell_{\max} = 3000$. *Mock data: nDGP cosmology with* $\Omega_{rc} = 0.25$ *(see Subsection 4.2.2). Models: the time-independent growth index parameterisation with screening (green), the time-dependent growth index parameterisation with screening and fixed* γ_1 *(orange), nDGP (purple). For nDGP and* $\gamma + q_1$ *the prior on* $\log_{10} M_c$ *is* $\mathcal{U}(13.12, 13.52)$, *while for the* $\gamma(z) + q_1$ *model it is* $\mathcal{U}(13.3, 13.34)$. *Grey lines mark the true values of the synthetic data.*

time-dependent growth index we infer slightly biased Ω_m but more accurate $\log 10^{10}\ A_s$. The tighter constraint on Ω_m with $\gamma(z)$ is due to a tighter prior on the baryonic parameter. In general, we notice that the uncertainties on cosmological parameters are in a good agreement between the exact and model-independent approaches. Therefore, we advocate that our model-independent approach performs as well as the exact modelling, but is more general.

In Fig. 6.9 we also notice that $\log_{10} M_c$ is biased towards higher values in all models. It is highly degenerate with the extended parameters $\log_{10}\Omega_{rc}$, γ, as well as with Ω_m, h, $\log 10^{10}\ A_s$. We impose an informative prior on the baryon feedback $[\log_{10} M_c^\mathrm{fid} - 0.2, \log_{10} M_c^\mathrm{fid} + 0.2]$ for nDGP and $\gamma + q_1$ based on the investigation from Subsection 6.1.3. For the $\gamma(z) + q_1$ model, we require tighter priors on the baryonic feedback and screening parameters: $[\log_{10} M_c^\mathrm{fid} - 0.02, \log_{10} M_c^\mathrm{fid} + 0.02]$ and $[-1, 1]$ respectively. Otherwise their prominent degeneracy is weakening the constraints of cosmological parameters, and the screening transition is poorly constrained while preferring larger values closer to the unscreened limit. The total neutrino mass is not constrained in the range of values that we emulated.

For completeness we list forecasted constraints on the nDGP parameter $\log_{10}\Omega_{rc}$ from the literature. In Ref. [493], for a setup similar to ours and with survey area of $15,000$ deg^2, the authors get from combined cosmic shear, photometric clustering and their cross-correlation analysis with the same fiducial value of $\log_{10}\Omega_{rc}$: $\sigma_{\log_{10}\Omega_{rc}} = 0.3$ (pessimistic) and $\sigma_{\log_{10}\Omega_{rc}} = 0.12$ (optimistic). However, this study does not include baryonic feedback effects, which we demonstrated to be degenerate with the extended parameters. In Ref. [483], for a different setup (5 redshift bins, number of galaxies per arcminute squared per tomographic bin $\bar{n} = 6$, similar shape noise, survey area $5,000$ deg^2) and for a comparably strong modification $\Omega_{rc} = 0.36$, the authors find in the optimistic scenario for cosmic shear $\sigma_{\log_{10}\Omega_{rc}} = 0.07$, varying three cosmological parameters (Ω_m, S_8, h), and omitting baryonic effects.

6.4 Conclusions

The growth index parameterisation is a single parameter extension of the standard cosmology which allows for deviations in the linear growth functions. Originally developed in the context of spectroscopic measurements, it serves as an indicator of the detection of MG theories. Previous studies have demonstrated its effectiveness for a few close-positioned redshift bins and up to mildly nonlinear scales [153]. In this chapter, we presented an analysis with this parameterisation extended to the nonlinear regime with a model-independent screening parameterisation, and applied this to cosmic shear forecasts. For weak lensing, most of the information comes from the small, nonlinear scales and is integrated over a broad range of redshifts, in our case $z \in [0.001, 2.5]$. Our theoretical

model for the shear angular power spectrum is based on the halo-based parameterisation introduced in Chapter 5 and was emulated with the `CosmoPower` emulator. We also take advantage of the following emulators to accelerate computation of the nonlinear matter power spectrum model: `BCEMU` for baryonic contribution and `bacco` [133] for the linear power spectrum as an input to `HMcode`.

To validate our model, we first tested it on noiseless mock data generated in the standard (ΛCDM) cosmology in a Stage-IV setup with a scale-cut $\ell_{\rm max} = 3000$. We recovered unbiased cosmological parameters and found the expected uncertainty on the growth index, γ, to be $\sigma_\gamma \approx 0.05$, noting a slight asymmetry in the errors when one baryonic feedback parameter is included. For a model without screening and employing standard structure formation rescaled to match the modifications on large scales, the obtained constraint was $\sigma_\gamma = 0.04$. We further compared the performance and differences between these two γ-models in the absence of baryonic feedback. We found that the form of our screening model at nonlinear scales results in tighter constraints on the growth index.

We then conducted a similar analysis on noiseless mock data computed in an nDGP cosmology. This MG theory exhibits enhanced structure growth on linear scales that transitions to GR behaviour on nonlinear scales via a screening mechanism. The analysis was performed on mock data with a rather strong deviation from GR (by 14% at low redshifts in the linear regime). We aimed to demonstrate the robustness of our modelling in this relatively extreme scenario to guarantee its validity in more realistic scenarios with a weaker deviation from the standard cosmology. We found that our model with screening, $\gamma + q_1$, performs well: it recovers cosmological parameters within 2σ, finds $\gamma \sim 0.38$ lower than its GR-limit $\gamma \sim 0.55$, and detects a screening transition with its associated parameter $q_1 \sim 0.29$.

We also obtained a bias towards higher values in the primordial amplitude A_s. This bias arises from differences in the time evolution of the linear growth factors between the growth index parameterisation and the nDGP model. This inaccurate representation of the time evolution of structure growth for scalar-tensor theories via a constant growth index parameterisation has been pointed out in Ref. [296]. To address this issue, we explored a time-dependent functional form $\gamma(z) = \gamma_0 + \gamma_1 z^2/(1+z)$. Incorporating this time-dependent growth index, we found that the bias in the amplitude vanishes. However, the constraints on the expansion rate and screening transition are weakened significantly when we considered this model. By fixing $\gamma_1 = -0.19$, we broke the corresponding degeneracies, and we recovered unbiased cosmological parameters with $\gamma_0 \sim 0.47$ and $q_1 \sim 0.57$.

We found that ignoring the screening transition leads to biases in the expansion rate and matter density, as well as to a false detection of γ that exceeds its GR-limit. This happens even with scale-cuts lower than the "pessimistic" scenario in Ref. [281], with

$\ell_{\rm max} = 1500$. This demonstrates the importance of the correct inclusion of a screening scale when extended cosmologies are considered.

We proceeded to study the degeneracies between the screening transition parameter q_1, baryonic feedback, and massive neutrinos. All three effects are nonlinear and result in the suppression of structure formation at small scales. As before, we explored the case with only one free baryonic feedback parameter M_c, which controls the slope of the gas distribution. We found a strong positive correlation between the screening and baryonic parameters. The suppression due to the screening was absorbed by the baryonic feedback if no priors on the latter were imposed. Both effects are prominent in the same range of scales and are highly degenerate. For this reason, we conclude that using cosmic shear alone a detection of the model-independent screening transition is possible only if tight priors on the baryonic parameters are imposed. We used the uniform prior $[\log_{10} M_c^{\rm fid} - 0.2, \log_{10} M_c^{\rm fid} + 0.2]$ motivated by cluster measurements in Ref. [473]. Alternatively, a cross-correlation of cosmic shear with X-ray/kSZ observations can break this degeneracy too. With the total neutrino mass as a free parameter, we found that it cannot be constrained with the cosmic shear data alone. This is in agreement with findings in Stage-III surveys [129] as well as in forecasts for Stage-IV experiments [492]. We also found no strong degeneracy between the screening transition and neutrino mass – while they have similar impact on structure formation, their scale-dependence and strength of impact differ.

Combining all the aforementioned nonlinear effects, we found that our model-independent approach performs well when compared against the exact modelling, and derived the following constraints in the full analysis on nDGP data with massive neutrinos and baryonic feedback with a narrow flat prior: $\sigma_{\log_{10}\Omega_{rc}} \approx 0.53$ (88%), $\sigma_\gamma \approx 0.06$ (13%), $\sigma_{q_1} \approx 0.19$ (58%).

To conclude, we outline the next necessary steps in preparation for a fully model-independent analysis for beyond-ΛCDM cosmologies with Stage-IV cosmic shear surveys. In order to reduce the error bars on extended and baryonic parameters, we advocate for the combination of cosmic shear with photometric galaxy clustering and the corresponding cross-correlation, i.e., the 3×2-point analysis. Similarly, a combination with spectroscopic galaxy clustering can alleviate the degeneracies and yield tighter constraints [281]. After demonstrating the robustness of the $\gamma(z)$ approach, we aim to explore a more agnostic approach, that would not require any assumption of the time-evolution in the linear growth. For example, we can bin $\mu(z)$ from Eq. 6.7 in redshift directly [113, 388]. The goal would be to find an optimal binning scheme. Additionally, as demonstrated before in Chapter 5, we can extend our modelling to include not only MG theories but also exotic dark energy models.

Chapter 7

Conclusion

The New York Times headline from the 4$^{\text{th}}$ of April 2024 pointed at *A Tantalizing "Hint" That Astronomers Got Dark Energy All Wrong* when discussing the first year DESI results [90]. Even for a broader audience it became evident that we are privileged to witness the era of precision cosmology, where the standard cosmological model is scrutinised by data of unprecedented quality and quantity. In lieu of the standard cosmology, a number of non-standard models have been proposed to resolve various conflicts between the observations and our cosmological theory. Some of the extended models attempt to shed light on the dark sector of the Universe, namely to provide insights on the nature of dark energy and dark matter. Another subclass, called modified gravity, offers an alternative for the case that gravitational interactions might not follow Einstein's theory of gravity on large cosmological scales. Powerful surveys, like DESI and Euclid, resolve small spatial separation scales and improve the signal-to-noise ratio allowing us to include smaller nonlinear scales in our analysis. In this thesis, our goal was to exploit these scales beyond the linear regime in order to probe dark energy and modified gravity models for galaxy clustering and weak lensing observables with the latest generation of cosmological surveys.

Summary

This thesis started with an introduction to cosmology in Chapter 1. We introduced ΛCDM, the standard cosmological model with the cosmological constant (Λ) and Cold Dark Matter (CDM). Within this standard model, we discussed how Large Scale Structure (LSS) forms and evolves in the Universe. We also discussed how we can test the rate of structure growth at various scales via measurements of the galaxy positions in redshift space (galaxy clustering) and the observed shapes of galaxies distorted by LSS (weak gravitational lensing). We also discussed 3 classes of extended cosmologies – Dark Energy models (DE), Modified Gravity (MG) models, massive neutrinos (ν) – and their impact on structure formation. We also discussed the Hubble and S_8 tensions, and

several problems with the cosmological constant. In Chapter 2 we outlined the basics of the cosmological statistical analysis, such as Bayesian versus Frequentist approaches to probability and Markov-Chain Monte-Carlo (MCMC) methods. In this chapter, we provided the reader with the details essential to reproduce and understand our findings. We also underlined the importance of the projection or prior-volume effects by providing a toy-model investigation, examples for real cosmological analyses and various potential solutions.

In Chapter 3, we introduced the Interacting Dark Energy model (IDE) we focus on. That is the so-called Dark Scattering model, characterised by pure momentum exchange between dark energy and dark matter. This IDE model extends the parameter space with respect to ΛCDM by two parameters, w and A, which define the DE equation of state and the strength of the coupling between dark energy and dark matter, respectively. We studied the power spectrum (Fourier transformed two-point correlation function) multipoles P_ℓ, and the bispectrum (Fourier transformed three-point correlation function) multipoles B_ℓ of dark matter halos in redshift space. We modeled our observables with the Effective Field Theory of Large Scale Structure (EFTofLSS), and we performed validation tests by means of an MCMC analysis using a large set of N-body CDM-only simulations. The simulations were run in the standard cosmology framework. We fixed the standard cosmological parameters to their true values from simulations, we varied the IDE and EFTofLSS nuisance parameters and studied their degeneracies. Our studies revealed that adding the bispectrum monopole with a scale cut $k^{l=0}_{\mathrm{max},B} = 0.111\ h\ \mathrm{Mpc}^{-1}$ to the power spectrum multipoles improves the constraints on the IDE parameters by $\sim 30\%$ without introducing biases in the parameter estimation. Unbiased parameter estimation here means that for the measurements from the ΛCDM simulations we recovered $w = -1$ and $A = 0$ as well as the bias parameters previously determined in Refs. [7–9] within the 2σ region.

Additionally, we found that the same improvement on the IDE parameter constraints can be achieved with $k^{l=0}_{\mathrm{max},B} = 0.1\ h\ \mathrm{Mpc}^{-1}$ when the bias relations are used. The fit function from the excursion set approach alone or combined with the fit from the separate universe simulation, imposes a connection between the bias parameters and, hence, shrinks the number of the varied parameters in the analysis. These fits in the bias relations rely on the simulations performed in the standard cosmological scenario. In contrast, the inclusion of the bispectrum quadrupole evades any assumptions about the cosmology or bias parameter relations. With an even lower scale cut for the bispectrum monopole and quadrupole $k^{l=0,2}_{\mathrm{max},B} = 0.09\ h\ \mathrm{Mpc}^{-1}$ we again achieved the same strength of the constraining power on the IDE parameters as in the base analysis. Such reduction in the scale cut might seem insignificant. However, one should keep in mind that the number of triangles for the bispectrum evaluation grows nonlinearly with the number of k-modes. For instance, for our choice of binning, the difference between $k^{l=0}_{\mathrm{max},B} = 0.111\ h\ \mathrm{Mpc}^{-1}$

and $k^{l=0}_{\mathrm{max},B} = 0.1\ h\ \mathrm{Mpc}^{-1}$ corresponds to a significant difference of 2054 versus 1475 triangles.

Next, we forecasted constraints assuming Stage-IV spectroscopic galaxy surveys specifications at $z = 1$ in the IDE scenario: $\sigma_w = 0.08$ and $\sigma_A = 2.51$ b GeV^{-1}. Additionally, we repeated the same base analysis for the dark energy model wCDM in a single redshift-bin. The constraint on the DE equation of state parameter we inferred is $\sigma_w = 0.1$.

Finally, we know that w and A, the linear bias parameter b_1 and the primordial clustering amplitude A_s – all four of them control the amplitude of the multipoles. Hence, when we varied A_s together with the previous set of parameters in the last step of our investigation, we obtained the expected degeneracies and shifts away from the fiducial values in the power spectrum multipoles analysis. The shift towards lower A_s values is a projection effect that we demonstrated via synthetic data. This bias can be avoided under the assumption of an informative Planck prior on the primordial amplitude. With or without the informative prior, the addition of the bispectrum monopole improved constraints on the linear bias parameters significantly, partially broke the amplitude related degeneracies and weakened the corresponding projection effects. This highlights that the inclusion of the bispectrum multipoles can play a crucial role in constraining extended cosmological models with spectroscopic galaxy clustering data.

Next, in Chapter 4, we moved from simulated to real data: we analysed the BOSS DR12 data using the same modelling code as in the previous chapter. We performed a Full-Shape (FS) analysis of the windowless power spectrum multipoles of the BOSS DR12 galaxies with the inclusion of post-reconstruction Baryonic Acoustic Oscillations (BAO) data. Additionally, we included BAO measurements obtained from a variety of datasets. Various previous studies of this dataset obtained cosmological constraints hinting at the S_8 tension, i.e., the growth of structure seems to be weaker at lower redshifts than predicted by the standard cosmological model. We studied a simple single parameter extension of ΛCDM, the so-called growth index (or γ) parameterisation. This parameterisation allows for deviations from the standard scenario in the growth functions: any value of the growth index larger than its ΛCDM limit $\gamma \simeq 0.55$ implies smaller growth rate. We also explored the case with the total neutrino mass as a free parameter, as they lead to the structure growth suppression as well.

Similar to the previous chapter, we found that informative priors proved crucial in alleviating parameter degeneracies and preventing strong projection effects in the posterior distributions. By applying a 3σ Planck prior on the primordial amplitude A_s and spectral index n_s, we obtained the tightest constraints of $\gamma = 0.647 \pm 0.085$ that is larger than (but still $\sim 1\sigma$ consistent with) the ΛCDM prediction. Similarly, for the massive neutrino scenario with the tight priors on both primordial parameters we obtained $\gamma = 0.612^{+0.075}_{-0.090}$ while $M_\nu < 0.298$ eV. These constraints point towards a resolution of the S_8 tension,

albeit without a large statistical significance.

We also investigated projection effects in the absence of priors on the primordial parameters with generated synthetic data-vectors and via a profile likelihood (PL) analysis. The former demonstrated a similar shift of the posterior in the A_s–γ plane as the one found in our baseline BOSS analysis. The latter revealed that the maximum of the PL was closer to the ΛCDM prediction than the peak of the marginalized posterior.

Additionally, we generated forecasts for a Stage-IV spectroscopic galaxy survey, specifically focusing on the DESI-like samples. To this end, we fitted synthetic data-vectors for three galaxy samples – BGS, LRGs and ELGs – each corresponding to different redshift bins, individually and jointly. Concentrating solely on the constraining power of the LSS, i.e., without priors on the primordial parameters, we found that forthcoming data can improve the measurement of γ by up to $\sim 85\%$ compared to the BOSS dataset. However, when neutrino mass is varied too, we found its constraints to be only marginally better than the current ones. Nevertheless, when we again adopted 3σ Planck priors on A_s and n_s, we obtained a $\sim 20\%$ improvement in the measurement of γ, and $\sim 35\%$ for M_ν with respect to the case with no priors.

Overall, we advocated for the combination of the power spectrum FS+BAO analysis with additional observables. Further investigation of the joint probes would be worth pursuing: either a joint analysis with Planck or Stage-IV Cosmic Microwave Background (CMB) experiments, or with weak lensing, or with the bispectrum as we argued in the previous chapter.

In the second part of the thesis, we switched our focus from the FS analysis of halos and galaxies in redshift space towards the development of modelling tools for the weak lensing observables. If for the spectroscopic measurements it was sufficient to modify only the linear growth functions, with extended cosmologies in the weak lensing framework deviations from ΛCDM on nonlinear scales cannot be neglected anymore. The small nonlinear scales of the cosmic shear measurement exhibit the highest signal-to-noise ratio for Stage-IV surveys. Their inclusion will be of utmost importance to distinguish between competing DE and MG models with distinct nonlinear behaviours.

Instead of studying DE and MG models on a case by case basis, in Chapter 5, we introduced a model-independent prescription for the nonlinear matter power spectrum. The calculation of the power spectrum is done in the halo model reaction framework that requires certain ingredients. Among them are the parameterisations of the background expansion history and of the linear as well as nonlinear growth equations. For the background and linear growth we considered the Effective Field Theory of Dark Energy (EFTofDE), specifically we implemented the corresponding α-parameterisation. Alternatively, we introduced the "minimal parameterisation" that includes the evolving DE parameters $w_0 w_a$ for the background and the growth index γ for the linear growth modifications. In the nonlinear regime, we explored two approaches: a nonlinear

parameterised-post Friedmannian (nPPF) method and an approximate phenomenological model based on the error function (Erf). Both of these nonlinear parameterisations are general and capture different screening mechanisms. Screening is a key phenomenological aspect of all viable MG theories, allowing recovery of General Relativity (GR) on small scales. The recovery of GR is mandatory to pass the Solar System tests, where GR exhibits highly accurate observational consistency. Further, both nonlinear parameterisations also have unscreened limits, hence, we are not restricted to theories exhibiting screening.

To evaluate the effectiveness of the parameterised approaches, we compared their predictions for the nonlinear matter power spectrum to exact reaction solutions and state-of-the-art emulators in three beyond-ΛCDM models: wCDM, Hu-Sawicki $f(R)$ and nDGP gravity. Being a DE model w_0w_aCDM includes no screening, and we could directly compare the halo model reaction approach with the emulator trained on numerical simulations. We obtained a 2% consistency with the emulator for $k \leq 3\ h\ \mathrm{Mpc}^{-1}$ at redshift $z = 0$ for a model with a moderate deviation from ΛCDM. For the $f(R)$ and nDGP models we fixed their background to ΛCDM and the linear growth to their true parameterisations via f_{R_0} and Ω_{rc}, respectively. For the $f(R)$ gravity with moderate deviation from ΛCDM, we found that the Erf model prediction for the reaction function stays within 1% of the exact solution for $k \leq 3\ h\ \mathrm{Mpc}^{-1}$. While the reaction function with the nPPF model stays within 2% of the exact solution for $k \leq 2\ h\ \mathrm{Mpc}^{-1}$. For weaker modifications these comparisons exhibited sub-1% agreement between the Erf model and the exact solution for $k \leq 5\ h\ \mathrm{Mpc}^{-1}$ at both redshifts $z = 0$ and $z = 1$. For the nPPF model the sub-1% agreement was achieved for $k \leq 3\ h\ \mathrm{Mpc}^{-1}$. However, the most remarkable agreement was established in the nDGP scenario: we found sub-1% agreement between the Erf and exact predictions down to $k = 5\ h\ \mathrm{Mpc}^{-1}$ even for a moderate modification at all redshifts. These tests suggested only an addition of (maximum of) 3 free constants within the Erf model, above the background and linear theory parameters, might be sufficient to model nonlinear, non-standard cosmology in the matter power spectrum at scales down to $k \leq 3\ h\ \mathrm{Mpc}^{-1}$ within 2% accuracy. Overall, the biggest inaccuracy is coming not from the reaction function but from another component of the halo model reaction approach, the so-called pseudo power spectrum. Improving the accuracy of the pseudo spectrum prescriptions will be important for Stage-IV surveys.

Lastly, we released an updated version of `ReACT` which includes the nonlinear power spectrum code and pedagogical Jupyter notebooks. In summary, this code presents a fast, accurate and highly general nonlinear power spectrum predictor for DE and MG models including massive neutrinos cosmologies. The parameters required are a minimal set of free, physically meaningful constants: either $H(a)$+ 4 α's (EFTofDE) or $w_0w_a\gamma$ ("minimal parameterisation") for the background and linear scales, and 3 q's (Erf) or 6 p's (nPPF) for the screening transition at nonlinear scales.

Following up from the promising conclusions of Chapter 5, in Chapter 6, we explored

the robustness of the "minimal parameterisation" on mock Stage-IV cosmic shear data. We compressed the parameterisation even further, up to $\gamma + q_1$ – the growth index and the screening scale. We performed an MCMC analysis on synthetic data in an nDGP cosmology with moderately enhanced growth on linear scales. We successfully identified a transition scale as well as the γ-value corresponding to the fiducial Ω_{rc}-value. However, we discovered that a constant γ-parameterisation is not sufficient to describe the time evolution of the structure growth for a broad class of scalar-tensor theories like nDGP: although the matter fluctuation amplitude can be constrained in the late Universe, its matching to the primordial amplitude fails. Nonetheless, a time-dependent growth index parameterisation, $\gamma(z)$, which we applied in our analysis mimics the time evolution of the nDGP linear growth much better. Its drawback is that it introduces extra freedom and degeneracies into the model that require more information than the cosmic shear measurements alone can offer. Cosmic shear measurements are also insufficient to constrain the total mass of neutrinos. And yet, the most important take-home message of Chapter 6 is that the screening transition and baryonic feedback are extremely degenerate. As a consequence, we strongly argue for using external information on the baryonic parameters or for the combination of the weak lensing probes with photometric clustering and their cross-correlation, or other additional probes, such as X-ray measurements, for example.

Lastly, we released the accompanying code repository, which includes the reaction boosts emulated for various extended models, as well as the corresponding data production pipeline. We also made public our `MGrowth` package for the calculation of the linear growth functions for various extended cosmologies, including the ones discussed in this thesis.

Prospects

As a continuation of Chapter 3, we have been working on jointly analysing the bispectrum and power spectrum multipoles for a Key Project paper of the Euclid collaboration. For that purpose we extended the official modelling code to include analytical marginalisation and the Alcock–Paczynski (AP) and Finger-of-God effects for the bispectrum. The implementation of the AP-effect is a Taylor expansion, assuming the true cosmology is close to the fiducial one. A detailed assessment of this approximation is part of our future investigations. Right now we have the first forecasting results and we are studying projection effects as an essential part of the preparations for Euclid's first data release.

As a continuation of the last project from Chapter 6, we have been studying the degeneracies with baryons and massive neutrinos in various DE and MG models (their descriptions are provided in Subsection 1.3.1): wCDM, w_0w_aCDM, nDGP, γ, $\gamma(z)$, binned-μ with 3x2-point correlation functions (cosmic shear, photometric galaxy clustering, and their cross-correlation) for photometric observables. For that purpose we have extended the prior range of the emulators discussed in Chapter 6, as well as

trained an HMcode emulator that proved to be of use not only for Euclid but for the DES collaboration as well.

In conclusion, our ultimate goal is to find an optimal model-independent approach for extended cosmologies and apply it to Stage-IV real data in the (ideally joint) spectroscopic and photometric analysis. This thesis contains important steps in this direction: modelling techniques and computational tools, which were validated on simulations and applied to real data. We hope they will prove to be useful for the new generation of the cosmological surveys, as we gradually learn to get cosmology *All Right* (in opposition to the New York Times headline).

Appendix A

Appendix to Chapter 3

A.1 Full Posterior Distributions

We collect here the full posterior distributions for the different runs described in the text.

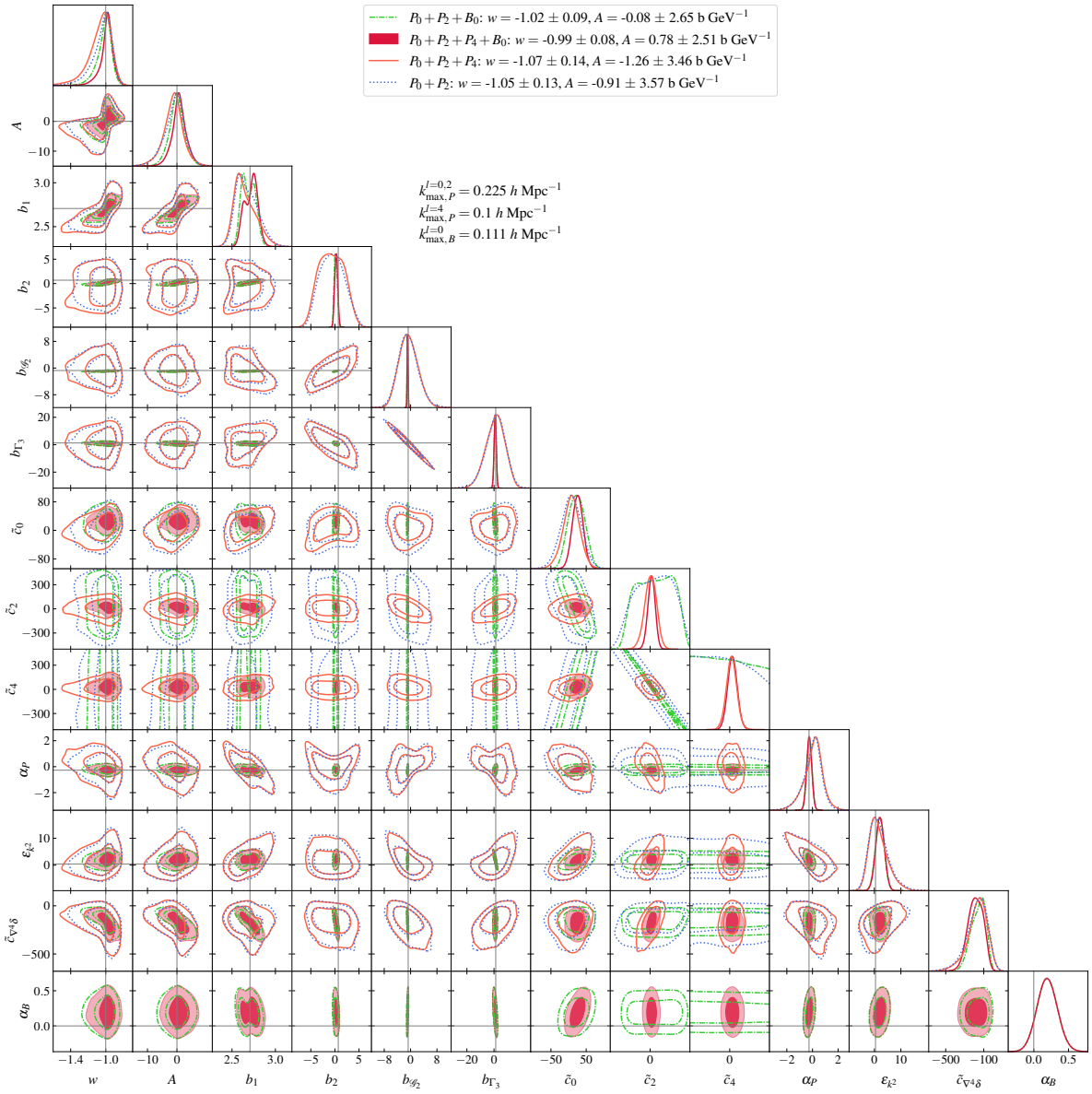

Figure A.1 *Posterior distributions for the base model with the scale cuts given in the triangle plot. The power spectrum monopole and quadrupole analysis is denoted by the dotted blue line, constraints from all power spectrum multipoles are given by the solid orange line, joint analysis of power spectrum monopole plus quadrupole and bispectrum monopole is presented by the dotted-dashed light-green line, and the full joint analysis is shown by the dark-red contours. Thin grey lines correspond to the fiducial values known from the fiducial cosmology and previous analysis of this data set in Refs. [7–9] .*

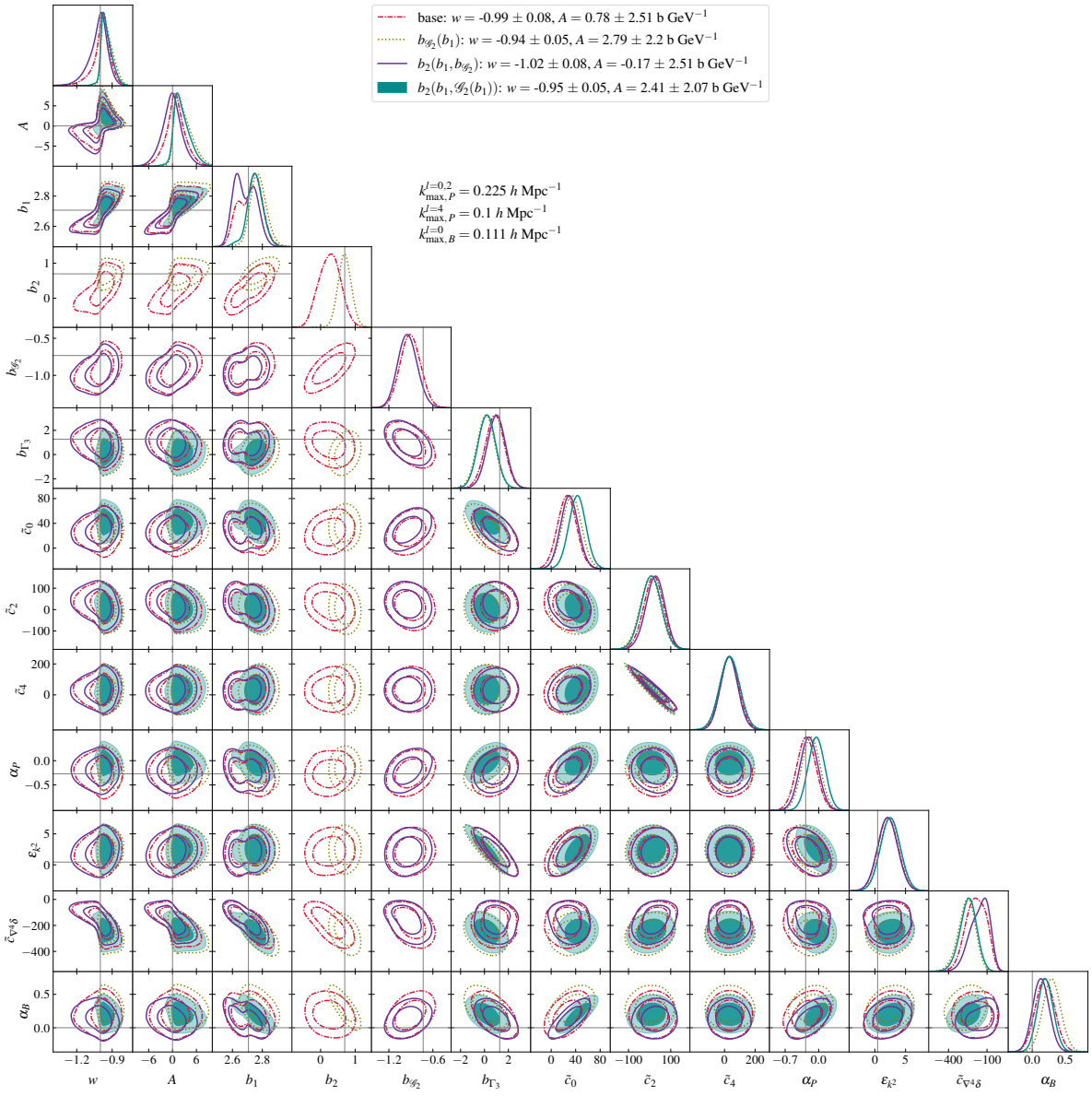

Figure A.2 *Posterior distributions for the $P_0 + P_2 + P_4 + B_0$ models with bias relations at the scale cuts given on the triangle plot. The joint analysis with the base model is shown by the dark-red dotted-dashed lines, olive dotted lines denote the tidal bias relation, purple solid lines represent the b_2-relation, the dark-cyan contours denote the combined relation of b_2 and $b_{\mathcal{G}_2}$. Thin grey lines correspond to the fiducial values known from the fiducial cosmology and previous analysis of this data set in Refs. [7–9].*

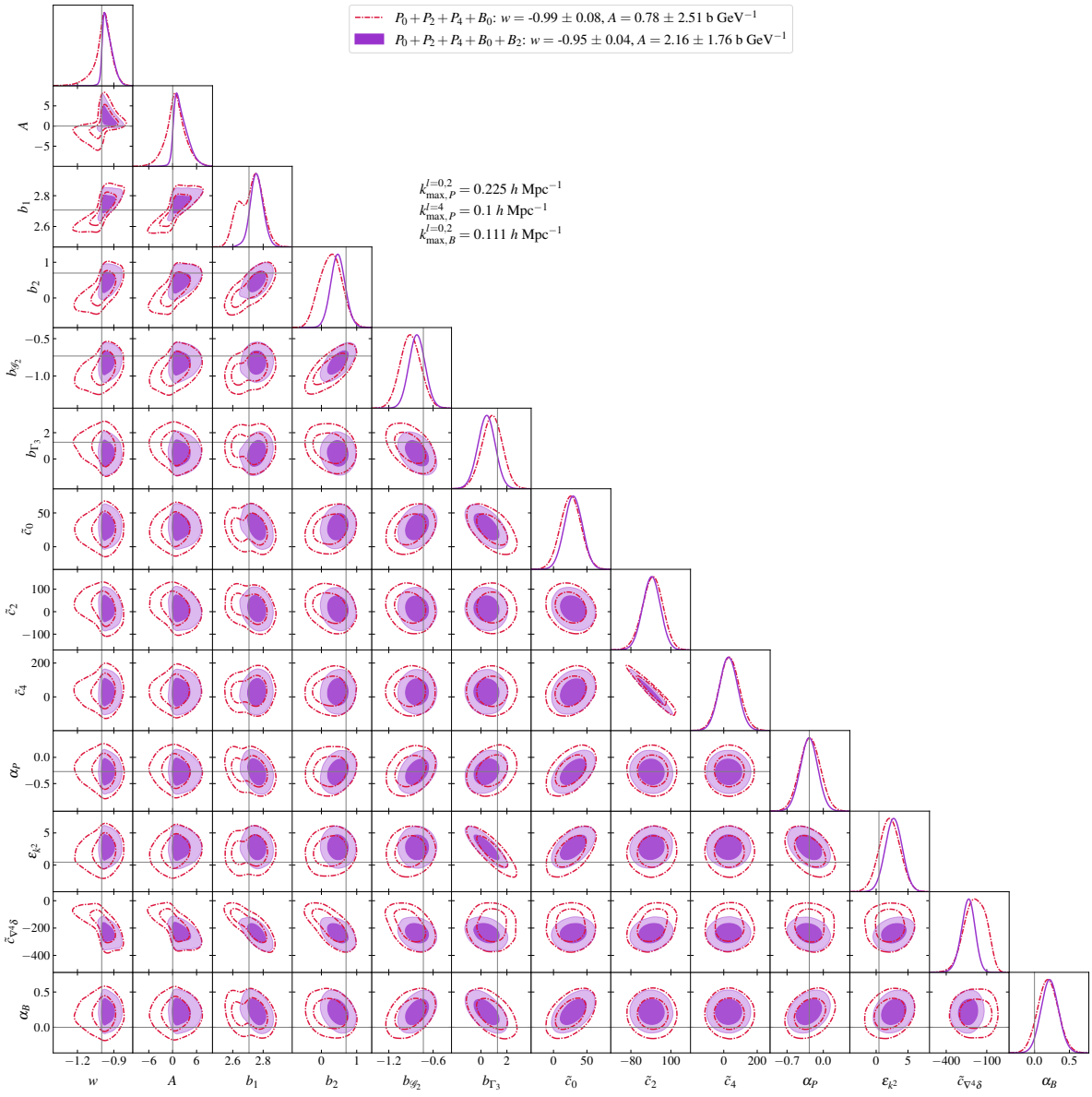

Figure A.3 *Posterior distributions for the base model with and without the bispectrum quadrupole at the scale cuts given on the triangle plot. The joint analysis with the bispectrum monopole is shown by the dark-red dotted-dashed lines, the joint analysis with the bispectrum monopole and quadrupole is denoted by the purple contours. Thin grey lines correspond to the fiducial values known from the fiducial cosmology and previous analysis of this data set in Refs. [7–9].*

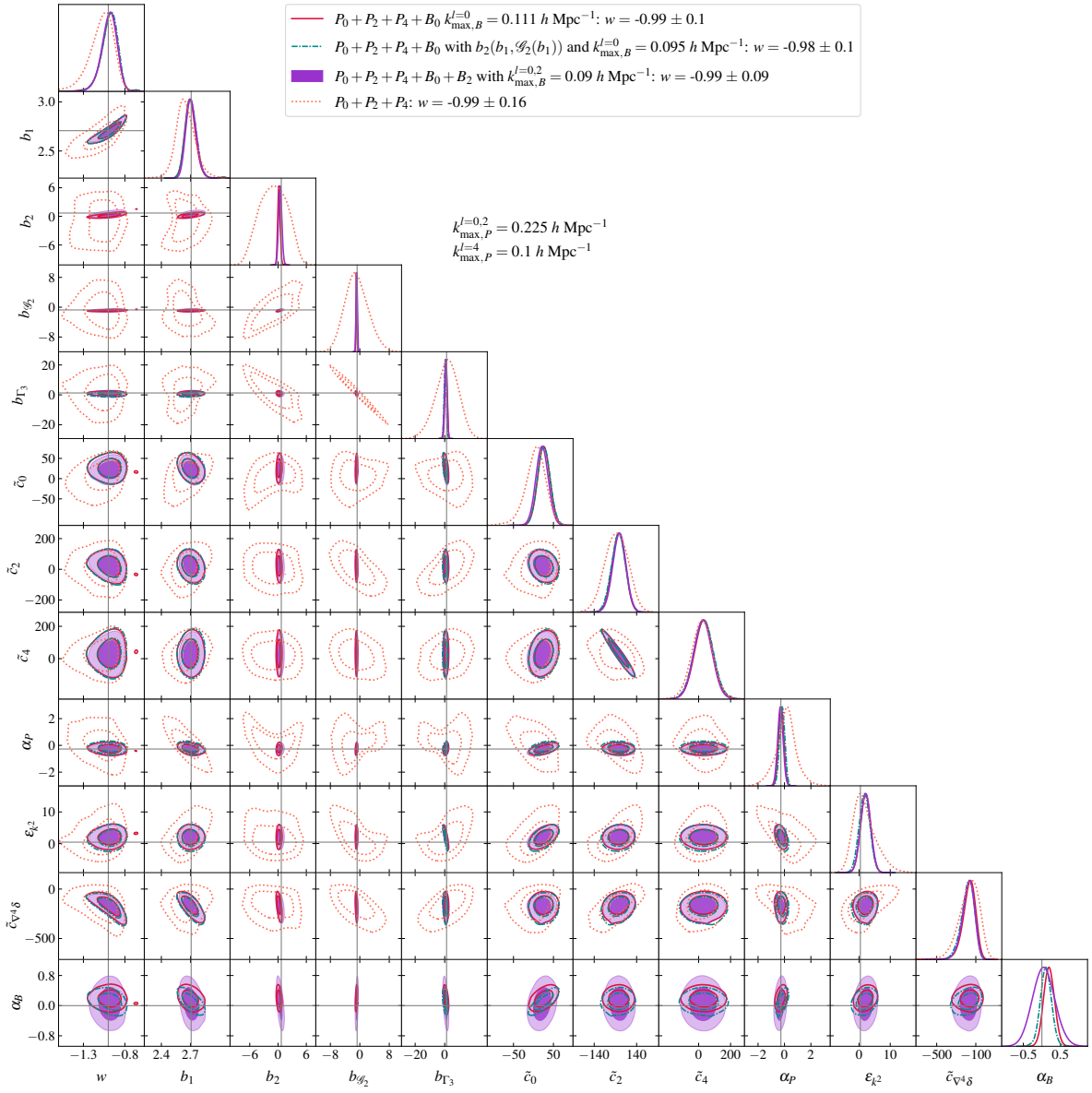

Figure A.4 *Posterior distributions for the wCDM model for four models at the scale cuts given on the triangle plot. The joint analysis with the bispectrum monopole is shown by the solid dark-red lines, the joint analysis with the bispectrum monopole with the combined bias relation is given by the dotted-dashed dark-cyan lines, the joint analysis with the bispectrum monopole and quadrupole is denoted by the purple contours, constraints from all power spectrum multipoles are shown by the dotted orange line. Thin grey lines correspond to the fiducial values known from the fiducial cosmology and previous analysis of this data set in Refs. [7–9].*

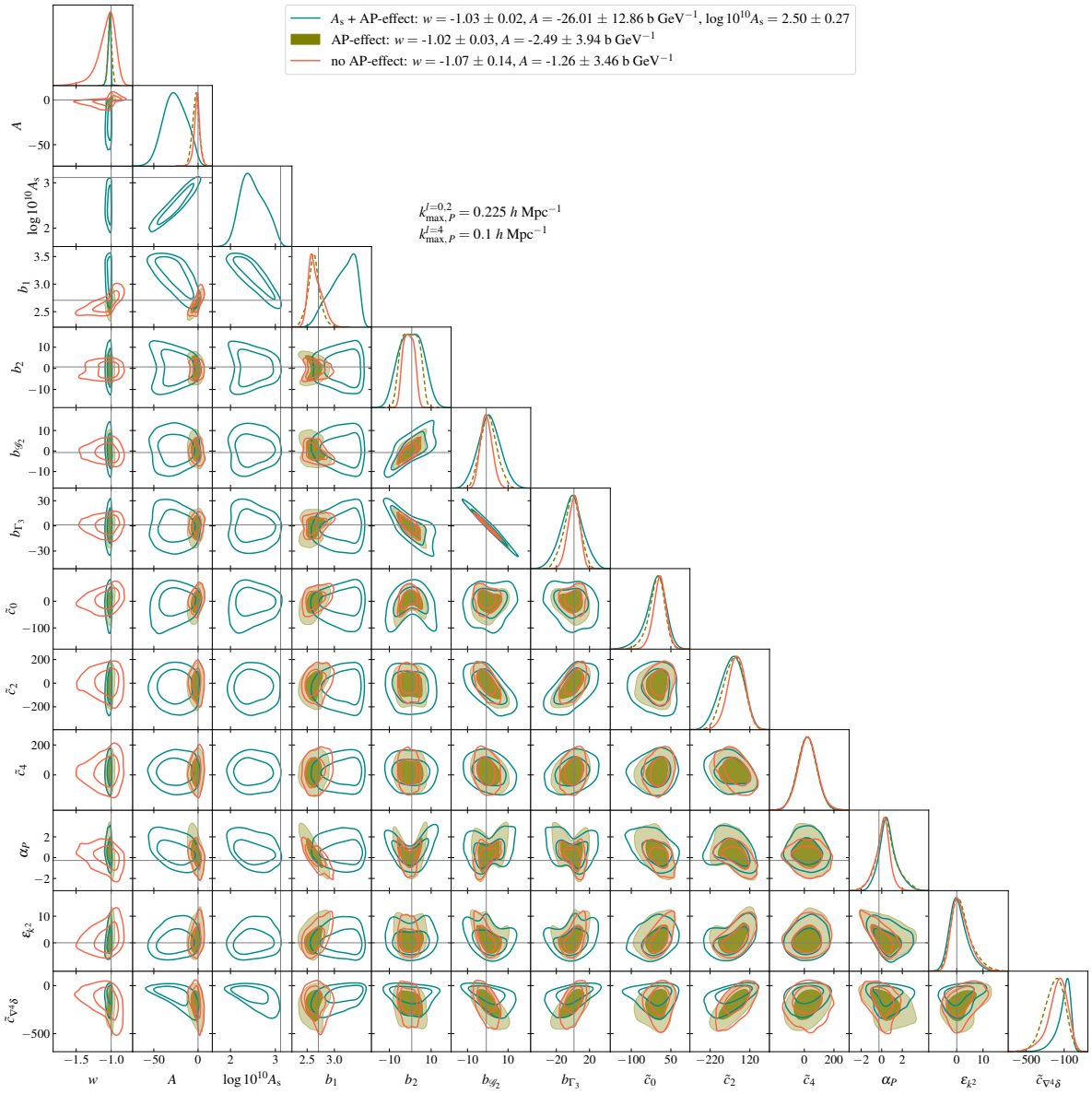

Figure A.5 *Posterior distributions for the demonstration of the AP-effect with the three power spectrum multipoles. The analysis with the variation of the scalar amplitude with a flat prior and addition of the AP-effect is shown by the solid dark-cyan lines, the analysis for variation of the IDE and nuisance parameters only with the addition of the AP-effect is shown with olive contours and constraints from all power spectrum multipoles without the AP-effect are given by the solid orange line (same as in Fig. A.1). Thin grey lines correspond to the fiducial values known from the fiducial cosmology and previous analysis of this data set in Refs. [7–9].*

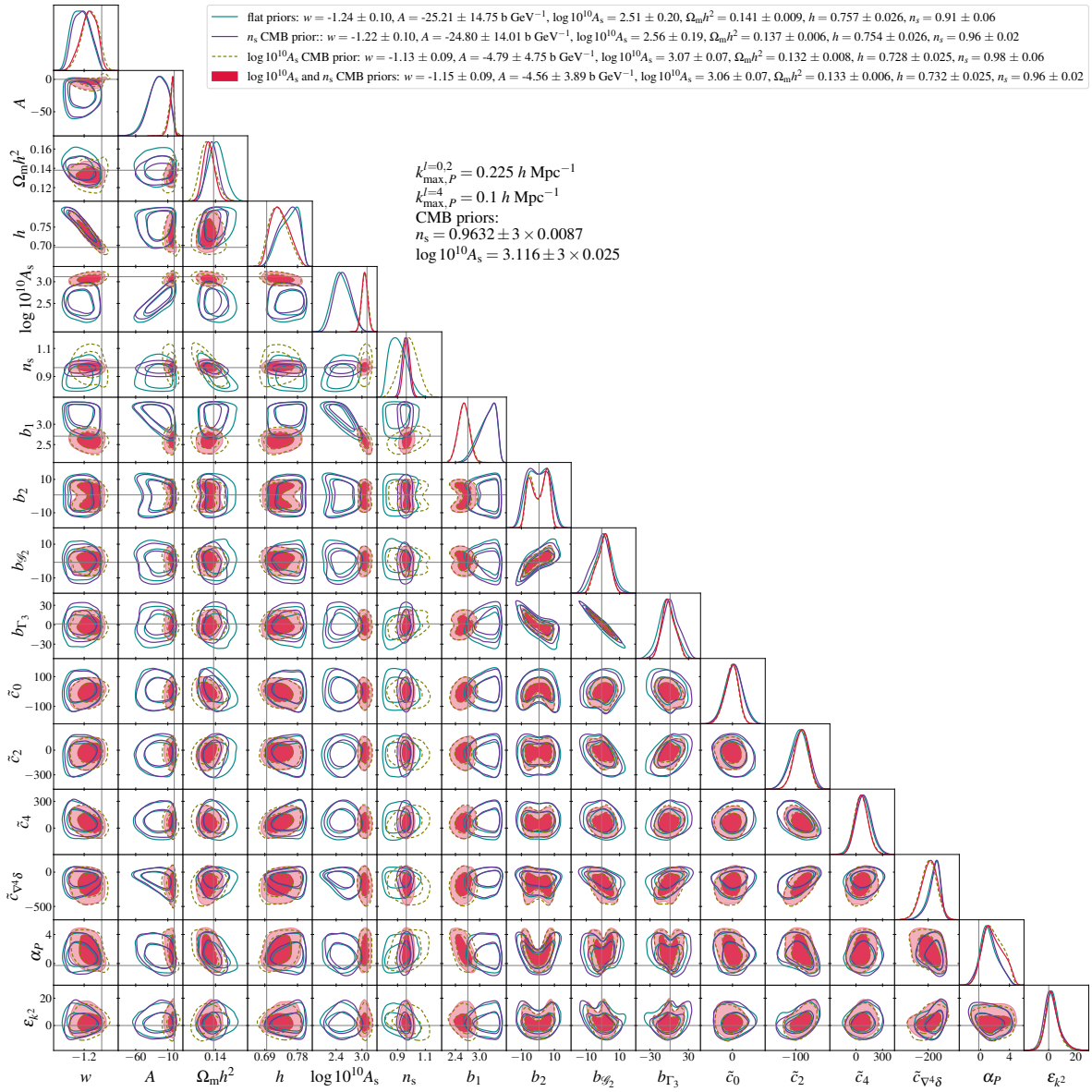

Figure A.6 *Posterior distributions for IDE model with the power spectrum multipoles only (the AP-effect included). The analysis with flat priors on all parameters is shown by the solid dark cyan lines, the analysis with the CMB prior on the primordial slope n_s is shown by the dark purple lines, the analysis with the CMB prior on the scalar amplitude A_s is shown by the olive dashed lines, the analysis with the CMB priors on both primordial parameters is shown by dark red contours. Thin grey lines correspond to the fiducial values known from the fiducial cosmology and previous analysis of this data set in Refs. [7–9].*

Appendix B

Appendix to Chapter 4

B.1 Full Contourplots

We show here the two-dimensional marginalised posteriors for the full parameter space sampled in the BOSS analysis presented in Subsection 4.3.1. The results for γCDM are shown in Fig. B.1, corresponding to the constraints on cosmological parameters shown in Fig. 4.1, while $\gamma\nu$CDM results are plotted in Fig. B.2, corresponding to the constraints on cosmolofical parameters shown in Fig. 4.2. The additional model parameters not shown are the ones we analytically marginalise over, namely b_{Γ_3}, the EFT counterterm parameters and the noise parameters. We follow the same color scheme as the main text for the three prior choices, and mark Planck best-fit values with dashed grey lines.

B.2 Massive Neutrinos with Fixed γ

We perform a complementary analysis of the BOSS data with free neutrino mass but with the γ parameter fixed to its ΛCDM value, $\gamma = 0.55$. The two-dimensional marginalised posteriors are shown in Fig. B.3, and the best-fits are summarised in Tab. B.1. We impose a wide, flat prior on the neutrino mass $\mathcal{U}(0, 1)$ eV, covering the parameter space allowed by the emulator for the linear power spectrum. We explore again the three options for the priors on the primordial parameters, and obtain the following constraints for the total neutrino mass: $M_\nu < 0.319$, best-fit 0.137 (baseline), $M_\nu = 0.34^{+0.13}_{-0.28}$, best-fit 0.141 (prior on A_s), $M_\nu = 0.29^{+0.12}_{-0.24}$, best-fit 0.111 (prior on A_s and n_s), where values are expressed in eV. Additionally, for the baseline analysis we find a higher value of the amplitude: $\log(10^{10}\ A_s) = 2.90^{+0.17}_{-0.21}$, as opposed to $\log(10^{10}\ A_s) = 2.67 \pm 0.17$ found in the ΛCDM analysis of Ref. [99] (that used the same pipeline and priors adopted here).

Comparing to previous constraints on the total neutrino mass from the full-shape analysis of BOSS data, we find our results to be in excellent agreement with Ref. [315]. There, the authors perform a similar EFT-based analysis of ΛCDM + massive neutrinos,

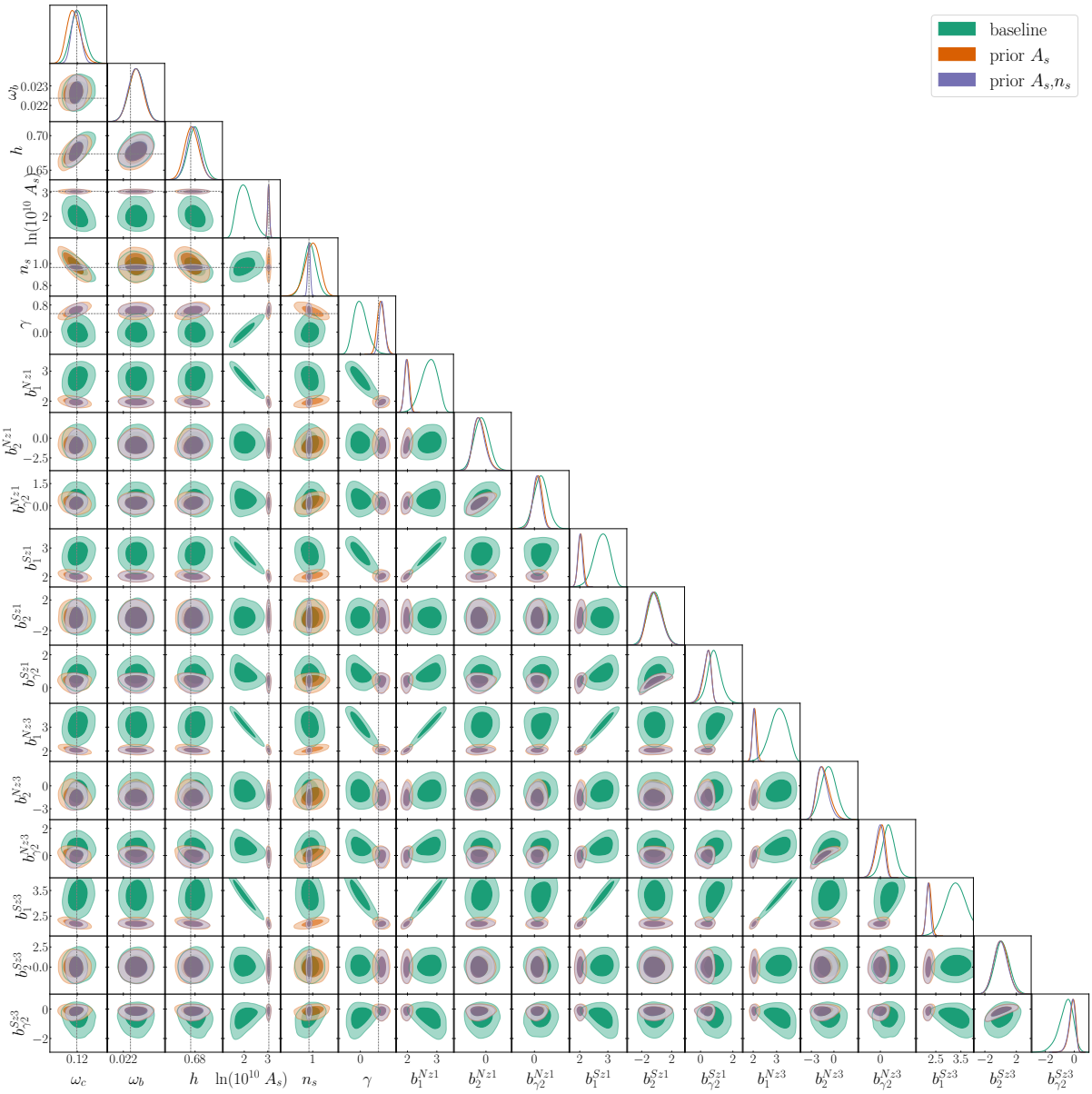

Figure B.1 *Two-dimensional marginalised posterior for all parameters for the BOSS analysis for γCDM and $k_{\rm max} = 0.2\ h\ {\rm Mpc}^{-1}$ (see Fig. 4.1). We use the same color scheme as the main text to show the three prior choices. Dashed grey lines mark the Planck best-fit values (ΛCDM prediction for γ).*

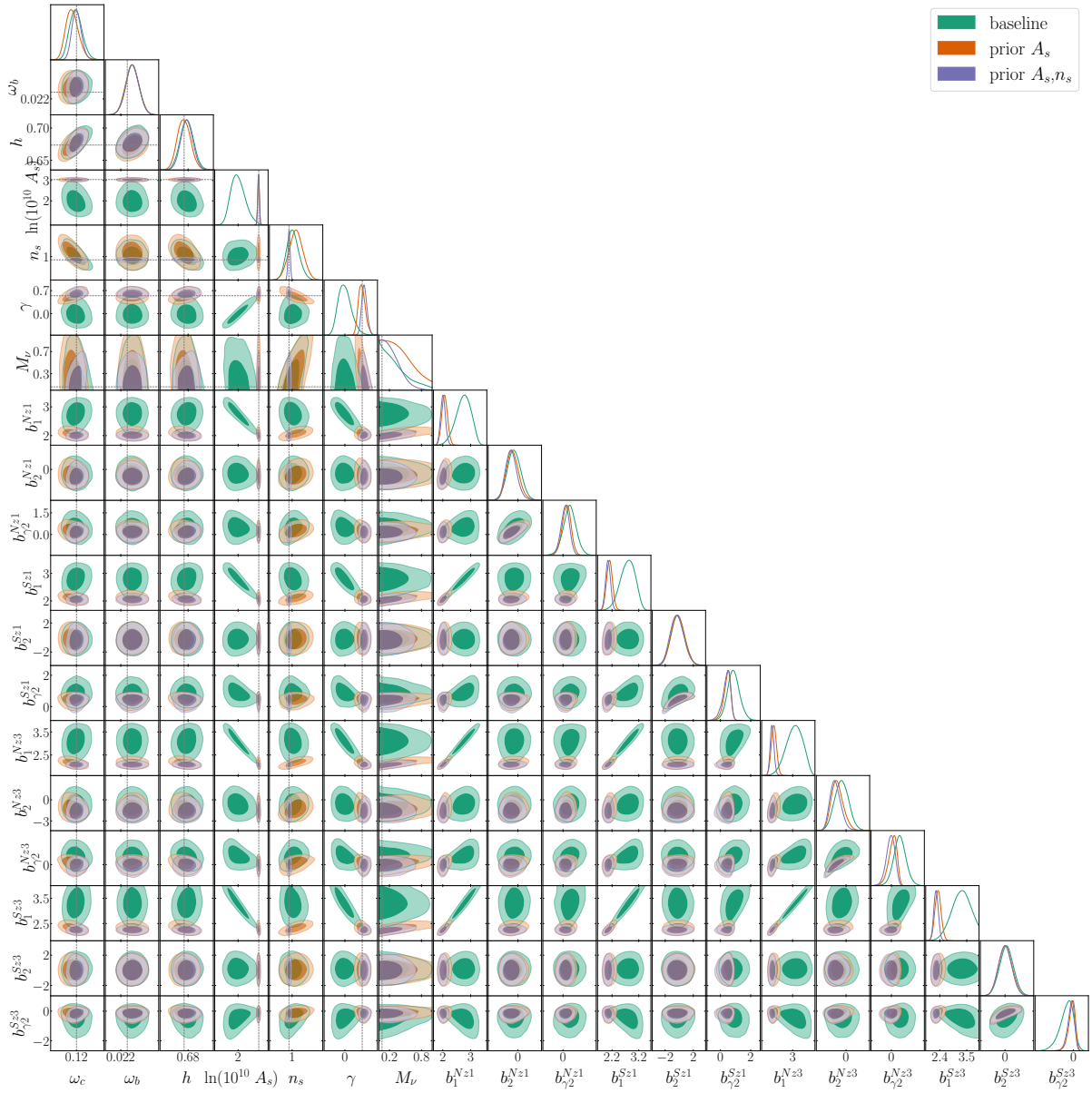

Figure B.2 *Two-dimensional marginalised posterior for all parameters for the BOSS analysis with $\gamma\nu CDM$ and $k_{\rm max} = 0.2\ h\ {\rm Mpc}^{-1}$ (see Fig. 4.2). We use the same color scheme as the main text to show the three prior choices. Dashed grey lines mark the Planck best-fit values (with the ΛCDM prediction for γ and minimal neutrino mass $M_\nu = 0.06$ eV).*

also finding that having the neutrino mass as a free parameter allows for a slightly larger value of A_s, closer to the Planck best-fit value, which is then balanced by a peak in the posterior at $M_\nu = 0.29^{+0.31}_{-0.18}$ eV. The same EFTofLSS model adopted in this work was also used in Ref. [123] to constrain the total neutrino mass from BOSS data. However, in that work the fit is performed jointly with CMB data from Planck, which results in significantly tighter constraints: $M_\nu < 0.16$ eV at 95% c.l..

Parameter	baseline	prior on A_s	prior on A_s, n_s
ω_c	$0.1189^{+0.0076}_{-0.0090}$	$0.1153^{+0.0058}_{-0.0072}$	$0.1195^{+0.0053}_{-0.0063}$
	(0.1147)	(0.1099)	(0.1132)
ω_b	0.02267 ± 0.00038	0.02265 ± 0.00038	0.02266 ± 0.00038
	(0.02237)	(0.02241)	(0.02260)
h	0.677 ± 0.011	0.6739 ± 0.0097	0.6770 ± 0.0096
	(0.675)	(0.676)	(0.676)
$\log(10^{10} A_s)$	$2.90^{+0.17}_{-0.21}$	3.037 ± 0.041	3.024 ± 0.040
	(3.00)	(3.07)	(3.04)
n_s	0.998 ± 0.071	$1.032^{+0.054}_{-0.048}$	0.968 ± 0.012
	(0.997)	(1.048)	(0.9691)
M_ν	< 0.319	$0.34^{+0.13}_{-0.28}$	$0.29^{+0.12}_{-0.24}$
	(0.137)	(0.141)	(0.111)
σ_8	$0.763^{+0.049}_{-0.081}$	$0.807^{+0.029}_{-0.033}$	$0.802^{+0.027}_{-0.032}$
	(0.783)	(0.802)	(0.779)

Table B.1 *Best-fit and 68% c.l. values for the analysis with free neutrino mass and* $\gamma = 0.55$ *for the three prior choices. We also derive best-fit values for* σ_8.

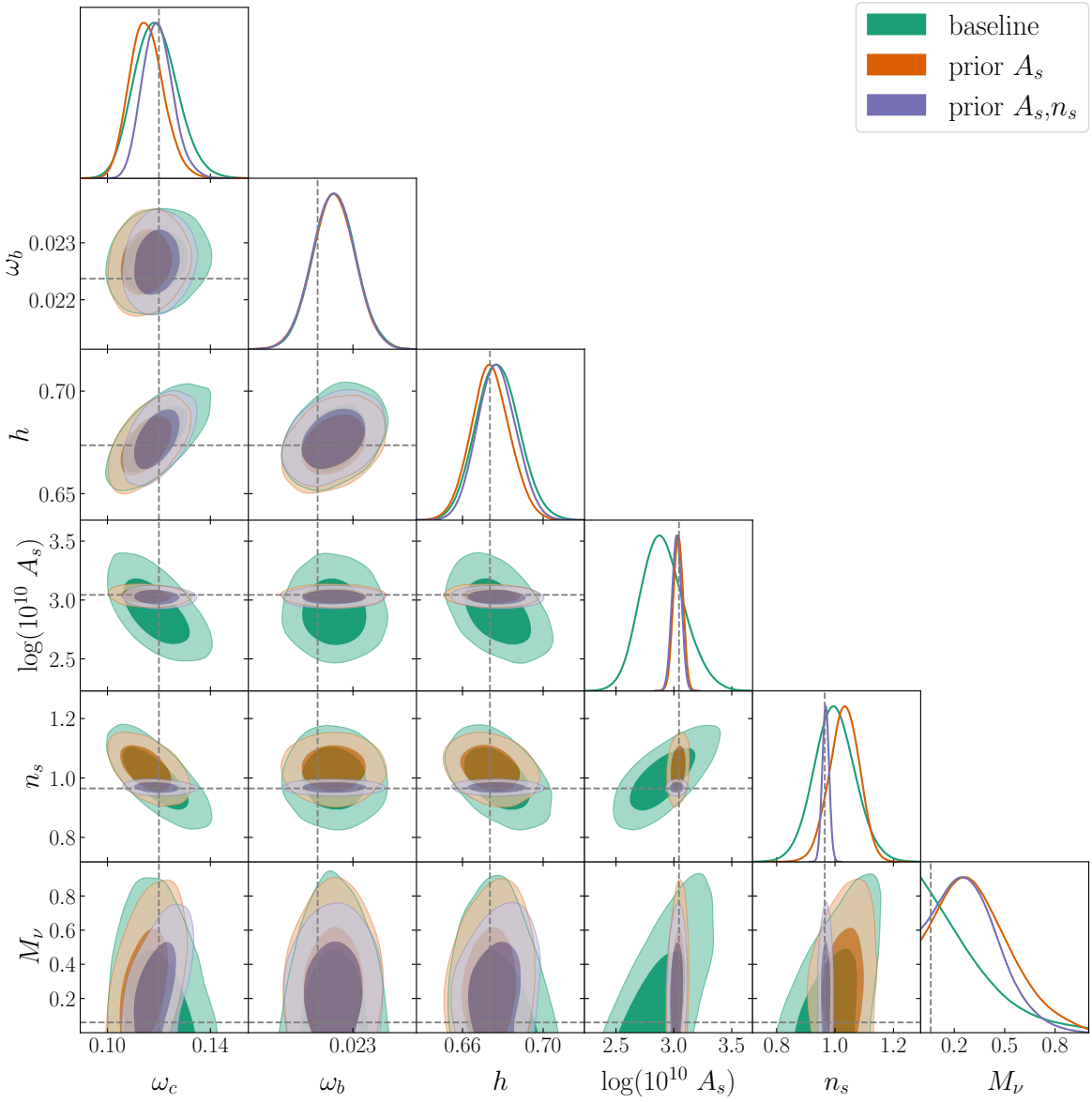

Figure B.3 *Marginalised posterior distribution for the cosmological parameters for ΛCDM with massive neutrinos and the three prior choices, as detailed in the legend. We fit all three multipoles and use* $k_{\rm max} = 0.2\ h\ {\rm Mpc}^{-1}$. *Grey dashed lines mark the Planck best-fit values.*

Appendix C

Appendix to Chapter 5

C.1 Linear Poisson Modifications

C.1.1 Horndeski in the α-Basis

The linear modification to the Poisson equation in the Horndeski class of EFTofDE, under the quasi-static approximation, and in the α-basis, $\{H, \alpha_M, \alpha_B, \alpha_K, \alpha_T\}$, is given by

$$\mu(k,a) = \frac{2}{\kappa^2}\frac{f_1(a) + f_2(a)a^2/k^2}{f_3(a) + f_4(a)a^2/k^2}\,, \tag{C.1}$$

where the constituent functions are given by

$$f_1 = B_2C_3 - C_1B_3\,, \tag{C.2}$$
$$f_2 = B_2C_\pi\,, \tag{C.3}$$
$$f_3 = A_1[B_3C_2 - B_1C_3(k,a)] + A_2[B_1C_1 - B_2C_2] + A_3[B_2C_3 - B_3C_1]\,, \tag{C.4}$$
$$f_4 = [A_3B_2 - A_1B_1]C_\pi\,. \tag{C.5}$$

Finally, we give the A, B and C functions in terms of the α-basis as [112]

$$A_1 = 2M^2\,, \tag{C.6}$$

$$A_2 = \alpha_B H M^2\,, \tag{C.7}$$

$$A_3 = 0\,, \tag{C.8}$$

$$B_1 = -\frac{1}{c_T^2}\,, \tag{C.9}$$

$$B_2 = 1\,, \tag{C.10}$$

$$B_3 = \frac{(-\alpha_M + \alpha_T)H}{c_T^2}\,, \tag{C.11}$$

$$C_1 = -B_3 M^2 c_T^2\,, \tag{C.12}$$

$$C_2 = \frac{A_2}{2}\,, \tag{C.13}$$

$$\begin{aligned} C_3 =& c + \frac{HM^2}{2}\Big[-2\alpha_T H + \alpha_M^2 c_T^2 H + aH\alpha_B' + aH\alpha_M' \\ &+ a\alpha_T H\alpha_M' + 2a\alpha_T H' + a^2\alpha_T' H' + \alpha_B[(1+\alpha_M)H + aH'] \\ &+ \alpha_M[H(1-\alpha_T + 2a\alpha_T') + ac_T^2 H'] + a^2 H\alpha_T''\Big]\,, \end{aligned} \tag{C.14}$$

$$\begin{aligned} C_\pi =& -\frac{1}{4}aH\Big[12cH' + HM^2(6\alpha_M^2 c_T^2 HH' \\ &+ 6\alpha_B(2a(H')^2 + H[(4+\alpha_M)H' + aH'']) \\ &+ \alpha_M(c_T^2(12a(H')^2 - \bar{R}') + 6H(2(2c_T^2 + a\alpha_T')H' + ac_T^2 H'')) \\ &+ a[12(\alpha_T + a\alpha_T')(H')^2 \\ &- \alpha_T'\bar{R}' + 6H(H'(\alpha_B' + c_T^2\alpha_M' + 5\alpha_T' + a\alpha_T'') + a\alpha_T' H'')])\Big]\,, \end{aligned} \tag{C.15}$$

where $c_T^2 = (1+\alpha_T)$ and $\bar{R}$ is the background Ricci scalar. The $c(a)$ parameter (Eq. 5.22) in the α-basis is given by

$$\begin{aligned} c(a) = -M^2\Big[&\frac{3H_0^2\Omega_{m,0}}{2a^3\kappa^2 M^2} + \frac{1}{2}H\Big(aH'[(2+\alpha_M)c_T^2 + a\alpha_T'] \\ &+ H(c_T^2[(\alpha_M - 1)\alpha_M + a\alpha_M'] + 2a\alpha_M\alpha_T' + a^2\alpha_T'')\Big)\Big]\,, \end{aligned} \tag{C.16}$$

where we have used $\rho_m = 3H_0^2\Omega_{m,0}/(\kappa^2 a^3)$, with $\Omega_{m,0}$ being the matter density fraction today and $H_0 = H(a=1)$ is the Hubble constant.

We note that in our code we make the redefinition $M^2\kappa^2 = M^2/m_0^2 \to M^2$ where m_0^2 is the Planck mass. Further, we comment on the flexibility offered here. One can choose to specify any two of $\{\alpha_M, M^2, H\}$. If H is specified then either α_M or M^2 must also be specified, with the third function given by the relation in Eq. 5.25. If H is not specified, then we must solve the Friedmann equations to obtain H. As a default in our code, H is specified and it is assumed that the specified expressions for α_M and M^2 are consistent

with Eq. 5.25.

We can also take the small scale ($k \to \infty$) limit of Eq. C.1 to get a simpler expression valid at scales where the QS is a safer approximation and for models exhibiting negligible scale dependence in the linear growth. This is given by

$$\mu_\infty = \frac{1}{M^2\kappa^2}\Big(1 + \alpha_T + \beta_\xi\Big)\,, \tag{C.17}$$

where

$$\beta_\xi = \frac{2}{c_s^2\alpha}\Big(c_T^2\frac{\alpha_B}{2} + \alpha_M - \alpha_T\Big)^2 \tag{C.18}$$

with c_s^2 and α and α given by Eq. 5.29 and Eq. 5.30.

C.1.2 Example: Hu-Sawicki $f(R)$

In this section we derive the relevant EFTofDE parameters and linear Poisson modification for the Hu-Sawicki form of $f(R)$ gravity [109]. This exercise is also performed in the `GtoPT` notebook provided in the `ACTio-ReACTio` github repository.

The action in $f(R)$ gravity is given by

$$\begin{aligned} S &= \int d^4x\sqrt{-g}\frac{1}{2\kappa^2}\Big(R + f(R)\Big) \\ &\approx \int d^4x\sqrt{-g}\frac{1}{2\kappa^2}\Big(R + f(\bar{R}) + f_R(\bar{R})(R-\bar{R})\Big) \\ &= \int d^4x\sqrt{-g}\frac{1}{2\kappa^2}\Big((1+f_R)R + f - f_R\bar{R}\Big)\,, \end{aligned} \tag{C.19}$$

where $f_R = df(R)/dR$ and we have performed a Taylor expansion in the second line. We can then map this action onto the functions given in Eq. 5.2 together with an identification of the scalar degree of freedom $\phi \equiv (1+f_R)/\kappa^2$ [494]:

$$G_2 = -\frac{1}{2\kappa^2}(\bar{R}f_R - f),\quad G_3 = 0,\quad \text{and}\quad G_4 = \frac{1}{2\kappa^2}(1+f_R)\,. \tag{C.20}$$

If we now write down the action in the ADM formalism and use the Gauss-Codazzi relation, we can compare to Eq. 5.18 and Eq. 5.19 to get

$$\Omega = (1+f_R),\ \Lambda = \frac{1}{2\kappa^2}(f - \bar{R}f_R),\ \ c = \bar{M}_2^2 = \bar{M}_1^3 = M_2^4 = 0\,. \tag{C.21}$$

Using Eq. 5.25 - Eq. 5.27 we have

$$\alpha_M = \frac{a f_R'}{1 + f_R}\,, \tag{C.22}$$

$$\alpha_T = 0\,, \tag{C.23}$$

$$\alpha_B = -\frac{a f_R'}{1 + f_R}\,, \tag{C.24}$$

$$\alpha_K = 0\,, \tag{C.25}$$

with

$$M^2 = \frac{(1 + f_R)}{\kappa^2}\,, \tag{C.26}$$

where a prime denotes a scale factor derivative. When substituting into the expressions in Appendix C.1.1 we get the following solution for μ (Eq. C.1)

$$\mu = \frac{1}{1 + f_R}\Big[1 + \Big(\frac{k}{a}\Big)^2 \frac{1}{3\tilde{\Pi}(k, a)}\Big]\,, \tag{C.27}$$

where

$$\tilde{\Pi}(k, a) = \left(\frac{k}{a}\right)^2 + (1 + f_R)\frac{\bar{R}_f}{3}\,, \tag{C.28}$$

and

$$\bar{R}_f \equiv \frac{d\bar{R}}{df_R} = f_{R\bar{R}}^{-1}\Big(= \frac{\bar{R}'}{f_R'}\Big)\,. \tag{C.29}$$

In the Hu-Sawicki model we have the following choice for $f(R)$

$$f(R) = -m^2 \frac{c_1 (R/m^2)^n}{c_2 (R/m^2)^n + 1}\,, \tag{C.30}$$

where in this work we set the index $n = 1$ and the mass scale m^2, c_1 and c_2 are free parameters to be constrained by data. Taking the derivative of Eq. C.30 with respect to R and the high curvature limit ($R \gg m^2$) gives

$$f_R = -\frac{c_1}{c_2^2}\Big(\frac{m^2}{R}\Big)^2\,. \tag{C.31}$$

By rearranging this equation and evaluating at the background level at $a = 1$ (today), we can apply the following standard reparameterisation

$$\frac{c_1}{c_2^2} = -\bar{f}_{R0}\Big(\frac{\bar{R}_0}{m^2}\Big)^2\,, \tag{C.32}$$

where $\bar{f}_{R0}$ is the background value of f_R evaluated today and is a free parameter governing the level of modification to ΛCDM at the level of structure formation. Substituting

Eq. C.32 into Eq. C.31 gives

$$f_R = \bar{f}_{R0}\left(\frac{\bar{R}_0}{R}\right)^2 . \tag{C.33}$$

Further, we have

$$f_{RR} = -2\bar{f}_{R0}\left(\frac{\bar{R}_0}{R}\right)^2 \frac{1}{R} . \tag{C.34}$$

Using the background expression for f_{RR} in Eq. C.29 and substituting into Eq. C.28 gives

$$\tilde{\Pi}(k,a) = \left(\frac{k}{a}\right)^2 + (1+f_R)\frac{1}{6|f_{R0}|}\frac{\bar{R}^3}{\bar{R}_0^2} . \tag{C.35}$$

Now if we approximate the background to be close to ΛCDM, as supported by observations and by construction for $|f_{\rm R0}| \ll 1$, we have

$$\bar{R} \approx 3\frac{H_0^2}{a^3}\left(\Omega_{m,0} + 4a^3\Omega_{\Lambda,0}\right) , \tag{C.36}$$

where $\Omega_{\Lambda,0} = 1 - \Omega_{m,0}$ for a flat ΛCDM universe. Taking $a = 1$ we have the curvature today

$$\bar{R}_0 \approx 3H_0^2\left(4 - 3\Omega_{m,0}\right) . \tag{C.37}$$

Finally substituting $\bar{R}$ and $\bar{R}_0$ in Eq. C.35 we get the expression for μ as it appears in `ACTio-ReACTio` [130]

$$\mu = 1 + \left(\frac{k}{a}\right)^2 \frac{1}{3\Pi(k,a)} , \tag{C.38}$$

with

$$\Pi(k,a) = \left(\frac{k}{a}\right)^2 + \frac{\Xi(a)^3}{2f_0(4-3\Omega_{\rm m,0})^2}, \tag{C.39}$$

$$\Xi(a) = \frac{\Omega_{\rm m,0} + 4a^3\Omega_{\Lambda,0}}{a^3}, \tag{C.40}$$

where $f_0 = |f_{\rm R0}|/H_0^2$.

We make the crucial note here that in the derivation above we have over-constrained our system. Namely we have specified all of Ω, c as well as set $H = H_{\Lambda\rm CDM}$. If we use Eq. C.22-Eq. C.26 together with $H = H_{\Lambda\rm CDM}$ we find that $c \neq 0$ and we don't recover Eq. C.38. This follows directly from the fact that $H_{\Lambda\rm CDM}$ is not an exact solution for the Friedmann equations in $f(R)$ which implicitly assumes $c = 0$.

In our code we give the option to over constrain by specifying $c(a)$. Alternatively, one can code in the Friedmann equations and solve for $H(a)$. This of course increases computational inefficiency. To partially alleviate this issue, we can also place the additional constraint on $c_s^2(a)$ instead of c which has well motivated physical priors (see text around Eq. 5.29). The relationship between $c_s^2(a)$ and $c(a)$ is derived from Eq. 5.29 and Eq. C.16. It is given explicitly in the `GtoPT` notebook as well as the `Actio-Reactio`

source code.

The derivation of the 2nd and 3rd order modifications to the Poisson equation (see Eq. 5.14) from the ADM decomposed action requires us to go to higher order in the metric perturbations. We do not do this here as we omit these corrections from our code due to computational difficulty and the low level of impact they have on the final nonlinear power spectrum (see Section 5.5). However, in the provided Mathematica notebook, `GtoPT`, one can go from a specified G_i of the Horndeski Lagrangian to μ, γ_2 and γ_3 following the map given in Ref. [365]. We provide a number of examples in that notebook and refer the reader to Refs. [130, 365] for the forms of μ, γ_2 and γ_3 in DGP and Hu-Sawicki $f(R)$ gravity.

C.2 Nonlinear Poisson Modifications

C.2.1 Exact Forms

We provide the exact forms for the nonlinear modification to the Poisson equation (see Eq. 5.13) in DGP and $f(R)$ gravity, which are reproduced from Ref. [130].

The modification in DGP is given by [339]

$$\mathcal{F}_{\rm DGP} = \frac{2}{3\beta(a)} \frac{\sqrt{1+s^3}-1}{s^3}, \tag{C.41}$$

where

$$s = \left[\frac{2\Omega_{m,0}(\delta+1)}{9a^3\beta(a)^2\Omega_{rc}}\right]^{\frac{1}{3}}, \tag{C.42}$$

δ being the nonlinear over-density given by

$$\delta = y^{-3}(1+\delta_i) - 1\,, \tag{C.43}$$

with δ_i being the initial over-density and

$$y \equiv \frac{R_{\rm TH}/a}{R_i/a_i}\,, \tag{C.44}$$

$R_{\rm TH}$ and R_i being the physical halo top-hat radius at the target scale factor a and the initial scale factor a_i respectively. $\Omega_{\rm rc} \equiv 1/(4H_0^2 r_c^2)$ where r_c is the cross-over scale and is the free parameter of the theory governing the level of modification. Finally, $\beta(a)$ is given by

$$\beta(a) \equiv 1 + \frac{H}{H_0}\frac{1}{\sqrt{\Omega_{\rm rc}}}\left(1 + \frac{aH'}{3H}\right). \tag{C.45}$$

The fully nonlinear modification in Hu-Sawicki $f(R)$ is given by [378]

$$\mathcal{F}_{\rm fR} = \min\left[O - O^2 + \frac{O^3}{3}, \frac{1}{3}\right], \tag{C.46}$$

where

$$O = \frac{f_0 y_h a (3\Omega_{m,0} - 4)^2}{\Omega_{m,0}(R_i/a_i)^2} \times \left[\tilde{G}(y_{\rm env}) - \tilde{G}(y_{\rm h})\right], \tag{C.47}$$

and

$$\tilde{G}(y) = \left[\frac{\Omega_{m,0}}{(ya)^3} + 4 - 4\Omega_{m,0}\right]^{-2}, \tag{C.48}$$

where y_h is the quantity solved for using $f(R)$ halos whereas $y_{\rm env}$ is that solved for in the environment, which is approximated by performing the same calculation but with $f_0 = 0$.

C.2.2 nPPF Forms

We also reproduce the nPPF expressions for both of these theories from Ref. [351]. In DGP we have the following values for the p_i parameters in Eq. 5.39

$$\begin{aligned} &p_1 = 2, \qquad p_2 = 1, \qquad p_3 = \frac{3}{2}, \\ &p_4(a) = 2\Big(\frac{\Omega_{\rm m,0}}{4\Omega_{\rm rc}}\frac{1}{9\beta(a)^2}\Big)^{1/3}, \qquad p_5 = -1, \qquad p_6 = 0, \\ &p_7 = 0\,, \end{aligned} \tag{C.49}$$

which reproduce Eq. C.41 exactly. Note if using Eq. 5.37 we simply set $p_2 = \frac{1}{3\beta(a)}$.

On the other hand, the Hu-Sawicki $f(R)$ parameterisation is not exact but is closely matched by the following parameters in the screening regime [351] for a given choice of p_1 (using Eq. 5.39)

$$\begin{aligned} &p_2 = 1, \qquad p_3 = 7, \\ &p_4 = 2\Omega_{\rm m,0}^{1/3}\Big[(\Omega_{\rm m,0} + 4(1-\Omega_{\rm m,0})^{-2}\frac{p_1}{3|f_{\rm R0}|}\Big]^{1/p_3}, \\ &p_5 = -1, \qquad p_6 = \frac{2}{3p_3}, \qquad p_7 = -\frac{6}{7}\,, \end{aligned} \tag{C.50}$$

where we used $\alpha = 1/(n+1) = 0.5$ [378] in Equation 5.6 of Ref. [351]. Again, if using Eq. 5.37 we set $p_2 = \frac{1}{3}$.

C.2.3 Comparisons

Here we provide some comparisons of the approximate expressions for $\mathcal{F}$ given by the nPPF model (Eq. 5.39) and the Erf model (Eq. 5.41) against the exact expressions in DGP (Eq. C.41) and $f(R)$ (Eq. C.46). Since the nPPF form is exact for DGP, we only

compare it in the $f(R)$ case. Unless otherwise stated, the fits are performed as described in Section 5.5 and shown in Tab. 5.3.

DGP

In Fig. C.1 we show the nonlinear modification to the Poisson equation, $1+\mathcal{F}$, in DGP for $\Omega_{\rm rc} = 0.25$ and $\Omega_{\rm rc} = 0.01$ as a function of top-hat radius parameter $y_{\rm h}$. We plot the exact solution given by Eq. C.41 given as solid curves to the best fit Erf model given as dashed curves. We see an additional redshift dependence of the screening scale becoming important for high z. As modifications to GR are expected to be small at high redshift, this deviation may not be so important, which is supported by Fig. 5.5. We have performed a fit of this redshift dependence and find it behaves very well as a power law, with an $\mathcal{O}(0.1)$ exponent (specifically ≤ 0.15), which is first of all small and second of all degenerate with q_2 and q_3, meaning the model likely has sufficient freedom to very well capture a DGP type of modification to gravity without biasing cosmological or gravitational constraints.

Hu-Sawicki $f(R)$

Here we check that the nPPF and Erf models can qualitatively reproduce the exact form of $\mathcal{F}$ (Eq. C.46) across all scales, masses and environments for Hu-Sawicki $f(R)$ gravity.

Before showing the results, we make a note on the best fitting parameters for the Erf model. We find that the fits in Tab. 5.3, performed by fitting the exact prediction for the reaction $\mathcal{R}$, do not give a very good agreement when comparing to the exact form of $\mathcal{F}$. In particular, we find that the mass dependence parameter, q_2, seems to be underestimated when fitting $\mathcal{R}$. This parameter dictates the left hand slope in the contour plots in this section. Such a discrepancy may be due to a number of factors including a missing redshift dependency, the details of the fit, degeneracies with q_3 and failings of the power law description. We find a better by-eye fit for $\mathcal{F}_{\rm Erf}$ across redshifts $z = 0, 1, 4$ and all values of $f_{\rm R0}$ is $q_2 = 0.85$. All other parameters are as in Tab. 5.3 unless otherwise stated.

In Fig. C.2 we show $1+\mathcal{F}$ for the exact (top panels), the Erf (middle panels) and the nPPF (lower panels) cases with $|f_{\rm R0}| = 10^{-5}$, characterising a moderate modification to ΛCDM. We do not show the $|f_{\rm R0}| = 10^{-6}, 10^{-7}$ cases which are qualitatively similar.

To check the effects of Yukawa suppression, we set $y_{\rm env} = 1$, which is the maximum value considered in the spherical collapse computation. We then plot $\mathcal{F}$ as a function of dimensionless top-hat radius parameter $y_{\rm h}$ and halo mass, which shows the screening regime and the onset of Yukawa suppression. For large masses and redshifts, screening occurs at larger physical scales while Yukawa suppression occurs at smaller scales. In all cases, the Yukawa suppression is only mildly relevant for $y_{\rm h} \to y_{\rm env}$ and very large masses.

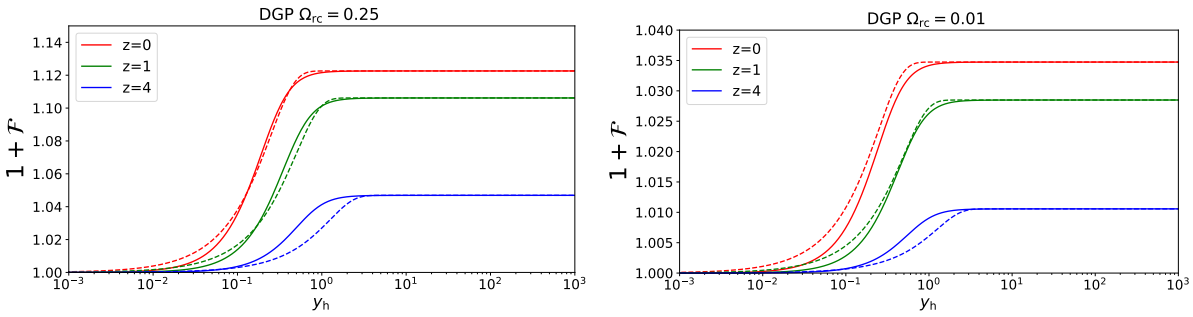

Figure C.1 *The modification to the Poisson equation* $1+\mathcal{F}$ *(see Eq. 5.13) in DGP gravity for* $\Omega_{rc} = 0.25$ *(left) and* $\Omega_{rc} = 0.01$ *(right). We plot the modifications as a function of normalised halo top-hat radius parameter for three different redshifts,* $z = 0$ *(red),* $z = 1$ *(green) and* $z = 4$ *(blue). The solid curves are the exact solution while the dashed curves are made using a single parameter fit to the exact* $\mathcal{R}$ *using Eq. 5.41 (see Tab. 5.3).*

The nPPF best fit value of p_8 gives a wrong Yukawa suppression scale, which is likely due to its global fit over all values of $y_{\rm env}$. Similarly, the Erf best fit screening scale, q_1, is also underestimated, likely for the same reasons.

Further, the nPPF shows a good match for the redshift dependence of the screening scale, while the Erf fit does significantly worse. We recall the nPPF uses a theoretically matched power law for this dependence (see Eq. 5.36 and Eq. C.50), while this dependence is fixed for the Erf case.

In Fig. C.3 we show $1+\mathcal{F}$ for $|f_{\rm R0}| = 10^{-5}$, with $y_{\rm env} = 0.3$, again for all cases. We find a good qualitative agreement between the nPPF and exact solutions. On the other hand, the comparisons again show there is an inaccurate redshift dependency in the screening scale of the Erf model, set by q_1. This was also seen in the DGP case. Despite this, the flexibility of the model still allows us to produce very accurate results at the power spectrum level (see Fig. 5.6) and so we do not feel introducing new freedom is warranted. We leave this issue to be further investigated in future work.

C.2.4 A Note on Notation

We would like to briefly discuss the inconsistency in the notation of previous related publications. The physical top-hat radius is denoted by $R_{\rm TH}$ in Refs. [130, 356], r in Ref. [358], R in Ref. [495] and ξ in Ref. [378]. From the definition of the physical top-hat radius and the conservation of mass $M = 4\pi\bar{\rho}_{\rm m}(\delta+1)R_{\rm TH}^3/3$ the expression for the nonlinear over-density is correctly given in Eq. C.43. Note the corresponding typos in the definition of the nonlinear over-density of Refs. [130, 356, 358] in Equations 34, B3 and 28 respectively. The connection between the physical top-hat radius and the initial comoving radius $R_{\rm th}$ [1] of the over-density is linear $R_{\rm TH}(a_i) = R_i = a_i R_{\rm th}$ initially but then due to

[1] Denoted Rth in the `ReACT` code.

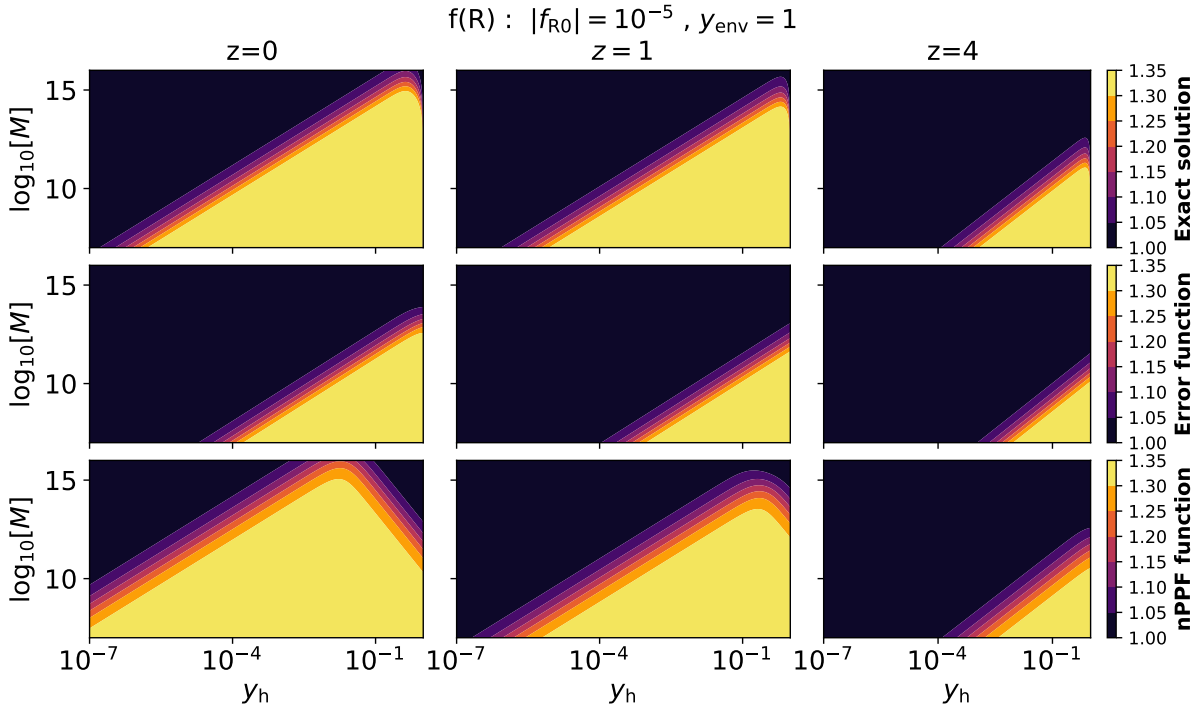

Figure C.2 *The modification to the Poisson equation* $1+\mathcal{F}$ *(see Eq. 5.13) in Hu-Sawicki* $f(R)$ *as a function of* $\log_{10}(M)$ *and top-hat radius parameter* y_h*. We set* $|f_{R0}| = 10^{-5}$ *and* $y_{env} = 1$*. The top panels show the exact solution, the middle panels show the phenomenological solution based on the error function and the bottom panels show the nPPF function. The left most column shows the functions for* $z = 0$*, the middle for* $z = 1$ *and the right most column for* $z = 4$*.*

the nonlinear evolution of the over-density it becomes $R_{\rm TH}(a) = yaR_{\rm th}$. This nonlinear evolution is encoded in the nonlinear scale factor ya with y given in Eq. C.44. Note that the expression for $\mathcal{F}$ in $f(R)$ gravity in Equation A2 of Ref. [356] and Equation. C15 of Ref. [130] is taken from Ref. [378] and includes $R_{\rm TH}$ which should be replaced by $R_{\rm th} = R_i/a_i$. While $\mathcal{F}$ in nDGP model from Ref. [495] is correctly given in these ReACT papers.

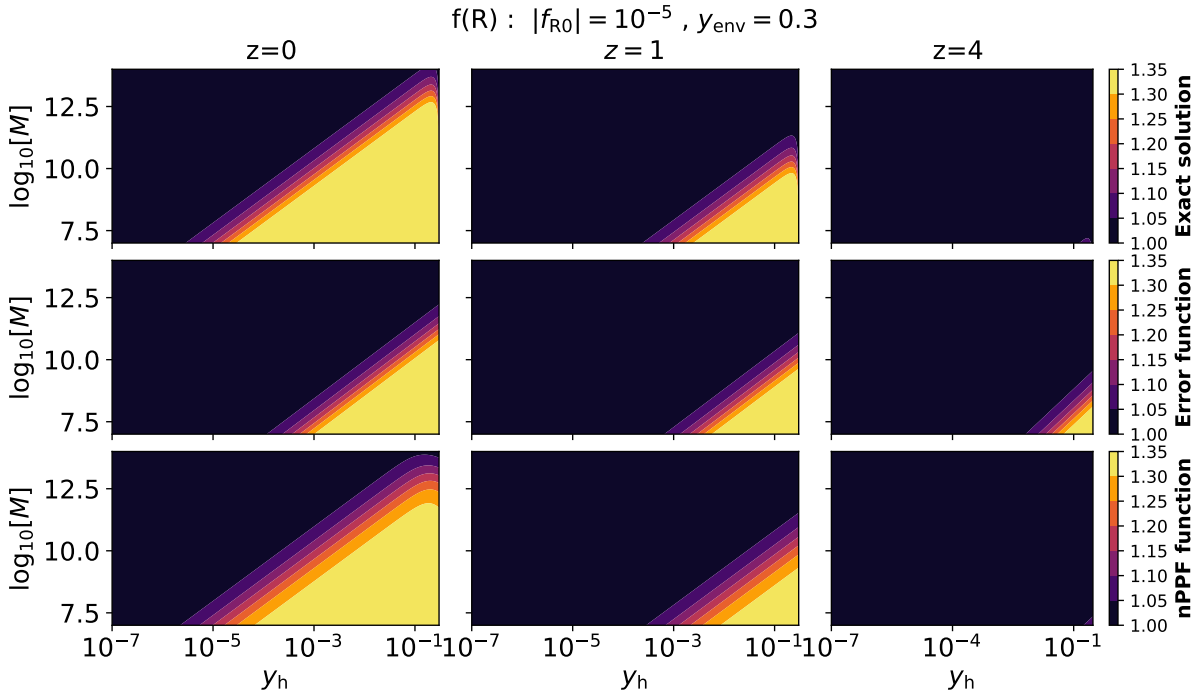

Figure C.3 *Same as Fig. C.2 but with* $y_{\rm env} = 0.3$.

Appendix D

Appendix to Chapter 6

D.1 Connection between the Growth Index and nDGP

For DGP models without an additional dark energy component, we have $\gamma_{\rm DGP} \approx 11/16$ (e.g., Ref. [423]). Here we will derive the value for when we include a dark energy contribution. Following the same steps as in Ref. [423], one can arrive to the following expression for the growth index by solving the linearised growth equation, taking a matter dominated era limit of $\Omega_w(a)/\Omega_{\rm m}(a) \ll 1$, Ω_w being the dark energy density fraction, and $(\mu_{\rm L} - 1) \ll 1$ (Eq. 22 in Ref. [423]):

$$\gamma = \frac{1}{2} + \frac{1}{4\Omega_w(a)} \int_0^1 \frac{{\rm d}u}{u} u^{5/2} \Omega_w(au) - \frac{3}{2\Omega_w(a)} \int_0^1 \frac{{\rm d}u}{u} [\mu_{\rm L}(au) - 1] u^{5/2} \,, \tag{D.1}$$

with $\Omega_w(a) = 1 - \Omega_{\rm m}(a)$. For early times $\Omega_w(a) \propto a^{-3w}$ and $\mu_{\rm L} - 1 = A\,\Omega_w(a)$, with A being a parameter to be determined. We can integrate the equation for γ to get

$$\gamma = \frac{3(1 - w - A)}{5 - 6w} \,, \tag{D.2}$$

where for GR $w = -1$ and $A = 0$, so one obtains the standard result of $\gamma_{\rm GR} = 6/11$.

Now, the Friedman equation for flat DGP models is given by ("+" for the normal branch or nDGP, "-" for the self-accelerating branch or sDGP):

$$H^2 \pm \frac{H}{r_c} = \frac{8\pi G}{3} \rho \,. \tag{D.3}$$

We have 2 options: assume that a) $\rho = \rho_{\rm m}$, hence the additional H/r_c-contribution acts like an effective dark energy component $\rho_w = \mp \frac{3}{8\pi G} \frac{H}{r_c}$; or b) $\rho = \rho_{\rm m} + \rho_{\rm DE}$, hence the effective dark energy has two contributions $\rho_w = \rho_{\rm DE} \mp \frac{3}{8\pi G} \frac{H}{r_c}$.

For the first case without dark energy we find from the Friedman equation: $\Omega_{\rm m}(a) = 1 \pm 2\sqrt{\Omega_{rc}}/E(a)$ or $E(a) = \mp\sqrt{\Omega_{rc}} + \sqrt{\Omega_{rc} + \Omega_{\rm m} a^{-3}}$. The former implies that from

$E(a=1)=1$ follows $\mp 2\sqrt{\Omega_{rc}} = 1-\Omega_{\rm m}$. Hence, for all realistic $\Omega_{\rm m}<1$ only the self-accelerating branch is relevant. From $\dot{\rho}_w = -3H(1+w)\rho_w$ and a derivative of Eq. D.3 we find $w=-1/(1+\Omega_{\rm m}(a))$. From Eq. 6.8 and Eq. 6.7 we compute $\beta = -\frac{1+\Omega_{\rm m}^2(a)}{1-\Omega_{\rm m}^2(a)}$ and $\mu_{\rm L}-1 = -\frac{1}{3}\frac{1-\Omega_{\rm m}^2(a)}{1+\Omega_{\rm m}^2(a)} = A\Omega_w(a)$ with $A=-\frac{1}{3}\frac{1+\Omega_{\rm m}(a)}{1+\Omega_{\rm m}^2(a)}$. Combining these findings together with the limit of $a\to 0$, i.e., $A\to -1/3$ and $w\to -1/2$, one gets $\gamma = 11/16$ from Eq. D.2 exactly like in Ref. [423] (recall Eq. D.1 is derived for early times).

Overall, for small values of Ω_{rc}, $\gamma = 11/16$ is a good approximation at all redshifts for this particular case of the flat DGP or sDGP model, where the value of the extended parameter is directly related to the matter density. While for larger values of Ω_{rc} (hence smaller values of $\Omega_{\rm m}$) as $a\to 1$, $A\to -1/3$ and $w\to -1$ (mimicking a cosmological constant today). This decreases the value of the growth index to $\gamma\to 7/11$, when computed according to Eq. D.2. Even the most extreme values of Ω_{rc} show at most 2% deviation at lower redshifts when compared against solutions from numerically equating $\mu_{\rm L}^{\gamma} = \mu_{\rm L}^{\rm DGP}$ at each redshift individually. However, note that in this scenario the growth index value is always larger than its GR limit. In other words, the structure growth is suppressed relative to the standard cosmology.

For the second case with the cosmological constant, Ω_{rc} becomes an independent parameter. We discuss only the case of including the cosmological constant, but the same logic can be applied to any other parameterisation of the dark energy component. We fix the expansion to the ΛCDM cosmology: from Eq. D.3, we have $E(a) = \mp\sqrt{\Omega_{rc}} + \sqrt{\Omega_{rc}+\Omega_{\rm m}a^{-3}+\Omega_{\rm DE}(a)}$, and from the equality $E = E_{\Lambda{\rm CDM}}$ we get $\Omega_{\rm DE}(a) = (1-\Omega_{\rm m}) \pm 2\sqrt{\Omega_{rc}}\sqrt{\Omega_{\rm m}a^{-3}+(1-\Omega_{\rm m})}$. From Eq. 6.8 and Eq. 6.7: $\mu_{\rm L}-1 = \frac{2\sqrt{\Omega_{rc}}}{3}\frac{1}{2\sqrt{\Omega_{rc}}\pm E(a)[2-\Omega_{\rm m}(a)]}$ with "+" for nDGP and "-" for sDGP. The corresponding limits are: $\mu_{\rm L}-1 \to \pm\frac{2\sqrt{\Omega_{rc}}}{3\sqrt{\Omega_{\rm m}}}a^{3/2}$ for early times, while the late-time limit tends to $\mu_{\rm L}-1 \to \frac{2\sqrt{\Omega_{rc}}}{3}\frac{1}{2\sqrt{\Omega_{rc}}\pm[2-\Omega_{\rm m}]}$. This means that at high redshift the assumption of $(\mu_{\rm L}-1)/\Omega_w(a) \approx$ const is not valid in this case as $\Omega_w(a)\propto a^3$, while $(\mu_{\rm L}-1)\propto a^{3/2}$. As a consequence the integration in Eq. D.2 for the early-time limit yields a diverging value of $\gamma = \gamma_{\rm GR} \mp \frac{\sqrt{\Omega_{rc}\Omega_{\rm m}}}{4(1-\Omega_{\rm m})a^{3/2}}$, with "-" for nDGP, "+" for sDGP. We can repeat this calculation for $a\to 1$ and get $\gamma = \gamma_{\rm GR} - \frac{2}{5}\frac{\sqrt{\Omega_{rc}}}{(2\sqrt{\Omega_{rc}}\pm[2-\Omega_{\rm m}])(1-\Omega_{\rm m})}$, with "+" for nDGP, "-" for sDGP. Therefore, the addition of the dark energy component in the nDGP model leads to $\gamma \leq 0.55$ for any $\Omega_{rc}\geq 0$, resulting in enhanced growth at linear scales and in agreement with our findings. We can insert our values for Ω_{rc} and $\Omega_{\rm m}$ for the late-time limit and obtain $\gamma \approx \gamma_{\rm GR} - 0.11 \approx 0.44$, which is in excellent agreement with our findings in Subsection 6.3.2 and Subsection 6.3.5.

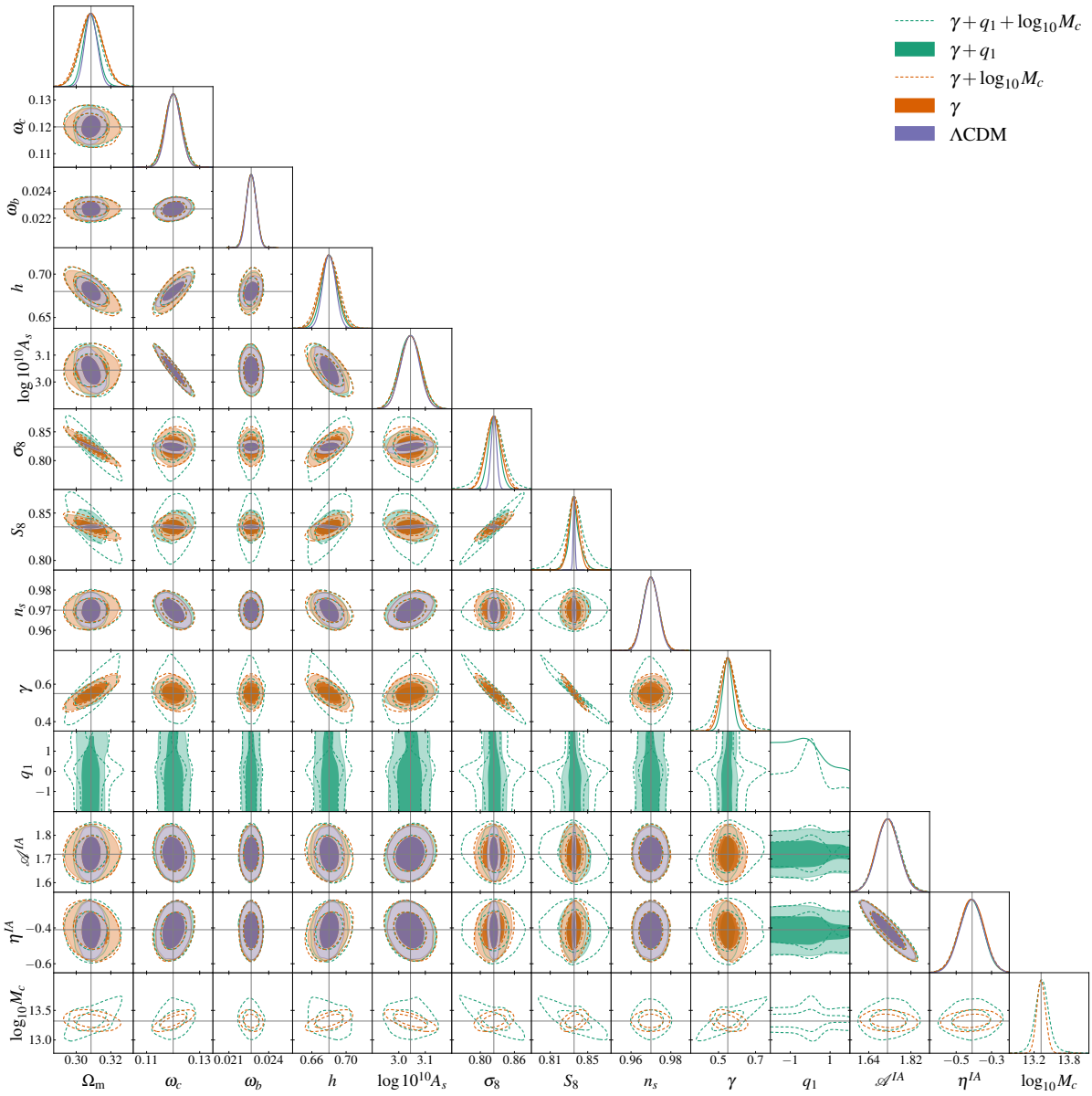

Figure D.1 *Full posterior distribution for validation with GR mock data for a Stage-IV cosmic shear setup with $\ell_{\max} = 3000$. Different colours correspond to the growth index model with screening (green), the growth index model with unmodified nonlinear growth (orange), and the model used to produce the mock data (purple). The dashed lines denote models with an additional baryonic feedback parameter.*

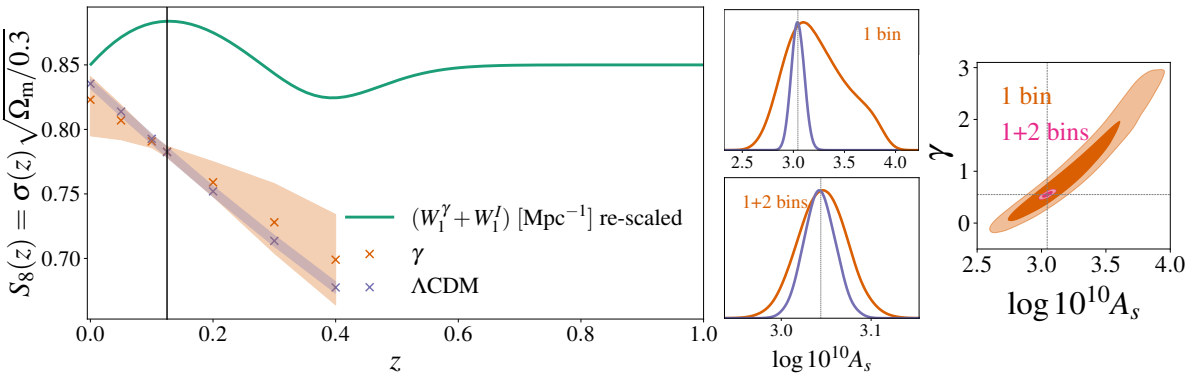

Figure D.2 *Varying only* Ω_m, S_8, γ *with re-scaled covariance and using linear scales. Left panel: constraints from the first redshift bin. Time evolution of* $S_8(z)$ *in the standard cosmology (purple crosses) and* γ*-parameterisation (*γ*-pseudo, orange crosses). Green solid line denotes the combination of the lensing and IA kernels (re-scaled and shifted for visualisation purposes). Black solid line denotes the maximum of the kernel and same constraints on* $S_8(z)$ *in both models. Middle panel: marginalised posterior distributions for* $\log 10^{10}$ A_s *from the first bin (upper plot) and combined first two bins (lower plot) in the standard cosmology (purple lines) and* γ*-parameterisation (orange lines). Right panel: marginalised posterior distribution for* γ *and* $\log 10^{10}$ A_s *with the first photometric bin (orange contour) and combined with the second photometric bin (pink contour). Dashed lines denote the fiducial values.*

D.2 Validation with GR: Full Posteriors and Discussion

In Fig. D.1 several degeneracies are apparent due to the fact that $C_\ell \propto \sigma_8^2 \Omega_m$: the negative correlations of $\sigma_8 - \Omega_m$ and $\gamma - \sigma_8$, and the positive correlation of $\gamma - \Omega_m$. We overlay contours from the ΛCDM modelling to showcase the strong positive correlation between $\log 10^{10}$ A_s and σ_8, which is weakened when an additional parameter controlling the amplitude of the power spectrum on large scales, γ, is added. However, in all scenarios $\log 10^{10}$ A_s is strongly anti-correlated with h and ω_c. We also note that the zNLA parameters $\mathcal{A}^{\rm IA}$ and $\eta^{\rm IA}$ are not strongly degenerate with any other parameters but are anti-correlated with one another; their constraints are model-independent. From the full posterior we also see that the screening scale is not detected, which is to be expect for $\mu_L^{\gamma \sim 0.55} \approx 1$ (see Eq. 6.10). Additionally, the growth index is anti-correlated with the expansion rate h, which is due to the inclusion of large scales, $10 < \ell < 100$, and tight informative priors on ω_b and n_s (see discussion in Appendix D.3).

From the same full posterior distribution we also notice that the γ+q_1 (solid green lines) and ΛCDM (solid purple lines) models constrain the background cosmological parameters, Ω_m, h, to the same level of uncertainty. This is well understood since γ only impacts the amplitude of the power spectrum and not the background. However, we notice drastically different constraints on σ_8 and S_8: the contours are much broader in the γ models than in the ΛCDM case. This difference arises due to strong sensitivity of the linear growth

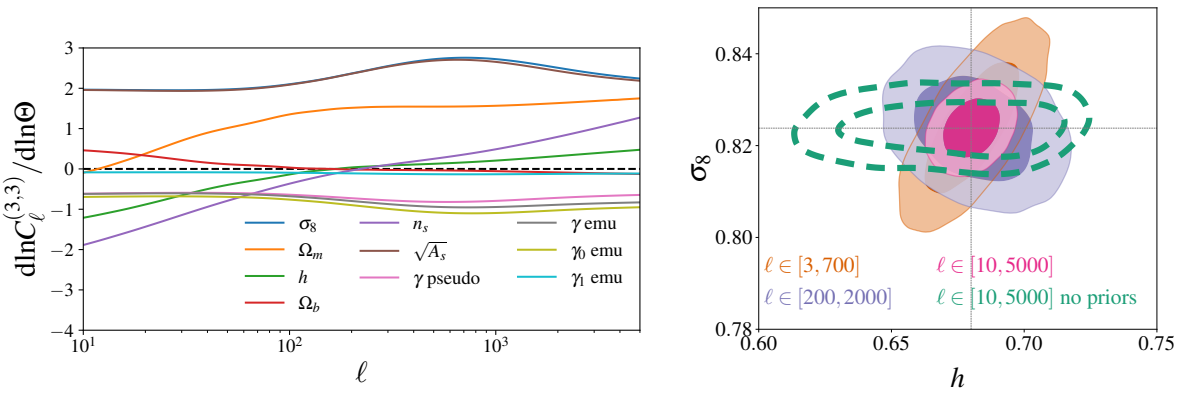

Figure D.3 *Left panel: parameter dependence of the shear angular power spectrum in the 3-3 redshift bin without shape noise. Right panel: change in the orientation of degeneracies between parameters depending on the scale-cuts and priors used.*

factor to the deviation of the growth index from its GR value at lower redshifts (see Fig. 6.1). To demonstrate this we fix all parameters in the model to their fiducial values and vary Ω_m, S_8 and γ in the first redshift bin with a re-scaled covariance by a factor of 250 (corresponding to smaller error bars), and using linear scales only, $\ell_\mathrm{max} = 500$. In the left panel of Fig. D.2 we show that, as expected, both models measure the same value of $S_8(z) = \sigma_8(z)\sqrt{\Omega_\mathrm{m}/0.3}$ around the peak of the first lensing kernel at $z = 0.125$. Therefore, it is the variation in γ-values that affects the inferred constraints of S_8 at redshift $z = 0$. For the first redshift bin, the constraints of the primordial amplitude demonstrate the same trend (see the upper middle panel of Fig. D.2). This changes as soon as we add additional redshift bins (in the lower middle panel). Overall, in Fig. D.1 with 10 redshift bins the constraints on the primordial amplitude are identical between both models since we match the growth at high redshift. Contrary to Stage-III surveys (see, for example, Ref. [207]), a Stage IV-like setup constrains the primordial amplitude well due to its wide redshift range and large number of redshift bins.

D.3 Expansion Rate: Note on Degeneracies and Priors

In Fig. D.1 we see strong degeneracies between all cosmological parameters and the expansion rate h. Fig. D.3 shows the derivatives of C_ℓ in the $3-3$ photo-z bin with respect to the parameters listed in the legend. From this figure, it is clear that C_ℓ is insensitive to h in the region of $10^2 < \ell < 10^3$. We also note the change in the dependence of C_ℓ on h in the $\ell < 10^2$ (prominent negative) and $\ell > 10^3$ (weak positive) regimes. From Eq. 6.3, we see that the impact of h on C_ℓ is coming purely from the matter power spectrum. In the linear regime, i.e., low ℓ and k, the matter power spectrum is an approximate power law with its slope depending on h, n_s and ω_b (for more detailed discussion see Ref. [11]).

We impose a Planck prior on n_s and a BBN prior on ω_b, which breaks this degeneracy. In the right panel of Fig. D.3, we demonstrate the rotation of degeneracy between σ_8 and h, when these informative priors are imposed in the analysis with GR model on GR mock data. For $\ell_{\rm max} = 700$, $\mathrm{dln}C_\ell/\mathrm{dln}h$ and $\mathrm{dln}C_\ell/\mathrm{dln}\sigma_8$ have opposite signs, hence the orange contour demonstrates a positive correlation. The situation changes to the negative correlation for $\ell \in [200, 2000]$ (the purple contour). When all scales are combined (the pink contour), the orientation of the degeneracy still slightly prefers the positive correlation characteristic for lower ℓ-values. However, this is no longer the case, when the priors are omitted (the dashed green contour). Similar arguments are applicable to all other cosmological parameters and their degeneracies with h. Also note that due to the choice of a diagonal Gaussian covariance, our constraints can be considered optimistic.

D.4 Test with nDGP: Full Posteriors and Discussion

In Fig. D.4 we show the two-dimensional marginalised posteriors for the full parameter space in $\gamma + q_1$ (green) and γ-pseudo (orange) models with $\ell_{\rm max} = 3000$ and $\ell_{\rm max} = 1000$, respectively. The only significantly biased parameter is $\log 10^{10}\, A_s$, which is explained by a different time evolution of the linear growth factor in nDGP and the growth index parameterisation. In Fig. 6.1 we see that for values of $\gamma \sim 0.3 - 0.4$ we obtain an offset of $D_\gamma/D_{\rm nDGP} \sim 0.97 - 0.98$. From the posterior maxima and the input fiducial values $A_s^{\rm mean}/A_s^{\rm fid} = 1.06$ ($\Delta A_s = 6\%$). Therefore, lower (than in nDGP) values of the growth factor in the growth index model are compensated by a higher value of the primordial amplitude. We note that while the posterior-maxima of ω_c and h are unbiased, their 2-dimensional contour demonstrates a 1σ bias that later propagates to a 1σ lower posterior maximum for $\Omega_{\rm m}$. We also found this bias when sampling in $\Omega_{\rm m}$ directly.

We notice that even for $\ell_{\rm max} = 1000$, there is a significant bias in h as well as in γ. Surprisingly, the pseudo γ model finds a value of σ_8 at its GR value (a lower than expected value compared to nDGP), which is compensated by high values of $\Omega_{\rm m}$ (1σ bias towards lower values in ω_c and 3σ bias towards lower values in h).

In Fig. D.5 we show the two-dimensional marginalised posteriors for the full parameter space in the $\gamma(z) + q_1$ model. Clearly, the bias towards higher values in $\log 10^{10}\, A_s$ vanishes due to a more accurate representation of the growth evolution. However, we notice significantly weaker constraints on h. This is expected from the degeneracy between the expansion rate and γ (in this case γ_0, γ_1). We show that this degeneracy is broken when γ_1 is fixed.

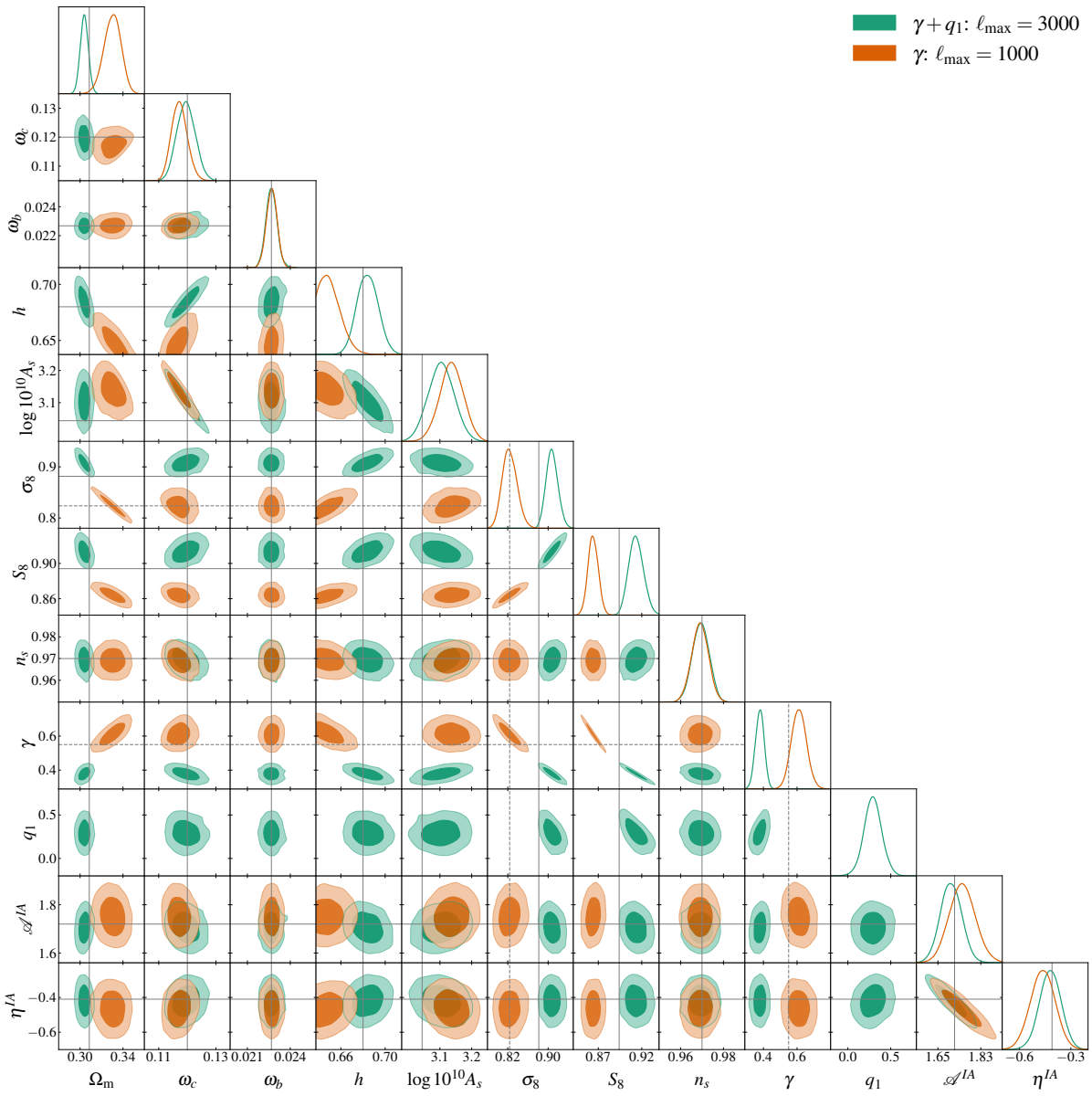

Figure D.4 *Full posterior distribution for showcasing the screening impact with nDGP mock data for a Stage-IV cosmic shear setup. Different colours correspond to the screened growth index model with* $\ell_{\rm max} = 3000$ *(green) and the pseudo model with modified linear growth and standard nonlinear structure formation with* $\ell_{\rm max} = 1000$ *(orange). Solid grey lines mark the true values of the synthetic data, dashed grey lines mark the parameter values in the standard cosmology.*

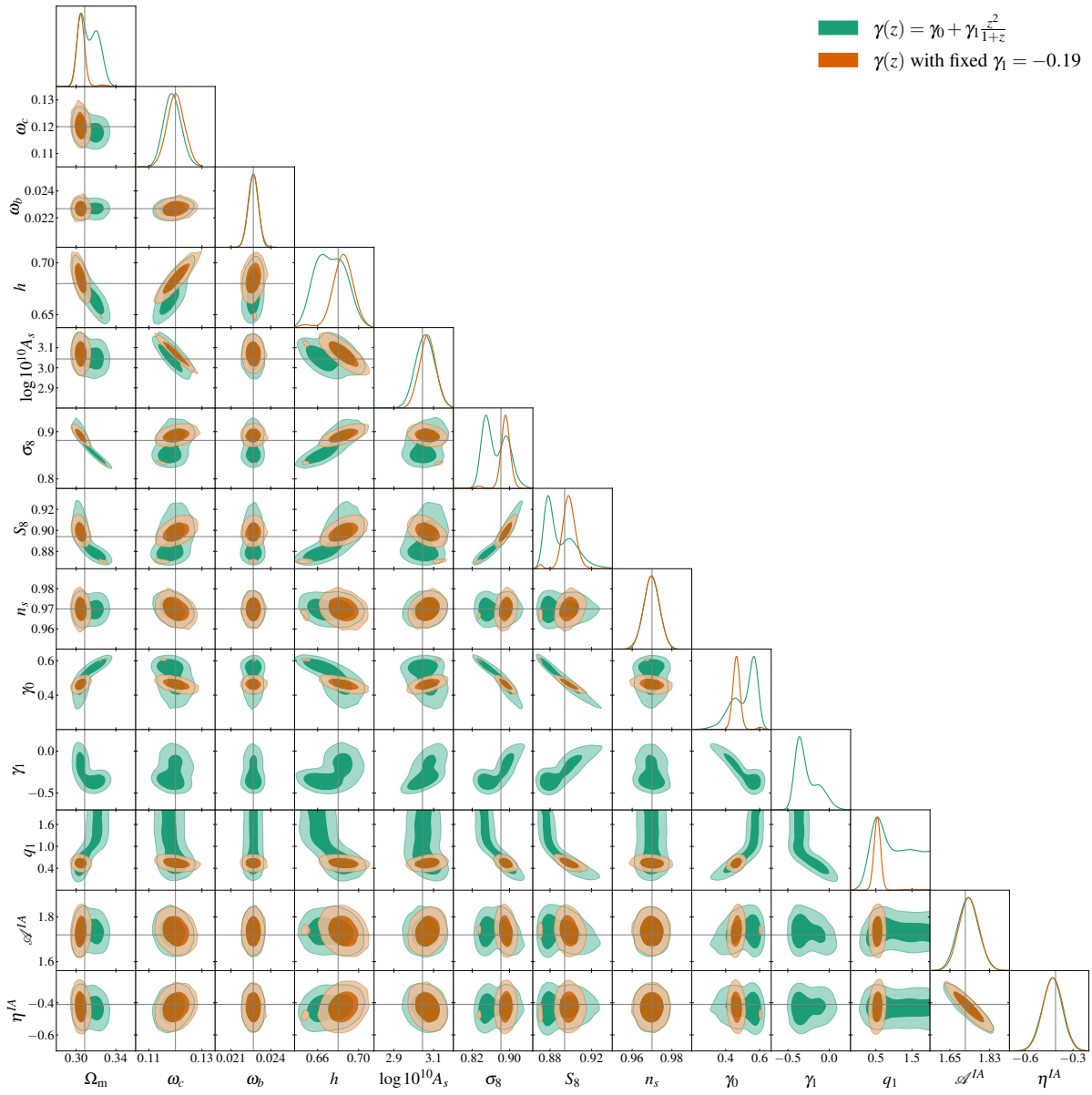

Figure D.5 *Full posterior distribution for tests with nDGP mock data for a Stage-IV cosmic shear setup with $\ell_{\max} = 3000$. Different colours correspond to the time-dependent growth index model (green) and the same model but with the second coefficient fixed to $\gamma_1 = -0.19$ (orange). Grey lines mark the true values of the synthetic data.*

D.5 Other Full Posteriors

In Fig. D.6 and Fig. D.7 we show the two-dimensional marginalised posteriors for the full parameter space in the analyses mentioned in the main text.

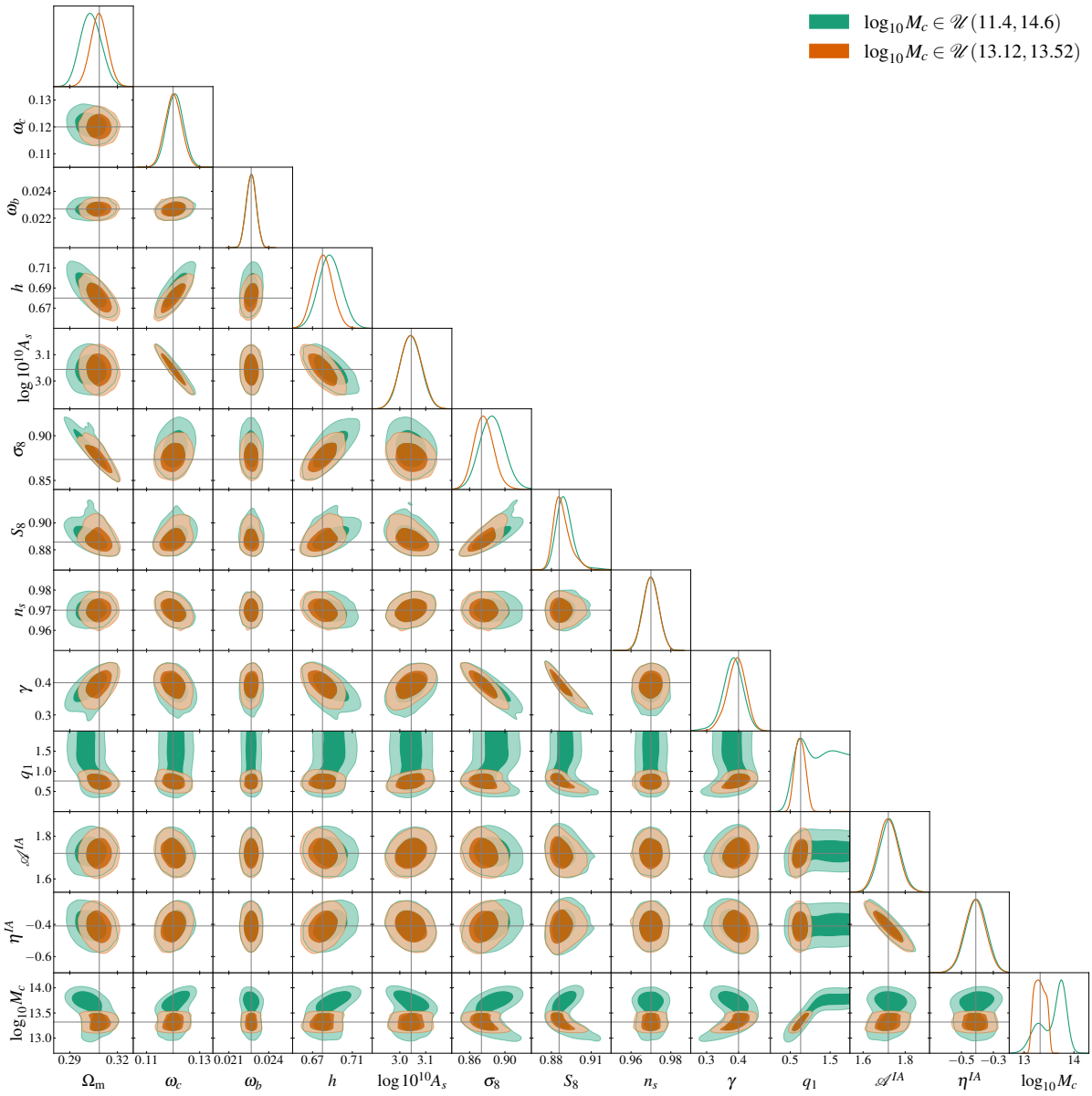

Figure D.6 *Full posterior distribution for investigating the degeneracy between the screening and baryonic parameters on γ+q_1 mock data for a Stage-IV cosmic shear setup with $\ell_{\max} = 3000$. Different colours correspond to a flat broad prior on the baryonic feedback parameter $\log_{10} M_c$, (green) and a flat tight prior $\mathcal{U}(13.12, 13.52)$ on it (orange). Grey lines mark the true values of the synthetic data.*

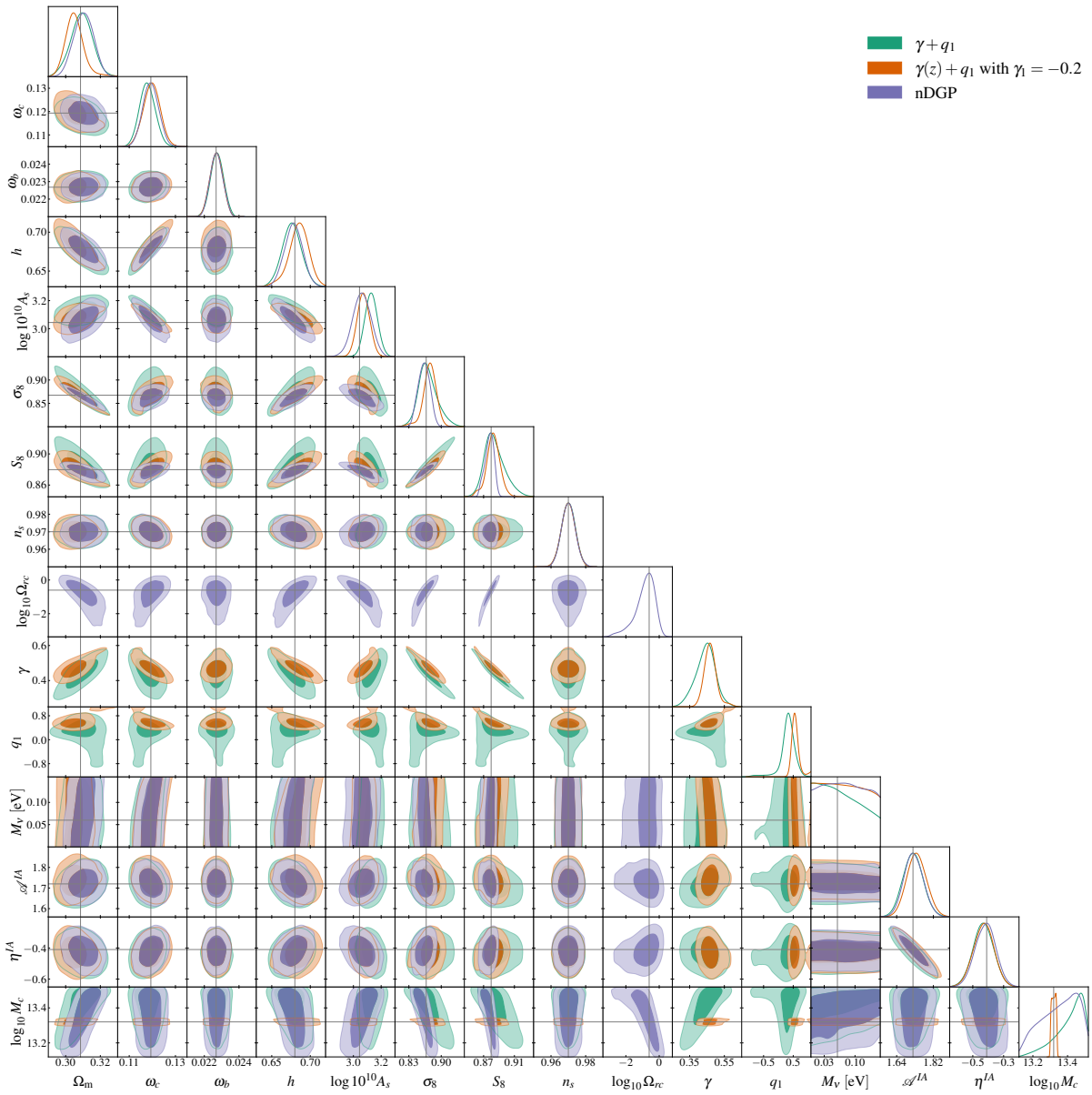

Figure D.7 *Full posterior distribution for the nDGP model with $\Omega_{rc} = 0.25$ for a Stage-IV cosmic shear setup with $\ell_{\max} = 3000$. Different colours correspond to the $\gamma + q_1$ model (green), the $\gamma(z) + q_1$ model with $\gamma_1 = -0.2$ (orange), and the exact nDGP model (purple). For nDGP and $\gamma + q_1$ the prior on $\log_{10} M_c$ is $\mathcal{U}(13.12, 13.52)$, while for the $\gamma(z) + q_1$ model it is $\mathcal{U}(13.3, 13.34)$. Grey lines mark the true values of the synthetic data.*

Bibliography

[1] Elcio Abdalla et al. Cosmology intertwined: A review of the particle physics, astrophysics, and cosmology associated with the cosmological tensions and anomalies. *JHEAp*, 34:49–211, 2022. doi: 10.1016/j.jheap.2022.04.002.

[2] Maria Tsedrik, Benjamin Bose, Pedro Carrilho, Alkistis Pourtsidou, Sefa Pamuk, Santiago Casas, and Julien Lesgourgues. Stage-IV Cosmic Shear with Modified Gravity and Model-independent Screening. *arXiv e-prints*, art. arXiv:2404.11508, April 2024. doi: 10.48550/arXiv.2404.11508.

[3] Marco Baldi and Fergus Simpson. Simulating momentum exchange in the dark sector. *Mon. Not. Roy. Astron. Soc.*, 449(3):2239–2249, May 2015. doi: 10.1093/mnras/stv405.

[4] Matteo Cataneo, Lucas Lombriser, Catherine Heymans, Alexander Mead, Alexandre Barreira, Sownak Bose, and Baojiu Li. On the road to percent accuracy: non-linear reaction of the matter power spectrum to dark energy and modified gravity. *Mon. Not. Roy. Astron. Soc.*, 488(2):2121–2142, 2019. doi: 10.1093/mnras/stz1836.

[5] Mark Subbarao, Miguel Aragon-Calvo, Hsiao-Wen Chen, Jean Quashnock, Alexander Szalay, and Donald York. Visualization of large scale structure from the sloan digital sky survey. *New Journal of Physics*, 10:125015, December 2008. doi: 10.1088/1367-2630/10/12/125015.

[6] Bernardita Ried Guachalla, Dylan Britt, Daniel Gruen, and Oliver Friedrich. Informed Total-Error-Minimizing Priors: Interpretable cosmological parameter constraints despite complex nuisance effects. *arXiv e-prints*, art. arXiv:2405.00261, April 2024. doi: 10.48550/arXiv.2405.00261.

[7] Andrea Oddo, Emiliano Sefusatti, Cristiano Porciani, Pierluigi Monaco, and Ariel G. Sánchez. Toward a robust inference method for the galaxy bispectrum: likelihood function and model selection. *JCAP*, 2020(3):056, March 2020. doi: 10.1088/1475-7516/2020/03/056.

[8] Andrea Oddo, Federico Rizzo, Emiliano Sefusatti, Cristiano Porciani, and Pierluigi Monaco. Cosmological parameters from the likelihood analysis of the galaxy power spectrum and bispectrum in real space. *JCAP*, 2021(11):038, November 2021. doi: 10.1088/1475-7516/2021/11/038.

[9] Federico Rizzo, Chiara Moretti, Kevin Pardede, Alexander Eggemeier, Andrea Oddo, Emiliano Sefusatti, Cristiano Porciani, and Pierluigi Monaco. The halo

bispectrum multipoles in redshift space. *JCAP*, 2023(1):031, January 2023. doi: 10.1088/1475-7516/2023/01/031.

[10] DESI Collaboration, A. Aghamousa, et al. The DESI Experiment Part I: Science,Targeting, and Survey Design. *arXiv e-prints*, art. arXiv:1611.00036, October 2016. doi: 10.48550/arXiv.1611.00036.

[11] Alex Hall. Cosmology from weak lensing alone and implications for the Hubble tension. *Mon. Not. Roy. Astron. Soc.*, 505(4):4935–4955, 2021. doi: 10.1093/mnras/stab1563.

[12] Scott Dodelson and Fabian Schmidt. *Modern Cosmology*. Elsevier Press, Cambridge, 2020. doi: 10.1016/C2017-0-01943-2.

[13] Daniel Baumann. *Cosmology*. Cambridge University Press, July 2022. ISBN 978-1-108-93709-2, 978-1-108-83807-8. doi: 10.1017/9781108937092.

[14] Valentin Assassi, Marko Simonović, and Matias Zaldarriaga. Efficient evaluation of angular power spectra and bispectra. *JCAP*, 11:054, 2017. doi: 10.1088/1475-7516/2017/11/054.

[15] J. E. Campagne, J. Neveu, and S. Plaszczynski. Angpow: a software for the fast computation of accurate tomographic power spectra. *Astron. Astrophys.*, 602:A72, 2017. doi: 10.1051/0004-6361/201730399.

[16] Xiao Fang, Elisabeth Krause, Tim Eifler, and Niall MacCrann. Beyond Limber: Efficient computation of angular power spectra for galaxy clustering and weak lensing. *JCAP*, 05:010, 2020. doi: 10.1088/1475-7516/2020/05/010.

[17] Job Feldbrugge. Complex evaluation of angular power spectra: Going beyond the Limber approximation. *Phys. Rev. D*, 108(10):103007, 2023. doi: 10.1103/PhysRevD.108.103007.

[18] Sofia Chiarenza, Marco Bonici, Will Percival, and Martin White. BLAST: Beyond Limber Angular power Spectra Toolkit. A fast and efficient algorithm for 3x2 pt analysis. *arXiv e-prints*, art. arXiv:2410.03632, October 2024. doi: 10.48550/arXiv.2410.03632.

[19] D. Nelson Limber. The Analysis of Counts of the Extragalactic Nebulae in Terms of a Fluctuating Density Field. II. *Astrophys. J.*, 119:655, 1954. doi: 10.1086/145870.

[20] Planck Collaboration, P. A. R. Ade, et al. Planck 2013 results. XVI. Cosmological parameters. *Astron. Astrophys.*, 571:A16, 2014. doi: 10.1051/0004-6361/201321591.

[21] Planck Collaboration, P. A. R. Ade, et al. Planck 2015 results. XIII. Cosmological parameters. *Astron. Astrophys.*, 594:A13, 2016. doi: 10.1051/0004-6361/201525830.

[22] Planck Collaboration, N. Aghanim, et al. Planck 2018 results. VI. Cosmological parameters. *Astron. Astrophys.*, 641:A6, 2020. doi: 10.1051/0004-6361/201833910. [Erratum: Astron.Astrophys. 652, C4 (2021)].

[23] Ya. B. Zeldovich. A Hypothesis, unifying the structure and the entropy of the universe. *Mon. Not. Roy. Astron. Soc.*, 160:1P–3P, 1972. doi: 10.1093/mnras/160.1.1P.

[24] Antony Lewis and Anthony Challinor. CAMB: Code for Anisotropies in the Microwave Background. Astrophysics Source Code Library, record ascl:1102.026, February 2011.

[25] Julien Lesgourgues. The Cosmic Linear Anisotropy Solving System (CLASS) I: Overview. *arXiv e-prints*, art. arXiv:1104.2932, April 2011.

[26] Francisco-Shu Kitaura, Gustavo Yepes, and Francisco Prada. Modelling Baryon Acoustic Oscillations with Perturbation Theory and Stochastic Halo Biasing. *Mon. Not. Roy. Astron. Soc.*, 439:21, 2014. doi: 10.1093/mnrasl/slt172.

[27] Pierluigi Monaco, Tom Theuns, and Giuliano Taffoni. The pinocchio algorithm: pinpointing orbit-crossing collapsed hierarchical objects in a linear density field. *Mon. Not. Roy. Astron. Soc.*, 331(3):587–608, April 2002. doi: 10.1046/j.1365-8711.2002.05162.x.

[28] Matteo Zennaro, Raul E. Angulo, Marcos Pellejero-Ibáñez, Jens Stücker, Sergio Contreras, and Giovanni Aricò. The BACCO simulation project: biased tracers in real space. *Mon. Not. Roy. Astron. Soc.*, 524(2):2407–2419, 2023. doi: 10.1093/mnras/stad2008.

[29] Marcos Pellejero-Ibanez, Jens Stuecker, Raul E. Angulo, Matteo Zennaro, Sergio Contreras, and Giovanni Arico. Modelling galaxy clustering in redshift space with a Lagrangian bias formalism and N-body simulations. *Mon. Not. Roy. Astron. Soc.*, 514(3):3993–4007, 2022. doi: 10.1093/mnras/stac1602.

[30] Jan Niklas Grieb, Ariel G. Sánchez, Salvador Salazar-Albornoz, and Claudio Dalla Vecchia. Gaussian covariance matrices for anisotropic galaxy clustering measurements. *Mon. Not. Roy. Astron. Soc.*, 457(2):1577–1592, April 2016. doi: 10.1093/mnras/stw065.

[31] Raul E. Angulo, Matteo Zennaro, Sergio Contreras, Giovanni Aricò, Marcos Pellejero-Ibañez, and Jens Stücker. The BACCO simulation project: exploiting the full power of large-scale structure for cosmology. *Mon. Not. Roy. Astron. Soc.*, 507(4):5869–5881, November 2021. doi: 10.1093/mnras/stab2018.

[32] Euclid Collaboration, M. Knabenhans, et al. Euclid preparation: IX. EuclidEmulator2 – power spectrum emulation with massive neutrinos and self-consistent dark energy perturbations. *Mon. Not. Roy. Astron. Soc.*, 505(2):2840–2869, 2021. doi: 10.1093/mnras/stab1366.

[33] F. Bernardeau, S. Colombi, E. Gaztañaga, and R. Scoccimarro. Large-scale structure of the Universe and cosmological perturbation theory. *Phys. Rept.*, 367 (1-3):1–248, September 2002. doi: 10.1016/S0370-1573(02)00135-7.

[34] Atsushi Taruya, Takahiro Nishimichi, and Shun Saito. Baryon acoustic oscillations in 2D: Modeling redshift-space power spectrum from perturbation theory. *Phys. Rev. D*, 82(6):063522, September 2010. doi: 10.1103/PhysRevD.82.063522.

[35] Marika Asgari, Alexander J. Mead, and Catherine Heymans. The halo model for cosmology: a pedagogical review. *arXiv e-prints*, art. arXiv:2303.08752, March 2023. doi: 10.48550/arXiv.2303.08752.

[36] Planck Collaboration, P. A. R. Ade, et al. Planck 2015 results. XV. Gravitational lensing. *Astron. Astrophys.*, 594:A15, 2016. doi: 10.1051/0004-6361/201525941.

[37] Daniel J. Eisenstein and Wayne Hu. Baryonic Features in the Matter Transfer Function. *Astrophys. J.*, 496(2):605–614, March 1998. doi: 10.1086/305424.

[38] Kazunori Akiyama et al. First M87 Event Horizon Telescope Results. IV. Imaging the Central Supermassive Black Hole. *Astrophys. J. Lett.*, 875(1):L4, 2019. doi: 10.3847/2041-8213/ab0e85.

[39] Ingrid H. Stairs. Testing general relativity with pulsar timing. *Living Rev. Rel.*, 6: 5, 2003. doi: 10.12942/lrr-2003-5.

[40] B. P. Abbott et al. Observation of Gravitational Waves from a Binary Black Hole Merger. *Phys. Rev. Lett.*, 116(6):061102, 2016. doi: 10.1103/PhysRevLett.116.061102.

[41] B. P. Abbott et al. Multi-messenger Observations of a Binary Neutron Star Merger. *Astrophys. J. Lett.*, 848(2):L12, 2017. doi: 10.3847/2041-8213/aa91c9.

[42] Adam G. Riess et al. Observational evidence from supernovae for an accelerating universe and a cosmological constant. *Astron. J.*, 116:1009–1038, 1998. doi: 10.1086/300499.

[43] Dragan Huterer and Daniel L Shafer. Dark energy two decades after: Observables, probes, consistency tests. *Rept. Prog. Phys.*, 81(1):016901, 2018. doi: 10.1088/1361-6633/aa997e.

[44] B. Bose, M. Tsedrik, J. Kennedy, L. Lombriser, A. Pourtsidou, and A. Taylor. Fast and accurate predictions of the non-linear matter power spectrum for general models of Dark Energy and Modified Gravity. *Mon. Not. Roy. Astron. Soc.*, 519 (3):4780–4800, March 2023. doi: 10.1093/mnras/stac3783.

[45] KiDS Collaboration, Catherine Heymans, et al. KiDS-1000 Cosmology: Multi-probe weak gravitational lensing and spectroscopic galaxy clustering constraints. *Astron. Astrophys.*, 646:A140, February 2021. doi: 10.1051/0004-6361/202039063.

[46] Oliver H. E. Philcox, Mikhail M. Ivanov, Marko Simonović, and Matias Zaldarriaga. Combining full-shape and BAO analyses of galaxy power spectra: a 1.6% CMB-independent constraint on H_0. *JCAP*, 2020(5):032, May 2020. doi: 10.1088/1475-7516/2020/05/032.

[47] Adam G. Riess, Dan Scolnic, Gagandeep S. Anand, Louise Breuval, Stefano Casertano, Lucas M. Macri, Siyang Li, Wenlong Yuan, Caroline D. Huang, Saurabh Jha, Yukei S. Murakami, Rachael Beaton, Dillon Brout, Tianrui Wu, Graeme E. Addison, Charles Bennett, Richard I. Anderson, Alexei V. Filippenko, and Anthony Carr. JWST Validates HST Distance Measurements: Selection of Supernova Subsample Explains Differences in JWST Estimates of Local H0. *arXiv e-prints*, art. arXiv:2408.11770, August 2024. doi: 10.48550/arXiv.2408.11770.

[48] Adam G. Riess, Stefano Casertano, Wenlong Yuan, J. Bradley Bowers, Lucas Macri, Joel C. Zinn, and Dan Scolnic. Cosmic Distances Calibrated to 1% Precision with

Gaia EDR3 Parallaxes and Hubble Space Telescope Photometry of 75 Milky Way Cepheids Confirm Tension with ΛCDM. *Astrophys. J. Lett.*, 908(1):L6, 2021. doi: 10.3847/2041-8213/abdbaf.

[49] M. J. Reid, D. W. Pesce, and A. G. Riess. An improved distance to ngc 4258 and its implications for the hubble constant. *The Astrophysical Journal Letters*, 886(2): L27, nov 2019. doi: 10.3847/2041-8213/ab552d.

[50] Vivian Poulin, Tristan L. Smith, and Tanvi Karwal. The Ups and Downs of Early Dark Energy solutions to the Hubble tension: A review of models, hints and constraints circa 2023. *Phys. Dark Univ.*, 42:101348, 2023. doi: 10.1016/j.dark.2023.101348.

[51] Sunny Vagnozzi. Seven Hints That Early-Time New Physics Alone Is Not Sufficient to Solve the Hubble Tension. *Universe*, 9(9):393, 2023. doi: 10.3390/universe9090393.

[52] Wendy L. Freedman, Barry F. Madore, In Sung Jang, Taylor J. Hoyt, Abigail J. Lee, and Kayla A. Owens. Status Report on the Chicago-Carnegie Hubble Program (CCHP): Three Independent Astrophysical Determinations of the Hubble Constant Using the James Webb Space Telescope. *arXiv e-prints*, art. arXiv:2408.06153, August 2024. doi: 10.48550/arXiv.2408.06153.

[53] Abigail J. Lee, Wendy L. Freedman, Barry F. Madore, In Sung Jang, Kayla A. Owens, and Taylor J. Hoyt. The Chicago-Carnegie Hubble Program: The JWST J-region Asymptotic Giant Branch (JAGB) Extragalactic Distance Scale. *arXiv e-prints*, art. arXiv:2408.03474, August 2024. doi: 10.48550/arXiv.2408.03474.

[54] Adam G. Riess, Gagandeep S. Anand, Wenlong Yuan, Stefano Casertano, Andrew Dolphin, Lucas M. Macri, Louise Breuval, Dan Scolnic, Marshall Perrin, and I. Richard Anderson. JWST Observations Reject Unrecognized Crowding of Cepheid Photometry as an Explanation for the Hubble Tension at 8σ Confidence. *Astrophys. J. Lett.*, 962(1):L17, 2024. doi: 10.3847/2041-8213/ad1ddd.

[55] DES Collaboration, R. Camilleri, et al. The Dark Energy Survey Supernova Program: An updated measurement of the Hubble constant using the Inverse Distance Ladder. *arXiv e-prints*, art. arXiv:2406.05049, June 2024. doi: 10.48550/arXiv.2406.05049.

[56] DES Collaboration, R. Camilleri, et al. The Dark Energy Survey Supernova Program: Investigating Beyond-ΛCDM. *arXiv e-prints*, art. arXiv:2406.05048, June 2024. doi: 10.48550/arXiv.2406.05048.

[57] Khaled Said et al. DESI Peculiar Velocity Survey – Fundamental Plane. *arXiv e-prints*, art. arXiv:2408.13842, August 2024. doi: 10.48550/arXiv.2408.13842.

[58] Daniel Scolnic et al. The Hubble Tension in our own Backyard: DESI and the Nearness of the Coma Cluster. *arXiv e-prints*, art. arXiv:2409.14546, September 2024. doi: 10.48550/arXiv.2409.14546.

[59] William Sheu, Anowar J. Shajib, Tommaso Treu, Alessandro Sonnenfeld, Simon Birrer, Michele Cappellari, Lindsay J. Oldham, and Chin Yi Tan. Project Dinos II: Redshift evolution of dark and luminous matter density profiles in strong-lensing elliptical galaxies across $0.1 < z < 0.9$. *arXiv e-prints*, art. arXiv:2408.10316, August 2024. doi: 10.48550/arXiv.2408.10316.

[60] S. Birrer et al. TDCOSMO - IV. Hierarchical time-delay cosmography – joint inference of the Hubble constant and galaxy density profiles. *Astron. Astrophys.*, 643:A165, 2020. doi: 10.1051/0004-6361/202038861.

[61] Kenneth C. Wong et al. H0LiCOW – XIII. A 2.4 per cent measurement of H0 from lensed quasars: 5.3σ tension between early- and late-Universe probes. *Mon. Not. Roy. Astron. Soc.*, 498(1):1420–1439, 2020. doi: 10.1093/mnras/stz3094.

[62] Oliver H. E. Philcox and Mikhail M. Ivanov. BOSS DR12 full-shape cosmology: Λ CDM constraints from the large-scale galaxy power spectrum and bispectrum monopole. *Phys. Rev. D*, 105(4):043517, February 2022. doi: 10.1103/PhysRevD.105.043517.

[63] Alexandra Amon and George Efstathiou. A non-linear solution to the S_8 tension? *Mon. Not. Roy. Astron. Soc.*, 516(4):5355–5366, 2022. doi: 10.1093/mnras/stac2429.

[64] Giovanni Aricò, Raul E. Angulo, Matteo Zennaro, Sergio Contreras, Angela Chen, and Carlos Hernández-Monteagudo. DES Y3 cosmic shear down to small scales: constraints on cosmology and baryons. *Astron. Astrophys.*, 678:A109, 2023. doi: 10.1051/0004-6361/202346539.

[65] Alkistis Pourtsidou and Thomas Tram. Reconciling CMB and structure growth measurements with dark energy interactions. *Phys. Rev.*, D94(4):043518, 2016. doi: 10.1103/PhysRevD.94.043518.

[66] Nhat-Minh Nguyen, Dragan Huterer, and Yuewei Wen. Evidence for Suppression of Structure Growth in the Concordance Cosmological Model. *Phys. Rev. Lett.*, 131 (11):111001, 2023. doi: 10.1103/PhysRevLett.131.111001.

[67] Karim Carrion, Pedro Carrilho, Alessio Spurio Mancini, Alkistis Pourtsidou, and Juan Carlos Hidalgo. Dark Scattering: accelerated constraints from KiDS-1000 with `ReACT` and `CosmoPower`. *Mon. Not. Roy. Astron. Soc.*, 532(4):3914–3925, August 2024. doi: 10.1093/mnras/stae1663.

[68] Lavinia Heisenberg, Hector Villarrubia-Rojo, and Jann Zosso. Simultaneously solving the H0 and $\sigma 8$ tensions with late dark energy. *Phys. Dark Univ.*, 39:101163, 2023. doi: 10.1016/j.dark.2022.101163.

[69] S. Perlmutter et al. Measurements of Omega and Lambda from 42 high redshift supernovae. *Astrophys. J.*, 517:565–586, 1999. doi: 10.1086/307221.

[70] eBOSS Collaboration, Shadab Alam, et al. Completed SDSS-IV extended Baryon Oscillation Spectroscopic Survey: Cosmological implications from two decades of spectroscopic surveys at the Apache Point Observatory. *Phys. Rev. D*, 103(8): 083533, 2021. doi: 10.1103/PhysRevD.103.083533.

[71] Jerome Martin. Everything You Always Wanted To Know About The Cosmological Constant Problem (But Were Afraid To Ask). *Comptes Rendus Physique*, 13:566–665, 2012. doi: 10.1016/j.crhy.2012.04.008.

[72] Antonio Padilla. Lectures on the Cosmological Constant Problem, 2015.

[73] Steven Weinberg. The Cosmological Constant Problem. *Rev.Mod.Phys.*, 61:1–23, 1989. doi: 10.1103/RevModPhys.61.1.

[74] Christos Charmousis, Edmund J. Copeland, Antonio Padilla, and Paul M. Saffin. General second order scalar-tensor theory, self tuning, and the Fab Four. *Phys.Rev.Lett.*, 108:051101, 2012. doi: 10.1103/PhysRevLett.108.051101.

[75] Stephen Appleby and Eric V. Linder. The Well-Tempered Cosmological Constant: The Horndeski Variations. *JCAP*, 12:036, 2020. doi: 10.1088/1475-7516/2020/12/036.

[76] Daniel Sobral Blanco and Lucas Lombriser. Local self-tuning mechanism for the cosmological constant. *Phys. Rev. D*, 102(4):043506, 2020. doi: 10.1103/PhysRevD.102.043506.

[77] Arnaz Khan and Andy Taylor. A minimal self-tuning model to solve the cosmological constant problem. *JCAP*, 10:075, 2022. doi: 10.1088/1475-7516/2022/10/075.

[78] C. P. Burgess. Supersymmetric large extra dimensions and the cosmological constant: An Update. *Annals Phys.*, 313:283–401, 2004. doi: 10.1016/j.aop.2004.04.012.

[79] H. E. S. Velten, R. F. vom Marttens, and W. Zimdahl. Aspects of the cosmological "coincidence problem". *Eur. Phys. J. C*, 74(11):3160, 2014. doi: 10.1140/epjc/s10052-014-3160-4.

[80] Luca Amendola et al. Cosmology and fundamental physics with the Euclid satellite. *Living Reviews in Relativity*, 21(1):2, April 2018. doi: 10.1007/s41114-017-0010-3.

[81] Austin Joyce, Bhuvnesh Jain, Justin Khoury, and Mark Trodden. Beyond the Cosmological Standard Model. *Phys.Rept.*, 568:1–98, 2015. doi: 10.1016/j.physrep.2014.12.002.

[82] Dragan Huterer and Glenn Starkman. Parameterization of dark-energy properties: A Principal-component approach. *Phys. Rev. Lett.*, 90:031301, 2003. doi: 10.1103/PhysRevLett.90.031301.

[83] Francesca Gerardi, Matteo Martinelli, and Alessandra Silvestri. Reconstruction of the Dark Energy equation of state from latest data: the impact of theoretical priors. *JCAP*, 07:042, 2019. doi: 10.1088/1475-7516/2019/07/042.

[84] DESI Collaboration, R. Calderon, et al. DESI 2024: Reconstructing Dark Energy using Crossing Statistics with DESI DR1 BAO data. *arXiv e-prints*, art. arXiv:2405.04216, May 2024. doi: 10.48550/arXiv.2405.04216.

[85] Michel Chevallier and David Polarski. Accelerating universes with scaling dark matter. *Int. J. Mod. Phys. D*, 10:213–224, 2001. doi: 10.1142/S0218271801000822.

[86] Eric V. Linder. Exploring the expansion history of the universe. *Phys. Rev. Lett.*, 90:091301, 2003. doi: 10.1103/PhysRevLett.90.091301.

[87] Eric V. Linder. The Mirage of w=-1. *arXiv e-prints*, art. arXiv:0708.0024, August 2007. doi: 10.48550/arXiv.0708.0024.

[88] N. Suzuki et al. The Hubble Space Telescope Cluster Supernova Survey: V. Improving the Dark Energy Constraints Above z>1 and Building an Early-Type-Hosted Supernova Sample. *Astrophys. J.*, 746:85, 2012. doi: 10.1088/0004-637X/746/1/85.

[89] Planck Collaboration, N. Aghanim, et al. Planck 2018 results. VI. Cosmological parameters. *Astron. Astrophys.*, 641:A6, 2020. doi: 10.1051/0004-6361/201833910.

[90] DESI Collaboration, A. G. Adame, et al. DESI 2024 VI: Cosmological Constraints from the Measurements of Baryon Acoustic Oscillations. *arXiv e-prints*, art. arXiv:2404.03002, April 2024. doi: 10.48550/arXiv.2404.03002.

[91] DESI Collaboration, K. Lodha, et al. DESI 2024: Constraints on Physics-Focused Aspects of Dark Energy using DESI DR1 BAO Data. *arXiv e-prints*, art. arXiv:2405.13588, May 2024. doi: 10.48550/arXiv.2405.13588.

[92] C. Wetterich. Cosmology and the Fate of Dilatation Symmetry. *Nucl. Phys. B*, 302: 668–696, 1988. doi: 10.1016/0550-3213(88)90193-9.

[93] Robert J. Scherrer. Mapping the Chevallier-Polarski-Linder parametrization onto Physical Dark Energy Models. *Phys. Rev. D*, 92(4):043001, 2015. doi: 10.1103/PhysRevD.92.043001.

[94] Roland de Putter and Eric V. Linder. Calibrating Dark Energy. *JCAP*, 10:042, 2008. doi: 10.1088/1475-7516/2008/10/042.

[95] David J. E. Marsh, Philip Bull, Pedro G. Ferreira, and Andrew Pontzen. Quintessence in a quandary: Prior dependence in dark energy models. *Phys. Rev. D*, 90(10):105023, 2014. doi: 10.1103/PhysRevD.90.105023.

[96] William J. Wolf and Pedro G. Ferreira. Underdetermination of dark energy. *Phys. Rev. D*, 108(10):103519, 2023. doi: 10.1103/PhysRevD.108.103519.

[97] Minsu Park, Marco Raveri, and Bhuvnesh Jain. Reconstructing Quintessence. *Phys. Rev. D*, 103(10):103530, 2021. doi: 10.1103/PhysRevD.103.103530.

[98] Marco Raveri, Levon Pogosian, Matteo Martinelli, Kazuya Koyama, Alessandra Silvestri, and Gong-Bo Zhao. Principal reconstructed modes of dark energy and gravity. *JCAP*, 02:061, 2023. doi: 10.1088/1475-7516/2023/02/061.

[99] Pedro Carrilho, Chiara Moretti, and Alkistis Pourtsidou. Cosmology with the EFTofLSS and BOSS: dark energy constraints and a note on priors. *JCAP*, 2023 (1):028, January 2023. doi: 10.1088/1475-7516/2023/01/028.

[100] Emilio Bellini and Ignacy Sawicki. Maximal freedom at minimum cost: linear large-scale structure in general modifications of gravity. *JCAP*, 07:050, 2014. doi: 10.1088/1475-7516/2014/07/050.

[101] Joe Kennedy, Lucas Lombriser, and Andy Taylor. Reconstructing Horndeski models from the effective field theory of dark energy. *Phys. Rev.*, D96(8):084051, 2017. doi: 10.1103/PhysRevD.96.084051.

[102] Giulia Cusin, Matthew Lewandowski, and Filippo Vernizzi. Nonlinear Effective Theory of Dark Energy. *JCAP*, 04:061, 2018. doi: 10.1088/1475-7516/2018/04/061.

[103] Jérémie Francfort, Basundhara Ghosh, and Ruth Durrer. Cosmological Number Counts in Einstein and Jordan frames. *JCAP*, 09:071, 2019. doi: 10.1088/1475-7516/2019/09/071.

[104] Clifford M. Will. The Confrontation between General Relativity and Experiment. *Living Rev. Rel.*, 17:4, 2014. doi: 10.12942/lrr-2014-4.

[105] Justin Khoury and Mark Wyman. N-Body Simulations of DGP and Degravitation Theories. *Phys.Rev.*, D80:064023, 2009. doi: 10.1103/PhysRevD.80.064023.

[106] Clare Burrage and Jeremy Sakstein. Tests of Chameleon Gravity. *Living Rev. Rel.*, 21(1):1, 2018. doi: 10.1007/s41114-018-0011-x.

[107] G.R. Dvali, Gregory Gabadadze, and Massimo Porrati. 4-D gravity on a brane in 5-D Minkowski space. *Phys.Lett.*, B485:208–214, 2000. doi: 10.1016/S0370-2693(00)00669-9.

[108] Markus A. Luty, Massimo Porrati, and Riccardo Rattazzi. Strong interactions and stability in the DGP model. *JHEP*, 09:029, 2003. doi: 10.1088/1126-6708/2003/09/029.

[109] Wayne Hu and Ignacy Sawicki. Models of f(R) Cosmic Acceleration that Evade Solar-System Tests. *Phys.Rev.*, D76:064004, 2007. doi: 10.1103/PhysRevD.76.064004.

[110] Simone Peirone, Kazuya Koyama, Levon Pogosian, Marco Raveri, and Alessandra Silvestri. Large-scale structure phenomenology of viable Horndeski theories. *Phys. Rev. D*, 97(4):043519, 2018. doi: 10.1103/PhysRevD.97.043519.

[111] Luca Amendola, Martin Kunz, Mariele Motta, Ippocratis D. Saltas, and Ignacy Sawicki. Observables and unobservables in dark energy cosmologies. *Phys. Rev. D*, 87(2):023501, 2013. doi: 10.1103/PhysRevD.87.023501.

[112] Levon Pogosian and Alessandra Silvestri. What can cosmology tell us about gravity? Constraining Horndeski gravity with Σ and μ. *Phys. Rev. D*, 94(10):104014, 2016. doi: 10.1103/PhysRevD.94.104014.

[113] Levon Pogosian, Marco Raveri, Kazuya Koyama, Matteo Martinelli, Alessandra Silvestri, Gong-Bo Zhao, Jian Li, Simone Peirone, and Alex Zucca. Imprints of cosmological tensions in reconstructed gravity. *Nature Astron.*, 6(12):1484–1490, 2022. doi: 10.1038/s41550-022-01808-7.

[114] Fergus Simpson et al. CFHTLenS: Testing the Laws of Gravity with Tomographic Weak Lensing and Redshift Space Distortions. *Mon. Not. Roy. Astron. Soc.*, 429: 2249, 2013. doi: 10.1093/mnras/sts493.

[115] DES Collaboration, T. M. C. Abbott, et al. Dark Energy Survey Year 3 results: Constraints on extensions to ΛCDM with weak lensing and galaxy clustering. *Phys. Rev. D*, 107(8):083504, 2023. doi: 10.1103/PhysRevD.107.083504.

[116] Super-Kamiokande Collaboration, Y. Fukuda, et al. Evidence for oscillation of atmospheric neutrinos. *Phys. Rev. Lett.*, 81:1562–1567, 1998. doi: 10.1103/PhysRevLett.81.1562.

[117] SNO Collaboration, Q. R. Ahmad, et al. Direct evidence for neutrino flavor transformation from neutral current interactions in the Sudbury Neutrino Observatory. *Phys. Rev. Lett.*, 89:011301, 2002. doi: 10.1103/PhysRevLett.89.011301.

[118] M. C. Gonzalez-Garcia, Michele Maltoni, and Thomas Schwetz. Updated fit to three neutrino mixing: status of leptonic CP violation. *JHEP*, 11:052, 2014. doi: 10.1007/JHEP11(2014)052.

[119] Ivan Esteban, M. C. Gonzalez-Garcia, Michele Maltoni, Thomas Schwetz, and Albert Zhou. The fate of hints: updated global analysis of three-flavor neutrino oscillations. *JHEP*, 09:178, 2020. doi: 10.1007/JHEP09(2020)178.

[120] KATRIN Collaboration, M. Aker, et al. Improved Upper Limit on the Neutrino Mass from a Direct Kinematic Method by KATRIN. *Phys. Rev. Lett.*, 123(22): 221802, 2019. doi: 10.1103/PhysRevLett.123.221802.

[121] KATRIN Collaboration, M. Aker, et al. Direct neutrino-mass measurement with sub-electronvolt sensitivity. *Nature Phys.*, 18(2):160–166, 2022. doi: 10.1038/s41567-021-01463-1.

[122] Maria Archidiacono, Thejs Brinckmann, Julien Lesgourgues, and Vivian Poulin. Physical effects involved in the measurements of neutrino masses with future cosmological data. *JCAP*, 02:052, 2017. doi: 10.1088/1475-7516/2017/02/052.

[123] Mikhail M. Ivanov, Marko Simonović, and Matias Zaldarriaga. Cosmological Parameters and Neutrino Masses from the Final Planck and Full-Shape BOSS Data. *Phys. Rev. D*, 101(8):083504, 2020. doi: 10.1103/PhysRevD.101.083504.

[124] Jack J. Bennett, Gilles Buldgen, Pablo F. De Salas, Marco Drewes, Stefano Gariazzo, Sergio Pastor, and Yvonne Y. Y. Wong. Towards a precision calculation of $N_{\rm eff}$ in the Standard Model II: Neutrino decoupling in the presence of flavour oscillations and finite-temperature QED. *JCAP*, 04:073, 2021. doi: 10.1088/1475-7516/2021/04/073.

[125] Masatoshi Shoji and Eiichiro Komatsu. Massive Neutrinos in Cosmology: Analytic Solutions and Fluid Approximation. *Phys. Rev. D*, 81:123516, 2010. doi: 10.1103/PhysRevD.81.123516. [Erratum: Phys.Rev.D 82, 089901 (2010)].

[126] Julien Lesgourgues and Sergio Pastor. Neutrino mass from Cosmology. *Adv. High Energy Phys.*, 2012:608515, 2012. doi: 10.1155/2012/608515.

[127] DES Collaboration, T. M. C. Abbott, et al. Dark Energy Survey Year 3 results: Cosmological constraints from galaxy clustering and weak lensing. *Phys. Rev. D*, 105(2):023520, 2022. doi: 10.1103/PhysRevD.105.023520.

[128] Arthur Loureiro et al. Cosmological measurements from angular power spectra analysis of BOSS DR12 tomography. *Mon. Not. Roy. Astron. Soc.*, 485(1):326–355, 2019. doi: 10.1093/mnras/stz191.

[129] H. Hildebrandt et al. KiDS+VIKING-450: Cosmic shear tomography with optical and infrared data. *Astron. Astrophys.*, 633:A69, 2020. doi: 10.1051/0004-6361/201834878.

[130] Benjamin Bose, Matteo Cataneo, Tilman Tröster, Qianli Xia, Catherine Heymans, and Lucas Lombriser. On the road to per cent accuracy IV: ReACT – computing the non-linear power spectrum beyond ΛCDM. *Mon. Not. Roy. Astron. Soc.*, 498 (4):4650–4662, 2020. doi: 10.1093/mnras/staa2696.

[131] Emanuele Castorina, Carmelita Carbone, Julien Bel, Emiliano Sefusatti, and Klaus Dolag. DEMNUni: the clustering of large-scale structures in the presence of massive neutrinos. *JCAP*, 2015(7):043–043, July 2015. doi: 10.1088/1475-7516/2015/07/043.

[132] Matteo Zennaro, Julien Bel, Francisco Villaescusa-Navarro, Carmelita Carbone, Emiliano Sefusatti, and Luigi Guzzo. Initial Conditions for Accurate N-Body Simulations of Massive Neutrino Cosmologies. *Mon. Not. Roy. Astron. Soc.*, 466 (3):3244–3258, 2017. doi: 10.1093/mnras/stw3340.

[133] Giovanni Aricò, Raul E. Angulo, and Matteo Zennaro. Accelerating Large-Scale-Structure data analyses by emulating Boltzmann solvers and Lagrangian Perturbation Theory. *arXiv e-prints*, art. arXiv:2104.14568, April 2021. doi: 10.48550/arXiv.2104.14568.

[134] Simeon Bird, Matteo Viel, and Martin G. Haehnelt. Massive Neutrinos and the Non-linear Matter Power Spectrum. *Mon. Not. Roy. Astron. Soc.*, 420:2551–2561, 2012. doi: 10.1111/j.1365-2966.2011.20222.x.

[135] Steen Hannestad, Amol Upadhye, and Yvonne Y. Y. Wong. Spoon or slide? The non-linear matter power spectrum in the presence of massive neutrinos. *JCAP*, 11: 062, 2020. doi: 10.1088/1475-7516/2020/11/062.

[136] Arthur Loureiro et al. On The Upper Bound of Neutrino Masses from Combined Cosmological Observations and Particle Physics Experiments. *Phys. Rev. Lett.*, 123 (8):081301, 2019. doi: 10.1103/PhysRevLett.123.081301.

[137] Euclid Collaboration, J. Adamek, et al. Euclid: Modelling massive neutrinos in cosmology – a code comparison. *JCAP*, 06:035, 2023. doi: 10.1088/1475-7516/2023/06/035.

[138] Julian Adamek, Ruth Durrer, and Martin Kunz. Relativistic N-body simulations with massive neutrinos. *JCAP*, 11:004, 2017. doi: 10.1088/1475-7516/2017/11/004.

[139] Matteo Zennaro, Raúl E. Angulo, Giovanni Aricò, Sergio Contreras, and Marcos Pellejero-Ibáñez. How to add massive neutrinos to your ΛCDM simulation - extending cosmology rescaling algorithms. *Mon. Not. Roy. Astron. Soc.*, 489(4): 5938–5951, 2019. doi: 10.1093/mnras/stz2612.

[140] Nick Kaiser. Clustering in real space and in redshift space. *Mon. Not. Roy. Astron. Soc.*, 227:1–21, July 1987. doi: 10.1093/mnras/227.1.1.

[141] Andreas A. Berlind and David H. Weinberg. The Halo occupation distribution: Towards an empirical determination of the relation between galaxies and mass. *Astrophys. J.*, 575:587–616, 2002. doi: 10.1086/341469.

[142] Risa H. Wechsler and Jeremy L. Tinker. The Connection between Galaxies and their Dark Matter Halos. *Ann. Rev. Astron. Astrophys.*, 56:435–487, 2018. doi: 10.1146/annurev-astro-081817-051756.

[143] Ya. B. Zeldovich. Particle production in cosmology. *Pisma Zh. Eksp. Teor. Fiz.*, 12:443–447, 1970.

[144] Takahiko Matsubara. Nonlinear Perturbation Theory Integrated with Nonlocal Bias, Redshift-space Distortions, and Primordial Non-Gaussianity. *Phys. Rev. D*, 83: 083518, 2011. doi: 10.1103/PhysRevD.83.083518.

[145] Vincent Desjacques, Donghui Jeong, and Fabian Schmidt. Large-scale galaxy bias. *Phys. Rept.*, 733:1–193, February 2018. doi: 10.1016/j.physrep.2017.12.002.

[146] Jaiyul Yoo and Vincent Desjacques. All-Sky Analysis of the General Relativistic Galaxy Power Spectrum. *Phys. Rev. D*, 88(2):023502, 2013. doi: 10.1103/PhysRevD.88.023502.

[147] Leonardo Senatore and Matias Zaldarriaga. Redshift Space Distortions in the Effective Field Theory of Large Scale Structures. *arXiv e-prints*, art. arXiv:1409.1225, September 2014.

[148] Daniel Baumann, Alberto Nicolis, Leonardo Senatore, and Matias Zaldarriaga. Cosmological non-linearities as an effective fluid. *JCAP*, 2012(7):051, July 2012. doi: 10.1088/1475-7516/2012/07/051.

[149] John Joseph M. Carrasco, Mark P. Hertzberg, and Leonardo Senatore. The effective field theory of cosmological large scale structures. *Journal of High Energy Physics*, 2012:82, September 2012. doi: 10.1007/JHEP09(2012)082.

[150] Anton Chudaykin, Mikhail M. Ivanov, Oliver H. E. Philcox, and Marko Simonović. Nonlinear perturbation theory extension of the Boltzmann code CLASS. *Phys. Rev. D*, 102(6):063533, September 2020. doi: 10.1103/PhysRevD.102.063533.

[151] Mikhail M. Ivanov, Oliver H. E. Philcox, Takahiro Nishimichi, Marko Simonović, Masahiro Takada, and Matias Zaldarriaga. Precision analysis of the redshift-space galaxy bispectrum. *Phys. Rev. D*, 105(6):063512, March 2022. doi: 10.1103/PhysRevD.105.063512.

[152] Guido d'Amico, Jérôme Gleyzes, Nickolas Kokron, Katarina Markovic, Leonardo Senatore, Pierre Zhang, Florian Beutler, and Héctor Gil-Marín. The cosmological analysis of the SDSS/BOSS data from the Effective Field Theory of Large-Scale Structure. *JCAP*, 2020(5):005, May 2020. doi: 10.1088/1475-7516/2020/05/005.

[153] Chiara Moretti, Maria Tsedrik, Pedro Carrilho, and Alkistis Pourtsidou. Modified gravity and massive neutrinos: constraints from the full shape analysis of BOSS galaxies and forecasts for Stage IV surveys. *JCAP*, 12:025, 2023. doi: 10.1088/1475-7516/2023/12/025.

[154] Théo Simon, Pierre Zhang, Vivian Poulin, and Tristan L. Smith. On the consistency of effective field theory analyses of BOSS power spectrum. *arXiv e-prints*, art. arXiv:2208.05929, August 2022. doi: 10.48550/arXiv.2208.05929.

[155] Euclid Collaboration, B. Bose, et al. Euclid preparation. Modelling spectroscopic clustering on mildly nonlinear scales in beyond-ΛCDM models. *arXiv e-prints*, art. arXiv:2311.13529, November 2023. doi: 10.48550/arXiv.2311.13529.

[156] Shi-Fan Chen, Zvonimir Vlah, and Martin White. Consistent Modeling of Velocity Statistics and Redshift-Space Distortions in One-Loop Perturbation Theory. *JCAP*, 07:062, 2020. doi: 10.1088/1475-7516/2020/07/062.

[157] Shi-Fan Chen, Zvonimir Vlah, Emanuele Castorina, and Martin White. Redshift-Space Distortions in Lagrangian Perturbation Theory. *JCAP*, 03:100, 2021. doi: 10.1088/1475-7516/2021/03/100.

[158] Joseph E. McEwen, Xiao Fang, Christopher M. Hirata, and Jonathan A. Blazek. FAST-PT: a novel algorithm to calculate convolution integrals in cosmological perturbation theory. *JCAP*, 2016(9):015, September 2016. doi: 10.1088/1475-7516/2016/09/015.

[159] Xiao Fang, Jonathan A. Blazek, Joseph E. McEwen, and Christopher M. Hirata. FAST-PT II: an algorithm to calculate convolution integrals of general tensor quantities in cosmological perturbation theory. *JCAP*, 2017(2):030, February 2017. doi: 10.1088/1475-7516/2017/02/030.

[160] Marko Simonović, Tobias Baldauf, Matias Zaldarriaga, John Joseph Carrasco, and Juna A. Kollmeier. Cosmological perturbation theory using the FFTLog: formalism and connection to QFT loop integrals. *JCAP*, 04:030, 2018. doi: 10.1088/1475-7516/2018/04/030.

[161] Roman Scoccimarro and H. M. P. Couchman. A fitting formula for the nonlinear evolution of the bispectrum. *Mon. Not. Roy. Astron. Soc.*, 325:1312, 2001. doi: 10.1046/j.1365-8711.2001.04281.x.

[162] Hume A. Feldman, Nick Kaiser, and John A. Peacock. Power spectrum analysis of three-dimensional redshift surveys. *Astrophys. J.*, 426:23–37, 1994. doi: 10.1086/174036.

[163] Davide Bianchi, Héctor Gil-Marín, Rossana Ruggeri, and Will J. Percival. Measuring line-of-sight dependent Fourier-space clustering using FFTs. *Mon. Not. Roy. Astron. Soc.*, 453(1):L11–L15, 2015. doi: 10.1093/mnrasl/slv090.

[164] Roman Scoccimarro. Fast Estimators for Redshift-Space Clustering. *Phys. Rev. D*, 92(8):083532, 2015. doi: 10.1103/PhysRevD.92.083532.

[165] Florian Beutler, Shun Saito, Hee-Jong Seo, Jon Brinkmann, Kyle S. Dawson, Daniel J. Eisenstein, Andreu Font-Ribera, Shirley Ho, Cameron K. McBride, Francesco Montesano, Will J. Percival, Ashley J. Ross, Nicholas P. Ross, Lado Samushia, David J. Schlegel, Ariel G. Sánchez, Jeremy L. Tinker, and Benjamin A. Weaver. The clustering of galaxies in the SDSS-III Baryon Oscillation Spectroscopic Survey: testing gravity with redshift space distortions using the power spectrum multipoles. *Mon. Not. Roy. Astron. Soc.*, 443(2):1065–1089, September 2014. doi: 10.1093/mnras/stu1051.

[166] M. J. Wilson, J. A. Peacock, A. N. Taylor, and S. de la Torre. Rapid modelling of the redshift-space power spectrum multipoles for a masked density field. *Mon. Not. Roy. Astron. Soc.*, 464(3):3121–3130, 2017. doi: 10.1093/mnras/stw2576.

[167] Kevin Pardede, Federico Rizzo, Matteo Biagetti, Emanuele Castorina, Emiliano Sefusatti, and Pierluigi Monaco. Bispectrum-window convolution via Hankel transform. *JCAP*, 10:066, 2022. doi: 10.1088/1475-7516/2022/10/066.

[168] Oliver H. E. Philcox. Cosmology without window functions: Quadratic estimators for the galaxy power spectrum. *Phys. Rev. D*, 103(10):103504, May 2021. doi: 10.1103/PhysRevD.103.103504.

[169] Oliver H. E. Philcox. Cosmology without window functions. II. Cubic estimators for the galaxy bispectrum. *Phys. Rev. D*, 104(12):123529, December 2021. doi: 10.1103/PhysRevD.104.123529.

[170] Oliver H. E. Philcox and Thomas Flöss. PolyBin3D: A Suite of Optimal and Efficient Power Spectrum and Bispectrum Estimators for Large-Scale Structure. *arXiv e-prints*, art. arXiv:2404.07249, April 2024. doi: 10.48550/arXiv.2404.07249.

[171] C. Alcock and B. Paczynski. An evolution free test for non-zero cosmological constant. *Nature*, 281:358, October 1979. doi: 10.1038/281358a0.

[172] BOSS Collaboration, Éric Aubourg, et al. Cosmological implications of baryon acoustic oscillation measurements. *Phys. Rev. D*, 92(12):123516, 2015. doi: 10.1103/PhysRevD.92.123516.

[173] R. E. Griffiths, S. Casertano, M. Im, and K. U. Ratnatunga. Weak gravitational lensing around field galaxies in Hubble Space Telescope survey images. *Month. Not.of the Roy. Astr. Soc.*, 282(4):1159–1163, 10 1996. ISSN 0035-8711. doi: 10.1093/mnras/282.4.1159.

[174] Planck Collaboration, N. Aghanim, et al. Planck 2018 results. VIII. Gravitational lensing. *Astron. Astrophys.*, 641:A8, September 2020. doi: 10.1051/0004-6361/201833886.

[175] Martin Kilbinger. Cosmology with cosmic shear observations: a review. *Reports on Progress in Physics*, 78(8):086901, July 2015. doi: 10.1088/0034-4885/78/8/086901.

[176] Matthias Bartelmann and Matteo Maturi. Weak gravitational lensing. *Scholarpedia*, 12(1):32440, January 2017. doi: 10.4249/scholarpedia.32440.

[177] Rachel Mandelbaum. Weak lensing for precision cosmology. *Ann. Rev. Astron. Astrophys.*, 56:393–433, 2018. doi: 10.1146/annurev-astro-081817-051928.

[178] Wayne Hu. Weak lensing of the CMB: A harmonic approach. *Phys. Rev. D*, 62: 043007, 2000. doi: 10.1103/PhysRevD.62.043007.

[179] Martin Kilbinger et al. Precision calculations of the cosmic shear power spectrum projection. *Mon. Not. Roy. Astron. Soc.*, 472(2):2126–2141, 2017. doi: 10.1093/mnras/stx2082.

[180] Marilena LoVerde and Niayesh Afshordi. Extended Limber Approximation. *Phys. Rev. D*, 78:123506, 2008. doi: 10.1103/PhysRevD.78.123506.

[181] LSST Dark Energy Science Collaboration, C. D. Leonard, et al. The N5K Challenge: Non-Limber Integration for LSST Cosmology. *Open Journal of Astrophysics*, 6:1, 2023. doi: 10.21105/astro.2212.04291.

[182] William R. Coulton, Jia Liu, Mathew S. Madhavacheril, Vanessa Böhm, and David N. Spergel. Constraining Neutrino Mass with the Tomographic Weak Lensing Bispectrum. *JCAP*, 05:043, 2019. doi: 10.1088/1475-7516/2019/05/043.

[183] Gary Steigman. Primordial Nucleosynthesis in the Precision Cosmology Era. *Ann. Rev. Nucl. Part. Sci.*, 57:463–491, 2007. doi: 10.1146/annurev.nucl.56.080805.140437.

[184] Erik Aver, Keith A. Olive, and Evan D. Skillman. The effects of He I λ10830 on helium abundance determinations. *JCAP*, 07:011, 2015. doi: 10.1088/1475-7516/2015/07/011.

[185] Ryan J. Cooke, Max Pettini, and Charles C. Steidel. One Percent Determination of the Primordial Deuterium Abundance. *Astrophys. J.*, 855(2):102, 2018. doi: 10.3847/1538-4357/aaab53.

[186] BOSS Collaboration, Shadab Alam, et al. The clustering of galaxies in the completed SDSS-III Baryon Oscillation Spectroscopic Survey: cosmological analysis of the DR12 galaxy sample. *Mon. Not. Roy. Astron. Soc.*, 470(3):2617–2652, 2017. doi: 10.1093/mnras/stx721.

[187] DESI Collaboration, A. Aghamousa, et al. The DESI Experiment Part I: Science,Targeting, and Survey Design. *arXiv e-prints*, art. arXiv:1611.00036, October 2016. doi: 10.48550/arXiv.1611.00036.

[188] Y. Mellier et al. Euclid. I. Overview of the Euclid mission. *arXiv e-prints*, art. arXiv:2405.13491, May 2024. doi: 10.48550/arXiv.2405.13491.

[189] David J. C. Mackay. *Information Theory, Inference and Learning Algorithms.* Cambridge University Press, 2003.

[190] Roberto Trotta. Bayesian Methods in Cosmology. *arXiv e-prints*, art. arXiv:1701.01467, January 2017. doi: 10.48550/arXiv.1701.01467.

[191] T. Bayes. An essay towards solving a problem in the doctrine of chances. *Phil. Trans. of the Royal Soc. of London*, 53:370–418, 1763.

[192] Max Tegmark, Andy Taylor, and Alan Heavens. Karhunen-Loeve eigenvalue problems in cosmology: How should we tackle large data sets? *Astrophys. J.*, 480:22, 1997. doi: 10.1086/303939.

[193] Max Tegmark. Measuring Cosmological Parameters with Galaxy Surveys. *Phys. Rev. Lett.*, 79(20):3806–3809, November 1997. doi: 10.1103/PhysRevLett.79.3806.

[194] M.G. Kendall and A. Stuart. *The Advanced Theory of Statistics. Vol. 2: Inference and: Relationsship*. Griffin, 1973.

[195] F. James and M. Roos. Minuit: A System for Function Minimization and Analysis of the Parameter Errors and Correlations. *Comput. Phys. Commun.*, 10:343–367, 1975. doi: 10.1016/0010-4655(75)90039-9.

[196] Tanvi Karwal, Yashvi Patel, Alexa Bartlett, Vivian Poulin, Tristan L. Smith, and Daniel N. Pfeffer. Procoli: Profiles of cosmological likelihoods. *arXiv e-prints*, art. arXiv:2401.14225, January 2024. doi: 10.48550/arXiv.2401.14225.

[197] Emil Brinch Holm, Laura Herold, Théo Simon, Elisa G. M. Ferreira, Steen Hannestad, Vivian Poulin, and Thomas Tram. Bayesian and frequentist investigation of prior effects in EFT of LSS analyses of full-shape BOSS and eBOSS data. *Phys. Rev. D*, 108(12):123514, 2023. doi: 10.1103/PhysRevD.108.123514.

[198] Andreas Nygaard, Emil Brinch Holm, Steen Hannestad, and Thomas Tram. Fast and effortless computation of profile likelihoods using CONNECT. *JCAP*, 11:064, 2023. doi: 10.1088/1475-7516/2023/11/064.

[199] A. N. Taylor and T. D. Kitching. Analytic Methods for Cosmological Likelihoods. *Mon. Not. Roy. Astron. Soc.*, 408:865, 2010. doi: 10.1111/j.1365-2966.2010.17201.x.

[200] Boryana Hadzhiyska, Kevin Wolz, Susanna Azzoni, David Alonso, Carlos García-García, Jaime Ruiz-Zapatero, and Anže Slosar. Cosmology with 6 parameters in the Stage-IV era: efficient marginalisation over nuisance parameters. *The Open Journal of Astrophysics*, 6:23, July 2023. doi: 10.21105/astro.2301.11895.

[201] H. Jeffreys. *Theory of Probability*. International series of monographs on physics. Clarendon Press, 1998. ISBN 9780198503682.

[202] Michael Bartholomew-Biggs, Steven Brown, Bruce Christianson, and Laurence Dixon. Automatic differentiation of algorithms. *Journal of Computational and Applied Mathematics*, 124(1):171–190, 2000. ISSN 0377-0427. doi: https://doi.org/10.1016/S0377-0427(00)00422-2. Numerical Analysis 2000. Vol. IV: Optimization and Nonlinear Equations.

[203] Guido D'Amico, Leonardo Senatore, and Pierre Zhang. Limits on wCDM from the EFTofLSS with the PyBird code. *JCAP*, 2021(1):006, January 2021. doi: 10.1088/1475-7516/2021/01/006.

[204] Mikhail M. Ivanov, Carolina Cuesta-Lazaro, Siddharth Mishra-Sharma, Andrej Obuljen, and Michael W. Toomey. Full-shape analysis with simulation-based priors: constraints on single field inflation from BOSS. *arXiv e-prints*, art. arXiv:2402.13310, February 2024. doi: 10.48550/arXiv.2402.13310.

[205] Hanyu Zhang, Marco Bonici, Guido D'Amico, Simone Paradiso, and Will J. Percival. HOD-informed prior for EFT-based full-shape analyses of LSS. *arXiv e-prints*, art. arXiv:2409.12937, September 2024. doi: 10.48550/arXiv.2409.12937.

[206] Andresa Campos, Simon Samuroff, and Rachel Mandelbaum. An empirical approach to model selection: weak lensing and intrinsic alignments. *Mon. Not. Roy. Astron. Soc.*, 525(2):1885–1901, 2023. doi: 10.1093/mnras/stad2213.

[207] B. Joachimi et al. KiDS-1000 methodology: Modelling and inference for joint weak gravitational lensing and spectroscopic galaxy clustering analysis. *Astron. Astrophys.*, 646:A129, 2021. doi: 10.1051/0004-6361/202038831.

[208] P. R. V. Chintalapati, G. Gutierrez, and M. H. L. S. Wang. Systematic study of projection biases in weak lensing analysis. *Phys. Rev. D*, 105(4):043515, 2022. doi: 10.1103/PhysRevD.105.043515.

[209] P. R. V. Chintalapati, G. Gutierrez, and M. H. L. S. Wang. A systematic study of projection biases in the Weak Lensing analysis of cosmic shear and the combination of galaxy clustering and galaxy-galaxy lensing. *arXiv e-prints*, art. arXiv:2403.08101, March 2024. doi: 10.48550/arXiv.2403.08101.

[210] Daniel Foreman-Mackey, David W. Hogg, Dustin Lang, and Jonathan Goodman. emcee: The MCMC Hammer. *Publ. Astron. Soc. Pac.*, 125(925):306, March 2013. doi: 10.1086/670067.

[211] Minas Karamanis, Florian Beutler, John A. Peacock, David Nabergoj, and Uros Seljak. Accelerating astronomical and cosmological inference with preconditioned Monte Carlo. *Mon. Not. Roy. Astron. Soc.*, 516(2):1644–1653, 2022. doi: 10.1093/mnras/stac2272.

[212] Johannes U. Lange. nautilus: boosting Bayesian importance nested sampling with deep learning. *Mon. Not. Roy. Astron. Soc.*, 525(2):3181–3194, 2023. doi: 10.1093/mnras/stad2441.

[213] Joshua S. Speagle. dynesty: a dynamic nested sampling package for estimating Bayesian posteriors and evidences. *Mon. Not. Roy. Astron. Soc.*, 493(3):3132–3158, 2020. doi: 10.1093/mnras/staa278.

[214] W. J. Handley, M. P. Hobson, and A. N. Lasenby. PolyChord: nested sampling for cosmology. *Mon. Not. Roy. Astron. Soc.*, 450(1):L61–L65, 2015. doi: 10.1093/mnrasl/slv047.

[215] Andrew Gelman and Donald B. Rubin. Inference from Iterative Simulation Using Multiple Sequences. *Statist. Sci.*, 7:457–472, 1992. doi: 10.1214/ss/1177011136.

[216] Nicholas Metropolis, Arianna W. Rosenbluth, Marshall N. Rosenbluth, Augusta H. Teller, and Edward Teller. Equation of State Calculations by Fast Computing Machines. *Journal of Chemical Physics*, 21(6):1087–1092, June 1953. doi: 10.1063/1.1699114.

[217] W. K. Hastings. Monte Carlo Sampling Methods using Markov Chains and their Applications. *Biometrika*, 57(1):97–109, April 1970. doi: 10.1093/biomet/57.1.97.

[218] Antony Lewis and Sarah Bridle. Cosmological parameters from CMB and other data: A Monte Carlo approach. *Phys. Rev.*, D66:103511, 2002. doi: 10.1103/PhysRevD.66.103511.

[219] Jonathan Goodman and Jonathan Weare. Ensemble samplers with affine invariance. *Communications in Applied Mathematics and Computational Science*, 5(1):65–80, January 2010. doi: 10.2140/camcos.2010.5.65.

[220] Jun Liu and Rong Chen. Sequential monte carlo methods for dynamic systems. *Journal of the American Statistical Association*, 93, 04 1998. doi: 10.1080/01621459.1998.10473765.

[221] Minas Karamanis, David Nabergoj, Florian Beutler, John A. Peacock, and Uros Seljak. pocoMC: A Python package for accelerated Bayesian inference in astronomy and cosmology. *J. Open Source Softw.*, 7(79):4634, 2022. doi: 10.21105/joss.04634.

[222] John Skilling. Skilling, j.: Nested sampling for general bayesian computation. bayesian anal. 1(4), 833-860. *Bayesian Analysis*, 1:833–860, 12 2006. doi: 10.1214/06-BA127.

[223] Greg Ashton et al. Nested sampling for physical scientists. *Nature*, 2, 2022. doi: 10.1038/s43586-022-00121-x.

[224] F. Feroz, M. P. Hobson, and M. Bridges. MultiNest: an efficient and robust Bayesian inference tool for cosmology and particle physics. *Mon. Not. Roy. Astron. Soc.*, 398:1601–1614, 2009. doi: 10.1111/j.1365-2966.2009.14548.x.

[225] A. Pourtsidou, C. Skordis, and E. J. Copeland. Models of dark matter coupled to dark energy. *Phys. Rev. D*, 88(8):083505, October 2013. doi: 10.1103/PhysRevD.88.083505.

[226] Nicola Tamanini. Phenomenological models of dark energy interacting with dark matter. *Phys. Rev. D*, 92(4):043524, August 2015. doi: 10.1103/PhysRevD.92.043524.

[227] Ryotaro Kase and Shinji Tsujikawa. Weak cosmic growth in coupled dark energy with a Lagrangian formulation. *Physics Letters B*, 804:135400, May 2020. doi: 10.1016/j.physletb.2020.135400.

[228] Jussi Väliviita, Elisabetta Majerotto, and Roy Maartens. Large-scale instability in interacting dark energy and dark matter fluids. *JCAP*, 2008(7):020, July 2008. doi: 10.1088/1475-7516/2008/07/020.

[229] Fergus Simpson. Scattering of dark matter and dark energy. *Phys. Rev. D*, 82(8):083505, October 2010. doi: 10.1103/PhysRevD.82.083505.

[230] Alkistis Pourtsidou and Thomas Tram. Reconciling CMB and structure growth measurements with dark energy interactions. *Phys. Rev. D*, 94(4):043518, August 2016. doi: 10.1103/PhysRevD.94.043518.

[231] A. Spurio Mancini and A. Pourtsidou. KiDS-1000 cosmology: machine learning - accelerated constraints on interacting dark energy with COSMOPOWER. *Mon. Not. Roy. Astron. Soc.*, 512(1):L44–L48, May 2022. doi: 10.1093/mnrasl/slac019.

[232] Diego Blas, Julien Lesgourgues, and Thomas Tram. The Cosmic Linear Anisotropy Solving System (CLASS). Part II: Approximation schemes. *JCAP*, 2011(7):034, July 2011. doi: 10.1088/1475-7516/2011/07/034.

[233] C. Skordis, A. Pourtsidou, and E. J. Copeland. Parametrized post-Friedmannian framework for interacting dark energy theories. *Phys. Rev. D*, 91(8):083537, April 2015. doi: 10.1103/PhysRevD.91.083537.

[234] Marco Baldi and Fergus Simpson. Structure formation simulations with momentum exchange: alleviating tensions between high-redshift and low-redshift cosmological probes. *Mon. Not. Roy. Astron. Soc.*, 465(1):653–666, February 2017. doi: 10.1093/mnras/stw2702.

[235] Martín Crocce and Román Scoccimarro. Nonlinear evolution of baryon acoustic oscillations. *Phys. Rev. D*, 77(2):023533, January 2008. doi: 10.1103/PhysRevD.77.023533.

[236] Leonardo Senatore and Matias Zaldarriaga. The IR-resummed Effective Field Theory of Large Scale Structures. *JCAP*, 2015(2):013–013, February 2015. doi: 10.1088/1475-7516/2015/02/013.

[237] Zvonimir Vlah, Martin White, and Alejandro Aviles. A Lagrangian effective field theory. *JCAP*, 2015(9):014–014, September 2015. doi: 10.1088/1475-7516/2015/09/014.

[238] Tobias Baldauf, Lorenzo Mercolli, Mehrdad Mirbabayi, and Enrico Pajer. The bispectrum in the Effective Field Theory of Large Scale Structure. *JCAP*, 2015(5):007, May 2015. doi: 10.1088/1475-7516/2015/05/007.

[239] Ashley Perko, Leonardo Senatore, Elise Jennings, and Risa H. Wechsler. Biased Tracers in Redshift Space in the EFT of Large-Scale Structure. *arXiv e-prints*, art. arXiv:1610.09321, October 2016. doi: 10.48550/arXiv.1610.09321.

[240] Zvonimir Vlah and Martin White. Exploring redshift-space distortions in large-scale structure. *JCAP*, 2019(3):007, March 2019. doi: 10.1088/1475-7516/2019/03/007.

[241] Guido D'Amico, Yaniv Donath, Matthew Lewandowski, Leonardo Senatore, and Pierre Zhang. The BOSS bispectrum analysis at one loop from the Effective Field Theory of Large-Scale Structure. *arXiv e-prints*, art. arXiv:2206.08327, June 2022.

[242] J. N. Fry and Enrique Gaztanaga. Biasing and Hierarchical Statistics in Large-Scale Structure. *Astrophys. J.*, 413:447, August 1993. doi: 10.1086/173015.

[243] Kwan Chuen Chan, Román Scoccimarro, and Ravi K. Sheth. Gravity and large-scale nonlocal bias. *Phys. Rev. D*, 85(8):083509, April 2012. doi: 10.1103/PhysRevD.85.083509.

[244] Tobias Baldauf, Uroš Seljak, Vincent Desjacques, and Patrick McDonald. Evidence for quadratic tidal tensor bias from the halo bispectrum. *Phys. Rev. D*, 86(8):083540, October 2012. doi: 10.1103/PhysRevD.86.083540.

[245] Patrick McDonald and Arabindo Roy. Clustering of dark matter tracers: generalizing bias for the coming era of precision LSS. *JCAP*, 2009(8):020, August 2009. doi: 10.1088/1475-7516/2009/08/020.

[246] Uroš Seljak, Nico Hamaus, and Vincent Desjacques. How to Suppress the Shot Noise in Galaxy Surveys. *Phys. Rev. Lett.*, 103(9):091303, August 2009. doi: 10.1103/PhysRevLett.103.091303.

[247] Kerstin Paech, Nico Hamaus, Ben Hoyle, Matteo Costanzi, Tommaso Giannantonio, Steffen Hagstotz, Georg Sauerwein, and Jochen Weller. Cross-correlation of galaxies and galaxy clusters in the Sloan Digital Sky Survey and the importance of non-Poissonian shot noise. *Mon. Not. Roy. Astron. Soc.*, 470(3):2566–2577, September 2017. doi: 10.1093/mnras/stx1354.

[248] Tobias Baldauf, Uroš Seljak, Robert E. Smith, Nico Hamaus, and Vincent Desjacques. Halo stochasticity from exclusion and nonlinear clustering. *Phys. Rev. D*, 88(8):083507, October 2013. doi: 10.1103/PhysRevD.88.083507.

[249] Alexander Eggemeier, Román Scoccimarro, Martin Crocce, Andrea Pezzotta, and Ariel G. Sánchez. Testing one-loop galaxy bias: Power spectrum. *Phys. Rev. D*, 102(10):103530, November 2020. doi: 10.1103/PhysRevD.102.103530.

[250] Valentin Assassi, Daniel Baumann, Daniel Green, and Matias Zaldarriaga. Renormalized halo bias. *JCAP*, 2014(8):056–056, August 2014. doi: 10.1088/1475-7516/2014/08/056.

[251] Tomohiro Fujita and Zvonimir Vlah. Perturbative description of biased tracers using consistency relations of LSS. *JCAP*, 2020(10):059, October 2020. doi: 10.1088/1475-7516/2020/10/059.

[252] G. D'Amico, M. Marinucci, M. Pietroni, and F. Vernizzi. The large scale structure bootstrap: perturbation theory and bias expansion from symmetries. *JCAP*, 2021 (10):069, October 2021. doi: 10.1088/1475-7516/2021/10/069.

[253] Tobias Baldauf, Mehrdad Mirbabayi, Marko Simonović, and Matias Zaldarriaga. Equivalence principle and the baryon acoustic peak. *Phys. Rev. D*, 92(4):043514, August 2015. doi: 10.1103/PhysRevD.92.043514.

[254] Diego Blas, Mathias Garny, Mikhail M. Ivanov, and Sergey Sibiryakov. Time-sliced perturbation theory for large scale structure I: general formalism. *JCAP*, 2016(7):052, July 2016. doi: 10.1088/1475-7516/2016/07/052.

[255] Román Scoccimarro, H. M. P. Couchman, and Joshua A. Frieman. The Bispectrum as a Signature of Gravitational Instability in Redshift Space. *Astrophys. J.*, 517(2):531–540, June 1999. doi: 10.1086/307220.

[256] Yaniv Donath and Leonardo Senatore. Biased tracers in redshift space in the EFTofLSS with exact time dependence. *JCAP*, 2020(10):039, October 2020. doi: 10.1088/1475-7516/2020/10/039.

[257] Pierre Zhang and Yifu Cai. BOSS full-shape analysis from the EFTofLSS with exact time dependence. *JCAP*, 2022(1):031, January 2022. doi: 10.1088/1475-7516/2022/01/031.

[258] Mikhail M. Ivanov, Marko Simonović, and Matias Zaldarriaga. Cosmological parameters from the BOSS galaxy power spectrum. *JCAP*, 2020(5):042, May 2020. doi: 10.1088/1475-7516/2020/05/042.

[259] Robert E. Smith, Román Scoccimarro, and Ravi K. Sheth. Scale dependence of halo and galaxy bias: Effects in real space. *Phys. Rev. D*, 75(6):063512, March 2007. doi: 10.1103/PhysRevD.75.063512.

[260] Dimitry Ginzburg, Vincent Desjacques, and Kwan Chuen Chan. Shot noise and biased tracers: A new look at the halo model. *Phys. Rev. D*, 96(8):083528, October 2017. doi: 10.1103/PhysRevD.96.083528.

[261] Katarina Markovic, Benjamin Bose, and Alkistis Pourtsidou. Assessing non-linear models for galaxy clustering I: unbiased growth forecasts from multipole expansion. *The Open Journal of Astrophysics*, 2(1):13, November 2019. doi: 10.21105/astro.1904.11448.

[262] Praful Gagrani and Lado Samushia. Information Content of the Angular Multipoles of Redshift-Space Galaxy Bispectrum. *Mon. Not. Roy. Astron. Soc.*, 467(1):928–935, May 2017. doi: 10.1093/mnras/stx135.

[263] Martha Lippich, Ariel G. Sánchez, Manuel Colavincenzo, Emiliano Sefusatti, Pierluigi Monaco, Linda Blot, Martin Crocce, Marcelo A. Alvarez, Aniket Agrawal, Santiago Avila, Andrés Balaguera-Antolínez, Richard Bond, Sandrine Codis, Claudio Dalla Vecchia, Antonio Dorta, Pablo Fosalba, Albert Izard, Francisco-Shu Kitaura, Marcos Pellejero-Ibanez, George Stein, Mohammadjavad Vakili, and Gustavo Yepes. Comparing approximate methods for mock catalogues and covariance matrices - I. Correlation function. *Mon. Not. Roy. Astron. Soc.*, 482(2):1786–1806, January 2019. doi: 10.1093/mnras/sty2757.

[264] Ariel G. Sánchez, Eyal A. Kazin, Florian Beutler, Chia-Hsun Chuang, Antonio J. Cuesta, Daniel J. Eisenstein, Marc Manera, Francesco Montesano, Robert C. Nichol, Nikhil Padmanabhan, Will Percival, Francisco Prada, Ashley J. Ross, David J. Schlegel, Jeremy Tinker, Rita Tojeiro, David H. Weinberg, Xiaoying Xu, J. Brinkmann, Joel R. Brownstein, Donald P. Schneider, and Daniel Thomas. The clustering of galaxies in the SDSS-III Baryon Oscillation Spectroscopic Survey: cosmological constraints from the full shape of the clustering wedges. *Mon. Not. Roy. Astron. Soc.*, 433(2):1202–1222, August 2013. doi: 10.1093/mnras/stt799.

[265] Emiliano Munari, Pierluigi Monaco, Emiliano Sefusatti, Emanuele Castorina, Faizan G. Mohammad, Stefano Anselmi, and Stefano Borgani. Improving fast generation of halo catalogues with higher order Lagrangian perturbation theory. *Mon. Not. Roy. Astron. Soc.*, 465(4):4658–4677, March 2017. doi: 10.1093/mnras/stw3085.

[266] Max Tegmark. Measuring Cosmological Parameters with Galaxy Surveys. *Phys. Rev. Lett.*, 79(20):3806–3809, November 1997. doi: 10.1103/PhysRevLett.79.3806.

[267] Elena Sellentin and Alan F. Heavens. Parameter inference with estimated covariance matrices. *Mon. Not. Roy. Astron. Soc.*, 456(1):L132–L136, February 2016. doi: 10.1093/mnrasl/slv190.

[268] Alexander Eggemeier, Román Scoccimarro, Robert E. Smith, Martin Crocce, Andrea Pezzotta, and Ariel G. Sánchez. Testing one-loop galaxy bias: Joint analysis of power spectrum and bispectrum. *Phys. Rev. D*, 103(12):123550, June 2021. doi: 10.1103/PhysRevD.103.123550.

[269] Robert E. Smith, Ravi K. Sheth, and Román Scoccimarro. Analytic model for the bispectrum of galaxies in redshift space. *Phys. Rev. D*, 78(2):023523, July 2008. doi: 10.1103/PhysRevD.78.023523.

[270] Ken Osato, Takahiro Nishimichi, Francis Bernardeau, and Atsushi Taruya. Perturbation theory challenge for cosmological parameters estimation: Matter power spectrum in real space. *Phys. Rev. D*, 99(6):063530, March 2019. doi: 10.1103/PhysRevD.99.063530.

[271] Yun Wang. Figure of merit for dark energy constraints from current observational data. *Phys. Rev. D*, 77(12):123525, June 2008. doi: 10.1103/PhysRevD.77.123525.

[272] Pedro Carrilho, Chiara Moretti, Benjamin Bose, Katarina Markovič, and Alkistis Pourtsidou. Interacting dark energy from redshift-space galaxy clustering. *JCAP*, 2021(10):004, October 2021. doi: 10.1088/1475-7516/2021/10/004.

[273] Titouan Lazeyras, Christian Wagner, Tobias Baldauf, and Fabian Schmidt. Precision measurement of the local bias of dark matter halos. *JCAP*, 2016(2): 018, February 2016. doi: 10.1088/1475-7516/2016/02/018.

[274] D. Gualdi and L. Verde. Galaxy redshift-space bispectrum: the importance of being anisotropic. *JCAP*, 2020(6):041, June 2020. doi: 10.1088/1475-7516/2020/06/041.

[275] Davide Gualdi, Héctor Gil-Marín, and Licia Verde. Joint analysis of anisotropic power spectrum, bispectrum and trispectrum: application to N-body simulations. *JCAP*, 2021(7):008, July 2021. doi: 10.1088/1475-7516/2021/07/008.

[276] Guido D'Amico, Yaniv Donath, Leonardo Senatore, and Pierre Zhang. Limits on Clustering and Smooth Quintessence from the EFTofLSS. *arXiv e-prints*, art. arXiv:2012.07554, December 2020.

[277] Adrià Gómez-Valent. Fast test to assess the impact of marginalization in Monte Carlo analyses and its application to cosmology. *Phys. Rev. D*, 106(6):063506, 2022. doi: 10.1103/PhysRevD.106.063506.

[278] L. Piga, M. Marinucci, G. D'Amico, M. Pietroni, F. Vernizzi, and B. S. Wright. Constraints on modified gravity from the BOSS galaxy survey. *JCAP*, 2023(4):038, April 2023. doi: 10.1088/1475-7516/2023/04/038.

[279] Planck Collaboration, N. Aghanim, et al. Planck 2018 results. VI. Cosmological parameters. *Astron. Astrophys.*, 641:A6, September 2020. doi: 10.1051/0004-6361/201833910.

[280] Oliver H. E. Philcox, Mikhail M. Ivanov, Giovanni Cabass, Marko Simonović, Matias Zaldarriaga, and Takahiro Nishimichi. Cosmology with the Redshift-Space Galaxy Bispectrum Monopole at One-Loop Order. *arXiv e-prints*, art. arXiv:2206.02800, June 2022.

[281] Euclid Collaboration, A. Blanchard, et al. Euclid preparation. VII. Forecast validation for Euclid cosmological probes. *Astron. Astrophys.*, 642:A191, October 2020. doi: 10.1051/0004-6361/202038071.

[282] Julien Lesgourgues and Sergio Pastor. Massive neutrinos and cosmology. *Phys. Rept.*, 429(6):307–379, July 2006. doi: 10.1016/j.physrep.2006.04.001.

[283] Daniel Baumann, Alberto Nicolis, Leonardo Senatore, and Matias Zaldarriaga. Cosmological non-linearities as an effective fluid. *JCAP*, 2012(7):051, July 2012. doi: 10.1088/1475-7516/2012/07/051.

[284] John Joseph M. Carrasco, Mark P. Hertzberg, and Leonardo Senatore. The effective field theory of cosmological large scale structures. *Journal of High Energy Physics*, 2012:82, September 2012. doi: 10.1007/JHEP09(2012)082.

[285] Lucía Fonseca de la Bella, Donough Regan, David Seery, and Shaun Hotchkiss. The matter power spectrum in redshift space using effective field theory. *JCAP*, 2017 (11):039, November 2017. doi: 10.1088/1475-7516/2017/11/039.

[286] Maria Tsedrik, Chiara Moretti, Pedro Carrilho, Federico Rizzo, and Alkistis Pourtsidou. Interacting dark energy from the joint analysis of the power spectrum and bispectrum multipoles with the EFTofLSS. *Mon. Not. Roy. Astron. Soc.*, 520 (2):2611–2632, April 2023. doi: 10.1093/mnras/stad260.

[287] Muntazir Mehdi Abidi and Tobias Baldauf. Cubic halo bias in Eulerian and Lagrangian space. *JCAP*, 2018(7):029, July 2018. doi: 10.1088/1475-7516/2018/07/029.

[288] Emanuele Castorina, Emiliano Sefusatti, Ravi K. Sheth, Francisco Villaescusa-Navarro, and Matteo Viel. Cosmology with massive neutrinos II: on the universality of the halo mass function and bias. *JCAP*, 2014(2):049, February 2014. doi: 10.1088/1475-7516/2014/02/049.

[289] Zvonimir Vlah, Uroš Seljak, Man Yat Chu, and Yu Feng. Perturbation theory, effective field theory, and oscillations in the power spectrum. *JCAP*, 2016(3):057, March 2016. doi: 10.1088/1475-7516/2016/03/057.

[290] Antony Lewis, Anthony Challinor, and Anthony Lasenby. Efficient computation of CMB anisotropies in closed FRW models. *Astrophys. J.*, 538:473–476, 2000. doi: 10.1086/309179.

[291] Alessio Spurio Mancini, Davide Piras, Justin Alsing, Benjamin Joachimi, and Michael P. Hobson. CosmoPower: emulating cosmological power spectra for accelerated Bayesian inference from next-generation surveys. *Mon. Not. Roy. Astron. Soc.*, 511(2):1771–1788, 2022. doi: 10.1093/mnras/stac064.

[292] P. James Peebles. *The Large-Scale Structure of the Universe*. Princeton University Press, 11 1980. ISBN 978-0-691-08240-0, 978-0-691-20983-8, 978-0-691-20671-4.

[293] Eric V. Linder. Cosmic growth history and expansion history. *Phys.Rev.*, D72: 043529, 2005. doi: 10.1103/PhysRevD.72.043529.

[294] R. Calderon, D. Felbacq, R. Gannouji, D. Polarski, and A. A. Starobinsky. Global properties of the growth index of matter inhomogeneities in the Universe. *Phys. Rev. D*, 100(8):083503, October 2019. doi: 10.1103/PhysRevD.100.083503.

[295] R. Calderon, D. Felbacq, R. Gannouji, D. Polarski, and A. A. Starobinsky. Global properties of the growth index: Mathematical aspects and physical relevance. *Phys. Rev. D*, 101(10):103501, May 2020. doi: 10.1103/PhysRevD.101.103501.

[296] Yuewei Wen, Nhat-Minh Nguyen, and Dragan Huterer. Sweeping Horndeski canvas: new growth-rate parameterization for modified-gravity theories. *JCAP*, 09:028, 2023. doi: 10.1088/1475-7516/2023/09/028.

[297] Hernán E. Noriega, Alejandro Aviles, Sebastien Fromenteau, and Mariana Vargas-Magaña. Fast computation of non-linear power spectrum in cosmologies with massive neutrinos. *JCAP*, 2022(11):038, November 2022. doi: 10.1088/1475-7516/2022/11/038.

[298] Daniel Baumann, Daniel Green, and Benjamin Wallisch. Searching for light relics with large-scale structure. *JCAP*, 2018(8):029, August 2018. doi: 10.1088/1475-7516/2018/08/029.

[299] Benjamin Giblin, Matteo Cataneo, Ben Moews, and Catherine Heymans. On the road to per cent accuracy – II. Calibration of the non-linear matter power spectrum for arbitrary cosmologies. *Mon. Not. Roy. Astron. Soc.*, 490(4):4826–4840, 2019. doi: 10.1093/mnras/stz2659.

[300] Aoife Boyle and Fabian Schmidt. Neutrino mass constraints beyond linear order: cosmology dependence and systematic biases. *JCAP*, 2021(4):022, April 2021. doi: 10.1088/1475-7516/2021/04/022.

[301] Shun Saito, Masahiro Takada, and Atsushi Taruya. Nonlinear power spectrum in the presence of massive neutrinos: Perturbation theory approach, galaxy bias, and parameter forecasts. *Phys. Rev. D*, 80(8):083528, October 2009. doi: 10.1103/PhysRevD.80.083528.

[302] Michele Levi and Zvonimir Vlah. Massive neutrinos in nonlinear large scale structure: A consistent perturbation theory. *arXiv e-prints*, art. arXiv:1605.09417, May 2016. doi: 10.48550/arXiv.1605.09417.

[303] Leonardo Senatore and Matias Zaldarriaga. The Effective Field Theory of Large-Scale Structure in the presence of Massive Neutrinos. *arXiv e-prints*, art. arXiv:1707.04698, July 2017. doi: 10.48550/arXiv.1707.04698.

[304] Alejandro Aviles and Arka Banerjee. A Lagrangian perturbation theory in the presence of massive neutrinos. *JCAP*, 2020(10):034, October 2020. doi: 10.1088/1475-7516/2020/10/034.

[305] Alejandro Aviles, Arka Banerjee, Gustavo Niz, and Zachary Slepian. Clustering in massive neutrino cosmologies via Eulerian Perturbation Theory. *JCAP*, 2021(11):028, November 2021. doi: 10.1088/1475-7516/2021/11/028.

[306] SDSS Collaboration, Shadab Alam, et al. The Eleventh and Twelfth Data Releases of the Sloan Digital Sky Survey: Final Data from SDSS-III. *The Astrophysical Journal Supplement Series*, 219(1):12, July 2015. doi: 10.1088/0067-0049/219/1/12.

[307] Héctor Gil-Marín, Will J. Percival, Joel R. Brownstein, Chia-Hsun Chuang, Jan Niklas Grieb, Shirley Ho, Francisco-Shu Kitaura, Claudia Maraston, Francisco Prada, Sergio Rodríguez-Torres, Ashley J. Ross, Lado Samushia, David J. Schlegel, Daniel Thomas, Jeremy L. Tinker, and Gong-Bo Zhao. The clustering of galaxies in the SDSS-III Baryon Oscillation Spectroscopic Survey: RSD measurement from the LOS-dependent power spectrum of DR12 BOSS galaxies. *Mon. Not. Roy. Astron. Soc.*, 460(4):4188–4209, August 2016. doi: 10.1093/mnras/stw1096.

[308] Florian Beutler, Hee-Jong Seo, Shun Saito, Chia-Hsun Chuang, Antonio J. Cuesta, Daniel J. Eisenstein, Héctor Gil-Marín, Jan Niklas Grieb, Nick Hand, Francisco-Shu Kitaura, Chirag Modi, Robert C. Nichol, Matthew D. Olmstead, Will J. Percival, Francisco Prada, Ariel G. Sánchez, Sergio Rodriguez-Torres, Ashley J. Ross, Nicholas P. Ross, Donald P. Schneider, Jeremy Tinker, Rita Tojeiro, and Mariana Vargas-Magaña. The clustering of galaxies in the completed SDSS-III Baryon Oscillation Spectroscopic Survey: anisotropic galaxy clustering in Fourier space. *Mon. Not. Roy. Astron. Soc.*, 466(2):2242–2260, April 2017. doi: 10.1093/mnras/stw3298.

[309] Florian Beutler, Chris Blake, Matthew Colless, D. Heath Jones, Lister Staveley-Smith, Lachlan Campbell, Quentin Parker, Will Saunders, and Fred Watson. The 6dF Galaxy Survey: baryon acoustic oscillations and the local Hubble constant. *Mon. Not. Roy. Astron. Soc.*, 416(4):3017–3032, October 2011. doi: 10.1111/j.1365-2966.2011.19250.x.

[310] Ashley J. Ross, Lado Samushia, Cullan Howlett, Will J. Percival, Angela Burden, and Marc Manera. The clustering of the SDSS DR7 main Galaxy sample - I. A 4 per cent distance measure at z = 0.15. *Mon. Not. Roy. Astron. Soc.*, 449(1):835–847, May 2015. doi: 10.1093/mnras/stv154.

[311] Hélion du Mas des Bourboux, James Rich, Andreu Font-Ribera, Victoria de Sainte Agathe, James Farr, Thomas Etourneau, Jean-Marc Le Goff, Andrei Cuceu, Christophe Balland, Julian E. Bautista, Michael Blomqvist, Jonathan Brinkmann, Joel R. Brownstein, Solène Chabanier, Edmond Chaussidon, Kyle Dawson, Alma X. González-Morales, Julien Guy, Brad W. Lyke, Axel de la Macorra, Eva-Maria Mueller, Adam D. Myers, Christian Nitschelm, Andrea Muñoz Gutiérrez, Nathalie Palanque-Delabrouille, James Parker, Will J. Percival, Ignasi Pérez-Ràfols, Patrick Petitjean, Matthew M. Pieri, Corentin Ravoux, Graziano Rossi, Donald P. Schneider, Hee-Jong Seo, Anže Slosar, Julianna Stermer, M. Vivek, Christophe Yèche, and Samantha Youles. The Completed SDSS-IV Extended Baryon Oscillation Spectroscopic Survey: Baryon Acoustic Oscillations with Lyα Forests. *Astrophys. J.*, 901(2):153, October 2020. doi: 10.3847/1538-4357/abb085.

[312] Francisco-Shu Kitaura, Sergio Rodríguez-Torres, Chia-Hsun Chuang, Cheng Zhao, Francisco Prada, Héctor Gil-Marín, Hong Guo, Gustavo Yepes, Anatoly Klypin, Claudia G. Scóccola, Jeremy Tinker, Cameron McBride, Beth Reid, Ariel G. Sánchez, Salvador Salazar-Albornoz, Jan Niklas Grieb, Mariana Vargas-Magana,

Antonio J. Cuesta, Mark Neyrinck, Florian Beutler, Johan Comparat, Will J. Percival, and Ashley Ross. The clustering of galaxies in the SDSS-III Baryon Oscillation Spectroscopic Survey: mock galaxy catalogues for the BOSS Final Data Release. *Mon. Not. Roy. Astron. Soc.*, 456(4):4156–4173, March 2016. doi: 10.1093/mnras/stv2826.

[313] Sergio A. Rodríguez-Torres, Chia-Hsun Chuang, Francisco Prada, Hong Guo, Anatoly Klypin, Peter Behroozi, Chang Hoon Hahn, Johan Comparat, Gustavo Yepes, Antonio D. Montero-Dorta, Joel R. Brownstein, Claudia Maraston, Cameron K. McBride, Jeremy Tinker, Stefan Gottlöber, Ginevra Favole, Yiping Shu, Francisco-Shu Kitaura, Adam Bolton, Román Scoccimarro, Lado Samushia, David Schlegel, Donald P. Schneider, and Daniel Thomas. The clustering of galaxies in the SDSS-III Baryon Oscillation Spectroscopic Survey: modelling the clustering and halo occupation distribution of BOSS CMASS galaxies in the Final Data Release. *Mon. Not. Roy. Astron. Soc.*, 460(2):1173–1187, August 2016. doi: 10.1093/mnras/stw1014.

[314] Nils Schöneberg, Julien Lesgourgues, and Deanna C. Hooper. The BAO+BBN take on the Hubble tension. *JCAP*, 2019(10):029, October 2019. doi: 10.1088/1475-7516/2019/10/029.

[315] Thomas Colas, Guido d'Amico, Leonardo Senatore, Pierre Zhang, and Florian Beutler. Efficient cosmological analysis of the SDSS/BOSS data from the Effective Field Theory of Large-Scale Structure. *JCAP*, 2020(6):001, June 2020. doi: 10.1088/1475-7516/2020/06/001.

[316] Agne Semenaite, Ariel G. Sánchez, Andrea Pezzotta, Jiamin Hou, Alexander Eggemeier, Martin Crocce, Cheng Zhao, Joel R. Brownstein, Graziano Rossi, and Donald P. Schneider. Beyond ΛCDM constraints from the full shape clustering measurements from BOSS and eBOSS. *arXiv e-prints*, art. arXiv:2210.07304, October 2022. doi: 10.48550/arXiv.2210.07304.

[317] Eva-Maria Mueller, Will Percival, Eric Linder, Shadab Alam, Gong-Bo Zhao, Ariel G. Sánchez, Florian Beutler, and Jon Brinkmann. The clustering of galaxies in the completed SDSS-III Baryon Oscillation Spectroscopic Survey: constraining modified gravity. *Mon. Not. Roy. Astron. Soc.*, 475(2):2122–2131, April 2018. doi: 10.1093/mnras/stx3232.

[318] Florian Beutler, Shun Saito, Joel R. Brownstein, Chia-Hsun Chuang, Antonio J. Cuesta, Will J. Percival, Ashley J. Ross, Nicholas P. Ross, Donald P. Schneider, Lado Samushia, Ariel G. Sánchez, Hee-Jong Seo, Jeremy L. Tinker, Christian Wagner, and Benjamin A. Weaver. The clustering of galaxies in the SDSS-III Baryon Oscillation Spectroscopic Survey: signs of neutrino mass in current cosmological data sets. *Mon. Not. Roy. Astron. Soc.*, 444(4):3501–3516, November 2014. doi: 10.1093/mnras/stu1702.

[319] Héctor Gil-Marín, Will J. Percival, Licia Verde, Joel R. Brownstein, Chia-Hsun Chuang, Francisco-Shu Kitaura, Sergio A. Rodríguez-Torres, and Matthew D. Olmstead. The clustering of galaxies in the SDSS-III Baryon Oscillation Spectroscopic Survey: RSD measurement from the power spectrum and bispectrum

of the DR12 BOSS galaxies. *Mon. Not. Roy. Astron. Soc.*, 465(2):1757–1788, February 2017. doi: 10.1093/mnras/stw2679.

[320] Anton Chudaykin and Mikhail M. Ivanov. Measuring neutrino masses with large-scale structure: Euclid forecast with controlled theoretical error. *JCAP*, 2019(11): 034, November 2019. doi: 10.1088/1475-7516/2019/11/034.

[321] Laura Herold, Elisa G. M. Ferreira, and Eiichiro Komatsu. New Constraint on Early Dark Energy from Planck and BOSS Data Using the Profile Likelihood. *Astrophys. J. Lett.*, 929(1):L16, April 2022. doi: 10.3847/2041-8213/ac63a3.

[322] B. Joachimi and A. N. Taylor. Forecasts of non-Gaussian parameter spaces using Box-Cox transformations. *Mon. Not. Roy. Astron. Soc.*, 416(2):1010–1022, September 2011. doi: 10.1111/j.1365-2966.2011.19107.x.

[323] Laura Wolz, Martin Kilbinger, Jochen Weller, and Tommaso Giannantonio. On the validity of cosmological Fisher matrix forecasts. *JCAP*, 2012(9):009, September 2012. doi: 10.1088/1475-7516/2012/09/009.

[324] Nicola Bellomo, José Luis Bernal, Giulio Scelfo, Alvise Raccanelli, and Licia Verde. Beware of commonly used approximations. Part I. Errors in forecasts. *JCAP*, 2020 (10):016, October 2020. doi: 10.1088/1475-7516/2020/10/016.

[325] José Luis Bernal, Nicola Bellomo, Alvise Raccanelli, and Licia Verde. Beware of commonly used approximations. Part II. Estimating systematic biases in the best-fit parameters. *JCAP*, 2020(10):017, October 2020. doi: 10.1088/1475-7516/2020/10/017.

[326] Arthur Stril, Robert N. Cahn, and Eric V. Linder. Testing standard cosmology with large-scale structure. *Mon. Not. Roy. Astron. Soc.*, 404(1):239–246, May 2010. doi: 10.1111/j.1365-2966.2010.16193.x.

[327] Andreu Font-Ribera, Patrick McDonald, Nick Mostek, Beth A. Reid, Hee-Jong Seo, and Anže Slosar. DESI and other Dark Energy experiments in the era of neutrino mass measurements. *JCAP*, 2014(5):023, May 2014. doi: 10.1088/1475-7516/2014/05/023.

[328] José Fonseca, Jan-Albert Viljoen, and Roy Maartens. Constraints on the growth rate using the observed galaxy power spectrum. *JCAP*, 2019(12):028, December 2019. doi: 10.1088/1475-7516/2019/12/028.

[329] Jan-Albert Viljoen, José Fonseca, and Roy Maartens. Constraining the growth rate by combining multiple future surveys. *JCAP*, 2020(9):054, September 2020. doi: 10.1088/1475-7516/2020/09/054.

[330] Digvijay Wadekar and Román Scoccimarro. Galaxy power spectrum multipoles covariance in perturbation theory. *Phys. Rev. D*, 102(12):123517, December 2020. doi: 10.1103/PhysRevD.102.123517.

[331] Digvijay Wadekar, Mikhail M. Ivanov, and Roman Scoccimarro. Cosmological constraints from BOSS with analytic covariance matrices. *Phys. Rev. D*, 102(12): 123521, December 2020. doi: 10.1103/PhysRevD.102.123521.

[332] Benjamin Audren, Julien Lesgourgues, Simeon Bird, Martin G. Haehnelt, and Matteo Viel. Neutrino masses and cosmological parameters from a Euclid-like survey: Markov Chain Monte Carlo forecasts including theoretical errors. *JCAP*, 01:026, 2013. doi: 10.1088/1475-7516/2013/01/026.

[333] ChangHoon Hahn, Francisco Villaescusa-Navarro, Emanuele Castorina, and Roman Scoccimarro. Constraining M_ν with the bispectrum. Part I. Breaking parameter degeneracies. *JCAP*, 2020(3):040, March 2020. doi: 10.1088/1475-7516/2020/03/040.

[334] ChangHoon Hahn and Francisco Villaescusa-Navarro. Constraining M_ν with the bispectrum. Part II. The information content of the galaxy bispectrum monopole. *JCAP*, 2021(4):029, April 2021. doi: 10.1088/1475-7516/2021/04/029.

[335] Pedro G. S. Fernandes, Pedro Carrilho, Timothy Clifton, and David J. Mulryne. The 4D Einstein–Gauss–Bonnet theory of gravity: a review. *Class. Quant. Grav.*, 39(6):063001, 2022. doi: 10.1088/1361-6382/ac500a.

[336] Gregory Walter Horndeski. Second-order scalar-tensor field equations in a four-dimensional space. *Int.J.Theor.Phys.*, 10:363–384, 1974. doi: 10.1007/BF01807638.

[337] Clifford M. Will. *Theory and Experiment in Gravitational Physics*. Cambridge University Press, 1993.

[338] Kazuya Koyama. Gravity beyond general relativity. *Int. J. Mod. Phys.*, D27(15): 1848001, 2018. doi: 10.1142/S0218271818480012.

[339] Fabian Schmidt, Wayne Hu, and Marcos Lima. Spherical Collapse and the Halo Model in Braneworld Gravity. *Phys.Rev.*, D81:063005, 2010. doi: 10.1103/PhysRevD.81.063005.

[340] Lucas Lombriser. Constraining chameleon models with cosmology. *Annalen Phys.*, 526:259–282, 2014. doi: 10.1002/andp.201400058.

[341] Christian Arnold, Baojiu Li, Benjamin Giblin, Joachim Harnois-Déraps, and Yan-Chuan Cai. forge: the f(R)-gravity cosmic emulator project – I. Introduction and matter power spectrum emulator. *Mon. Not. Roy. Astron. Soc.*, 515(3):4161–4175, 2022. doi: 10.1093/mnras/stac1091.

[342] César Hernández-Aguayo, Cheng-Zong Ruan, Baojiu Li, Christian Arnold, Carlton M. Baugh, Anatoly Klypin, and Francisco Prada. Fast full N-body simulations of generic modified gravity: derivative coupling models. *JCAP*, 01 (01):048, 2022. doi: 10.1088/1475-7516/2022/01/048.

[343] Ewald Puchwein, Marco Baldi, and Volker Springel. Modified Gravity-GADGET: A new code for cosmological hydrodynamical simulations of modified gravity models. *Mon.Not.Roy.Astron.Soc.*, 436:348, 2013. doi: 10.1093/mnras/stt1575.

[344] Philippe Brax and Patrick Valageas. Impact on the power spectrum of Screening in Modified Gravity Scenarios. *Phys. Rev. D*, 88(2):023527, 2013. doi: 10.1103/PhysRevD.88.023527.

[345] Philippe Brax and Patrick Valageas. K-mouflage Cosmology: Formation of Large-Scale Structures. *Phys. Rev. D*, 90(2):023508, 2014. doi: 10.1103/PhysRevD.90.023508.

[346] Shahab Joudaki, Pedro G. Ferreira, Nelson A. Lima, and Hans A. Winther. Testing gravity on cosmic scales: A case study of Jordan-Brans-Dicke theory. *Phys. Rev. D*, 105(4):043522, 2022. doi: 10.1103/PhysRevD.105.043522.

[347] Hans A. Winther, Kazuya Koyama, Marc Manera, Bill S. Wright, and Gong-Bo Zhao. COLA with scale-dependent growth: applications to screened modified gravity models. *JCAP*, 08:006, 2017. doi: 10.1088/1475-7516/2017/08/006.

[348] Giulia Gubitosi, Federico Piazza, and Filippo Vernizzi. The Effective Field Theory of Dark Energy. *JCAP*, 1302:032, 2013. doi: 10.1088/1475-7516/2013/02/032.

[349] Jolyon K. Bloomfield, Eanna E. Flanagan, Minjoon Park, and Scott Watson. Dark energy or modified gravity? An effective field theory approach. *JCAP*, 1308:010, 2013. doi: 10.1088/1475-7516/2013/08/010.

[350] Noemi Frusciante and Louis Perenon. Effective field theory of dark energy: A review. *Phys. Rept.*, 857:1–63, 2020. doi: 10.1016/j.physrep.2020.02.004.

[351] Lucas Lombriser. A parametrisation of modified gravity on nonlinear cosmological scales. *JCAP*, 11:039, 2016. doi: 10.1088/1475-7516/2016/11/039.

[352] A. Spurio Mancini, F. Köhlinger, B. Joachimi, V. Pettorino, B. M. Schäfer, R. Reischke, Edo van Uitert, S. Brieden, M. Archidiacono, and J. Lesgourgues. KiDS + GAMA: constraints on horndeski gravity from combined large-scale structure probes. *Mon. Not. Roy. Astron. Soc.*, 490(2):2155–2177, 2019. doi: 10.1093/mnras/stz2581.

[353] Dina Traykova, Emilio Bellini, and Pedro G. Ferreira. The phenomenology of beyond Horndeski gravity. *JCAP*, 08:035, 2019. doi: 10.1088/1475-7516/2019/08/035.

[354] Euclid Collaboration, R. Laureijs, et al. Euclid Definition Study Report. *arXiv e-prints*, art. arXiv:1110.3193, October 2011. doi: 10.48550/arXiv.1110.3193.

[355] LSST Collaboration, Željko Ivezić, et al. LSST: from Science Drivers to Reference Design and Anticipated Data Products. *Astrophys. J.*, 873(2):111, 2019. doi: 10.3847/1538-4357/ab042c.

[356] Matteo Cataneo, J.D. Emberson, Derek Inman, Joachim Harnois-Deraps, and Catherine Heymans. On the road to per cent accuracy – III. Non-linear reaction of the matter power spectrum to massive neutrinos. *Mon. Not. Roy. Astron. Soc.*, 491 (3):3101–3107, 2020. doi: 10.1093/mnras/stz3189.

[357] Benjamin Bose, Hans A. Winther, Alkistis Pourtsidou, Santiago Casas, Lucas Lombriser, Qianli Xia, and Matteo Cataneo. Hybrid $P_\ell(k)$: general, unified, non-linear matter power spectrum in redshift space. *JCAP*, 09:001, 2020. doi: 10.1088/1475-7516/2020/09/001.

[358] Pedro Carrilho, Karim Carrion, Benjamin Bose, Alkistis Pourtsidou, Juan Carlos Hidalgo, Lucas Lombriser, and Marco Baldi. On the road to per cent accuracy VI: the non-linear power spectrum for interacting dark energy with baryonic feedback and massive neutrinos. *Mon. Not. Roy. Astron. Soc.*, 512(3):3691–3702, 2022. doi: 10.1093/mnras/stac641.

[359] Asantha Cooray and Ravi K. Sheth. Halo Models of Large Scale Structure. *Phys. Rept.*, 372:1–129, 2002. doi: 10.1016/S0370-1573(02)00276-4.

[360] Alexander Mead, John Peacock, Catherine Heymans, Shahab Joudaki, and Alan Heavens. An accurate halo model for fitting non-linear cosmological power spectra and baryonic feedback models. *Mon. Not. Roy. Astron. Soc.*, 454(2):1958–1975, 2015. doi: 10.1093/mnras/stv2036.

[361] Alexander Mead, Catherine Heymans, Lucas Lombriser, John Peacock, Olivia Steele, and Hans Winther. Accurate halo-model matter power spectra with dark energy, massive neutrinos and modified gravitational forces. *Mon. Not. Roy. Astron. Soc.*, 459(2):1468–1488, 2016. doi: 10.1093/mnras/stw681.

[362] A. J. Mead, S. Brieden, T. Tröster, and C. Heymans. HMCODE-2020: improved modelling of non-linear cosmological power spectra with baryonic feedback. *Mon. Not. Roy. Astron. Soc.*, 502(1):1401–1422, March 2021. doi: 10.1093/mnras/stab082.

[363] Benjamin Bose, Bill S. Wright, Matteo Cataneo, Alkistis Pourtsidou, Carlo Giocoli, Lucas Lombriser, Ian G. McCarthy, Marco Baldi, Simon Pfeifer, and Qianli Xia. On the road to per cent accuracy – V. The non-linear power spectrum beyond ΛCDM with massive neutrinos and baryonic feedback. *Mon. Not. Roy. Astron. Soc.*, 508 (2):2479–2491, 2021. doi: 10.1093/mnras/stab2731.

[364] Shankar Agarwal and Hume A. Feldman. The effect of massive neutrinos on the matter power spectrum. *Mon. Not. Roy. Astron. Soc.*, 410:1647, 2011. doi: 10.1111/j.1365-2966.2010.17546.x.

[365] Benjamin Bose and Kazuya Koyama. A Perturbative Approach to the Redshift Space Power Spectrum: Beyond the Standard Model. *JCAP*, 1608(08):032, 2016. doi: 10.1088/1475-7516/2016/08/032.

[366] Daniel B. Thomas. Cosmological gravity on all scales: simple equations, required conditions, and a framework for modified gravity. *Phys. Rev. D*, 101(12):123517, 2020. doi: 10.1103/PhysRevD.101.123517.

[367] Johannes Noller, Francesca von Braun-Bates, and Pedro G. Ferreira. Relativistic scalar fields and the quasistatic approximation in theories of modified gravity. *Phys. Rev. D*, 89(2):023521, 2014. doi: 10.1103/PhysRevD.89.023521.

[368] Johannes Noller, Luca Santoni, Enrico Trincherini, and Leonardo G. Trombetta. Scalar-tensor cosmologies without screening. *JCAP*, 01:045, 2021. doi: 10.1088/1475-7516/2021/01/045.

[369] Noemi Frusciante, Georgios Papadomanolakis, and Alessandra Silvestri. An Extended action for the effective field theory of dark energy: a stability analysis and a complete guide to the mapping at the basis of EFTCAMB. *JCAP*, 07:018, 2016. doi: 10.1088/1475-7516/2016/07/018.

[370] Joe Kennedy, Lucas Lombriser, and Andy Taylor. Reconstructing Horndeski theories from phenomenological modified gravity and dark energy models on cosmological scales. *Phys. Rev.*, D98(4):044051, 2018. doi: 10.1103/PhysRevD.98.044051.

[371] Lucas Lombriser, Charles Dalang, Joe Kennedy, and Andy Taylor. Inherently stable effective field theory for dark energy and modified gravity. *JCAP*, 01:041, 2019. doi: 10.1088/1475-7516/2019/01/041.

[372] Rafaela Gsponer and Johannes Noller. Tachyonic stability priors for dark energy. *Phys. Rev. D*, 105(6):064002, 2022. doi: 10.1103/PhysRevD.105.064002.

[373] Giulia Cusin, Matthew Lewandowski, and Filippo Vernizzi. Dark Energy and Modified Gravity in the Effective Field Theory of Large-Scale Structure. *JCAP*, 04:005, 2018. doi: 10.1088/1475-7516/2018/04/005.

[374] Yuichiro Takushima, Ayumu Terukina, and Kazuhiro Yamamoto. Third order solutions of cosmological density perturbations in Horndeski?s most general scalar-tensor theory with the Vainshtein mechanism. *Phys. Rev.*, D92(10):104033, 2015. doi: 10.1103/PhysRevD.92.104033.

[375] Fabian Schmidt, Marcos Vinicius Lima, Hiroaki Oyaizu, and Wayne Hu. Non-linear Evolution of f(R) Cosmologies III: Halo Statistics. *Phys.Rev.*, D79:083518, 2009. doi: 10.1103/PhysRevD.79.083518.

[376] Baojiu Li and George Efstathiou. An Extended Excursion Set Approach to Structure Formation in Chameleon Models. *Mon. Not. Roy. Astron. Soc.*, 421:1431, 2012. doi: 10.1111/j.1365-2966.2011.20404.x.

[377] Justin Khoury and Amanda Weltman. Chameleon fields: Awaiting surprises for tests of gravity in space. *Phys.Rev.Lett.*, 93:171104, 2004. doi: 10.1103/PhysRevLett.93.171104.

[378] Lucas Lombriser, Kazuya Koyama, and Baojiu Li. Halo modelling in chameleon theories. *JCAP*, 03:021, 2014. doi: 10.1088/1475-7516/2014/03/021.

[379] Kurt Hinterbichler and Justin Khoury. Symmetron Fields: Screening Long-Range Forces Through Local Symmetry Restoration. *Phys.Rev.Lett.*, 104:231301, 2010. doi: 10.1103/PhysRevLett.104.231301.

[380] Laura Taddei, Riccardo Catena, and Massimo Pietroni. Spherical collapse and halo mass function in the symmetron model. *Phys. Rev. D*, 89(2):023523, 2014. doi: 10.1103/PhysRevD.89.023523.

[381] E. Babichev, C. Deffayet, and R. Ziour. k-Mouflage gravity. *Int. J. Mod. Phys. D*, 18:2147–2154, 2009. doi: 10.1142/S0218271809016107.

[382] A.I. Vainshtein. To the problem of nonvanishing gravitation mass. *Phys.Lett.*, B39: 393–394, 1972. doi: 10.1016/0370-2693(72)90147-5.

[383] Lucas Lombriser and Andy Taylor. Classifying Linearly Shielded Modified Gravity Models in Effective Field Theory. *Phys.Rev.Lett.*, 114(3):031101, 2015. doi: 10.1103/PhysRevLett.114.031101.

[384] Ryan McManus, Lucas Lombriser, and Jorge Peñarrubia. Finding Horndeski theories with Einstein gravity limits. *JCAP*, 11:006, 2016. doi: 10.1088/1475-7516/2016/11/006.

[385] Cyril Renevey, Joe Kennedy, and Lucas Lombriser. Parameterised post-Newtonian formalism for the effective field theory of dark energy via screened reconstructed Horndeski theories. *JCAP*, 12:032, 2020. doi: 10.1088/1475-7516/2020/12/032.

[386] Farbod Hassani and Lucas Lombriser. N-body simulations for parametrized modified gravity. *Mon. Not. Roy. Astron. Soc.*, 497(2):1885–1894, 2020. doi: 10.1093/mnras/staa2083.

[387] Alessandra Silvestri, Levon Pogosian, and Roman V. Buniy. Practical approach to cosmological perturbations in modified gravity. *Phys. Rev. D*, 87(10):104015, 2013. doi: 10.1103/PhysRevD.87.104015.

[388] Sankarshana Srinivasan, Daniel B. Thomas, Francesco Pace, and Richard Battye. Cosmological gravity on all scales. Part II. Model independent modified gravity N-body simulations. *JCAP*, 06:016, 2021. doi: 10.1088/1475-7516/2021/06/016.

[389] Ignacy Sawicki and Emilio Bellini. Limits of quasistatic approximation in modified-gravity cosmologies. *Phys. Rev. D*, 92(8):084061, 2015. doi: 10.1103/PhysRevD.92.084061.

[390] Francesco Pace, Richard Battye, Emilio Bellini, Lucas Lombriser, Filippo Vernizzi, and Boris Bolliet. Comparison of different approaches to the quasi-static approximation in Horndeski models. *JCAP*, 06:017, 2021. doi: 10.1088/1475-7516/2021/06/017.

[391] Bin Hu, Marco Raveri, Noemi Frusciante, and Alessandra Silvestri. Effective Field Theory of Cosmic Acceleration: an implementation in CAMB. *Phys.Rev.*, D89(10):103530, 2014. doi: 10.1103/PhysRevD.89.103530.

[392] Marco Raveri, Bin Hu, Noemi Frusciante, and Alessandra Silvestri. Effective Field Theory of Cosmic Acceleration: constraining dark energy with CMB data. *Phys.Rev.*, D90(4):043513, 2014. doi: 10.1103/PhysRevD.90.043513.

[393] Cedric Deffayet, Oriol Pujolas, Ignacy Sawicki, and Alexander Vikman. Imperfect Dark Energy from Kinetic Gravity Braiding. *JCAP*, 10:026, 2010. doi: 10.1088/1475-7516/2010/10/026.

[394] Ryuichi Takahashi, Masanori Sato, Takahiro Nishimichi, Atsushi Taruya, and Masamune Oguri. Revising the Halofit Model for the Nonlinear Matter Power Spectrum. *Astrophys. J.*, 761:152, 2012. doi: 10.1088/0004-637X/761/2/152.

[395] Euclid Collaboration, A. Blanchard, et al. Euclid preparation: VII. Forecast validation for Euclid cosmological probes. *Astron. Astrophys.*, 642:A191, 2020. doi: 10.1051/0004-6361/202038071.

[396] Lucas Lombriser and Andy Taylor. Semi-dynamical perturbations of unified dark energy. *JCAP*, 11:040, 2015. doi: 10.1088/1475-7516/2015/11/040.

[397] Claudia de Rham and Scott Melville. Gravitational Rainbows: LIGO and Dark Energy at its Cutoff. *Phys. Rev. Lett.*, 121(22):221101, 2018. doi: 10.1103/PhysRevLett.121.221101.

[398] Paolo Creminelli, Giovanni Tambalo, Filippo Vernizzi, and Vicharit Yingcharoenrat. Dark-energy instabilities induced by gravitational waves. *JCAP*, 2020(5):002, May 2020. doi: 10.1088/1475-7516/2020/05/002.

[399] Scott Melville and Johannes Noller. Positivity in the Sky: Constraining dark energy and modified gravity from the UV. *Phys. Rev. D*, 101(2):021502, 2020. doi: 10.1103/PhysRevD.101.021502. [Erratum: Phys.Rev.D 102, 049902 (2020)].

[400] Claudia de Rham, Scott Melville, and Johannes Noller. Positivity bounds on dark energy: when matter matters. *JCAP*, 08:018, 2021. doi: 10.1088/1475-7516/2021/08/018.

[401] B. P. Abbott et al. Gravitational Waves and Gamma-rays from a Binary Neutron Star Merger: GW170817 and GRB 170817A. *Astrophys. J.*, 848(2):L13, 2017. doi: 10.3847/2041-8213/aa920c.

[402] Antonio De Felice and Shinji Tsujikawa. Conditions for the cosmological viability of the most general scalar-tensor theories and their applications to extended Galileon dark energy models. *JCAP*, 1202:007, 2012. doi: 10.1088/1475-7516/2012/02/007.

[403] Johannes Noller. Cosmological constraints on dark energy in light of gravitational wave bounds. *Phys. Rev. D*, 101(6):063524, 2020. doi: 10.1103/PhysRevD.101.063524.

[404] Noemi Frusciante, Simone Peirone, Santiago Casas, and Nelson A. Lima. Cosmology of surviving Horndeski theory: The road ahead. *Phys. Rev. D*, 99(6):063538, 2019. doi: 10.1103/PhysRevD.99.063538.

[405] Lucas Lombriser and Andy Taylor. Breaking a Dark Degeneracy with Gravitational Waves. *JCAP*, 1603(03):031, 2016. doi: 10.1088/1475-7516/2016/03/031.

[406] Lucas Lombriser and Nelson A. Lima. Challenges to Self-Acceleration in Modified Gravity from Gravitational Waves and Large-Scale Structure. *Phys. Lett.*, B765:382–385, 2017. doi: 10.1016/j.physletb.2016.12.048.

[407] Paolo Creminelli and Filippo Vernizzi. Dark Energy after GW170817 and GRB170817A. *Phys. Rev. Lett.*, 119(25):251302, 2017. doi: 10.1103/PhysRevLett.119.251302.

[408] Jose María Ezquiaga and Miguel Zumalacárregui. Dark Energy After GW170817: Dead Ends and the Road Ahead. *Phys. Rev. Lett.*, 119(25):251304, 2017. doi: 10.1103/PhysRevLett.119.251304.

[409] T. Baker, E. Bellini, P. G. Ferreira, M. Lagos, J. Noller, and I. Sawicki. Strong constraints on cosmological gravity from GW170817 and GRB 170817A. *Phys. Rev. Lett.*, 119(25):251301, 2017. doi: 10.1103/PhysRevLett.119.251301.

[410] Jeremy Sakstein and Bhuvnesh Jain. Implications of the Neutron Star Merger GW170817 for Cosmological Scalar-Tensor Theories. *Phys. Rev. Lett.*, 119(25): 251303, 2017. doi: 10.1103/PhysRevLett.119.251303.

[411] Richard A. Battye, Francesco Pace, and Damien Trinh. Gravitational wave constraints on dark sector models. *Phys. Rev.*, D98(2):023504, 2018. doi: 10.1103/PhysRevD.98.023504.

[412] Paolo Creminelli, Matthew Lewandowski, Giovanni Tambalo, and Filippo Vernizzi. Gravitational Wave Decay into Dark Energy. *JCAP*, 1812(12):025, 2018. doi: 10.1088/1475-7516/2018/12/025.

[413] Tessa Baker et al. Measuring the propagation speed of gravitational waves with LISA. *JCAP*, 08(08):031, 2022. doi: 10.1088/1475-7516/2022/08/031.

[414] Allan Adams, Nima Arkani-Hamed, Sergei Dubovsky, Alberto Nicolis, and Riccardo Rattazzi. Causality, analyticity and an IR obstruction to UV completion. *JHEP*, 10:014, 2006. doi: 10.1088/1126-6708/2006/10/014.

[415] Eugeny Babichev, Viatcheslav Mukhanov, and Alexander Vikman. k-Essence, superluminal propagation, causality and emergent geometry. *JHEP*, 02:101, 2008. doi: 10.1088/1126-6708/2008/02/101.

[416] Clare Burrage, Claudia de Rham, Lavinia Heisenberg, and Andrew J. Tolley. Chronology Protection in Galileon Models and Massive Gravity. *JCAP*, 07:004, 2012. doi: 10.1088/1475-7516/2012/07/004.

[417] Claudia de Rham and Andrew J. Tolley. Causality in curved spacetimes: The speed of light and gravity. *Phys. Rev. D*, 102(8):084048, 2020. doi: 10.1103/PhysRevD.102.084048.

[418] Harvey S. Reall. Causality in gravitational theories with second order equations of motion. *Phys. Rev. D*, 103(8):084027, 2021. doi: 10.1103/PhysRevD.103.084027.

[419] Zhiqi Huang. Observational effects of a running Planck mass. *Phys. Rev. D*, 93(4): 043538, 2016. doi: 10.1103/PhysRevD.93.043538.

[420] Emilio Bellini, Antonio J. Cuesta, Raul Jimenez, and Licia Verde. Constraints on deviations from ΛCDM within Horndeski gravity. *JCAP*, 2016(2):053–053, February 2016. doi: 10.1088/1475-7516/2016/02/053.

[421] Johannes Noller and Andrina Nicola. Cosmological parameter constraints for Horndeski scalar-tensor gravity. *Phys. Rev. D*, 99(10):103502, 2019. doi: 10.1103/PhysRevD.99.103502.

[422] Kevork N. Abazajian et al. CMB-S4 Science Book, First Edition, 10 2016.

[423] Eric V. Linder and Robert N. Cahn. Parameterized Beyond-Einstein Growth. *Astropart. Phys.*, 28:481–488, 2007. doi: 10.1016/j.astropartphys.2007.09.003.

[424] Hans Winther, Santiago Casas, Marco Baldi, Kazuya Koyama, Baojiu Li, Lucas Lombriser, and Gong-Bo Zhao. Emulators for the nonlinear matter power spectrum beyond ΛCDM. *Phys. Rev. D*, 100(12):123540, 2019. doi: 10.1103/PhysRevD.100.123540.

[425] Matteo Cataneo, David Rapetti, Lucas Lombriser, and Baojiu Li. Cluster abundance in chameleon $f(R)$ gravity I: toward an accurate halo mass function prediction. *JCAP*, 12:024, 2016. doi: 10.1088/1475-7516/2016/12/024.

[426] Gong-Bo Zhao. Modeling the Nonlinear Clustering in Modified Gravity Models. I. A Fitting Formula for the Matter Power Spectrum of $f(R)$ Gravity. *Astrophys. J. Suppl.*, 211:23, 2014. doi: 10.1088/0067-0049/211/2/23.

[427] Michele Mancarella, Joe Kennedy, Benjamin Bose, and Lucas Lombriser. Seeking new physics in cosmology with Bayesian neural networks: Dark energy and modified gravity. *Phys. Rev. D*, 105(2):023531, 2022. doi: 10.1103/PhysRevD.105.023531.

[428] Aurel Schneider, Alexandre Refregier, Sebastian Grandis, Dominique Eckert, Nicola Stoira, Tomasz Kacprzak, Mischa Knabenhans, Joachim Stadel, and Romain Teyssier. Baryonic effects for weak lensing. Part II. Combination with X-ray data and extended cosmologies. *JCAP*, 04:020, 2020. doi: 10.1088/1475-7516/2020/04/020.

[429] Matteo Cataneo, David Rapetti, Fabian Schmidt, Adam B. Mantz, Steven W. Allen, Douglas E. Applegate, Patrick L. Kelly, Anja von der Linden, and R. Glenn Morris. New constraints on $f(R)$ gravity from clusters of galaxies. *Phys. Rev. D*, 92(4):044009, 2015. doi: 10.1103/PhysRevD.92.044009.

[430] Harry Desmond and Pedro G. Ferreira. Galaxy morphology rules out astrophysically relevant Hu-Sawicki $f(R)$ gravity. *Phys. Rev. D*, 102(10):104060, 2020. doi: 10.1103/PhysRevD.102.104060.

[431] Philippe Brax, Santiago Casas, Harry Desmond, and Benjamin Elder. Testing Screened Modified Gravity. *Universe*, 8(1):11, 2021. doi: 10.3390/universe8010011.

[432] KiDS Collaboration, Tilman Tröster, et al. KiDS-1000 Cosmology: Constraints beyond flat ΛCDM. *Astron. Astrophys.*, 649:A88, 2021. doi: 10.1051/0004-6361/202039805.

[433] Bartolomeo Fiorini, Kazuya Koyama, Albert Izard, Hans A. Winther, Bill S. Wright, and Baojiu Li. Fast generation of mock galaxy catalogues in modified gravity models with COLA. *JCAP*, 09:021, 2021. doi: 10.1088/1475-7516/2021/09/021.

[434] Bill S. Wright, Ashim Sen Gupta, Tessa Baker, and Georgios Valogiannis. `Hi-COLA`: Fast, approximate simulations of structure formation in Horndeski gravity, March 2023.

[435] Guilherme Brando, Bartolomeo Fiorini, Kazuya Koyama, and Hans A. Winther. Enabling matter power spectrum emulation in beyond-ΛCDM cosmologies with COLA. *JCAP*, 09:051, 2022. doi: 10.1088/1475-7516/2022/09/051.

[436] Jérôme Gleyzes, David Langlois, Michele Mancarella, and Filippo Vernizzi. Effective Theory of Interacting Dark Energy. *JCAP*, 08:054, 2015. doi: 10.1088/1475-7516/2015/08/054.

[437] C. Skordis, A. Pourtsidou, and E. J. Copeland. Parametrized post-Friedmannian framework for interacting dark energy theories. *Phys. Rev.*, D91(8):083537, 2015. doi: 10.1103/PhysRevD.91.083537.

[438] Shadab Alam, Shirley Ho, and Alessandra Silvestri. Testing deviations from ΛCDM with growth rate measurements from six large-scale structure surveys at z =0.06–1. *Mon. Not. Roy. Astron. Soc.*, 456(4):3743–3756, 2016. doi: 10.1093/mnras/stv2935.

[439] Ismael Tereno, Elisabetta Semboloni, and Tim Schrabback. COSMOS weak-lensing constraints on modified gravity. *Astron. Astrophys.*, 530:A68, 2011. doi: 10.1051/0004-6361/201016273.

[440] David Alonso, Emilio Bellini, Pedro G. Ferreira, and Miguel Zumalacárregui. Observational future of cosmological scalar-tensor theories. *Phys. Rev. D*, 95(6):063502, 2017. doi: 10.1103/PhysRevD.95.063502.

[441] Robert Reischke, Alessio Spurio Mancini, Björn Malte Schäfer, and Philipp M. Merkel. Investigating scalar–tensor gravity with statistics of the cosmic large-scale structure. *Mon. Not. Roy. Astron. Soc.*, 482(3):3274–3287, 2019. doi: 10.1093/mnras/sty2919.

[442] A. Spurio Mancini, R. Reischke, V. Pettorino, B. M. Schäfer, and M. Zumalacárregui. Testing (modified) gravity with 3D and tomographic cosmic shear. *Mon. Not. Roy. Astron. Soc.*, 480(3):3725–3738, 2018. doi: 10.1093/mnras/sty2092.

[443] Alexandre Barreira, Baojiu Li, Wojciech A. Hellwing, Carlton M. Baugh, and Silvia Pascoli. Nonlinear structure formation in the Cubic Galileon gravity model. *JCAP*, 1310:027, 2013. doi: 10.1088/1475-7516/2013/10/027.

[444] Claire Lamman, Eleni Tsaprazi, Jingjing Shi, Nikolina Niko Šarčević, Susan Pyne, Elisa Legnani, and Tassia Ferreira. The IA Guide: A Breakdown of Intrinsic Alignment Formalisms. *The Open Journal of Astrophysics*, 7:14, February 2024. doi: 10.21105/astro.2309.08605.

[445] Sarah Bridle and Lindsay King. Dark energy constraints from cosmic shear power spectra: impact of intrinsic alignments on photometric redshift requirements. *New J. Phys.*, 9:444, 2007. doi: 10.1088/1367-2630/9/12/444.

[446] Rachel Mandelbaum et al. The WiggleZ Dark Energy Survey: Direct constraints on blue galaxy intrinsic alignments at intermediate redshifts. *Mon. Not. Roy. Astron. Soc.*, 410:844, 2011. doi: 10.1111/j.1365-2966.2010.17485.x.

[447] Anya Paopiamsap, Natalia Porqueres, David Alonso, Joachim Harnois-Deraps, and C. Danielle Leonard. Accuracy requirements on intrinsic alignments for Stage-IV cosmic shear. *The Open Journal of Astrophysics*, 7:34, May 2024. doi: 10.33232/001c.117419.

[448] Jonathan Blazek, Matthew McQuinn, and Uros Seljak. Testing the tidal alignment model of galaxy intrinsic alignment. *JCAP*, 05:010, 2011. doi: 10.1088/1475-7516/2011/05/010.

[449] Denise M. Schmitz, Christopher M. Hirata, Jonathan Blazek, and Elisabeth Krause. Time evolution of intrinsic alignments of galaxies. *JCAP*, 07:030, 2018. doi: 10.1088/1475-7516/2018/07/030.

[450] Sukhdeep Singh, Rachel Mandelbaum, and Surhud More. Intrinsic alignments of SDSS-III BOSS LOWZ sample galaxies. *Mon. Not. Roy. Astron. Soc.*, 450(2):2195–2216, 2015. doi: 10.1093/mnras/stv778.

[451] DES Collaboration, S. Samuroff, et al. The Dark Energy Survey Year 3 and eBOSS: constraining galaxy intrinsic alignments across luminosity and colour space. *Mon. Not. Roy. Astron. Soc.*, 524(2):2195–2223, 2023. doi: 10.1093/mnras/stad2013.

[452] Giovanni Aricò, Raul E. Angulo, Matteo Zennaro, Sergio Contreras, Angela Chen, and Carlos Hernández-Monteagudo. DES Y3 cosmic shear down to small scales: Constraints on cosmology and baryons. *Astron. Astrophys.*, 678:A109, 2023. doi: 10.1051/0004-6361/202346539.

[453] KiDS Collaboration, T. M. C. Abbott, et al. DES Y3 + KiDS-1000: Consistent cosmology combining cosmic shear surveys. *Open J. Astrophys.*, 6:2305.17173, 2023. doi: 10.21105/astro.2305.17173.

[454] C. Danielle Leonard, Markus Michael Rau, and Rachel Mandelbaum. Photometric redshifts and intrinsic alignments: Degeneracies and biases in the 3 $\times$2 pt analysis. *Phys. Rev. D*, 109(8):083528, April 2024. doi: 10.1103/PhysRevD.109.083528.

[455] Alexander Mead. Spherical collapse, formation hysteresis and the deeply non-linear cosmological power spectrum. *Mon. Not. Roy. Astron. Soc.*, 464(2):1282–1293, 2017. doi: 10.1093/mnras/stw2312.

[456] A. J. Mead, S. Brieden, T. Tröster, and C. Heymans. HMCODE-2020: improved modelling of non-linear cosmological power spectra with baryonic feedback. *Mon. Not. Roy. Astron. Soc.*, 502(1):1401–1422, March 2021. doi: 10.1093/mnras/stab082.

[457] R.E. Smith et al. Stable clustering, the halo model and nonlinear cosmological power spectra. *Mon.Not.Roy.Astron.Soc.*, 341:1311, 2003. doi: 10.1046/j.1365-8711.2003.06503.x.

[458] Euclid Collaboration, Mischa Knabenhans, et al. Euclid preparation: II. The EuclidEmulator – A tool to compute the cosmology dependence of the nonlinear matter power spectrum. *Mon. Not. Roy. Astron. Soc.*, 484:5509–5529, 2019. doi: 10.1093/mnras/stz197.

[459] Ravi K. Sheth and Giuseppe Tormen. Large scale bias and the peak background split. *Mon. Not. Roy. Astron. Soc.*, 308:119, 1999. doi: 10.1046/j.1365-8711.1999.02692.x.

[460] Ravi K. Sheth and Giuseppe Tormen. An Excursion Set Model of Hierarchical Clustering : Ellipsoidal Collapse and the Moving Barrier. *Mon. Not. Roy. Astron. Soc.*, 329:61, 2002. doi: 10.1046/j.1365-8711.2002.04950.x.

[461] Julio F. Navarro, Carlos S. Frenk, and Simon D.M. White. A Universal density profile from hierarchical clustering. *Astrophys.J.*, 490:493–508, 1997. doi: 10.1086/304888.

[462] Gregory W. Horndeski and Alessandra Silvestri. 50 Years of Horndeski Gravity: Past, Present and Future. *Int. J. Theor. Phys.*, 63(2):38, 2024. doi: 10.1007/s10773-024-05558-2.

[463] Kazuya Koyama and Roy Maartens. Structure formation in the dgp cosmological model. *JCAP*, 01:016, 2006. doi: 10.1088/1475-7516/2006/01/016.

[464] Kazuya Koyama and Fabio P. Silva. Non-linear interactions in a cosmological background in the DGP braneworld. *Phys. Rev. D*, 75:084040, 2007. doi: 10.1103/PhysRevD.75.084040.

[465] Ian G. McCarthy, Joop Schaye, Simeon Bird, and Amandine M. C. Le Brun. The BAHAMAS project: Calibrated hydrodynamical simulations for large-scale structure cosmology. *Mon. Not. Roy. Astron. Soc.*, 465(3):2936–2965, 2017. doi: 10.1093/mnras/stw2792.

[466] Volker Springel et al. First results from the IllustrisTNG simulations: matter and galaxy clustering. *Mon. Not. Roy. Astron. Soc.*, 475(1):676–698, 2018. doi: 10.1093/mnras/stx3304.

[467] Joop Schaye et al. The FLAMINGO project: cosmological hydrodynamical simulations for large-scale structure and galaxy cluster surveys. *Mon. Not. Roy. Astron. Soc.*, 526(4):4978–5020, 2023. doi: 10.1093/mnras/stad2419.

[468] Aurel Schneider, Romain Teyssier, Joachim Stadel, Nora Elisa Chisari, Amandine M. C. Le Brun, Adam Amara, and Alexandre Refregier. Quantifying baryon effects on the matter power spectrum and the weak lensing shear correlation. *JCAP*, 03:020, 2019. doi: 10.1088/1475-7516/2019/03/020.

[469] Aurel Schneider and Romain Teyssier. A new method to quantify the effects of baryons on the matter power spectrum. *JCAP*, 12:049, 2015. doi: 10.1088/1475-7516/2015/12/049.

[470] Sambit K. Giri and Aurel Schneider. Emulation of baryonic effects on the matter power spectrum and constraints from galaxy cluster data. *JCAP*, 12(12):046, 2021. doi: 10.1088/1475-7516/2021/12/046.

[471] Aurel Schneider, Sambit K. Giri, Stefania Amodeo, and Alexandre Refregier. Constraining baryonic feedback and cosmology with weak-lensing, X-ray, and kinematic Sunyaev–Zeldovich observations. *Mon. Not. Roy. Astron. Soc.*, 514(3):3802–3814, 2022. doi: 10.1093/mnras/stac1493.

[472] DES Collaboration, A. Chen, et al. Constraining the baryonic feedback with cosmic shear using the DES Year-3 small-scale measurements. *Mon. Not. Roy. Astron. Soc.*, 518(4):5340–5355, 2023. doi: 10.1093/mnras/stac3213.

[473] Sebastian Grandis, Giovanni Arico', Aurel Schneider, and Laila Linke. Determining the baryon impact on the matter power spectrum with galaxy clusters. *Mon. Not. Roy. Astron. Soc.*, 528(3):4379–4392, 2024. doi: 10.1093/mnras/stae259.

[474] DES Collaboration, L. Bigwood, et al. Weak lensing combined with the kinetic Sunyaev Zel'dovich effect: A study of baryonic feedback. *arXiv e-prints*, art. arXiv:2404.06098, April 2024. doi: 10.48550/arXiv.2404.06098.

[475] Giovanni Aricò, Raul E. Angulo, Carlos Hernández-Monteagudo, Sergio Contreras, Matteo Zennaro, Marcos Pellejero-Ibañez, and Yetli Rosas-Guevara. Modelling the large-scale mass density field of the universe as a function of cosmology and baryonic physics. *Mon. Not. Roy. Astron. Soc.*, 495(4):4800–4819, July 2020. doi: 10.1093/mnras/staa1478.

[476] Giovanni Aricò, Raul E. Angulo, Sergio Contreras, Lurdes Ondaro-Mallea, Marcos Pellejero-Ibañez, and Matteo Zennaro. The BACCO simulation project: a baryonification emulator with neural networks. *Mon. Not. Roy. Astron. Soc.*, 506 (3):4070–4082, 2021. doi: 10.1093/mnras/stab1911.

[477] Elisabetta Semboloni, Henk Hoekstra, Joop Schaye, Marcel P. van Daalen, and Ian J. McCarthy. Quantifying the effect of baryon physics on weak lensing tomography. *Mon. Not. Roy. Astron. Soc.*, 417:2020, 2011. doi: 10.1111/j.1365-2966.2011.19385.x.

[478] Tim Eifler, Elisabeth Krause, Scott Dodelson, Andrew Zentner, Andrew Hearin, and Nickolay Gnedin. Accounting for baryonic effects in cosmic shear tomography: Determining a minimal set of nuisance parameters using PCA. *Mon. Not. Roy. Astron. Soc.*, 454(3):2451–2471, 2015. doi: 10.1093/mnras/stv2000.

[479] Irshad Mohammed and Nickolay Y. Gnedin. Baryonic Effects in Cosmic Shear Tomography: PCA Parameterization and the Importance of Extreme Baryonic Models. *Astrophys. J.*, 863(2):173, 2018. doi: 10.3847/1538-4357/aad3b1.

[480] Hung-Jin Huang, Tim Eifler, Rachel Mandelbaum, and Scott Dodelson. Modelling baryonic physics in future weak lensing surveys. *Mon. Not. Roy. Astron. Soc.*, 488 (2):1652–1678, 2019. doi: 10.1093/mnras/stz1714.

[481] B. Joachimi and S. L. Bridle. Simultaneous measurement of cosmology and intrinsic alignments using joint cosmic shear and galaxy number density correlations. *Astron. Astrophys.*, 523:A1, 2010. doi: 10.1051/0004-6361/200913657.

[482] A Spurio Mancini, F Köhlinger, B Joachimi, V Pettorino, B M Schäfer, R Reischke, E van Uitert, S Brieden, M Archidiacono, and J Lesgourgues. KiDS + GAMA: constraints on horndeski gravity from combined large-scale structure probes. *Mon. Not. Roy. Astron. Soc.*, 490(2):2155–2177, 09 2019. ISSN 0035-8711. doi: 10.1093/mnras/stz2581.

[483] Joachim Harnois-Déraps, Cesar Hernandez-Aguayo, Carolina Cuesta-Lazaro, Christian Arnold, Baojiu Li, Christopher T. Davies, and Yan-Chuan Cai. mglens: Modified gravity weak lensing simulations for emulation-based cosmological inference. *Mon. Not. Roy. Astron. Soc.*, 525(4):6336–6358, 2023. doi: 10.1093/mnras/stad2700.

[484] Bartolomeo Fiorini, Kazuya Koyama, and Tessa Baker. Fast production of cosmological emulators in modified gravity: the matter power spectrum. *JCAP*, 12:045, 2023. doi: 10.1088/1475-7516/2023/12/045.

[485] Euclid Collaboration, S. Casas, et al. Euclid: Validation of the MontePython forecasting tools. *Astron. Astrophys.*, 682:A90, February 2024. doi: 10.1051/0004-6361/202346772.

[486] Maximilian von Wietersheim-Kramsta, Kiyam Lin, Nicolas Tessore, Benjamin Joachimi, Arthur Loureiro, Robert Reischke, and Angus H. Wright. KiDS-SBI: Simulation-Based Inference Analysis of KiDS-1000 Cosmic Shear. *arXiv e-prints*, art. arXiv:2404.15402, April 2024. doi: 10.48550/arXiv.2404.15402.

[487] Christian Arnold and Baojiu Li. Simulating galaxy formation in f(R) modified gravity: Matter, halo, and galaxy-statistics. *Mon. Not. Roy. Astron. Soc.*, 490(2): 2507–2520, 2019. doi: 10.1093/mnras/stz2690.

[488] César Hernández-Aguayo, Christian Arnold, Baojiu Li, and Carlton M. Baugh. Galaxy formation in the brane world I: overview and first results. *Mon. Not. Roy. Astron. Soc.*, 503(3):3867–3885, 2021. doi: 10.1093/mnras/stab694.

[489] Marcel P. van Daalen, Joop Schaye, C. M. Booth, and Claudio Dalla Vecchia. The effects of galaxy formation on the matter power spectrum: A challenge for precision cosmology. *Mon. Not. Roy. Astron. Soc.*, 415:3649–3665, 2011. doi: 10.1111/j.1365-2966.2011.18981.x.

[490] Aurel Schneider, Nicola Stoira, Alexandre Refregier, Andreas J. Weiss, Mischa Knabenhans, Joachim Stadel, and Romain Teyssier. Baryonic effects for weak lensing. Part I. Power spectrum and covariance matrix. *JCAP*, 04:019, 2020. doi: 10.1088/1475-7516/2020/04/019.

[491] Willem Elbers, Carlos S. Frenk, Adrian Jenkins, Baojiu Li, John C. Helly, Roi Kugel, Matthieu Schaller, Joop Schaye, Joey Braspenning, Juliana Kwan, Ian G. McCarthy, Jaime Salcido, Marcel P. van Daalen, Bert Vandenbroucke, and Silvia Pascoli. The FLAMINGO project: the coupling between baryonic feedback and cosmology in light of the S_8 tension. *arXiv e-prints*, art. arXiv:2403.12967, March 2024. doi: 10.48550/arXiv.2403.12967.

[492] Alessio Spurio Mancini and Benjamin Bose. On the degeneracies between baryons, massive neutrinos and f(R) gravity in Stage IV cosmic shear analyses. *The Open Journal of Astrophysics*, 6:40, November 2023. doi: 10.21105/astro.2305.06350.

[493] Euclid Collaboration, N. Frusciante, et al. Euclid: Constraining linearly scale-independent modifications of gravity with the spectroscopic and photometric primary probes. *arXiv e-prints*, art. arXiv:2306.12368, June 2023. doi: 10.48550/arXiv.2306.12368.

[494] Antonio de Felice, Tsutomu Kobayashi, and Shinji Tsujikawa. Effective gravitational couplings for cosmological perturbations in the most general scalar-tensor theories with second-order field equations. *Physics Letters B*, 706(2):123–133, December 2011. doi: 10.1016/j.physletb.2011.11.028.

[495] Fabian Schmidt. Dynamical Masses in Modified Gravity. *Phys.Rev.*, D81:103002, 2010. doi: 10.1103/PhysRevD.81.103002.